



TECHNISCHE
UNIVERSITÄT
WIEN

DISSERTATION

ICs for Optical Wireless Communication

ausgeführt zum Zwecke der Erlangung des akademischen Grades
eines Doktors der technischen Wissenschaften unter der Leitung von

Univ.-Prof. Dr.-Ing. Horst Zimmermann
am Institute of Electrodynamics, Microwave and Circuit Engineering

eingereicht an der Technischen Universität Wien
Fakultät für Elektrotechnik und Informationstechnik

von

Dipl.-Ing. Paul Brandl

Matrikelnummer: 0030043

Hanningerweg 20

4501 Neuhofen an der Krems

Neuhofen, im Oktober 2016

For Moritz, Oliver and Pablo

Kurzfassung

Seit Beginn des Informationszeitalters, steigt die Menge der erzeugten und ausgetauschten Daten exponentiell an. Heutzutage werden diese Daten hauptsächlich durch ein weltumspannendes Glasfasernetz übertragen. Diese breitbandigen Glasfasersysteme werden mittlerweile nicht nur bis zu Verteilerstationen verlegt, sondern erreichen auch einzelne Gebäude und Büros. Das bezeichnet man als „Fiber-to-the-home“. Auf Grund dieser Entwicklung, nimmt auch die Datenmenge, die zwischen kabellosen Kommunikationsgeräten (Rechner, Smartphones, usw.) und diversen Zugriffspunkten des dahinterliegenden Kommunikationsnetzes ausgetauscht werden, kontinuierlich zu. Deshalb sind optische, kabellose Kommunikationssysteme eine wertvolle Ergänzung zu den immer mehr überlasteten, drahtlosen lokalen Netzwerken (WLAN).

In diese Dissertation wird die Entwicklung, Vermessung und Anwendung von opto-elektronischen integrierten Schaltungen beschrieben. Diese Schaltungen arbeiten als Empfänger von Daten in optischen, kabellosen Kommunikationssystemen innerhalb eines Raumes bzw. Gebäudes. Die entscheidenden Unterschiede zu Empfängern für Glasfasersystemen sind der größere Durchmesser der Photodiode, sowie die Problematik der zusätzlichen Störungseinflüsse auf Grund von Hintergrundlicht. Der Fokus dieser Arbeit liegt in der Entwicklung von voll integrierten optischen Empfängern in zwei unterschiedlichen Standardhalbleiterprozessen. Der erste Empfänger wurde in einer $0.35\ \mu\text{m}$ BiCMOS Silizium Technologie entwickelt mit dem Ziel einer möglichst hohen Datenrate. Dabei konnten die Vorteile von bipolaren Transistoren gegenüber Feldeffekttransistoren für den Bau von rauscharmen, schnellen Verstärkerschaltungen ausgenutzt werden. Der zweite Empfänger wurde in einer $0.35\ \mu\text{m}$ CMOS Silizium Technologie für Hochvoltanwendungen entwickelt mit dem Ziel einer möglichst hohen Empfindlichkeit. Dazu wurde eine Lawinenverstärkungs-Photodiode in den Empfänger integriert. Durch die Verstärkung der Photodiode konnte die Empfindlichkeit um mehr als 13 dB verbessert werden im Vergleich zu einer baugleichen Schaltung mit einer pn-Photodiode. Die volle Integration der Photodiode mit einer Verstärkerschaltung in einem Chip

reduziert entscheidend die Kosten der Verbindungs- und Aufbautechnik. Parasitäre Kapazitäten können durch das Wegfallen von zusätzlichen Bondpads minimiert werden und der Einfluss von Induktivitäten verursacht durch Bonddrähte wird gänzlich vermieden.

Als zusätzliche Besonderheit besitzen beide Chips ein Sensorsystem welches aus 4 weiteren Photodioden besteht. Die zusätzlichen Photodioden sind um die zentrale Photodiode angeordnet, wobei die zentrale Photodiode der Kommunikation dient. Die Photoströme von jeweils 2 gegenüberliegenden Photodioden bilden die Eingangssignale für einen Differenzverstärker. Das Ausgangssignal des Differenzverstärkers wird als Indikator benutzt, um die Position des Laserspots auf der Photodiodenanordnung zu bestimmen. Damit kann die optimale Positionierung des Laserspots erreicht werden.

Ein weiterer Teil dieser Arbeit beschäftigt sich mit der Entwicklung eines Senders, um die Empfänger innerhalb eines realen Kommunikationssystems zu testen. Der Sender verwendet einen VCSEL als Quelle, ein optisches System zur Fokussierung des Laserstrahls sowie einen auslenkbaren Spiegel. Der Spiegel ist auf einem MEMS montiert welcher die Position auf Grund der Elektrostatik verändern kann. Der sich ergebende Laserstrahl wurde mittels einer Kamera vermessen. Die Auslenkung des Laserstrahls konnte mit Hilfe des oben beschriebenen Sensorsystems justiert werden. In mehreren Kommunikationsexperimenten wurden die Empfänger getestet und vermessen. Im Vergleich zum aktuellen Stand der Technik konnte die Empfindlichkeit und Geschwindigkeit der Empfänger verbessert werden. Durch die erzielten Verbesserungen des Senders und Empfängers, konnte der Abstand zwischen Sender und Empfänger von ca. 3,5 m auf 19 m vergrößert werden und die Datenrate wurde von 1,25 GBit/s auf 3 GBit/s erhöht.

Abstract

Since the beginning of the age of information, the amount of transferred data is continuously and exponentially increasing. A global optical communication system based on optical fibers serves for transmitting these data. Nowadays, these broadband optical fiber systems begin to reach our offices and buildings. This is known by the keyword "fiber-to-the-home". Because of this development, the data amount between access points to these backbone networks and wireless communication devices (e.g. laptop, smart phones) is also continuously increasing. Therefore, optical wireless communication systems can complement wireless local area networks which suffer already from a congestion of available frequency bandwidth.

This PhD thesis describes the development, the characterization, and the application of opto-electronic integrated circuits working as receivers in optical wireless communication systems for indoor data transmission. The focus is the development of monolithically integrated optical receivers in two different standard silicon semiconductor technologies. The full integration of photodiodes with amplification circuits in one chip reduces the costs for integrated circuit packaging in a crucial way. The parasitic capacitance can be minimized by avoiding bonding pads and the inductive influence of bond wires can be eliminated completely. The main difference of wireless receivers compared to fiber receivers is the diameter of the photodiode as well as the additional noise caused by background lighting. One receiver was fabricated in a $0.35\ \mu\text{m}$ silicon BiCMOS technology aiming a high data rate. The available bipolar transistors allowed for high speed amplifiers of low noise. The other receiver was fabricated in a $0.35\ \mu\text{m}$ standard silicon high-voltage CMOS technology aiming a high sensitivity. To get high sensitivity, an avalanche photodiode was integrated into a CMOS receiver. Due to the photodiode's amplification, the sensitivity was improved by more than 13 dB compared to an identical receiver circuit with simple pn-photodiode.

As additional specialty, both receivers feature 4 more photodiodes which built a

sensor system. These 4 photodiodes were placed around the central photodiode where the central photodiode served for communication. The photocurrent of 2 opposite situated photodiodes fed a differential amplifier. With the output signal of the differential amplifier the position of the laser spot impinging the photodiode array was determined. Consequently, the optimal spot's position was achieved.

A further part of the thesis was the development of a transmitter for testing the receivers in a real communication scenario. A VCSEL built the source of the transmitter followed by an optical system for adjusting the focus of the laser ray. The direction of the laser ray was influenced by a steerable mirror. This mirror was mounted on a MEMS which changed the position by applying electrostatic force. The laser ray was characterized with the help of a camera. The displacement of the laser ray was adjusted with the above mentioned sensor system. In several communication experiments, the receivers were tested and characterized. In comparison to the state-of-the-art, the sensitivity and speed of the receivers were improved. Based on the transmitter concept and the receivers' improvements, the distance between transmitter and receiver was increased from approx. 3.5 m to 19 m as well as the data rate was enhanced from 1.25 Gbit/s to 3 Gbit/s.

Acknowledgment

I wish to express my sincere gratitude to my supervisor Univ.-Prof. Dr.-Ing. Horst Zimmermann for his continuous support and making this PhD thesis possible. Furthermore, I would like to thank Ao. Univ.-Prof. Dipl.-Ing. Dr. Erich Leitgeb from the Institute of Microwave and Photonic Engineering at the Technische Universität Graz and Ao. Univ.-Prof. Dr. Martin Gröschl from the Institute of Applied Physics at the Technische Universität Wien for acting as co-examiners.

I would like to thank all my colleagues at the Institute of Electrodynamics, Microwave and Circuit Engineering for the encouraging discussions and friendly work atmosphere. Special thanks go to Reinhard Enne, Wolfgang Gaberl, Andreas Polzer and Stefan Schidl for their assistance during the chip design phase and their support in the lab. I like also to thank Tomislav Jukic for his support during numerous measurement campaigns and Alexander Weiss for doing programming work. Moreover, I would also like to thank Reinhard Lang for his support during the construction of the optical transmitter and many other mechanical assemblies.

I wish to thank my parents for their support. Many thanks goes to my friends Günter, Karl, Markus and Robert for bringing regularly relief into the workaday life.

Last but not least, I would like to express my deepest gratitude to Karin for her unlimited patience over the last years. She did not only support me by spell-checking many papers and this work but was always there for me.

Contents

Kurzfassung	iv
Abstract	vii
Acknowledgments	ix
Abbreviations and Symbols	xiii
1. Introduction	1
1.1. Problem Specification	3
1.1.1. Optical Wireless Communication	3
1.1.2. Optical Receiver Design	7
1.2. Aims and Objective	13
1.3. Methodology	15
1.3.1. Optoelectronic Integrated Circuits	15
1.3.2. Optical Transmitter	21
1.4. Resume of Journal Papers	22
1.4.1. Elsevier Optics Communication 2012	23
1.4.2. IET Electronics Letters 2013	23
1.4.3. IEEE PTL 2013	23
1.4.4. Wiley ETT 2014	24
1.4.5. OSA Optics Letters 2014	24
1.4.6. IEEE JSTQE 2014	25
1.4.7. IET Electronics Letters 2014	25
1.4.8. IEEE PTL 2015	25
1.4.9. IEEE JSSC 2016	26
1.5. Scientific Contribution	26
2. Publications	29
2.1. Elsevier Optics Communication 2012	29
2.2. IET Electronics Letters 2013	33

Contents

2.3. IEEE PTL 2013	36
2.4. Wiley ETT 2014	41
2.5. OSA Optics Letters 2014	51
2.6. IEEE JSTQE 2014	56
2.7. IET Electronics Letters 2014	67
2.8. IEEE PTL 2015	70
2.9. IEEE JSSC 2016	75
3. Comparison and Conclusion	87
Bibliography	91
Appendix	99
A. Matlab-Code	101
A.1. Irradiance distribution of laser source	101
A.2. APD Ionization Coefficient	109
B. PCB Layouts	119
B.1. PCB for VCSEL and Laser driver	119
B.2. PCB for BiCMOS OEIC	122
B.3. PCB for HV-CMOS APD-OEIC	125
C. List of Own Publications	129
D. Curriculum Vitae	135

Abbreviations and Symbols

APD	avalanche photodiode
ARC	anti-reflection coating
ASIC	application-specific integrated circuit
BER	bit error ratio
BiCMOS	bipolar CMOS
BJT	bipolar junction transistor
<i>BW</i>	bandwidth
CMOS	complementary metal–oxide–semiconductor
ESD	electrostatic damage
FOV	field-of-view
<i>f</i>	frequency
<i>f_T</i>	transit frequency
FTTH	fiber-to-the-home
<i>h</i>	Planck constant
HV-CMOS	high-voltage CMOS
<i>i_{ph}</i>	photocurrent
IC	integrated circuit
ICs	integrated circuits
IM-DD	intensity-modulation direct-detection
<i>i_n^{rms}</i>	input-referred RMS noise current
<i>I_n²(f)</i>	input-referred noise current spectrum
<i>i_n²</i>	total noise current power

k_{eff}	effective ionization ratio of an APD
IrDA	Infrared Data Association
ISM	industrial, scientific, and medical
k	Boltzmann's constant
LD	laser diode
LED	light emitting diode
LOS	line-of-sight
MEMS	micro-electro-mechanical system
MOS-FET	metal-oxide-semiconductor field-effect transistor
NRZ	non-return-to-zero
OEIC	optoelectronic integrated circuit
OOK	on-off keying
OWC	optical wireless communication
P_{opt}	optical power
PCB	printed circuit board
PD	photodiode
pin	positive-intrinsic-negative
PRBS	pseudorandom bit sequence
q	elementary charge
R	responsivity
RF	radio frequency
R_{FB}	feedback resistor
rms	root mean square
Si	silicon
SNR	signal-to-noise ratio
c	speed of light
T	absolute temperature in degrees kelvin
TIA	transimpedance amplifier

VCSEL	vertical-cavity surface-emitting laser
VLC	visible light communication
VLCC	Visible Light Communication Consortium
λ	wavelength

1. Introduction

Optical communication has made a decisive contribution to the transition of the humanity into the information age. Huge data rates are transported via optical fibers around the world offering various broadband services such as high-definition TV, video telephone, high-speed internet access, etc. Known as fiber-to-the-home (FTTH), this high data rate traffic reaches our homes, offices etc. and the data has to be distributed in indoor networks. Wireless data distribution by means of wireless LAN IEEE 802.11 technology has been widely established in the case of radio frequency (RF) systems. The exploding number of wireless devices communicating in the industrial, scientific, and medical (ISM) radio spectrum is causing congestion and reliable communication is impeded by mutual interferences.

As an alternative, photonic home area networks can serve as complement to RF systems [1]. Optical interconnects benefit from nearly unbounded and license-free bandwidth, low propagation losses, reduced crosstalk and immunity to electromagnetic fields. Therefore, an optical wireless communication (OWC) system can improve on RF systems in areas where bandwidth or regulatory limitations exist and in applications where security is important. In most OWC systems, the transmitter is built with a cheap laser diode (LD) or light emitting diode (LED) and the receiver consists of a photodiode (PD) and an amplifier circuitry [2]. A block diagram of a generalized OWC system is illustrated in Fig. 1.1. Compared to receivers for fiber communication systems, the PD must have a larger collection area which can be increased with an optical concentrator. The transmitter power is strictly limited due to eye safety regulations [3]. Also, OWC systems operate in higher noise environments because of ambient light. The receiver design is extremely cost sensitive due to the fact that OWC receivers are intended for mass production. In most cases the receiver is integrated in an electronic way. The optical detector is a discrete device and the subsequent electronic circuitry is realized as either one or several integrated circuits (ICs). An alternative is an optoelectronic integrated circuit (OEIC) where the detector is monolithically integrated in

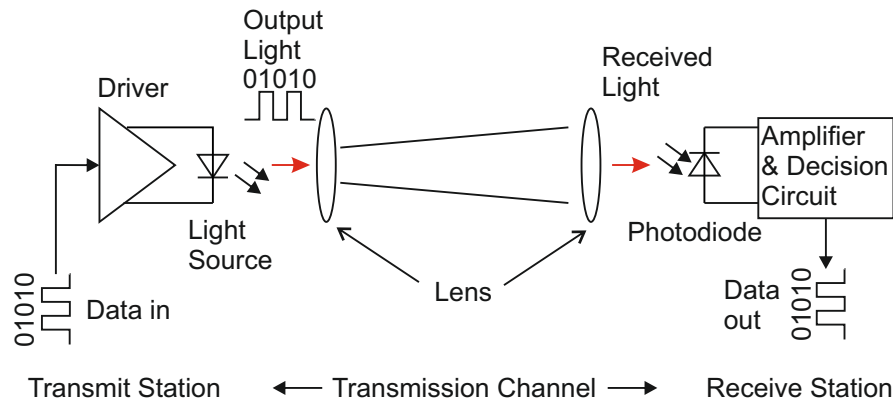


Figure 1.1.: Block diagram of an optical wireless communication system showing the front end of transmitter and receiver.

a chip with an amplifier. Compared to discrete receivers, OEIC technology has the advantages of reduced size, lower packaging cost and smaller interconnect parasitics.

This PhD thesis focuses on the design of monolithic integrated optical receiver chips in silicon technologies and their application in OWC systems for indoor use. This includes the following items:

- the development and characterization of integrated PDs realized as positive-intrinsic-negative (pin)-PD and as avalanche photodiode (APD),
- the design of integrated analog circuits and its characterization,
- the realization of the OEICs in $0.5\ \mu\text{m}$ bipolar CMOS¹ (BiCMOS), $0.35\ \mu\text{m}$ BiCMOS and $0.35\ \mu\text{m}$ high-voltage CMOS (HV-CMOS) technology,
- the development of a transmitter based on a vertical-cavity surface-emitting laser (VCSEL),
- the design of an optical unit for steering the laser ray built with a micro-electro-mechanical system (MEMS),
- the measurement of the laser ray characteristics,
- several communication experiments and
- an automatic alignment system based on image recognition.

The results were presented in 14 peer-reviewed publications (five conference papers

¹complementary metal-oxide-semiconductor (CMOS)

and nine journal papers). This thesis is structured as a cumulative work. It consists of an introduction chapter, followed by the journal papers, and a concluding chapter. The introduction is subdivided into 5 sections: problem specification, aims and objective, methodology, resume of publications, and scientific contribution. The following nine journal papers describe the achieved results with the different technologies. For the first journal paper the results obtained from an OEIC realized in 0.5 μm bipolar CMOS (BiCMOS) have been used. The journal papers 2 - 6 represent achievements obtained from an OEIC built in a 0.35 μm BiCMOS technology. The last three journal papers (7 - 9) deal with the results from a device developed in 0.35 μm HV-CMOS. In the conclusion the developed OEICs are compared to devices from literature.

1.1. Problem Specification

The development of wireless optical systems for communication requires multidisciplinary skills involving a wide range of areas including, among others, optical design, photonics, optoelectronics, electronics design, communications and information theory, modulation and equalization, and optical network architectures.

1.1.1. Optical Wireless Communication

The beginning of optical wireless communication can be dated back to the use of signal fires for sending a message. A first, more technological approach has been conducted by Alexander Graham Bell with his photophone in 1880 [4]. He used a diaphragm mirror to modulate the intensity of sunlight to transmit information over a distance of hundreds meters. A selenium crystal has been used as receiver which converted the optical signal into an electrical current.

The modern era of indoor OWC was initiated in 1979 with the pioneering work performed by F.R. Gfeller and U. Bapst. They suggested the use of diffuse emissions in the infrared band for an indoor communication network [5]. Since that time, a lot of work has been done in designing transmitter and receiver optics and electronics, developing new channel topologies, channel characterizing, and in the area of communication system design. Five generic system configurations have

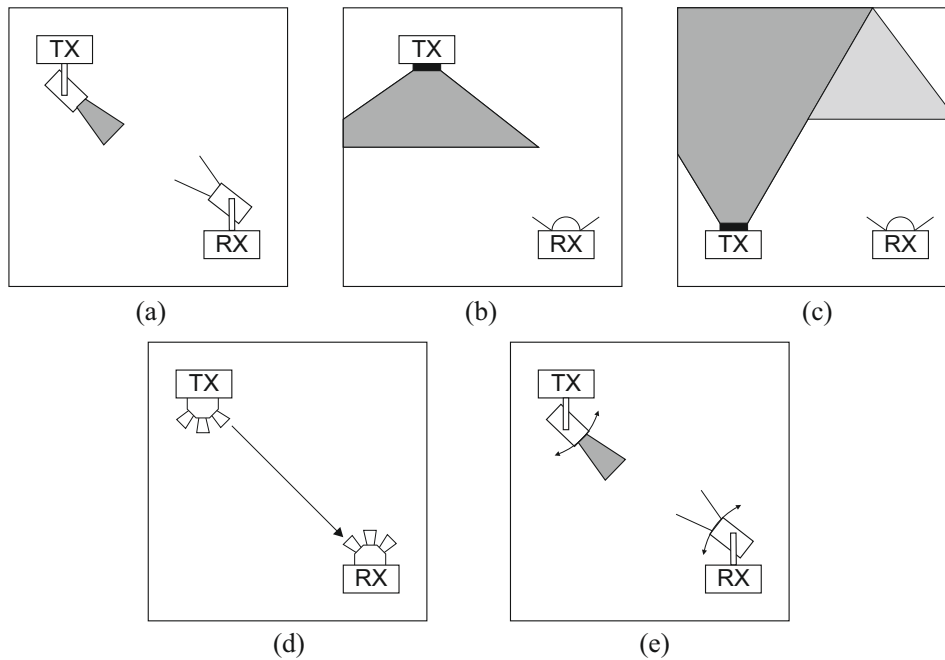


Figure 1.2.: Link configurations: (a) directed LOS, (b) non-directed LOS, (c) diffuse, (d) cellular, and (e) tracked

been proposed for optical wireless applications within the last 30 years: line-of-sight (LOS), non-LOS, cellular or angle-diversity, diffuse, and tracked. Fig. 1.2 gives an overview of the link configurations.

LOS

A directed LOS system shows a high power efficiency due to narrow beam transmitters and narrow field-of-view (FOV) receivers. Further, optical concentrators can be employed because of the narrow FOV receivers. The transmitter has to form a beam directed to the receiver and the latter has to focus on the incoming beam accurately to ensure large receive signal-to-noise ratio (SNR) and, hence, high data rate. Directed LOS systems do not suffer from multipath propagation, and ambient background light is largely rejected [6]. For high data rate transmission with a directed LOS link, accurate alignment of the transmitter and receiver is required limiting user mobility. The system is highly susceptible to blocking due to fact that

an uninterrupted line of sight path between transmitter and receiver is needed. In the early 1980's directed-LOS [7] and hybrid-LOS links have been established in remote-control units for low-bit-rate communication controlling domestic electrical equipment. Hybrid-LOS links combine transmitters and receivers with different degrees of directionality. Typically, these links transmit using a single LED with an emission wavelength between 850 nm and 950 nm and an average power of several tens of mW concentrated within a semi-angle of 15° - 30° [8]. In 1993 one of the most successful standards, the Infrared Data Association (IrDA) standard, was formed [9]. Today, a 4 Mbit/s data transfer rate is established for a LOS link with a maximum distance of 1 m. Further, products operating at 16 Mbit/s exist and IrDA members are working on an 10 Gbit/s standard over a distance of 10 cm.

non-LOS

Non-directed LOS systems use a wide beam transmitter and a wide FOV receiver to obtain an increased coverage area and to facilitate the pointing. These systems avoid the stringent condition for a precise alignment of transmitter and receivers, but at the expense of reduced irradiance compared to direct LOS. The lower irradiance level at the receiver will not allow for high data rates. In [10], a 155 Mbit/s link with a large-area silicon APD has been implemented. In the last years, visible light communication (VLC) technology has gained a lot of attention in academia and industry. This technology is driven by the progress in the development of white LEDs for solid-state lighting and at the same time the use of such LEDs for wireless data transmission [11]. A lot of pioneering work has been done by the Visible Light Communication Consortium (VLCC) in Japan [12] which has lead to the IEEE 802.15.7 standard for short-range Optical Wireless Communication in 2011 [13].

Diffuse

In diffuse configurations, the link coverage relies upon the reflections of room boundaries. This configuration was proposed in [5] with a wide beam transmitter pointing vertically upward towards the ceiling. The receiver had a wide FOV to collect the signal leading to some convenient attributes. Diffuse systems do not

require any pointing, nor a LOS path between transmitter and receiver permitting nearly unlimited mobility. However, diffuse link topologies suffer from high optical path losses due to the reflection before the reception. Those losses are in the range of 30 dB to 70 dB resulting into systems with a high-power transmitter and a highly-sensitive receiver. Nevertheless, the research community has shown great interest in diffuse configuration. In [8], an experimental link with bit rates up to 50 Mbit/s has been reported.

Cellular or angle-diversity

Significant performance improvements for non-directed LOS and diffuse systems can be achieved by using multiple-transmitter and multiple-receiver structures. This so called cellular or angle-diversity systems offer a coarse pointing and spatial diversity and can be implemented in two ways [14, 15]. Multiple receiving elements each with a non-imaging concentrator are oriented in different directions. This is one way to implement an angle-diversity receiver resulting into a bulky, expensive device. The other way is the imaging angle-diversity receiver or so called "fly-eye receiver" proposed by Yun and Kavehrad [16]. In the context of the European Union project OMEGA, a 1.25 Gbit/s angle diversity optical wireless system has been implemented [17]. The distance of 3 m was covered with three transmitters of 25 mW each. Each transmitter and receiver had a FOV of 8°. It can be concluded that the transmitter and receiver device still had to be adjusted and at the same time a lot of optical transmit power had to be used. Therefore, such a large FOV does not really make sense.

Tracked LOS

Tracked LOS systems offer high data rates of directed LOS and at the same time increased coverage. Mechanical steerable optics was used in [18] to build a tracked system with a bit rate of 1 Gbit/s. The drawback of mechanical steerable optics are costs and the bulky size. In [19], a system including electronic tracking at the receiver and the transmitter by arrays of photo detectors and laser diodes, respectively, was presented. The experimental system showed 155 Mbit/s wireless transmission over a distance of nearly 2 m. A tracked system based on a mechanical positioning mechanism at the receiver was proposed in [20, 21].

There are several more engineering aspects when designing a OWC system. The main element of the transmitter is in most cases a LD or LED. Those devices have to be selected accordingly to several parameters including: (1) wavelength, (2) modulation bandwidth, (3) optical transmission power (eye safety regulations), and (4) beam divergence. For beam shaping, an optical element like lenses or diffusers can be applied. An OWC receiver consists typically of an optical concentrator (lenses, compound parabolic concentrator) followed by an optical filter rejecting ambient light. A photodetector converts the optical signal into a corresponding current and further electronic circuitry provides amplification, filtering, and data recovery. A detailed discussion of all these aspects go far beyond the scope of this thesis. The publications [8, 22–25] give a good overview and include many references about research performed in the field of indoor OWC within the last 20 years. The above mentioned publications include also information on optical channel modeling and modulation schemes for OWC. More information on those topics can be found in the books from Barry [6], Hranilovic [26], and Ghassemlooy et al [27]. In contrast to conventional RF systems, the optical channel uses intensity-modulation direct-detection (IM-DD) signaling resulting into two significant differences. First, the transmitted signal is always positive. Secondly, the average amplitude is limited in an IM-DD channel compared to a conventional RF channel where the average power is restricted. This is because the optical receiver responds on power which is converted into a photocurrent. Due to the simplicity and bandwidth efficiency of non-return-to-zero (NRZ) on-off keying (OOK), this is the most popular modulation format for optical communication systems [28].

1.1.2. Optical Receiver Design

This section summarizes the theory for optical receiver design in a short form. Converting the light signal from optical into electrical domain is the main task of an optical receiver. Fig. 1.3 shows a block diagram of a typical optical receiver. OWC receivers are very similar to fiber-based receivers which consist essentially of a photodetector and an amplifier. The photodetector is usually a pin-PD or an APD and it generates a photocurrent in response to the impinging optical signal. The generated photocurrent is amplified and converted in a voltage. In most cases this first amplifier is realized as transimpedance amplifier (TIA) due to its advantages compared to low-impedance or high-impedance amplifier design [29]. The output voltage signal from the TIA is amplified by a subsequent limiting amplifier which

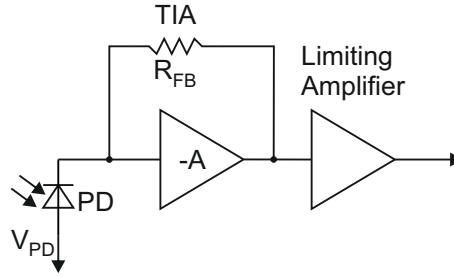


Figure 1.3.: Block diagram of typical optical receiver realized as transimpedance amplifier (TIA).

consists typically of several gain stages and an output driver.

Max Planck found in 1900 that the energy and momentum of light is quantized in the so called photons. The energy E_{ph} of one photon with a frequency (f) is

$$E_{ph} = h \cdot f \quad (1.1)$$

where $h = 6.625 \times 10^{-34}$ is the Planck constant. The interaction of light with semiconductor devices is based on the photoelectric effect explained by Albert Einstein in 1905 for the first time. This effect is a particle-particle process between photons and electrons of a material. Semiconductor photodetectors use the internal photoelectric effect in the form of absorption [30]. The energy of a photon is absorbed and one electron is pushed from the valence band into the conduction band. To enable this effect, the energy of the impinging photon must be higher than the energy of the semiconductor bandgap E_g

$$E_{ph} = hf = h \frac{c}{\lambda} \geq E_g \quad (1.2)$$

with the speed of light (c) and the wavelength (λ). The E_g of silicon (Si) is 1.12 eV which results into a maximum detectable λ of approx. 1110 nm. When photons are penetrating a semiconductor, the optical field decays exponentially. Therefore, the material can be characterized by an absorption length α or a penetration depth $1/\alpha$ which is a strong function of wavelength. The optical signal power is reduced to $1/e$ at the point of the penetration depth [29]. There is an inherent tradeoff between quantum efficiency (desire a long absorption region) and bandwidth (minimize the transit time) of a detector expressed by the length of the absorbing region.

The photocurrent (i_{ph}) for a certain optical power (P_{opt}) is given by

$$i_{ph} = \frac{\eta q}{hf} P_{opt} \quad (1.3)$$

where the elementary charge (q) is 1.602×10^{-19} C and $0 \leq \eta \leq 1$ is the photodetector's quantum efficiency. The responsivity (R) of the semiconductor material is derived from the above stated Eq. (1.3)

$$R = \frac{\eta q}{hf} \quad (1.4)$$

where R has the dimension of A/W.

Photodiode

The PD is a p - n junction working as photodetector converting the optical signal into an electrical signal. The main requirements of optical wireless detectors are [2]:

- High responsivity at the operating wavelength.
- High fidelity or linearity.
- Large detection area to increase the effective detection FOV and to facilitate the alignment.
- Short response time to operate the system into the GHz domain.
- Minimum noise and dark current.
- Minimum excess noise factor for APDs.
- High reliability and stability.
- Capable of being monolithically integrated in case of OEICs [31].

A pin photodiode has a layer of intrinsic semiconductor material between the p and n layers. This increases the length of the depletion region which increases the quantum efficiency and decreases the junction capacitance [32]. Further, the electric field is nearly constant throughout the depletion region keeping the photo-generated electrons and holes moving at a high velocity (near their saturation velocity depending on the applied voltage). The combination of light induced photocurrent (i_{ph}) and conventional DC current-voltage can be written as

$$i_{diode} = i_s \left[\exp\left(\frac{qV_D}{kT}\right) - 1 \right] - i_{ph} \quad (1.5)$$

where i_s = reverse saturation current, V_D = voltage across the PD, k = Boltzmann's constant, and T = absolute temperature in degrees Kelvin. The main noise source associated with PDs is the shot noise generated from the light signal and can be modeled as a noise current with a value given by

$$i_n^2 = 2qi_{ph}BW, \quad (1.6)$$

where BW is the bandwidth of the system.

Avalanche Photodiode

An APD can generate many electron-hole pairs from a single absorbed photon due to a more sophisticated structure. Compared to the pin PD, the APD has an additional fourth layer which is higher doped than the intrinsic zone. In this fourth layer, additional carriers are generated by impact ionization and this layer is the so-called multiplication zone. The gain or multiplication factor of an APD is

$$M = \frac{i_{ph}}{i_{primary}}, \quad (1.7)$$

where $i_{primary}$ is the internal photocurrent before multiplication. The ionization coefficients, α_e for electrons and α_h for holes, describe the probability that an electron or hole will have an ionization collision within a unit length. The effective ionization ratio

$$k_{eff} = \frac{\alpha_h}{\alpha_e}, \quad (1.8)$$

is an important parameter for describing the APD performance [33]. The multiplication process in an APD is a random process. Therefore, the multiplication produces some additional noise expressed as excess noise factor. This noise factor is particularly sensitive to this ionization ratio and can be expressed as

$$F(M) = k_{eff}M + (1 - k_{eff}) \left(2 - \frac{1}{M}\right). \quad (1.9)$$

The smaller k_{eff} is, the better the APD is. For Si the values for k_{eff} are typically between 0.06 down to 0.02 [34], even values down to 0.002 have been reported for elaborated structures [35]. The noise current of an APD is expressed by

$$i_n^2 = 2qi_{ph}M^2F(M)BW. \quad (1.10)$$

A comprehensive analysis regarding different noise sources for pin and avalanche photodiode based wireless optical receivers can be found in [36].

Receiver performance

The theoretical analysis of an optical receiver design is based on the pioneering work done by Personick [37] resulting in lot of publications. [38] presents a compressed summary. The transimpedance amplifier design, as depicted in Fig. 1.3, shows the advantage of extended bandwidth and high-dynamic range compared to high impedance design. To minimize the drawback of higher noise levels because of thermal noise from the feedback resistor (R_{FB}), the feedback resistor should be as large as possible. The bandwidth of a TIA is mainly determined by this R_{FB} and the total input capacitance C_T including photodiode and stray capacitance. The -3 dB bandwidth is approximated by [39]

$$f_{-3dB} \approx \frac{1}{2\pi} \frac{A}{R_{FB}C_T} \quad (1.11)$$

where A is the amplification of an ideal voltage amplifier. One of the most important receiver characteristics is the sensitivity which is defined as the minimum average optical input power required to achieve a specified bit error ratio (BER) at a certain data rate. The optical sensitivity is [40]

$$\bar{P}_{sens} = \frac{Q \cdot i_n^{rms}}{R} \quad (1.12)$$

where i_n^{rms} is the input referred root mean square (rms) noise current and the Q -parameter is a measure of the ratio between signal and noise (a BER $\leq 10^{-9}$ corresponds to a $Q \approx 6$ [29]).

Equivalent input noise of BJT front-end

When a bipolar junction transistor (BJT) is the active front-end device in a common emitter configuration, the input referred noise current is given by [37, 38]

$$i_n^2 = \frac{4kT}{R_{FB}} I_2 BW + 2eI_b I_2 BW + \frac{2eI_c}{g_m^2} (2\pi C_T)^2 I_3 BW^3 + 4kTr_b (2\pi C_D)^2 I_3 BW^3 \quad (1.13)$$

where

BW bandwidth,
 R_{FB} feedback resistance,

1. Introduction

k	Boltzmann constant,
T	absolute temperature,
I_b and I_c	base and collector bias current,
r_b	base resistance of the transistor, and
g_m	transistor transconductance

given by $g_m = I_c/V_T$ with $V_T = kT/q$ the thermal voltage. The total capacitance C_T is given by

$$C_T = C_D + C_\pi + C_\mu \quad (1.14)$$

where C_π and C_μ are the transistor's small-signal model capacitances and C_D is the sum of the detector, stray, and feedback capacitance. I_2 and I_3 are weighting functions depending on the receiver's optical input and equalized output pulse shape (Personick integrals [37]); $I_2 = 0.562$ and $I_3 = 0.0868$ for a NRZ signal and an output pulse with a full raised cosine spectrum. For equation (1.13) an optimum collector current exists which minimizes the sum of the collector and base current noise contributions. I_b is proportional to I_c via the current gain β . On the other hand, the transconductance g_m is proportional to I_c and therefore the collector current noise is inversely proportional to I_c . At the optimum biasing current, the input noise current power can be approximated by [37, 38]

$$i_n^2 \approx \frac{4kT}{R_{FB}} I_2 BW + 8\pi k T C_T \sqrt{\frac{I_2 I_3}{\beta}} BW^2 + 4k T r_b (2\pi C_D)^2 I_3 BW^3 \quad (1.15)$$

Equivalent input noise of MOS-FET front-end

The equivalent input noise current power for a metal–oxide–semiconductor field-effect transistor (MOS-FET) front-end amplifier in common source configuration is given by

$$i_n^2 = \frac{4kT}{R_{FB}} I_2 BW + 2e I_g I_2 BW + \frac{4kT\Gamma}{g_m} (2\pi C_T)^2 f_c I_f BW^2 + \frac{4kT\Gamma}{g_m} (2\pi C_T)^2 I_3 BW^3 \quad (1.16)$$

where

I_g	MOS-FET gate current,
g_m	MOS-FET transconductance,
f_c	the $1/f$ noise corner frequency of the MOS-FET,
Γ	channel-noise factor (between 0.7 to 3.0), and

I_f a further weighting function [37] which corresponds to 0.0984 for the above mentioned signal.

The total capacitance C_T is given by

$$C_T = C_D + C_{gs} + C_{gd} + C_f \quad (1.17)$$

where C_D is the PD capacitance at the input, C_{gs} and C_{gd} are the gate-source and gate-drain capacitances of the MOS-FET, and C_f is the feedback capacitance.

The equivalent input noise current is given for a BJT front-end by (1.15) and for a MOS-FET front-end by (1.16). The noise shows a BW^3 dependence in the case of a MOS-FET. For the BJT, the noise varies with BW^2 when r_b is small and with BW^3 when the noise from the base resistance dominates. Therefore, at higher bit rates the noise produced by bipolar devices is less compared to noise from MOS-FET devices. At lower bit rates, the MOS-FET shows a better noise performance. Excluding sub-nanometer technologies, MOS-FETs are not generally used beyond a few GHz due to their higher capacitance and lower transit frequency (f_T) compared to BJTs. A further advantage of BJTs over MOS-FETs is the at least an order of magnitude higher transconductance.

1.2. Aims and Objective

The main research challenge was to build highly sensitive fully integrated optical receivers that allow for very high data rates at limited transmit power. The photodetector had to be designed well to allow for high speed communication and the photodetector's diameter had to be large to facilitate the alignment process of transmitter and receiver. In parallel, a transmitter with a light spot diameter of less than 1 cm in a few meters for a LOS OWC system had to be designed. This strong focusing allows for reduced transmit power and for increased transmission distances and higher data rates.

An important task was the construction of the focusing mechanics and the beam steering. The possibility of beam steering allows for a certain coverage area and therefore increases the mobility. Due to cost reasons, the opto-mechanical system

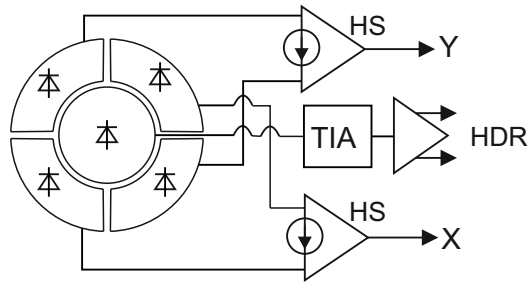


Figure 1.4.: Simplified block diagram of the optoelectronic integrated circuit with PD array and high-sensitivity (HS) and high data rate (HDR) receivers.

had to be built on off-the-shelf components and the dimensions had to be minimized. A theoretical approach for designing a mechanical system at the receiver side can be found in [21, 41]. In [42], an adaptive lens with a steerable mirror at the transmitter side was proposed. To minimize the dimensions, the usage of steerable mirrors based on MEMS technology was examined.

Another objective was to build a sensor system by a small array of PDs which allowed for determining the position of the laser spot on the photodetectors. The PD array is shown in Fig. 1.4. The four PDs surrounding the center PD serve for determining at which position the laser beam is impinging the PD array. Two oppositely situated PDs are connected to a highly-sensitive differential amplifier. This amplifier produces an output signal indicating the light power difference impinging at the opposing PDs. Based on this information, the steering of the laser beam can be adjusted in such a way that the most optical power is received by the center PD. The development of the whole control loop including the feedback channel to the transmitter is beyond the scope of this thesis. In an experiment, the adjustment of the laser without a feedback channel has been explored using imaging processing technology, see section 2.5. The center PD together with a high data rate receiver builds the main circuitry for communication purposes. In some previously presented receivers, either custom-designed compound semiconductor photodetectors [43, 44] were flip-chip bonded to amplifiers realized in a CMOS technology, or expensive, discrete receiver-optical sub-assemblies (ROSA) [45] were used. Compared to those strategies, the approach taken here was the development of fully integrated optical receivers to profit from the advantages of a monolithic solution [46, 47]. The main goal was to increase the sensitivity and bandwidth of the receivers in comparison with the state-of-the art. This led

to higher data rates and larger link distances of optical wireless communication systems.

Besides the integration of large-diameter pin PDs, this thesis also describes the development of an OEIC including a large-diameter APD. Recently published integrated APDs were mainly realized as simple pn-junction diodes in nm CMOS processes [48–50]. Those APDs suffer from a rather low responsivity due to the short absorption region. To tackle this issue, the goal was to implement an APD with a long absorption region. However, higher voltages are necessary to completely deplete this longer region. Therefore, a HV-CMOS technology was used to safely apply the high voltages and not to jeopardize the remaining circuits in the OEIC. This OEIC was then used to explore the advantage of signal amplification by the APD.

1.3. Methodology

Based on an existing OEIC in 0.5 μm BiCMOS technology, first communication experiments were established to figure out the main parameters and constraints. With the gained knowledge, two different types of receivers were designed: a high-speed receiver exploring the advantage of a 0.35 μm BiCMOS technology and a highly-sensitive receiver exploring the advantage of an integrated APD within a CMOS technology. The development includes semiconductor device modeling for the PDs, circuit simulation and designing the layout within the Cadence® Virtuoso® Environment resulting into an application-specific integrated circuit (ASIC). For each integrated circuit (IC) version, a printed circuit board (PCB) for testing purposes was prepared.

In parallel, a transmitter was developed based on a VCSEL and a MEMS mirror system.

1.3.1. Optoelectronic Integrated Circuits

In an opto-electronic integration, the detector is monolithically integrated with the preamplifier. This has the advantages of high performance, high reliability, reduced size, smaller interconnect parasitics, and lower packaging cost. However,

compared to hybrid counterparts, the OEIC receivers are often less sensitive because compromises must be made when the photodetector and transistors are fabricated on the same wafer and with the same set of processing steps. A pioneering work on Silicon monolithic integration of optical and electronic components on the same chip has been done by Yamamoto et al. [51]. Since then, numerous publications can be found in literature on various aspects of integration. Realizing photodetectors in standard CMOS / BiCMOS technologies were recently treated for example in [52–54]. The main influencing parameters when designing an integrated PD are the operating wavelength, the data rate, and the maximum applicable voltage. Those parameters determine the ideal thickness of the intrinsic zone. The dynamic responsivity and capacitance of the PD is heavily dependent on the thickness. An increased intrinsic zone leads to a higher responsivity and lower capacitance, but at the same time this thicker zone leads to longer transit time reducing the speed of the PD. This can be counteracted with an increased applied voltage rising the electric field and consequently the carrier velocity. The optimum is given when the strength of the electrical field is equally distributed within the space charge region and when the value of the field strength is high enough to reach the saturation drift velocity. The sensitivity of an integrated optical receiver is heavily dependent on the reached responsivity and capacitance values.

Numerous literature dealing with complete OEICs can be found in the included publications in the second part of the thesis. The books [31, 55, 56] summarize the development of OEICs. The design principles of circuits for optical receivers are discussed extensively in the books from Säckinger [40] and Razavi [39].

OEIC implementation in BiCMOS

The first OEIC was designed in a 0.35 μm BiCMOS technology. A p-substrate silicon wafer together with a low doped p-epitaxial layer on top of substrate was used for the implementation of the PDs. The BiCMOS process is based on an opto-CMOS process extended by three additional layers to generate a fast npn bipolar transistor in a standard buried collector technology. This opto-CMOS process offers a specific layer for implementing pin-PDs with an anti-reflection coating (ARC). Fig. 1.5 shows a cross section of the realized pin-PD and the structure of the vertical bipolar n-p-n transistor. In [47], a 0.6 μm BiCMOS technology with a PD diameter of 400 μm has been used to overcome a distance of 50 cm with a data rate of 1.25 Gbit/s. In

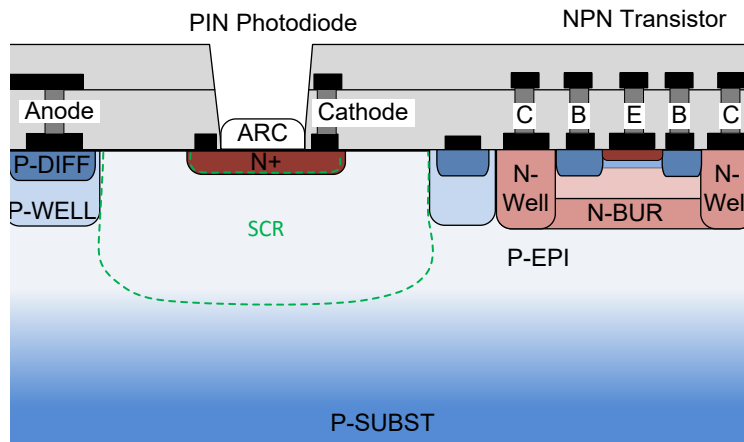


Figure 1.5.: Cross section of pin-PD and bipolar transistor implemented in $0.35\ \mu\text{m}$ BiCMOS technology, anti-reflection coating (ARC), space-charge region (SCR).

[57], a $0.6\ \mu\text{m}$ BiCMOS OEIC with a PD diameter of $300\ \mu\text{m}$ has been presented which achieved a sensitivity of $-20.1\ \text{dBm}$ at a data rate of $2.5\ \text{Gbit/s}$. Compared to those OEICs, the receivers' sensitivity in this thesis was increased by reducing the PD capacitance via reducing the area. By switching from $0.6\ \mu\text{m}$ to $0.35\ \mu\text{m}$ BiCMOS, the electronic noise was lowered due to a reduction of the thermal noise from the base resistance. At the same time, the transit frequency of the transistors was increased to allow for faster receiver designs.

The p-substrate works as anode of the PD and is connected via large-area p-diff and p-well contacts to minimize the resistance through the low-doped p epitaxial zone. The p-substrate was connected to a negative voltage supply to bias the pin-PD with a voltage of up to $-20\ \text{V}$. Not to provoke a premature electrical breakdown, all electrostatic damage (ESD) protection circuits were deleted from the pad layouts. A protection diode from signal pads to VDD remained within the complete OEIC and provoked a parasitic diode between the n-well and the substrate. This parasitic diode showed a breakdown voltage of approx. $11.6\ \text{V}$. Consequently with a VDD of $3.3\ \text{V}$, the voltage between ground and substrate was limited to a maximum value of $-8.3\ \text{V}$.

As discussed in section 1.1.2, the equivalent input noise current of the receiver is mainly defined by the parameters of the PD and the input transistor stage after

the PD. To minimize the noise current, the parameters of the input transistor were optimized according to the characteristic of the PD. The base resistance noise can be minimized by layout considerations through increasing the area, but having in mind the transistor's input capacitance C_π which also increases with the area. The collector shot noise current decreases with the collector current I_C by increasing $g_m = I_C/V_T$. However, the base shot noise current increases with the collector current. Therefore, an optimum collector current exists, but the optimization is complicated due to the fact that C_π also depends on I_C . The circuit depicted in Fig. 1.6 was used to find the optimum parameters for the input transistors. The PD was modeled with the current source I_{sig} and the capacitance C_{PD} . The first parameter I_C was applied to transistor T_2 and via a voltage-controlled voltage source E_1 the corresponding base current I_{base} was adjusted. This I_{base} was used to bring T_1 into the same working state through a current-controlled current source F_1 . V_{work} was set to approx. 2 V simulating the working point. The resulting current I_{work} was transferred to an output voltage V_{out} . The second parameter is the effective emitter area of the transistors. This area was uniformly varied for both transistors. The noise analysis was done with I_{sig} as input signal and V_{out} as output. The result was the input-referred noise current spectrum ($I_n^2(f)$). This spectrum was then integrated to the projected bandwidth of the TIA to get the input-referred noise current. The bandwidth of the TIA was set to 2 GHz. Finally, the square root was taken to get the input-referred RMS noise current (i_n^{rms}), see the following equation:

$$i_n^{rms} = \sqrt{\int_0^{BW} I_n^2(f)}. \quad (1.18)$$

The results of these simulations can be seen in Fig. 1.7. The optimum is reached for a collector current of approx. 2.11 mA and a transistor area of $70 \mu\text{m}^2$. After the parameters of the input transistors are determined, the remaining circuitry can be designed. However, a regular noise simulation must be done to check the influence of the additional components in the circuit and to stay on the optimum noise performance value. To minimize the influence of the following transistor stages on the overall noise performance, the gain of the first stage must be sufficiently high.

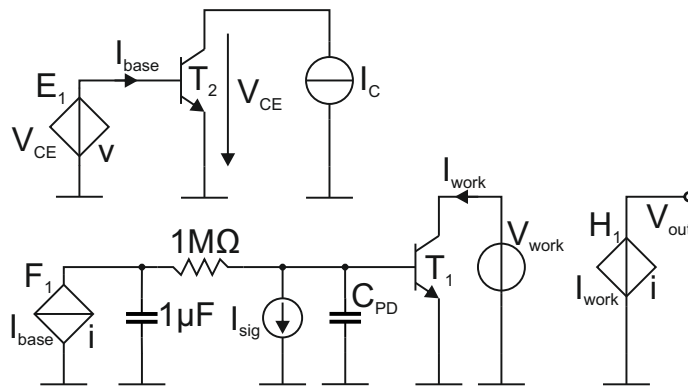


Figure 1.6.: Circuit diagram for simulating input-referred rms noise current depending on transistor area and collector current for a PD capacitance C_{PD} of 600 fF.

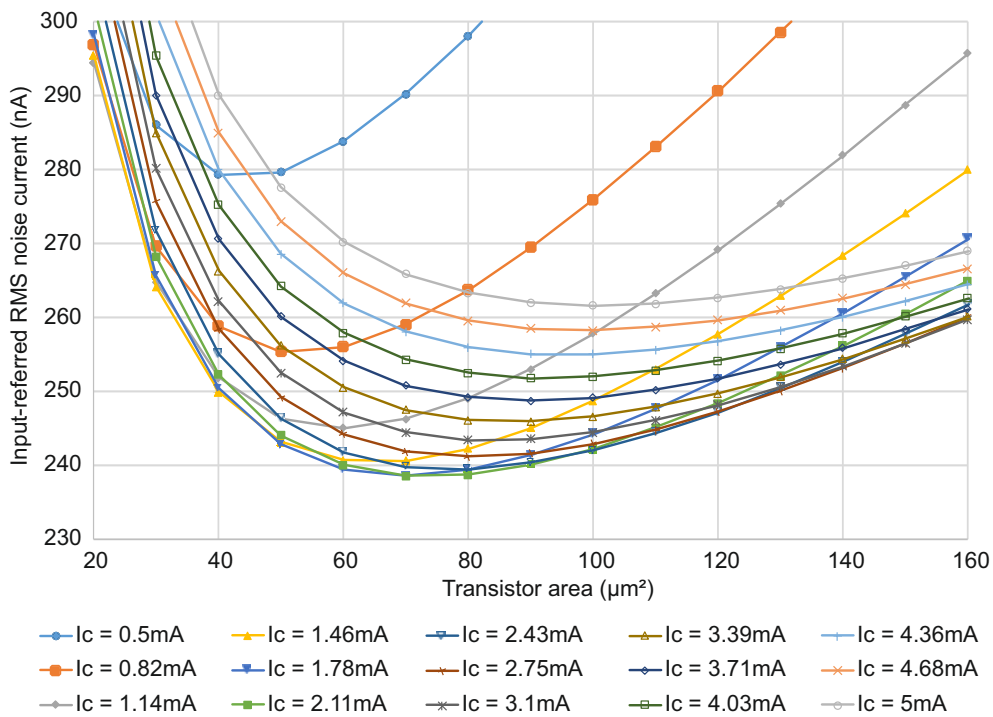


Figure 1.7.: Simulated input-referred rms noise current depending on transistor area and collector current for a PD capacitance of 600 fF.

OEIC implementation in HV-CMOS

The HV-CMOS technology was used to implement an APD and a CMOS circuitry in a single chip. This technology allows for applying the required high voltage needed by the APD while observing all process reliability operation specifications. The used HV-CMOS process offers different wells to isolate the MOS transistors down to substrate potentials of -100 V, see Fig. 1.8. Recently published monolithically integrated APDs use a simple pn-junction to reduce the required voltage for avalanche gain [49, 58]. However, these simple pn-junction APDs suffer from a higher excess noise factor. This is a result of the mixed carrier injection leading to an ionization coefficient close to unity because the absorption region serves at the same time as multiplication region. The used HV-CMOS technology allows for implementing an APD with a separated absorption and multiplication region. The effective ionization coefficient was determined by measuring the excess noise factor, see appendix A.2. As depicted in Fig. 1.8, the absorption region is built by the low-doped epitaxial zone and the deep n- well [59]. The multiplication takes place inside the deep p-well zone close to the highly doped n layer which works as cathode. On top of the n+ zone an ARC was placed. The deep p-well was embedded into the deep n layer to avoid edge breakdown. Further, the deep n well reduced the effective p doping of the deep p well and the p epitaxial zone. This leads to a deeper penetration of the depletion region into the epitaxial zone. The high p doped substrate builds the anode of the APD. The minimum noise in case of an MOS-FET front-end is mainly determined by the fourth term of equation (1.16) if $1/f$ noise contribution is insignificant:

$$i_{n,min}^2 = \frac{4kT\Gamma}{g_m} (2\pi C_T)^2 I_3 BW^3 \quad (1.19)$$

For Si APDs and most circuits with Si devices their gate leakage current I_g is very small and its contribution to the noise can be neglected. The minimum noise power depends on the bandwidth and on C_T^2/g_m . C_T consists of the capacitance of the PD and the transistor. The transconductance g_m and the capacitance of a MOS-FET are proportional to the gate width. Therefore, an optimal designed MOS-FET would have a capacitance equal to the PD's capacitance. In this design, the focus was placed on high sensitivity due to the fact that the used technology was not dedicated for high-frequency applications. The reached high sensitivity allowed for a free-space receiver design without any kind of optics at the receiver side. Consequently, the laser ray was received from a wide angle which led to a high FOV.

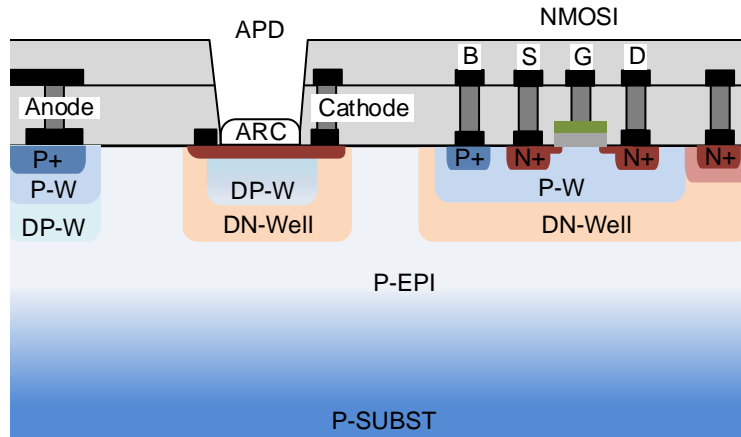


Figure 1.8.: Cross section of APD and isolated NMOS implemented in $0.35\ \mu\text{m}$ HV-CMOS technology, anti-reflection coating (ARC).

1.3.2. Optical Transmitter

To test the receivers in a real communication scenario, an optical transmitter based on a VCSEL and an optical system for focusing and steering the laser beam were developed. The laser diode (LD) works according to the principle of stimulated emission. The LD is emitting coherent light from a nearly punctiform area and can be directly modulated via the supply current. Cheap edge-emitting laser diodes in the red to near infrared wavelength region like Fabry-Perot lasers have the drawback of a reduced modulation frequency compared to VCSELs. Edge-emitting laser diodes show a cut-off frequency of approx. 1 GHz. In contrast, off-the-shelf VCSELs show a cut-off frequency of up to 5 GHz. However, the emitted optical power is limited to around 1 mW. A commercial VCSEL from Vixar [60] was selected which showed an output power of 2 mW and a $-3\ \text{dB}$ cut-off frequency of 3.5 GHz. The laser diode was connected to a laser driver MAX3740A from Maxim [61].

To get a narrow beam, a pick-up from a commercial optical disc drive working as focusing element was mounted in front of the LD. With one servomechanism of the pick-up, the distance between the lens and the LD was controlled. To get an appropriate pick-up, several CD-ROM drives were disassembled and

tested.

To mitigate the problem of a very limited coverage area of narrow beams, a laser beam steering possibility was included into the transmitter system. This was done by a steerable mirror based on a MEMS device. The challenge was to find a device with a static displacement. Mirrorcle delivered a gimbal-less two-axis scanning MEMS micro-mirror operating according to the principle of electrostatic force [62]. The device had four actuators, two for each axis working in opposing directions. The maximum deviation of one actuator was approx. 6° and was reached with a voltage of around 120 V. The mirror had a diameter of 3.6 mm and was coated with aluminum.

All components – the PCB with the LD and laser driver, the pick-up, and the PCB bearing the MEMS mirror – were assembled into a fully adjustable mechanical prototype to align all components in relation to the laser ray. To explore the characteristics of the laser ray in dependence of the focusing element, a camera was set up to measure the results, see appendix A.1. The prototype was mounted on a movable platform and the laser spot was focused onto a smooth wall. This spot was recorded with a monochrome CMOS camera at different distances between the transmitter and the wall. The calibration of the taken pictures was done with an optical power meter. Afterwards, the pictures and the measured parameters were analyzed with a developed MATLAB® program to determine the expansion of the laser beam.

1.4. Resume of Journal Papers

The next section gives a summary of the included journal papers. The first journal paper 2.1 deals with the results from a communication experiment with an already existing OEIC developed by the research group. The journals 2.2 - 2.6 report the results obtained from the OEIC developed in the $0.35\ \mu\text{m}$ BiCMOS technology. The performance and application of the APD-OEIC developed in a $0.35\ \mu\text{m}$ HV-CMOS technology is covered in the papers 2.7 - 2.9.

1.4.1. Elsevier Optics Communication 2012

In "Integrated optical receiver for indoor wireless gigabit communication" an existing OEIC was used to explore the usage of integrated receivers in optical wireless communication scenarios. The results were published in an Optics Communication journal from Elsevier, see section 2.1. The OEIC was developed in a 0.5 μm BiCMOS technology and included a 300 μm diameter pin-PD. With this chip and a 675 nm VCSEL, a 1.25 Gbit/s communication over a distance of 3.2 m was established. The weakness of the setup was mainly the laser source because a multi-mode fiber was pigtailed to the laser. On the other end of the fiber a collimator lens was attached. This setting led to a certain attenuation resulting into an output power of only 180 μW in a rather large beam spot diameter of approx. 4 cm in a distance of 3.2 m. To overcome this weakness, a convex lens was placed in front of the receiver to increase the optical receiver area. The main goal was confirmed by using an OEIC for building an optical wireless communication system.

1.4.2. IET Electronics Letters 2013

In the IET Electronics Letter "3 Gbit/s optical receiver IC with high sensitivity and large integrated pin photodiode", see section 2.2, the first measurement results obtained from the OEIC realized in the 0.35 μm BiCMOS technology were presented. The integrated pin-PD had a diameter of 200 μm . The letter dealt mainly with the circuit design and the measured performance of the OEIC like frequency response and sensitivity. The receiver showed a notable sensitivity of -23.4 dBm at a high data rate of 3 Gbit/s and a BER of 10^{-9} . This result speaks for the use of a bipolar technology for high data rate receivers.

1.4.3. IEEE PTL 2013

The complete optical wireless communication system was described for the first time in the IEEE Photonics Technology Letters "Optical Wireless Communication With Adaptive Focus and MEMS-Based Beam Steering", see section 2.3. The structure of the transmitter including the laser diode, the focusing element, and the MEMS mirror were explained. Details of the BiCMOS receiver circuitry regarding the surrounding PDs were included. The measurement procedure to characterize

the laser beam spot was explained and first results were presented. Also, the letter showed first results of the wireless communication experiments conducted with the new built transmitter. The system was able to establish a 3 Gbit/s data link over a distance of 7 m without the need of complex and costly optical components.

1.4.4. Wiley ETT 2014

The journal paper "Development of an optoelectronic integrated circuit for indoor optical wireless communication systems" was a special issue paper of Wiley Transactions on Emerging Telecommunications Technologies (ETT), see section 2.4. The paper emphasized the advantages and challenges of optoelectronic integration against hybrid solutions. Also, a comparison of recently published OEICs with rather large-diameter PDs was done within the paper. In a further part of the journal, the design of the optical transmitter was explained in detail. This part dealing with the transmitter was completed by results from the laser power distribution measurement.

1.4.5. OSA Optics Letters 2014

In "Automated alignment system for optical wireless communication systems using image recognition", an OSA Optics Letter, an alternative alignment strategy for the laser ray was proposed, see section 2.5. Instead of using the information from the surrounding PDs transferred to the transmitter via a feedback channel, an autonomous alignment took place by using image recognition. A CMOS camera was used at the transmitter side and an algorithm for image recognition to localize the receiver's position was developed. The main algorithms were taken from an open source computer vision library and the program was done in Python. A commercially available desktop computer has been used for executing the developed program. The resolution of the camera allowed for a successful establishment of a communication link over a distance of 3.5 m without any back channel from receiver to transmitter. The main programming work was done by Alexander Weiss.

1.4.6. IEEE JSTQE 2014

The IEEE Journal of Selected Topics in Quantum Electronics with the title "PIN Photodiode Optoelectronic Integrated Receiver used for 3-Gb/s Free-Space Optical Communication" was a special issue in the area of optical detectors, technologies and applications, see section 2.6. The journal paper included an in-depth discussion of the monolithically integrated pin-PD. This included semiconductor device simulations as well as responsivity, frequency, and capacitance measurements. A detailed circuit analysis of the differential TIA connected to the surrounding PDs was given. Parts of this differential TIA were developed by Stefan Schidl. Several diagrams obtained from the beam's expansion measurement with the camera were included. With the whole communication system, a maximum achievable link distance of 19 m was reached with a lens at the receiver and presented in the journal.

1.4.7. IET Electronics Letters 2014

In the IET Electronics Letter "Monolithically integrated optical receiver with large-area avalanche photodiode in high-voltage CMOS technology" the first measurement results obtained from the OEIC realized in the 0.35 μm HV-CMOS technology were presented, see section 2.7. The integrated APD had a diameter of 200 μm and operated at a bias voltage of around -65 V . The letter concentrated on the designed circuitry and on the performance of the OEIC like frequency response and sensitivity. The receiver showed a high sensitivity of -31.8 dBm at a data rate of 1 Gbit/s and a BER of 10^{-9} . This was a considerable improvement in sensitivity for an OEIC with a large-diameter APD. The layout of the APD was mainly drawn by Reinhard Enne.

1.4.8. IEEE PTL 2015

The APD's carrier ionization ratio determination and optical wireless communication experiments with the APD-OEIC were described in the IEEE Photonics Technology Letters paper "OWC Using a Fully Integrated Optical Receiver With Large-Diameter APD", see section 2.8. The letter included some theoretical APD

noise and BER calculations and corresponding measurements. The effective ionization coefficient was determined by an excess noise factor measurement. Due to the high sensitivity of the receiver, a lens-less 1 Gbit/s communication over a distance of 3 m was established. By omitting any kind of receiver optics, the receiving angle increased to 68° .

1.4.9. IEEE JSSC 2016

The IEEE Journal of Solid-State Circuits with the title "Optical Wireless APD Receiver With High Background-Light Immunity for Increased Communication Distances" presented in detail the whole HV-CMOS OEIC, see section 2.9. The journal included a section on the integrated APD and on the pn-PDs which built the surrounding PDs. The advantages and drawbacks of a differential receiver design compared to a single signal design were discussed for the high speed communication circuit. The differential highly sensitive TIA which was connected to the surrounding PDs was explained in detail. This differential TIA was mainly designed by Reinhard Enne. The performance of the APD-OEIC was compared with a pn-PD receiver. The transmitter was improved by using an adjustable collimator lens instead of the pick-up from an optical storage disc drive resulting into a superior focus of the laser ray. That fact resulted into an increased link distance of up to 7 m. The behavior of the receiver under different background light conditions was measured and represented in the journal. Finally, an extensive comparison with published OEICs concluded the paper.

1.5. Scientific Contribution

The main scientific contribution is the development of optoelectronic application-specific integrated circuits with large-diameter PDs in two different Si semiconductor technologies. A novelty is the realization of the complete chip structure consisting of three circuit blocks and five PDs produced in one single chip. One circuit block was designed as high-speed receiver connected to a $200\ \mu\text{m}$ diameter PD. Two highly sensitive differential TIAs built the remaining blocks. Four PDs surrounded the center PD where two opposite situated PDs were connected to one of the differential TIA.

The first circuit was realized in a 0.35 μm BiCMOS technology including a pin-PD. The pin-PD offered an order of magnitude higher responsivity-bandwidth product compared to PDs realized in nanometer CMOS processes. By using bipolar transistors, the noise contribution from the TIA was reduced considerably. The sensitivity was improved from 3.3 to 19 dB compared to results found in [57, 63–65]. Compared to [63, 65] the data rate was more than doubled, whereby the sensitivity was improved by more than 4 dB. Due to this novel, highly-sensitive integrated receiver, complex and expensive optical components at the receiver side were avoided compared to [41, 42]. The developed transmitter allowed for considerable reduction of transmit power. At the same time, the data rate was doubled as well as the communication distance was improved compared to [17, 45]. The potential of using imaging recognition for an automated alignment system for an indoor OWC system was verified.

For the second circuit, a 0.35 μm HV-CMOS technology was used. The specialty of the OEIC was the integration of an APD. At the date of publication, this was the most sensitive reported OEIC with a large-diameter APD monolithically integrated in a CMOS technology without process modifications. Compared to the developed pin-OEIC, the sensitivity was improved by approx. 7.5 dB. The data rate was increased tenfold compared to [66]. The same link distance was achieved as in [17, 45] with nearly the same data rate but without any optical component at the receiver side. By omitting any optical component at the receiver, the receiving angle increased by a factor of 7.5. For the first time, the influence of background illuminance on the BER was reported for an integrated APD receiver. This is especially important for wireless applications.

2. Publications

2.1. Elsevier Optics Communication 2012

Reprinted from Optics Communications, 285/6, P. Brandl, R. Swoboda, W. Gaberl, H. Zimmermann, Integrated optical receiver for indoor wireless gigabit communication, Pages No. 1075–1077, Copyright (2012), with permission from Elsevier. <http://dx.doi.org/10.1016/j.optcom.2011.11.111>

Contents lists available at [SciVerse ScienceDirect](#)

Optics Communications

journal homepage: www.elsevier.com/locate/optcom

Integrated optical receiver for indoor wireless gigabit communication

P. Brandl ^{a,*}, R. Swoboda ^b, W. Gaberl ^a, H. Zimmermann ^a^a Vienna University of Technology, Institute of Electrodynamics, Microwave and Circuit Engineering, Gusshausstrasse 25/354, 1040 Vienna, Austria^b A³PiCs Electronics Development GmbH, Webergasse 18, A-1200 Vienna, Austria

ARTICLE INFO

Article history:

Received 8 July 2011

Received in revised form 21 November 2011

Accepted 28 November 2011

Available online 14 December 2011

Keywords:

PIN photodiode

Integrated optical receiver

Optical wireless communication

ABSTRACT

A receiver with a monolithically integrated PIN photodiode in 0.5 μm BiCMOS technology has been developed for establishing an indoor 1.25 Gb/s optical wireless communication over a distance of 3.2 m using 180 μW of optical power.

© 2011 Elsevier B.V. All rights reserved.

1. Introduction

Optoelectronic integrated circuits are promising devices for future wireless data links within indoor environments such as an office. The state-of-the-art wireless radio access e.g. WLAN will not provide enough bandwidth for future high-demanding applications with data rates in the Gb/s range. The situation changes with optical transmission as the carrier frequencies are hundreds of THz, allowing huge system bandwidths [1]. Most optical wireless communication systems are using a modulated laser source as transmitter and a photodiode as receiver accompanied by optical elements e.g. lenses. Unlike optical fiber data links, free space serves in wireless links as transmission medium. One standard in optical wireless communication was set by the Infrared Data Association in 1993 [2]. The most challenging point for establishing an optical link depends on receiver's sensitivity. This is the minimal optical input power that is necessary to reach a certain bit error rate. On the other hand, the radiated laser energy is limited by reason of eye safety regulations. A part of the European-Community project OMEGA [3] was to investigate optical-wireless communications [4]. One of the technologies proposed was visible-light communications (VLC) [5], and the other was a 1.25 Gb/s line-of-sight infra-red communication system [6,7]. In [8], the benefits of VLC with focused and directed light beam over uniform lighting implementations were elaborated. Hence, aligned infrared-links will be our method of choice for high data rate links.

In [6,7], a 25 mW laser and a commercial discrete avalanche photodiode (APD) with a diameter of 500 μm [9] have been used. APDs have higher sensitivity than PIN photodiodes, but they need 120–

200 V and they cannot be realized in optoelectronic integrated circuits (OEIC). Due to cost and reliability reasons an implementation of optical receivers in silicon OEICs is a convenient alternative [10]. In former experiments [11,12] we used our own OEICs for optical wireless communication. These experiments have been done without receiver optics, which resulted in rather poor transmission path length for gigabit data rates. Here, we use a receiver optic and improve the photodiode as well as the receiver circuit with respect to speed and low-noise, respectively. A similar work has been done in [13], although the photodetector was based on an InGaAs metal-semiconductor-metal device flip-chip bonded to an amplifier in a 180 nm CMOS technology. In the first chapter the OEIC structure will be explained followed by a chapter presenting measurement results, and finally, the conclusion.

2. OEIC structure

Starting from the suggestions given in [14] and [15] a vertical PIN photodiode has been developed and implemented in a silicon OEIC in 0.5 μm BiCMOS technology. A bandwidth of only 300 MHz at a 3 V photodiode bias voltage was achieved in [14]. In [16], a bandwidth of 1 GHz at 2.5 V photodiode bias voltage was reported. Compared to [14] and [16], the thickness of the intrinsic layer was reduced to 9.5 μm in order to enhance the bandwidth. Bipolar transistors available in this BiCMOS technology allow building of circuits with higher data rates and photodiode capacitances in a better noise performance compared to only CMOS.

2.1. PIN photodiode

Fig. 1 shows the cross section of the PIN photodiode which is built by a p+ anode on top and an n+ buried cathode. A large drift zone

* Corresponding author. Tel.: +43 1 58801 354612.
E-mail address: paul.brandl@tuwien.ac.at (P. Brandl).

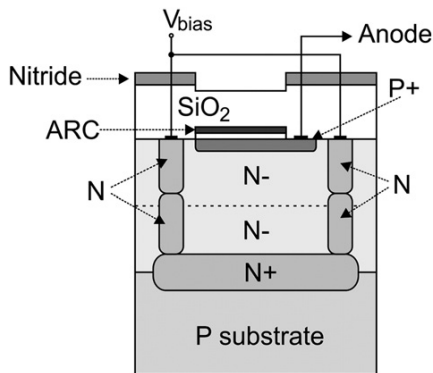


Fig. 1. Cross section of vertical PIN-photodiode.

arises from the implementation of a large intrinsic zone built by the n-area. This drift zone combined with a reverse bias voltage guarantees a high-speed device. For a wavelength of 660 nm a responsivity of 0.46A/W has been achieved with anti-reflection coating (ARC) optimized for the above mentioned wavelength. This ARC is formed by a thin oxide with a nitride layer on top having a layer thickness optimized for red light. The passivation nitride layer was opened above the photodiode (see Fig. 1). Thereby, optical interferences could be avoided in the isolation and passivation stack. For light with 850 nm, a responsivity of still 0.33A/W has been obtained. This results in quantum efficiencies of 85% and 48% for wavelength of 660 nm and 850 nm, respectively. The active diameter of the photodiode is 300 μm and it has a capacitance of 1.3 pF at a reverse bias of 4.2 V. The speed of the photodiode increases substantially by implementation of the 9.5 μm thick intrinsic (I) layer compared to [14] with an I-layer of 15 μm . Fig. 2 shows the -3 dB-cut-off frequency depending on the reverse bias voltage (V_{bias}). For a wavelength of 660 nm and a V_{bias} of 4 V we have measured a cut-off frequency of 1530 MHz. For 850 nm, the bandwidth of the vertical PIN photodiode is still 731 MHz at 4 V reverse bias. Compared to [17], where a bandwidth of 800 MHz for 675 nm and 400 MHz for 785 nm was reported for a PIN diode with 10 μm epitaxial layer and 3 V reverse bias, the bandwidth is considerably higher.

2.2. TIA

A simplified schematic of the entire OEIC is depicted in Fig. 3. It consists of the above mentioned PIN photodiode and a transimpedance amplifier (TIA) that converts the photocurrent I_{PH} to a

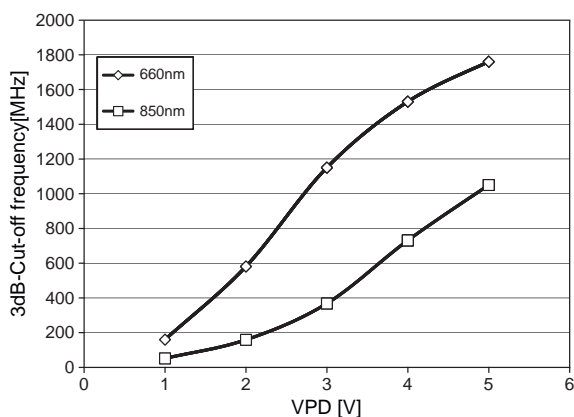


Fig. 2. -3 dB cut-off frequency vs. Photodiode reverse bias voltage for two wavelengths.

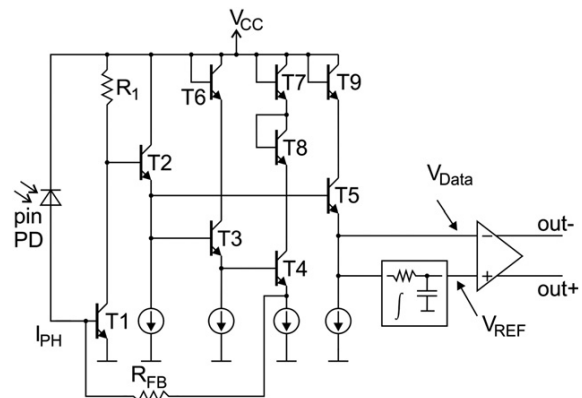


Fig. 3. Optical receiver (simplified schematic diagram).

corresponding voltage V_{DATA} . The voltage V_{REF} which is the averaged value of V_{DATA} is generated by a dummy TIA and a proportional integral (PI) controller. This is depicted as low pass in Fig. 3. These two voltages will be fed into a differential limiting post-amplifier followed by a 50 Ω output driver (both illustrated as op-amp symbol in Fig. 3). Transistor 1 (T1) from the TIA represents a common-emitter stage and provides voltage gain. The optimum bias current for T1 is set with R1. Impedance transformation as well as level shifting is done with T2, T3, T4 and T5. T6–T9 are working as diodes to reduce the collector-emitter-voltages of corresponding transistors. The TIA has an equivalent input current noise of 920 nA integrated over its bandwidth. The dummy TIA has the same structure as the main TIA. However, it has a reduced bandwidth to lower its noise contribution. It is regulated by a PI controller in such a way that it represents the average output voltage. The additional components (R, C) have been selected in order to achieve a lower 3 dB cut-off frequency of 45 kHz. Hence, low frequency parts of the signal, e.g. ambient light, are canceled out. The limiting post-amplifier has as input stage a differential amplifier succeeded by three stages of emitter followers. They serve for level shifting, impedance transformation for the output driver and they increase the gain-bandwidth product. The output driver consists of a differential amplifier with low gain, high bandwidth and is able to drive 50 Ω lines. The amplifier and driver together have 30 dB gain. The total transimpedance of the complete amplifier is 25 k Ω . The -3 dB bandwidth of the complete receiver OEIC is 900 MHz. The TIA front-end consumes 70 mW at 5 V supply voltage. Together with the post-amplifier and driver 170 mW are consumed. The total chip area including bond pads is 0.8 mm².

3. Measurement and results

For measurement, an optical communication link subdivided in a transmitter side and a receiver side has been established. Fig. 4 gives an overview of the optical measurement setup. The results have been obtained with a 2.5Gb/s bit-pattern generator and a Tektronix communication analyzer CSA8000.

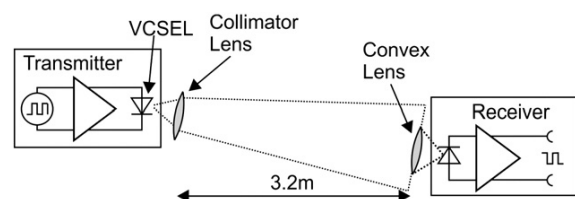


Fig. 4. Optical measurement setup.

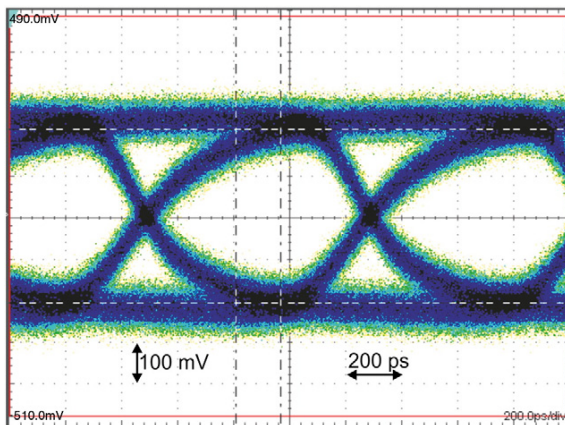


Fig. 5. Eye diagram at 1.25 Gb/s.

3.1. Transmitter side

A common 675 nm Vertical-Cavity Surface-Emitting Laser (VCSEL) was used as transmitter. This laser diode can be directly modulated with signals in the GHz range and this has been done with an extinction ratio of 1:7. A multi-mode fiber was pigtailed to the laser. On the other end of the fiber a collimator lens with a focal distance of 6.24 mm and a numerical aperture of 0.42 (Thorlabs A110TM-B) was attached. Behind the lens an emitted light power of 180 μW in a beam with a diameter of around 2 mm was measured. The beam enlarged to a diameter of 4 cm in a distance of 3.2 m where the receiver OEIC was placed. That results in an optical power density of 0.143 W/m^2 within the light spot diameter of 4 cm. However, this requires a constant intensity within the illuminated surface. To produce a data stream, the VCSEL was modulated by the bit pattern generator with a pseudo random bit sequence (2^7-1 pattern length).

3.2. Receiver side

The convex lens at the receiver side was a simple Polymethyl Methacrylate (PMMA) lens with a diameter of 20 mm and a focal distance of 12.5 mm. This optical piece was mounted to a XYZ translation stage in front of the OEIC. The receiver has been supplied with a voltage of 5 V, resulting in a total power consumption of 170 mW. The outputs of the OEIC were connected to the previously mentioned communication analyzer. Assuming that the losses of the lens are negligible, an average optical input power of 45 μW was calculated, corresponding to -13.5 dBm.

3.3. Result

The optical laser signal was focused on the photodiode. In Fig. 5 the eye diagram at a data rate of 1.25 Gb/s can be seen. It confirms

that the bandwidth and sensitivity of the receiver is good enough for free-space communication and there is still some reserve. The measured Q-factor is 6.46 which relates to a theoretical bit error rate of 5.24×10^{-11} at a data rate of 1.25 Gb/s.

4. Conclusion

The results demonstrate the potential of BiCMOS OEICs in 0.5 μm technology compared to discrete receivers with APDs and commercially available amplifiers. The circuit supply voltage of 5 V is sufficient for the PIN photodiode to achieve 1.25 Gb/s. This is in contrast to the high voltage needed for APDs. Furthermore, much less optical power than in [6] is needed for about the same communication distance. A low-cost silicon technology has been used for the implementation of a high-speed monolithically integrated optical receiver achieving a good sensitivity. Further, the optical power can be increased (e.g. to 1 mW, class 1 M) which would produce even better results like a higher data rate and/or a longer communication distance. For high data rate communication, optical transmission is a method of choice and it comes with the benefit that the spectrum is free and unregulated. OEICs with integrated PIN photodiodes together with cheap laser diodes will build the base for future communication devices.

References

- [1] J. Kahn, J. Barry, Proceedings of the IEEE 85 (Feb. 1997) 265.
- [2] www.irda.org, last accessed on 29th June 2011.
- [3] EU-FP7 project OMEGA www.ict-omega.eu, last accessed on 29th June 2011.
- [4] K. Langer, J. Vucic, 36th European Conference and Exhibition on Optical Communication (ECOC) 2010, Sept. 19–23 2010, We.6.B.1.
- [5] O. Bouchet, et al., IEEE 2010 GLOBECOM Workshops, Dec. 6–10 2010, p. 1042.
- [6] Hoa Le Minh, D. O'Brien, G. Faulkner, O. Bouchet, M. Wolf, L. Grobe, Li Jianhui, IEEE Photonics Technology Letters 22 (21) (Nov. 2010) 1598.
- [7] D. O'Brien, et al., IEEE 2010 GLOBECOM Workshops, Dec. 6–10 2010, p. 1047.
- [8] T. Borogovac, M. Rahaim, J.B. Carruthers, IEEE 2010 GLOBECOM Workshops, Dec. 6–10 2010, p. 1077.
- [9] www.silicon-sensor.de, last accessed on 30th June 2011.
- [10] T. Takimoto, N. Fukunaga, M. Kubo, N. Okabayashi, Consumer Electronics, IEEE Transactions on 44 (1) (Feb 1998) 137.
- [11] W. Gaberl, H. Zimmermann, 34th European Conference on Optical Communication (ECOC), 2008, Sept. 2008, P6.18.
- [12] W. Gaberl, R. Swoboda, H. Zimmermann, 35th European Conference on Optical Communication (ECOC), 2009, Sept. 2009, P4.13.
- [13] J. Zeng, V. Joyner, J. Liao, S. Deng, Z. Huang, 52nd IEEE International Midwest Symposium on Circuits and Systems, MWSCAS '09, Aug. 2–5 2009, p. 148.
- [14] M. Yamamoto, M. Kubo, K. Nakao, IEEE Transactions on Electron Devices ED-42, no. 1 (Jan. 1995) 58.
- [15] H. Zimmermann, "Integrated Silicon Optoelectronics", Springer Series in Optical Sciences, vol. 148, Springer-Verlag, Berlin, Heidelberg, 2010.
- [16] J. Sturm, M. Leifhelm, H. Schatzmayr, S. Groiss, H. Zimmermann, IEEE Journal of Solid-State Circuits 40 (7) (2005) 1406.
- [17] H. Zimmermann, A. Marchlewski, W. Gaberl, I. Jonak-Auer, G. Meinhardt, E. Wachmann, IEEE Photonics Technology Letters 21 (22) (Nov. 2009) 1656.

2.2. IET Electronics Letters 2013

Reproduced by permission of the Institution of Engineering & Technology. Full acknowledgment to P. Brandl and H. Zimmermann, "3 Gbit/s optical receiver IC with high sensitivity and large integrated pin photodiode", 11th April 2013.

3 Gbit/s optical receiver IC with high sensitivity and large integrated *pin* photodiode

P. Brandl and H. Zimmermann

An optoelectronic integrated circuit in a 0.35 μm BiCMOS technology containing a 200 μm diameter *pin* photodiode for optical wireless communication systems is presented. The design consists of a highly efficient integrated Si *pin* photodiode, a transimpedance amplifier and 50 Ω output driver. The overall transimpedance of the whole receiver is 86.6 dB Ω . At a data rate of 3 Gbit/s with a pseudorandom bit sequence of $2^{31} - 1$ a sensitivity of -23.4 dBm is achieved (BER = 10^{-9} , $\lambda = 675$ nm).

Introduction: Future in-home communication scenarios demand high data rates. To fulfil this requirement, the use of carriers in optical wavelength regions is indispensable [1]. Today, many off-the-shelf laser diodes or vertical-cavity-surface-emitting lasers (VCSELs) are available as transmitters. The information can be transported either through cheap plastic fibres or through a wireless channel. In both cases an optical receiver with a large diameter photodiode (PD) is needed. An economically attractive possibility is the use of an optoelectronic integrated circuit (OEIC) in standard silicon technologies.

A large PD area (using a simple pn-junction) results in a large capacitance but this will limit the speed of the receiver front-end. On the other hand, a smaller diameter of the PD will considerably complicate the alignment procedure. To satisfy the above-mentioned opposed constraints, a *pin* photodiode reduces the capacitance (owing to its thick depletion zone) and the use of BiCMOS technology is favoured against pure CMOS because of the fact that bipolar transistors have a better g_m/I ratio than MOS transistors [2]. The availability of bipolar circuits in BiCMOS allows for a higher PD capacitance, higher gain, higher data rate and less noise, i.e. higher sensitivity. In [3], a 0.6 μm BiCMOS technology was used to implement an OEIC with a *pin* PD with a diameter of 300 μm . The sensitivity was -20.1 dBm at a data rate of 2.5 Gbit/s with a bit error rate (BER) of 10^{-9} . In [4], the use of a receiver with an integrated 400 μm diameter photodiode (also realised in a 0.6 μm BiCMOS technology) led to a sensitivity of -19.6 dBm at a data rate of 1.25 Gbit/s with a BER of 10^{-9} and a PRBS length of $2^{15} - 1$. An OEIC with a 250 \times 250 μm quadratic PD in a 65 nm CMOS process was developed in [5]. The result was a data rate of 3.125 Gbit/s with a BER $< 10^{-12}$ and a PRBS of $2^{31} - 1$, but at the cost of a sensitivity of only -3.8 dBm. In [6], only the amplifier was implemented in 0.18 μm CMOS technology. This amplifier connected to a S5972 silicon *pin* PD from Hamamatsu (0.8 mm diameter) reached a sensitivity of -18.3 dBm at 1.25 Gbit/s with a PRBS of $2^{31} - 1$ at a BER of 10^{-12} .

A silicon OEIC with an integrated *pin* PD (to the best knowledge of the authors for the first time in 0.35 μm BiCMOS) is presented in this Letter. The reached data rate is 3 Gbit/s with a PRBS of $2^{31} - 1$ and a BER of 10^{-9} at a sensitivity of -23.4 dBm. This is a considerable improvement over the above-mentioned results, especially in consideration of a data rate of 1.25 Gbit/s with a sensitivity of -24.2 dBm, corresponding to an input current of only 2.05 μA .

Pin photodiode: The p^+ -doped substrate builds the anode of the *pin* PD. On top of the p^+ substrate a low doped ($< 5 \times 10^{13} \text{ cm}^{-3}$) p^- epitaxial layer is located, which forms the intrinsic zone of the *pin* PD. The cathode of the *pin* PD is realised by a 200 μm diameter highly-doped n^+ source/drain region. The diode is reverse biased by applying -7.5 V to the substrate contact of the chip in order to get a higher drift velocity. This improves the speed of the integrated PD, which results in a -3 dB cutoff frequency of 995 MHz at a wavelength of 675 nm. The process offers a third, deep n-well to isolate the n-channel MOSFETs from the negative substrate. With the above-mentioned reverse bias voltage of -7.5 V, the *pin* PD has a capacitance of 550 fF, which is less than a half of that of an n+/p-substrate diode. The top of the PD is covered with an antireflection coating, leading to a responsivity of 0.54 and 0.40 A/W at 675 and 850 nm, respectively. The responsivity-bandwidth product of this *pin* photodiode is an order of magnitude larger than that of PDs using normally doped pn diodes in standard nanometre CMOS technology [7].

OEIC: Fig. 1 shows a simplified circuit diagram of the entire OEIC. The photocurrent I_{PH} from the above explained *pin* PD is converted by a transimpedance amplifier (TIA) to a voltage signal. Transistor T1 builds a common-emitter stage which provides voltage gain. The overall noise of the whole receiver depends mainly on that first transistor T1, the feedback resistor R_{fb} and the (low) photodiode capacitance. T2 works as an emitter follower and transforms the impedance. T3 is used for level shifting. Moreover, the emitter followers T2 and T3 are used for gain peaking at high frequencies which increases the bandwidth of the whole receiver far above the -3 dB bandwidth of the *pin* PD. The current sources are realised with standard MOS transistors available in the utilised technology. The feedback resistor R_{fb} has a value of 830 Ω and the feedback capacitance C_{fb} is 10 fF, which is needed to guarantee stability of the TIA circuitry. The TIA consumes 10.7 mA.

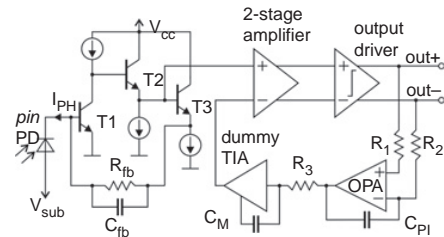


Fig. 1 Simplified circuit diagram of realised OEIC

The structure of the dummy TIA and the main TIA is the same except for the fact that the dummy TIA has an additional Miller capacitance C_M . This C_M (0.5 pF) is connected between the base and collector of T1' (T1' is equal to T1), which reduces the bandwidth of the dummy TIA to contribute less noise. The dummy TIA reproduces the average output voltage of the main TIA. This is done with the help of a proportional integral (PI) controller built with R_1 , R_2 , C_{PI} and an operational amplifier (OPA). The output of the OPA generates a current flowing through R_3 which corresponds to the average photocurrent I_{PH} and is fed into the input of the dummy TIA. The value of $R_1 = R_2 = 470$ k Ω and $C_{PI} = 10$ pF result in a -3 dB cutoff frequency of 33 kHz.

The voltages from the main TIA and the dummy TIA are fed into a differential amplifier which builds the input stage of the two-stage amplifier. Hence, the OEIC becomes insensitive to common-mode noise such as noise on the supply lines. Furthermore low-frequency parts of the input signal, like ambient light, will be cancelled out due to the above-mentioned controlling mechanism of the dummy TIA. The differential amplifier is followed by two stages of emitter-followers for impedance transformation and level shifting. Then, a second differential amplifier followed again by two emitter followers completes the two-stage amplifier, resulting in 27.8 dB gain.

The output driver consists of a differential limiting amplifier capable of delivering a differential output voltage of 300 mV into 50 Ω . The area of the complete chip produced in a 0.35 μm BiCMOS technology with an npn transit frequency of 20 GHz is $890 \times 1440 \mu\text{m}^2$.

Measurement and results: For measuring, the chip was glued and bonded on a PCB. As source, a VCSEL with a wavelength λ of 675 nm was modulated by an up to 12 Gbit/s digital bit pattern generator. The light signal from the VCSEL was brought via a multimode fibre to the *pin* PD. In between was a manual optical attenuator. The outputs of the OEIC were connected to a bit error analyser for counting bit errors or to an oscilloscope for observing the signal. Further, a vector network analyser R&S ZVM was used in order to measure the frequency response of the whole chip, see Fig. 2. The measured -3 dB bandwidth is 2.08 GHz. In Fig. 3, an eye diagram taken with a Tektronix oscilloscope TDS 6124C is depicted. The average optical power was -23.4 dBm at a data rate of 3 Gbit/s and a BER of 10^{-9} . Fig. 4 shows the results of the sensitivity measurements at different data rates, all with a PRBS of $2^{31} - 1$. The optical input power refers to the average optical input power. The chip is supplied with 3.3 V and has a total current consumption of 75 mA.

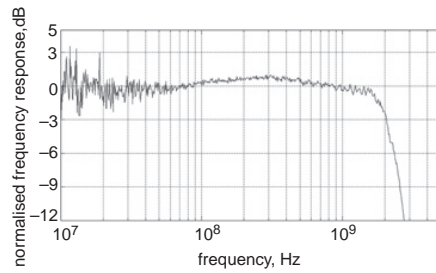


Fig. 2 Measured frequency response of whole receiver, $\lambda = 675$ nm

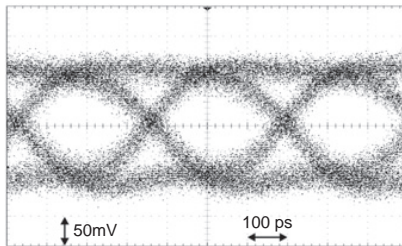


Fig. 3 Eye diagram of OEIC's output at 3 Gbit/s, $2^{31} - 1$ PRBS, BER = 10^{-9} with average optical input power of -23.4 dBm, $\lambda = 675$ nm, extinction ratio = 2

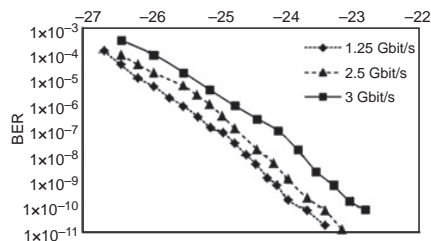


Fig. 4 Sensitivity at different data rates, $2^{31} - 1$ PRBS, $\lambda = 675$ nm

Conclusion: An OEIC fabricated with a standard opto-ASIC $0.35 \mu\text{m}$ BiCMOS process without any modification has been presented. This

OEIC has two major advantages compared to nanometre CMOS OEICs: the *pin* photodiode offers an order of magnitude higher responsivity–bandwidth product and the bipolar transistors reduce the TIA noise. The reached data rate and sensitivity are promising and speak for the use of monolithically integrated optical BiCMOS receivers in future optical communication systems. The OEIC with a highly efficient $200 \mu\text{m}$ integrated *pin* PD shows a sensitivity of -23.4 dBm at a data rate of 3 Gbit/s and a BER of 10^{-9} . This is 3.3 to 19 dB better than the results found in [3–6]. Compared to [4] and [6] the data rate is more than doubled, whereby the sensitivity is improved by more than 4 dB.

© The Institution of Engineering and Technology 2013
15 February 2013

doi: 10.1049/el.2013.0558

P. Brandl and H. Zimmermann (Institute of Electrodynamics, Microwave and Circuit Engineering, Vienna University of Technology, Gusshausstrasse 25/354, 1040 Vienna, Austria)

E-mail: paul.brandl@tuwien.ac.at

References

- 1 Home gigabit access. [Online], available: <http://www.ict-omega.eu>
- 2 Sansen, W.M.C.: 'Analog design essentials' (Springer, Dordrecht, The Netherlands, 2008), pp. 45–47
- 3 Swoboda, R., and Zimmermann, H.: '2.5 Gbit/s silicon receiver OEIC with large diameter photodiode', *Electron. Lett.*, 2004, **40**, (8), pp. 505–507
- 4 Atef, M., Swoboda, R., and Zimmermann, H.: '1.25 Gbit/s over 50 m step-index plastic optical fiber using a fully integrated optical receiver with an integrated equalizer', *IEEE J. Lightwave Technol.*, 2012, **30**, (1), pp. 118–122
- 5 Dong, Y., and Martin, K.W.: 'A high-speed fully-integrated POF receiver with large-area photo detectors in 65 nm CMOS', *IEEE J. Solid-State Circuits*, 2012, **47**, (9), pp. 2080–2092
- 6 Aznar, F., Sánchez-Azqueta, C., Celma, S., and Calvo, B.: 'Gigabit receiver over 1 mm SI-POF for home area networks', *IEEE J. Lightwave Technol.* 2012, **30**, (6), pp. 2668–2674
- 7 Nakhkoob, B., Ray, S., and Hella, M.M.: 'High speed photodiodes in standard nanometer scale CMOS technology: a comparative study', *Opt. Express*, **20**, (10), pp. 11256–11270

2.3. IEEE PTL 2013

© 2013 IEEE. Reprinted, with permission, from Paul Brandl, Stefan Schidl, Andreas Polzer, Wolfgang Gaberl, and Horst Zimmermann, "Optical Wireless Communication With Adaptive Focus and MEMS-Based Beam Steering", IEEE PHOTONICS TECHNOLOGY LETTERS, August 2013.

Optical Wireless Communication With Adaptive Focus and MEMS-Based Beam Steering

Paul Brandl, *Student Member, IEEE*, Stefan Schidl, Andreas Polzer, Wolfgang Gaberl, and Horst Zimmermann, *Senior Member, IEEE*

Abstract—An optical wireless communication system for an operation with wavelengths detectable by silicon optoelectronic integrated circuits is described. We use direct modulated vertical cavity surface emitting lasers as a transmitter. The field of view of the laser beam is adjusted with an adaptive optical system and aligned with a micro-electro-mechanical system based mirror for beam steering. To receive the modulated laser beam, we develop a receiver chip in 0.35 μm BiCMOS technology. The experimental system shows a 3 Gb/s wireless transmission over a distance of 7 m with a bit-error rate $<10^{-9}$ without cost intensive optical components and complex adjustment procedure.

Index Terms—Optical wireless communication, MEMS technology, beam steering, opto-electronic integrated circuit.

I. INTRODUCTION

THE increasing availability of high-data rate connections to peoples' homes demands for elaborated distribution possibilities inside rooms. To complement radio wireless links, optical links with their nearly unbounded bandwidth have been suggested [1]–[6]. Optical wireless communication (OWC) systems require a wide field of view (FOV) for a certain coverage area. A broad beam, however, is related to high attenuation. As a consequence, OWC systems demand a high level of transmit power to achieve a sufficient signal-to-noise ratio. However, the laser power is limited by eye safety rules. In order to mitigate these inconveniences, different configurations have been investigated. The use of non-imaging angle diversity (AD) receivers was proposed in [1]. In [2] an OWC system was realized based on non-imaging AD, but still 3 laser diodes (LD) each with 25 mW power were needed to transmit 1.25 Gb/s over 3 meters with a FOV of $25^\circ \times 8^\circ$. The first imaging AD fully integrated receiver was presented in [3]. The receiver consisted of an array of pin photodiodes (PDs) flip-chip bonded to a customized CMOS circuit. An imaging receiver with an electronic tracking system was proposed in [4]. There an array of vertical cavity surface emitting lasers (VCSELs) for a narrow high-speed link and a master-oscillator power amplifier laser with more than 400 mW for a wide-beam link were used. The advantage of reduced path loss

Manuscript received March 26, 2013; revised May 8, 2013 and May 29, 2013; accepted May 30, 2013. Date of publication June 6, 2013; date of current version July 9, 2013.

The authors are with the Vienna University of Technology, Institute of Electrodynamics, Microwave and Circuit Engineering, Vienna 1040, Austria (e-mail: paul.brandl@tuwien.ac.at; stefan.schidl@tuwien.ac.at; andreas.polzer@tuwien.ac.at; wolfgang.gaberl@tuwien.ac.at; horst.zimmermann@tuwien.ac.at).

Color versions of one or more of the figures in this letter are available online at <http://ieeexplore.ieee.org>.

Digital Object Identifier 10.1109/LPT.2013.2266574

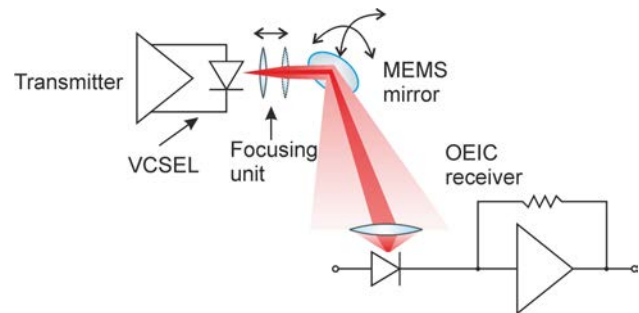


Fig. 1. Simplified schematic of optical wireless communication system.

with narrow beams was confirmed in [5]. For a certain FOV, a lens with a large acceptance angle at the receiver side and a positioning mechanism for the photodetector were proposed. The position of the photodetector was changed with a design similar to that of an optical pick up known from CD read heads. In [6], a 1550 nm system with a single channel imaging receiver with a 2-axis actuator was demonstrated. They used a fixed beam width and proposed to use MEMS for steering. Compared to [6], in [7] the receiving optics was changed to a compound parabolic concentrator followed by a coupling system consisting of multiple lenses and a fiber collimator.

We built a system for OWC where the transmitter can adapt its beam width and can position the beam by steering it with a MEMS based mirror. The developed OEIC not only receives the data stream as done by an imaging single channel in [5], it can also detect from which side the beam is coming. With this information we give feedback to the transmitter and it can align the center of the beam to the detector field. Compared to [6] and [7], we avoided complex and expensive optical components at the receiver side by using only one simple convex lens. The use of an aligned narrow beam reduces the required transmit power and increases channel bandwidth compared to other systems.

II. SYSTEM DESCRIPTION

A simplified schematic of the OWC system is shown in Fig. 1. For a distance between transmitter and receiver of 7 m and a FOV of $12^\circ \times 12^\circ$ we have a corresponding receiving area of 1.47 m horizontally (x) and 1.47 m vertically (y). We use a VCSEL with visible wavelength to facilitate coarse alignment of the beam. After the receiver is placed within the coverage area, the transmitter starts with a broad beam to move until the receiver detects a signal. Then the beam

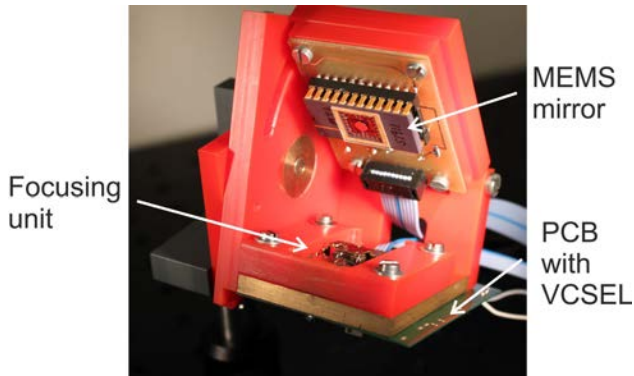


Fig. 2. Picture of transmitter.

is focused to a narrow beam width and is aligned with the receiver until the received power reaches a certain limit to guarantee a transmission with a BER $< 10^{-9}$.

A. Transmitter

The transmitter is depicted in Fig. 2. A commercial 680 nm VCSEL from Vixar (2 mW output power at 3.5 GHz) is modulated by a laser driver from Maxim (MAX3740A). This wavelength fits to the pin PD's responsivity maximum at 680 nm. To adjust the laser beam width we mounted a pick-up from a commercial optical disc drive into the optical axis of the VCSEL beam. We controlled the distance between the lens and the VCSEL with one of the two servomechanisms within the optical pick-up and thus adjusted the focusing of the laser ray. Using this mechanism, we are able to vary the beam width continuously. Following the beam, we mounted a gimbal-less two-axis scanning MEMS micro-mirror from Mirrorcle (S1911). The mirror plate has a diameter of 3.6 mm and is aluminum coated. Due to the small distances between laser, pick-up and mirror, the mirror has sufficient aperture size for different beam widths. The maximum mechanical mirror tilt is from -6° to $+6^\circ$ for both axes x and y . To align all components in relation to the laser ray we built a fully adjustable mechanical prototype, see Fig. 2. For example, we can tilt the mounting plate of the MEMS-mirror to adjust the angle of incidence in a range from 20° to 50° . The complete prototype can again be mounted on a coarse pointing system to increase coverage.

B. Receiver

For this system, we developed a novel receiver with integrated pin PDs in a standard opto-ASIC silicon $0.35 \mu\text{m}$ BiCMOS process without any modification. The high data rate (HDR) channel was described in [8]. The most important point in the design process is the PD's diameter. A large diameter, resulting in a large area, provokes a large capacitance and thus limits the bandwidth of the receiver front-end. In contrast to this, a smaller diameter of the PD considerably complicates the alignment procedure. Confronted with these opposed constraints, we decided to use a process which allows pin PDs with a reduced capacitance due to their thick

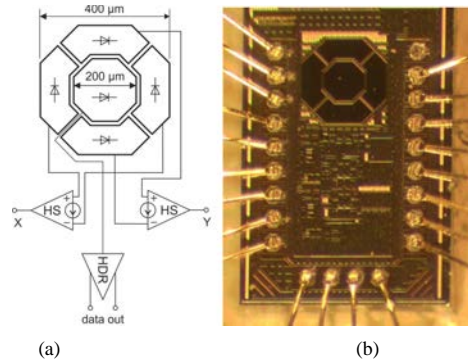


Fig. 3. Realized OEIC receiver, (a) simplified schematic of photodiodes and TIAs (HS: high sensitivity, HDR: high data rate), (b) photomicrograph of the bonded receiver.

depletion zone. A second benefit of the chosen process is the availability of bipolar transistors in BiCMOS compared to pure CMOS processes. Bipolar circuits allow higher gain, higher data rate and less noise due to the well-known fact that bipolar transistors have a larger transconductance g_m than MOS transistors at a reasonable power consumption.

There are 5 pin PDs realized as shown in Fig. 3. The cathodes of the pin PDs are built by a highly-doped n^+ region. A low doped p^- epitaxial layer forms the intrinsic zone of the pin PD. The p^+ doped substrate builds the anode. To get a high responsivity of 0.53 A/W at 680 nm, the top of the PDs is covered with an anti-reflection coating. With a reverse bias voltage of -7.5 V , the center $200 \mu\text{m}$ diameter pin PD has a low capacitance of only 550 fF. The cathode of each pin PD is connected to a transimpedance amplifier (TIA) to convert the photocurrent to a corresponding voltage signal. The center PD serves for communication and the attached high data rate (HDR) TIA is optimized for high speed. The output voltage from the TIA is fed into a differential amplifier stage. The OEIC is insensitive to common-mode noise. Very low-frequency parts of the input signal, like ambient light, are cancelled out [8]. This OEIC was characterized using an optical fiber and a variable attenuator. The whole receiver showed a sensitivity of -23.4 dBm for a BER of 10^{-9} at a data rate of 3 Gbps with a PRBS of $2^{31} - 1$ [8]. The HDR-TIA has an overall transimpedance of $21.3 \text{ k}\Omega$. The whole HDR channel including the 50Ω output driver has a current consumption of 65 mA at 3.3 V supply voltage.

For the surrounding photodiodes, which are used for alignment purposes, a differential design was chosen. This enables a simple detection of the difference in the illumination of the photodiodes. The attached TIAs were optimized for high sensitivity (HS). The HS receivers have a bandwidth of 1.6 MHz with a transimpedance of $100 \text{ k}\Omega$ and an equivalent input noise current of 1.3 nA. Each HS-TIA needs only a current of $320 \mu\text{A}$ at 3.3 V. The chip was glued and bonded onto a PCB. A simple convex lens (diameter = 20 mm, focal distance = 12 mm, acryl glass) in front of the chip served as an optical antenna. The chip was not placed exactly at the focal distance in order to get a widened focal point. This was done to minimize the influence of the incidence angle.

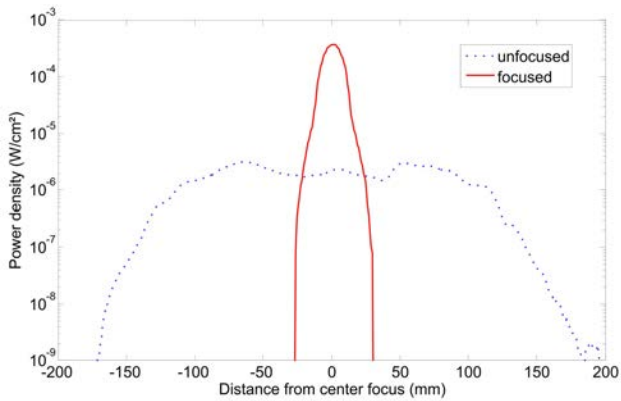


Fig. 4. Horizontal cross section of the VCSEL spot in a distance of 7 m.

III. SYSTEM VERIFICATION

To verify the operability of our proposed system and in particular our receiver, we tested the transmitter and receiver in our lab. The laser beam's initial deviation from the receiver was 20 cm horizontally and 10 cm vertically in a distance of 7 m. The transmitter was connected to a bit pattern generator and modulated with a 3 Gbps pseudorandom binary bit sequence (PRBS) of $2^{31}-1$. The average optical output power of the VCSEL was adjusted to 1.2 mW, which corresponds to 0.9 mW optical power after reflection by the mirror. The loss is due to imperfect reflectance of the mirror and the fact that the laser ray must pass two times a protective glass plate in front of the mirror. Nevertheless, we met the laser eye safety regulations. The extinction ratio of the laser was 9.5. To characterize the beam spot, we took pictures with a CCD-camera and calculated the power density at the above mentioned distance of 7 m. A horizontal cross section is depicted in Fig. 4 for unfocused and focused (to smallest possible spot size) lens positions, respectively. To calibrate the figure, we used an optical power meter with a photosensitive area of 1 cm². In the focused case, we obtained a light spot with a diameter of around 15 mm (FWHM) and measured an entire power of 370 μ W in an area of 1 cm². Behind the receiver lens we measured a maximum power of 0.58 mW due to the lens diameter of 20 mm, i. e. 3.14 cm² lens area. Each of the 4 actuators of the MEMS mirror (2 for each axis working in opposing directions) was connected to a high-voltage source, because the MEMS operates according to the principle of electrostatic force. For a maximum deviation of one actuator of 6°, the MEMS needs a voltage of 120 V.

The signals from the X and Y receivers were used to set the control signals for the MEMS-mirror and the pick-up manually in this initial research. However, since the MEMS mirror can scan the whole FOV of (1.47 m)² with wide beam in <88 ms, the connection can be built up in a short time when beam steering and focusing will be automated.

A high sensitivity is crucial to detect small differences in the illumination which translate to a non-perfect alignment of

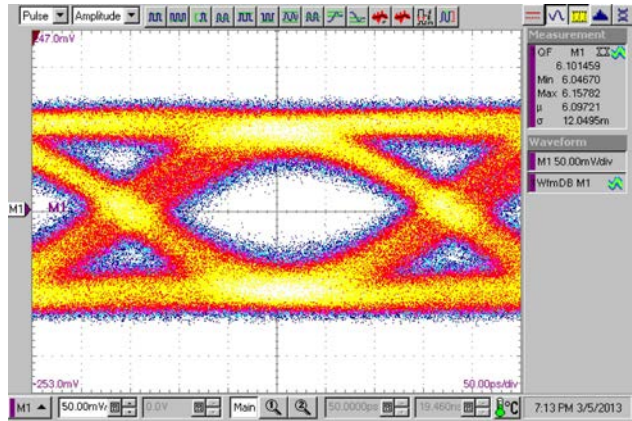


Fig. 5. Eye diagram measured at OEIC's output at 3 Gbit/s, $2^{31}-1$ PRBS, $\lambda = 680$ nm, extinction ratio = 9.5, over a distance of 7 m, 50 mV/div, 50 ps/div.

the beam onto the whole chip. With the HS-TIAs' equivalent input noise current of 1.3 nA and the responsivity of the photodiodes, a minimum detectable optical signal power of about 2.5 nW results. The OEIC was not placed exactly at the focus point of the receiver lens. The focused spot behind the receiver lens had a diameter of roughly 2 mm. At this diameter, the power density is still large enough for the HDR TIA to achieve a BER < 10^{-9} . By using this 2 mm spot diameter at the OEIC surface, we reduced the influence of imperfect aligned transmitter and receiver to an incidence angle of approximately of $\pm 4.5^\circ$ to the optical axis. The area of one outer PD segment was designed to be 0.026 mm². To notice a difference in illumination, an average power density in front of the convex lens of about 100 nW/cm² is needed. With the unfocused power spectrum pictured in Fig. 4, we therefore have a detectable spot with a diameter of roughly 28 cm. This facilitates the search and alignment process. As a last step, we aligned the optical beam and focused to a maximum power at the receiving lens. The data outputs were connected to a Tektronix communication signal analyzer CSA8000 and we made eye measurements, see Fig. 5. The measured Q-factor of 6.1 corresponds to a BER of 5.3×10^{-10} .

IV. CONCLUSION

We are presenting an OWC system operating at 3 Gbps over a distance of more than 7 m without the need of complex alignment procedure or costly optical components. This is achieved by variable beam width, MEMS steering and a novel OEIC receiver realized in a BiCMOS technology. This can open a door for making OWC systems a cheap mass product.

ACKNOWLEDGMENT

P. Brandl thanks R. Lang for mechanical constructions. The authors thank D. Sommer from XFAB for making the OPTO-ASIC process available.

REFERENCES

- [1] J. B. Carruthers and J. M. Kahn, "Angle diversity for nondirected wireless infrared communication," *IEEE Trans. Commun.*, vol. 48, no. 6, pp. 960–969, Jun. 2000.
- [2] H. Le Minh, *et al.*, "A 1.25-Gb/s indoor cellular optical wireless communications demonstrator," *IEEE Photon. Technol. Lett.*, vol. 22, no. 21, pp. 1598–1600, Nov. 1, 2010.
- [3] D. O'Brien, *et al.*, "Integrated transceivers for optical wireless communications," *IEEE J. Sel. Topics Quantum Electron.*, vol. 11, no. 1, pp. 173–183, Jan./Feb. 2005.
- [4] V. Jungnickel, A. Forck, T. Hausteiner, U. Kruger, V. Pohl, and C. von Helmolt, "Electronic tracking for wireless infrared communications," *IEEE Trans. Wireless Commun.*, vol. 2, no. 5, pp. 989–999, Sep. 2003.
- [5] M. Castillo-Vazquez and A. Puerta-Notario, "Single-channel imaging receiver for optical wireless communications," *IEEE Commun. Lett.*, vol. 9, no. 10, pp. 897–899, Oct. 2005.
- [6] K. Wang, A. Nirmalathas, C. Lim, and E. Skafidas, "High-speed indoor optical wireless communication system with single channel imaging receiver," *OSA Opt. Express*, vol. 20, no. 8, pp. 8442–8456, Apr. 2012.
- [7] K. Wang, A. Nirmalathas, C. Lim, and E. Skafidas, "Experimental demonstration of a full-duplex indoor optical wireless communication system," *IEEE Photon. Technol. Lett.*, vol. 24, no. 3, pp. 188–190, Feb. 1, 2012.
- [8] P. Brandl and H. Zimmermann, "3 Gbit/s optical receiver IC with high sensitivity and large integrated pin photodiode," *Electron. Lett.*, vol. 49, no. 8, pp. 552–554, Apr. 11, 2013.

2.4. Wiley ETT 2014

Permission is granted subject to an appropriate acknowledgment given to P. Brandl and H. Zimmermann, "Development of an optoelectronic integrated circuit for indoor optical wireless communication systems", John Wiley & Sons, Ltd. *Trans. Emerging Tel. Tech.* 25:629–637 (2014) © 2014 John Wiley & Sons, Ltd.
<http://dx.doi.org/10.1002/ett.2777>

SPECIAL ISSUE PAPER

Development of an optoelectronic integrated circuit for indoor optical wireless communication systems[†]

P. Brandl* and H. Zimmermann

Institute of Electrodynamics, Microwave and Circuit Engineering, Vienna University of Technology, Vienna, Austria

ABSTRACT

Indoor optical wireless communication systems use in most cases discrete built receivers. The analogue part of receivers consists of a photodetector and an amplifier. In this paper, we present a fully integrated optoelectronic integrated circuit that combines a photodetector and an amplifier into one single receiver chip. We show the evolution of such receivers and examine the benefits of their production as standard semiconductor chip. We developed a fully integrated receiver for a 3 Gbit/s communication in standard BiCMOS technology. We expanded the receiver by additional photodetectors to have the possibility of implementing an automatic alignment system. To demonstrate the performance of this receiver, we built a complete indoor optical wireless communication system. We increased the working area of the system by applying two strategies at the transmitter side. First, we used an adaptive optical system to influence the laser spot diameter. Second, to steer the laser beam, we included a micro-electro-mechanical system. Copyright © 2014 John Wiley & Sons, Ltd.

*Correspondence

P. Brandl, Institute of Electrodynamics, Microwave and Circuit Engineering, Vienna University of Technology, Vienna, Austria.

E-mail: paul.brandl@tuwien.ac.at

[†]This article was published online on 15 January 2014. Errors were subsequently identified. This notice is included in the online version to indicate that this has been corrected 05 February 2014.

Received 11 October 2013; Accepted 12 November 2013

1. INTRODUCTION

Because of the increasing demand for high data rate links, indoor and outdoor optical wireless communication (OWC) systems have been explored in many research works. Good examples are the running European COST Action IC1101 'Optical Wireless Communication—An Emerging Technology' [1] or the part of the European FP7 project 'OMEGA', which dealt with high data rate optical wireless links [2]. Several books [3–6] and an uncountable number of papers in the field of OWC have been published in the past years, most of them are about treating channel models, modulation schemata and system models. Some selected papers should be mentioned at this point, the pioneer work performed by Gfeller and Bapst [7] and the publications [8–11]. Those four papers give a good overview and include many references about research performed in the field of indoor OWC within the last 20 years. However, only a few publications have dealt with optimising the receiver for OWC systems, for example, the papers from Yun and Kavehrad [12], Kahn *et al* [13] and O'Brien *et al* [14]. In most trials of OWC systems, off-the-shelf receivers from the well-established optical fibre communication industry have been used. Optical wireless receiver

systems are very similar to fibre-based receivers, but they differ in the following points. First, optical wireless links are limited in its transmitter (TX) power because of eye safety regulations. The eye can focus light from around 400 up to 1400 nm. Consequently, the regulations are stricter in the near infrared range (700–1000 nm) as in the 1550 nm band. The great advantage of using the near infrared wavelengths is that these wavelengths match the responsivity peak of silicon photodiodes (PD) [5]. In the 1550 nm band, the devices are more expensive due to the fact that the detectors have to be made of III–V compound semiconductors, as for example InGaAs. Second, OWC systems operate in relatively high noise environments because of the ambient light. Third, the receiver must have a larger collection area compared with receivers for fibre communication systems. (For example, single-mode fibres have only a diameter of 8–10 μm .) The collection area can be increased with an optical concentrator, for example, a lens. Fourth, OWC receivers are intended for mass production, and therefore, the receiver design is extremely cost sensitive.

The availability of low-cost, low-capacitance, large-area, high-speed silicon PD favours the 650–850 nm band over the region beyond 1400 nm for most indoor OWC

link applications. The common positive intrinsic negative (pin) PD and the avalanche PD (APD) are the two most common types of silicon PD. In contrast to pin PD, APD have an additional layer, the multiplication region. This layer provides for an inherent current gain through avalanche multiplication of electron-hole pairs generated in the intrinsic layer. To obtain this process functional, APD must be operated at a high reverse bias of about 40–100 V [15, 16]. When there is little induced shot noise from low ambient light, APD benefit from their internal gain to overcome preamplifier thermal noise. Further, a much higher sensitivity can be reached than with a pin PD. However, when the ambient-light induced shot noise is predominant, the net signal-to-noise ratio decreases. The statistical nature of the ionisation process results in a multiplication noise, and the variance of the shot noise increases. Additional drawbacks of APD are the very temperature sensitive avalanche process, higher costs and the need for high bias voltages. APD are hard to realise in optoelectronic integrated circuits (OEIC). In [17], a first trial to build and include an APD in a standard complementary metal–oxide–semiconductor (CMOS) process is presented with the conclusion that it has a rather poor responsivity compared with discrete APD [16]. We will concentrate in the remaining discussion on ordinary pin PD.

2. OPTOELECTRONIC INTEGRATED CIRCUITS

For more than 20 years, optoelectronic integration is under investigation by many research institutions around the world. Compared with discrete built receivers, OEIC technology has the advantages of reduced size, lower packaging cost and smaller interconnect parasitics (Figure 1).

A bond wire has a certain inductance (L_B). This inductance together with the other circuit elements results in a second-order low-pass transfer function at the input node of a receiver optical sub assembly (system in a package). The transfer function $H(f)$ can be simplified written as follows:

$$H(f) \approx \frac{1}{1 + sR_{IN}C_{SUM} + s^2C_{SUM}L_B} \quad (1)$$

$$C_{SUM} = C_{PD} + 2C_{PAD} + C_{IN}$$

C_{PD} represents the parasitic capacitance, I_{PD} stands for the photo current of the PD and C_{PAD} is the pad capacitance. C_{IN} is the input capacitance, and R_{IN} is the input resistance of the first amplifier, respectively. The capacitance at the summing node of the amplifier input can be reduced if the photodetector and the amplifier are realised on the same chip, see (b) in Figure 1. Consequently, the transfer function of an OEIC can be simplified in the way that the third term in the denominator in Equation (1) is not existent, and the limitations imposed by the additional

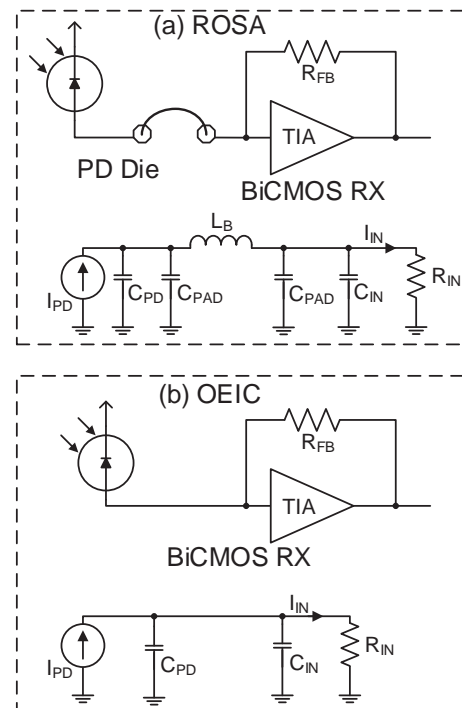


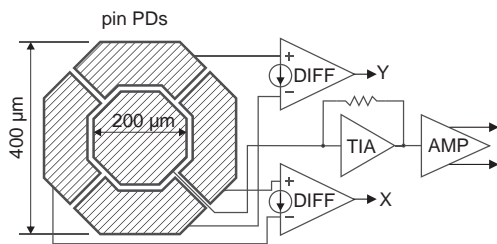
Figure 1. Optical receiver front-end and its equivalent circuit: (a) receiver optical sub assembly and (b) optoelectronic integrated circuit.

parasitic (C_{PAD}) are eliminated. A drawback is that OEIC receivers are often less sensitive than their discrete built counterparts. When the fabrication of photodetectors and transistors is performed on the same substrate and with the same processing steps, some compromises must be made. For example, Si detectors need a much thicker absorption zone than direct semiconductors (e.g. GaAs) due to the fact that the absorption coefficient of Si is an order of magnitude lower than that of direct semiconductors [18]. A work around consists by mounting a flip-chip detector on top of a circuit chip. In this case, the detector and the circuit technology can be selected and optimised independently. This strategy was pursued, for example, by O'Brien [14] and Zeng *et al.* [19]. In [20], a discrete built receiver with large-area PD was recently presented. This receiver was designed for polymer optical fibres (POF) applications. As a matter of fact, the increasing popularity of polymer optical fibres with large-core diameter (1 mm) as transmission media for in-house networks pushes the development of receivers with large-area PD. But those discrete built receivers incur a more complicated packaging and assembly process. Since the pioneering work on silicon monolithic integration of optical and electronic components on the same chip performed by Yamamoto *et al.* [21], many contributions have been reported in the literatures to this field [22–32].

The main driving parameters of a receiver are the bandwidth and the sensitivity. The optical receiver sensitivity is defined as the minimum average optical power necessary

Table I. Comparison with previously published optoelectronic integrated circuits receivers .

	[23]	[25]	[27]	[28]	[31]	[32]	This work
Photodiodes dimension [μm]	300 \emptyset	500 \emptyset	75 \times 75	1000 \emptyset	250 \times 250	400 \emptyset	200 \emptyset
Data rate [Gbit/s]	2.5	0.3	5	0.6	3.125	1.25	3
Sensitivity [dBm]	-20.1	-24.3	-3	-10	-3.8	-19.6	-23.4
Bit error rate	10^{-9}	NA	10^{-12}	NA	10^{-12}	10^{-9}	10^{-9}
Technology [μm]	0.6 BiCMOS	0.6 BiCMOS	0.18 CMOS	0.18 CMOS	65 nm CMOS	0.6 BiCMOS	0.35 BiCMOS
Wavelength [nm]	660	850	850	660	670	660	675
Responsivity [A/W]	0.36	0.315	0.052	0.25	NA	0.52	0.54
Chip size [mm ²]	0.77	2.88	0.72	3.6	0.27	1.31	1.29
Power consumption [mW]	170	27	183	40	50	100	237

**Figure 2.** Simplified schematic of realised optoelectronic integrated circuits receiver.

to achieve a certain bit error rate (BER). The bandwidth and the resulting data rate depend on the performance of the photodetector. The bandwidth of a PD depends mainly on the following parameters:

- The transit time, that is, the time it takes the photon-generated carriers to travel through the depletion region. In a pin PD, the depletion-layer width is approximately equal to the width of the intrinsic layer. This width controls the trade-off between efficiency (and consequently the responsivity) and speed. To minimise the transit time, the reverse bias voltage should be chosen high enough to saturate the carrier drift velocity.
- Electron-hole pairs created below the drift field where no electric field is present because they diffuse very slowly (e.g. some ns/ μm). Wavelengths longer than 780 nm should be avoided because of the large penetration depth and the need for a thick intrinsic layer.
- The electrical frequency response determined by the R-C time constant given by the parasitics at the input node. The main influencing value is the diode's capacitance C_{PD} [15] (Equation 1). The C_{PD} is dependent on the PD's area, but minimising the PD's area to reduce the capacitance is in opposite to one of the most important requirements for OWC detectors, a large detection surface area to facilitate the alignment procedure.

Table I compares some previously published OEIC receivers in which a rather large PD was used with our developed OEIC. We will give a detailed description of our chip in the following chapter.

3. DEVELOPED CHIP

We developed an OEIC with an integrated pin PD in a silicon 0.35 μm BiCMOS technology. Bipolar transistors available in this technology allow circuit design for higher gain and higher data rate, because of the fact that bipolar transistors have a better gm/I ratio than metal-oxide-semiconductor field effect transistor. Together with a minimised PD capacitance, we achieved a good noise performance. Figure 2 gives an overview of the realised chip. It can be seen that we realised five pin PD, and each cathode of the pin PD is connected to a transimpedance amplifier (TIA) to convert the photocurrent to a corresponding voltage signal. With this OEIC, we cannot only receive a data stream, but we can also detect which direction the beam is coming from. This information is useful for our TX concept of a laser beam that can be adjusted and aligned. This will be explained in more detail in Section 4.

3.1. Pin photodiodes

As mentioned earlier, we realised five pin PD. The anodes of the pin PD are built by the p+ doped substrate. A low doped ($< 5 \times 10^{13} \text{cm}^{-3}$) p- epitaxial layer is located on top of the substrate. This layer is working as intrinsic zone of each pin PD. The cathodes of the pin PD are realised by highly doped n+ regions (source/drain regions). The centre PD, serving for high data rate communication, has a diameter of 200 μm and a low capacitance of only 550 fF at a reverse bias voltage of -8 V. This voltage is applied to the substrate contact of the chip and improves the speed of the pin PD by increasing the drift velocity. Figure 3 shows the frequency response of the centre pin PD at a wavelength of 675 nm and a bias voltage of -8 V. We measured a -3 dB cut-off frequency of 1.1 GHz and at a wavelength of 675 nm. To improve the responsivity, the PD are covered with an anti-reflection coating. The responsivity is 0.54 A/W at 675 nm.

Each surrounding PD for adjusting the laser beam has an area of 0.026 mm². The opposite situated PD were connected to a differential TIA; this enables a simple detection of the difference in received light power. It converts the difference in photocurrent in a corresponding voltage signal. The two differential TIAs are optimised for high sensitivity

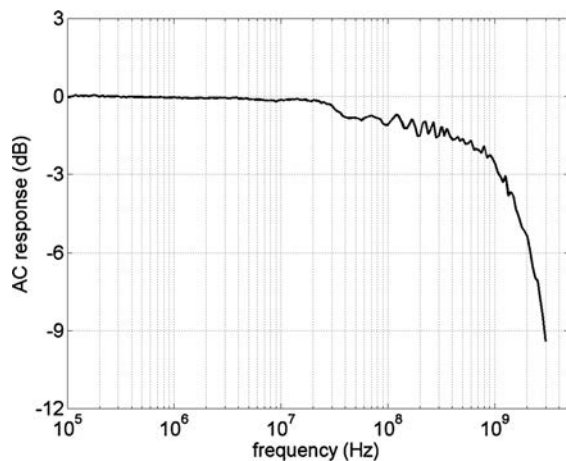


Figure 3. Normalised frequency response of 200 μm pin photodiodes, $\lambda = 675 \text{ nm}$, $V_{PD} = -8 \text{ V}$.

and have an equivalent input noise current of only 1.3 nA. They have a transimpedance of 100 k Ω and reach a -3 dB bandwidth of 1.6 MHz at a total current consumption of 640 μA at a supply voltage of 3.3 V.

3.2. High data rate receiver

The simplified circuit diagram of the high data rate receiver is shown in Figure 4. The photocurrent I_{PH} from the pin PD is converted by a TIA to a voltage signal. The TIA is composed of transistors T1, T2, T3, resistor R_{fb} , capacitance C_{fb} and some current sources. T1 works as a common-emitter stage, T2 builds an emitter follower and transforms the impedance and T3 shifts the voltage level. The emitter followers T2 and T3 produce a certain gain peaking at high frequencies, which increases the bandwidth of the complete OEIC. Standard MOS transistors build the current sources. The value of the feedback resistor R_{fb} is 830 Ω , and the feedback capacitance C_{fb} is 10 fF, which guarantees the stability of the TIA. The dummy TIA, which has the same characteristic as the main TIA except

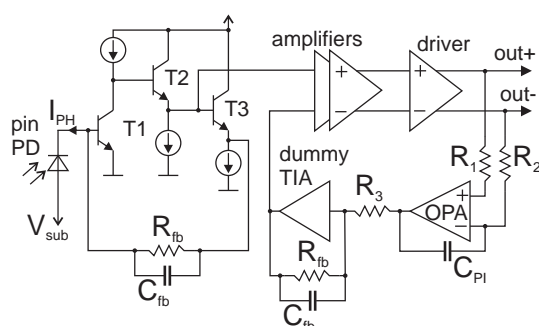


Figure 4. Simplified circuit diagram of the high data rate part of the realised optoelectronic integrated circuits receiver.

for the reduced bandwidth, reproduces the average output voltage of the main TIA. A proportional integral controller is built with an operational amplifier, R_1 , R_2 and C_{PI} . The average photocurrent I_{PH} is flowing through R_3 generated by the output of the operational amplifier and fed into the input of the dummy TIA. The outputs from the dummy TIA and the main TIA are connected to a differential amplifier, which builds the input stage of a two-stage amplifier. The amplifiers have a gain of 28 dB and are followed by a 50 Ω driver. This output driver delivers a differential output voltage of 300 mV into 50 Ω . The differential structure of the OEIC has the big advantage, which the OEIC becomes insensitive to common-mode noise and low-frequency parts of the input signal [33]. For example, signal parts from ambient light will be cancelled out by the controlling mechanism. The complete chip has an area of 890 \times 1450 μm^2 and has a total current consumption of 72 mA with a supply voltage of 3.3 V.

3.3. Performance of high data rate receiver

We determined the performance of the high data rate part of the receiver independent from the surrounding differential TIAs. For this, we brought the signal from a light source via a multimode fibre to the centre pin PD. As source, we used a vertical cavity surface emitting laser diode with a wavelength of 675 nm. As a first step, we measured the frequency response of the complete receiver path with a vector network analyzer. Our goal was to reach a data rate of 3 Gbit/s. In [15], a rule of thumb for the optimum receiver bandwidth dependent on the data rate is given. For non-return-to-zero receivers, the optimum -3 dB bandwidth for obtaining best sensitivity values is about

$$BW_{3dB} \approx \frac{2}{3} \times B \quad (2)$$

where B is the bit rate. We measured a -3 dB cut-off frequency of 2.1 GHz (Figure 5).

As second step, we tested the receiver concerning its sensitivity and connected the outputs of the OEIC to a bit error tester. Figure 6 shows the results at different data rates. All sensitivity measurements were performed with a pseudo-random binary sequence of $2^{31}-1$ and the input power is referred to the average optical input power. At a data rate of 3 Gbit/s, we obtained a sensitivity of -23.4 dBm at a BER of 10^{-9} . Especially, at a data rate of 1.25 Gbit/s, we measured a sensitivity of -24.2 dBm. This is a notable improvement to the aforementioned results (Table I).

4. OPTICAL WIRELESS COMMUNICATION SYSTEM

Among the numerous physical configurations for establishing an optical link [6], we decided for a line of sight system [34]. The big advantage of this approach is the minimised path loss with narrow beams, but the challenge is to achieve

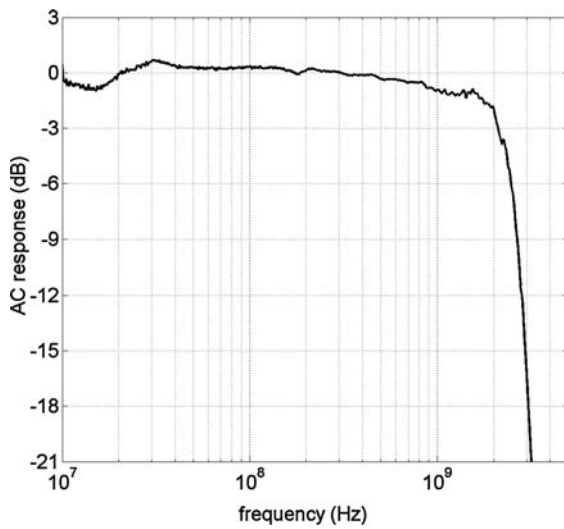


Figure 5. Normalised frequency response of complete high data rate receiver, $\lambda = 675$ nm.

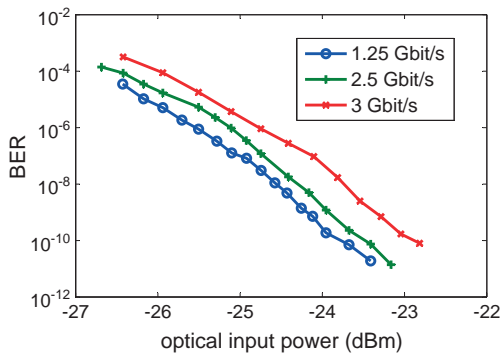


Figure 6. Sensitivity of high data rate receiver at different data rates, $\lambda = 675$ nm, pseudo-random binary sequence = $2^{31}-1$.

an adequate wide field of view (FOV) for a certain coverage area. In [35], it was proposed to use a fixed FOV and a lens with a large acceptance angle at the receiver. Further, it was suggested that the photodetector should be placed into the focus of the lens with a positioning mechanism. We aimed to implement a tracking possibility at the TX side. Unfortunately, mechanical steerable systems are bulky and expensive, but developments in the field of micro-electronic-mechanical systems (MEMS) represent a solution. To use a steerable mirror based on MEMS was also proposed in [36]. They used a 1550 nm system with a complex optical system at the receiver side consisting of a compound parabolic concentrator, multiple lenses and a fibre collimator. This was performed to collect sufficient light power for reaching a certain errorless data rate within their fixed FOV. We advanced our TX in the way that we could influence the beam spot diameter. We can scan a certain area with a broad beam until the surrounding PD detect a signal. This area will be determined by the used

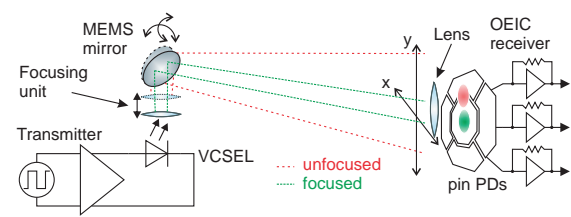


Figure 7. Schematic diagram of complete optical wireless communication system, not to scale.

MEMS device, as explained later on in this section. With the feedback from the developed OEIC, the TX can align and focus the beam on the receiver. This is performed until the received power has reached a power limit to guarantee a certain BER. With the fully adjustable laser beam and the appropriate receiver design, the alignment process is more facilitated, and the system is flexible in transmit distances. Figure 7 shows an overview of our proposed OWC system.

4.1. Transmitter

Figure 8 shows a photograph of the transmitter (TX). On the bottom of the photo, the printed circuit board (PCB) can be seen. The PCB carries a laser driver (MAX3740A from Maxim) and a commercial VCSEL from Vixar [37]. We selected that VCSEL because of the following reasons: First, at the time of building the TX, this device had the most available output power of 2 mW at a -3 dB modulation bandwidth of 3.5 GHz. Second, the somewhat unusual wavelength of 680 nm matched perfectly to the pin PD's responsivity maximum. Third, due to the fact that the

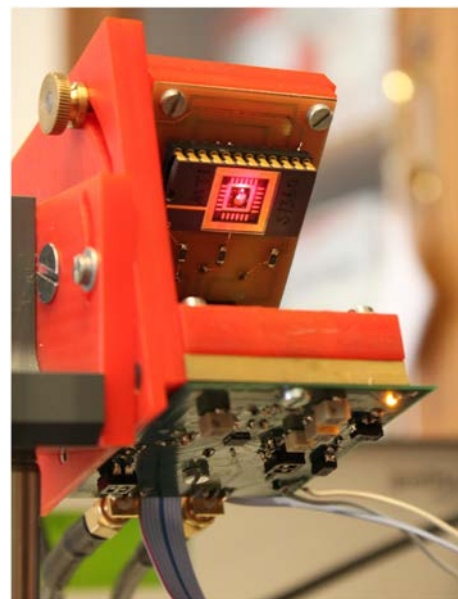


Figure 8. Photograph of transmitter.

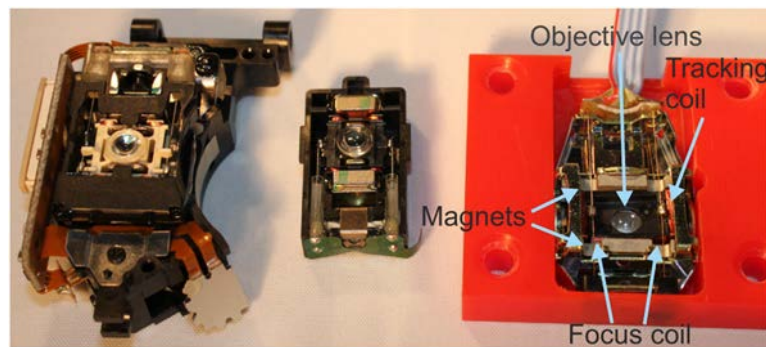


Figure 9. Dismounted pick-ups from standard CD/DVD-ROM drives.

wavelength is visible, the coarse alignment of the receiver is facilitated.

A pick-up from a commercial optical disc drive was mounted on the PCB to influence the laser beam width. Figure 9 shows three devices, two dismounted and one placed in a self-built bearing. We control the distance between VCSEL and lens with one of the two servomechanisms, in fact with the focus coil. We are able to vary the beam spot diameter continuously. To obtain an appropriate pick-up, we disassembled several CD/DVD-ROM drives.

We mounted a gimbal-less two-axis scanning MEMS micro-mirror from Mirrorcle [38] following the laser ray. The device operates according to the principle of electrostatic force and has four actuators, two for each axis working in opposing directions. The maximum deviation of one actuator is 6° and is reached with a maximum voltage of 120 V. Therefore, we have a total FOV of $24^\circ \times 24^\circ$ [Correction made here after initial online publication], and together with four high-voltage sources, we can reach each point within the FOV. The mirror has a diameter of 3.6 mm and is coated with aluminum. The MEMS has a step response time of around 8 ms for a 2.5 degree deviation. We built a fully adjustable mechanical prototype to align all components in relation to the laser ray (Figure 8).

4.2. Receiver

The earlier described OEIC was glued and bonded onto a PCB. A simple convex lens with a diameter of 20 mm was placed in front of the chip, see on the right side of Figure 10. In the photograph, the measurement set-up described in the next section can also be seen.

5. OPTICAL WIRELESS COMMUNICATION SYSTEM VERIFICATION

We placed the TX and the receiver (RX) at different distances in our laboratory. The TX was modulated with a 3 Gbit/s pseudo-random binary sequence of $2^{31}-1$ from a bit pattern generator. The optical output power of the



Figure 10. Photograph of receiver measurement set-up.

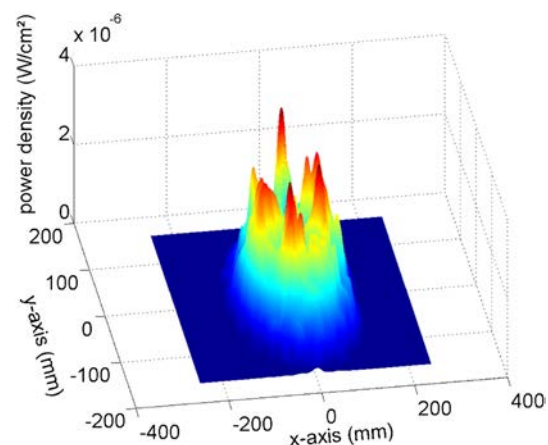


Figure 11. Unfocused vertical cavity surface emitting laser diode spot in a distance of 7 m.

VCSEL was adjusted in such a way that an eye-secure average optical power of 0.94 mW after the mirror was transmitted. The extinction ration of the VCSEL was adjusted to a value of 9.7 dB. We took pictures with a charge-coupled device-camera to characterise the beam spot. For calibration of the figures, we used an optical power metre with a photosensitive area of 1 cm^2 . Figure 11 shows the power density distribution in a distance of 7 m in the unfocused case and Figure 12 in the focused case. In the focused case, we measured a light spot with a diameter of around 15 mm (FWHM) and an entire power of $378 \mu\text{W}$ in an area of 1 cm^2 .

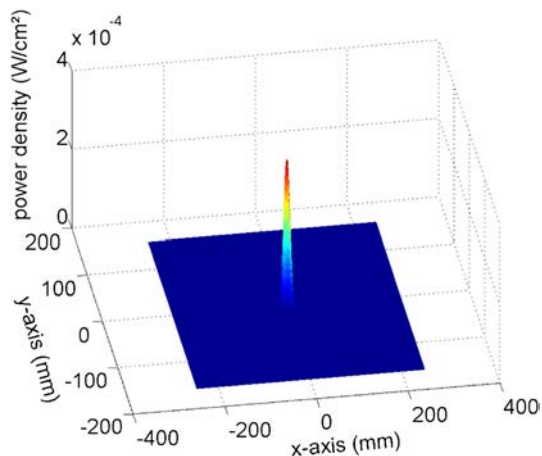


Figure 12. Focused vertical cavity surface emitting laser diode spot in a distance of 7 m.

The X and Y outputs from the differential TIAs were connected to voltmeters. These signals were used to control the MEMS-mirror and the pick-up manually in this initial research. In an ongoing project, we are working towards a system with a fully automated steering and focusing process. The PD has a responsivity of 0.53 A/W at 680 nm, this results in a minimum detectable optical signal power of 2.5 nW with the equivalent input noise current of 1.3 nA. Including the losses from the lens (5%) and a not perfectly focused point (diameter of 1 mm), we calculated a minimum power density in front of the lens of around 25 nW/cm². The detectable spot has roughly a diameter of 30 cm with the unfocused power spectrum pictured in Figure 11.

As already mentioned earlier, in Figure 10, the measurement set-up for the receiver can be seen. The data outputs of the receiver were connected to a digital serial analyzer to perform some eye measurements. The Figure 13 shows different eye measurements at different distances between the TX and RX. The eyes are clearly open, and there is still some room for more working distance.

6. CONCLUSION

At the beginnings of OWC, in most cases, standard receivers from the well-established fibre communication industry have been used. We pointed out the benefits and challenges of implementing OEIC in standard silicon technologies. The most important parameters for OWC receivers are the sensitivity, the bandwidth and the area of the photodetector. We developed an OEIC with a highly efficient 200 μm integrated pin PD in a 0.35 μm standard BiCMOS technology. The complete chip shows a notable sensitivity of -23.4 dBm at a data rate of 3 Gbit/s. The sensitivity and the reached data rate speak for using of OEIC in BiCMOS in future OWC systems. Further, we added some PD surrounding the centre PD for implementing an OWC

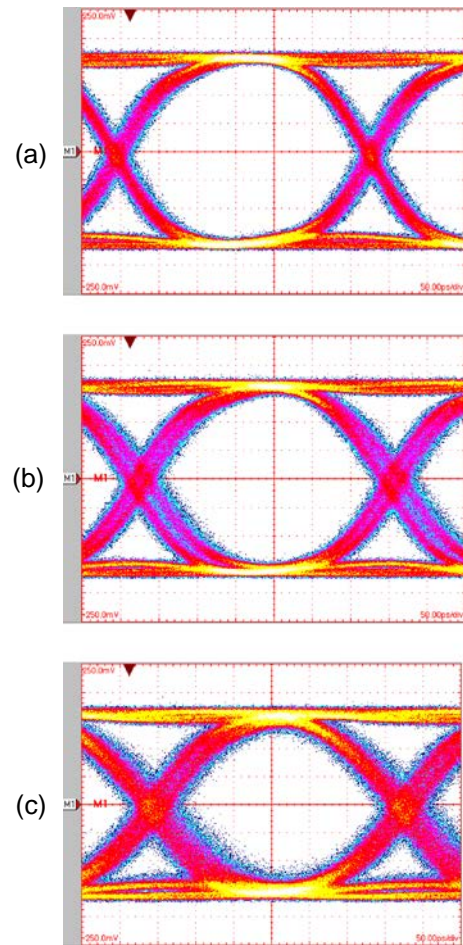


Figure 13. Eye diagrams measured at different distances between TX and RX: (a) 4m, (b) 8m and (c) 12m, 3Gbit/s, 2³¹-1 pseudo-random binary sequence, $\lambda = 680\text{nm}$, 50mV/div, 50ps/div.

system based on tracked line of sight links. These additional PD gave us the possibility of simple alignment and focusing of the laser beam. We described our TX design with an adjustable beam width and MEMS-based beam steering. The whole system allows errorless transmission over a distance of 12 m at a data rate of 3 Gbit/s.

ACKNOWLEDGEMENTS

P. Brandl thanks R. Lang for the mechanical constructions and S. Schidl, A. Polzer and W. Gaberl for their assistance during the chip design process. The authors thank D. Sommer from XFAB for making the OPTO-ASIC process available.

REFERENCES

1. www.cost.eu/domains_actions/ict/actions/ic1101. [25 September 2013].
2. O'Brien D, Turnbull R, Le-Minh H, Faulkner G, Bouchet O, Porcon P, El Tabach M, Gueutier E, Wolf M, Grobe L, Li J. High-speed optical wireless demonstrators: Conclusions and future directions. *IEEE Journal of Lightwave Technology* 2012; **30**(13): 2181–2187. DOI: 10.1109/JLT.2012.2193874.
3. Barry JR. *Wireless Infrared Communications*. Kluwer Academic Publishers Group: Norwell, Massachusetts 0261 USA, 1994. DOI:10.1007/978-1-4615-2700-8.
4. Hranilovic S. *Wireless Optical Communication Systems*. Springer: New York, 2005.
5. Ramirez-Iniguez R, Idrus SM, Sun Z. *Optical Wireless Communications: Ir For Wireless Connectivity*. Auerbach Publications: Boca Raton, FL, USA, 2008. DOI:10.1201/9781420013443.
6. Ghassemlooy Z, Popoola W, Rajbhandari S. *Optical Wireless Communications: System and Channel Modelling With MATLAB*, 1st ed. CRC Press, Inc.: Boca Raton, FL, USA, 2012. DOI:10.1201/b12687.
7. Gfeller FR, Bapst U. Wireless in-house data communication via diffuse infrared radiation. *Proceedings of the IEEE* 1979; **67**(11): 1474–1486. DOI: 10.1109/5.554222.
8. Kahn JM, Barry JR. Wireless infrared communications. *Proceedings of the IEEE* 1997; **85**(2): 265–298. DOI: 10.1109/5.554222.
9. Street A, Stavrinou P, O'Brien D, Edwards D. Indoor optical wireless systems—a review. *Optical and Quantum Electronics* 1997; **29**: 349–378. DOI: 10.1023/A:1018530828084.
10. O'Brien DC, Katz M, Wang P, Kalliojarvi K, Arnon S, Matsumoto M, Green RJ, Jivkova S. White Paper on Short Range Optical Wireless Communications, In *WG5 Session Wireless World Research Forum*, WWRFF12 Toronto, Canada, 4-5 November 2004; 1–22. http://wg5.wireless-world-research.org/WG5-wp3-Optical_Wireless_Communications-V2005.pdf. [11 December 2013].
11. Green R, Joshi H, Higgins M, Leeson M. Recent developments in indoor optical wireless [optical wireless communications]. *IET Communications* 2008; **2**(1): 3–10. DOI: 10.1049/iet-com:20060475.
12. Yun G, Kavehrad M. Spot-diffusing and fly-eye receivers for indoor infrared wireless communications, In *Proceedings of IEEE International Conference on Selected Topics in Wireless Communications, 1992*, Vancouver, Canada, 25-26 June, 1992; 262–265, DOI: 10.1109/ICWC.1992.200761.
13. Kahn JM, You R, Djahani P, Weisbin AG, Teik BK, Tang A. Imaging diversity receivers for high-speed infrared wireless communication. *IEEE Communications Magazine* Dec 1998; **36**(12): 88–94. DOI: 10.1109/35.735884.
14. O'Brien D, Faulkner G, Zyambo E, Jim K, Edwards D, Stavrinou P, Parry G, Bellon J, Sibley M, Lalithambika V, Joyner VM, Samsudin RJ, Holburn DM, Mears RJ. Integrated transceivers for optical wireless communications. *IEEE Journal of Selected Topics in Quantum Electronics* 2005; **11**(1): 173–183. DOI: 10.1109/JSTQE.2004.841471.
15. Säckinger E. *Broadband Circuits For Optical Fiber Communication*. John Wiley & Sons, Inc., 2005. DOI:10.1002/047172640.
16. www.first-sensor.com. *Ad500-1.3g-to5*, August 2013. Datasheet. [5 September 2013].
17. Youn JS, Lee MJ, Park KY, Choi WY. 10-Gb/s 850-nm CMOS OEIC receiver with a silicon avalanche photodetector. *IEEE Journal of Quantum Electronics* 2012; **48**(2): 229–236. DOI: 10.1109/JQE.2011.2170405.
18. Zimmermann H. *Integrated Silicon Optoelectronics*, 2nd ed., Vol. 148. Springer Berlin Heidelberg, 2010. DOI:10.1007/978-3-642-01521-2.
19. Zeng J, Joyner V, Liao J, Deng S, Huang Z. A 5Gb/s 7-channel current-mode imaging receiver front-end for free-space optical MIMO, In *52nd IEEE International Midwest Symposium on Circuits and Systems, 2009. MWSCAS '09.*, Cancun, Mexico, 2-5 August, 2009; 148–151, DOI: 10.1109/MWSCAS.2009.5236130.
20. Loquai S, Winkler F, Wabra S, Hartl E, Schmauss B, Ziemann O. High-speed, large-area pof receivers for fiber characterization and data transmission \geq 10-Gb/s based on MSM-photodetectors. *IEEE Journal of Lightwave Technology* 2013; **31**(7): 1132–1137. DOI: 10.1109/JLT.2013.2243699.
21. Yamamoto M, Kubo M, Nakao K. Si-oeic with a built-in pin-photodiode. *IEEE Transactions on Electron Devices* 1995; **42**(1): 58–63. DOI: 10.1109/16.370035.
22. Zimmermann H, Heide T. A monolithically integrated 1-gb/s optical receiver in 1- μ m CMOS technology. *IEEE Photonics Technology Letters* 2001; **13**(7): 711–713.
23. Swoboda R, Zimmermann H. 2.5 gbit/s silicon receiver oeic with large diameter photodiode. *Electronics Letters* 2004; **40**(8): 505–507. DOI: 10.1049/el:20040346.
24. Radovanovic S, Annema AJ, Nauta B. A 3-Gb/s optical detector in standard CMOS for 850-nm optical communication. *IEEE Journal of Solid-State Circuits* 2005; **40**(8): 1706–1717. DOI: 10.1109/JSSC.2005.852030.
25. Förtsch M, Zimmermann H, Pless H. 220-MHz monolithically integrated optical sensor with large-area integrated PIN photodiode. *IEEE Sensors Journal* 2006; **6**(2): 385–390. DOI: 10.1109/JSEN.2006.870168.

26. Chen WZ, Huang SH. A 2.5 gbps CMOS fully integrated optical receiver with lateral pin detector. In *IEEE Custom Integrated Circuits Conference, 2007. CICC '07.*, San Jose, USA, 16-19 September, 2007; 293–296, DOI: 10.1109/CICC.2007.4405736.
27. Kao TC, Musa F, Carusone A. A 5-gbit/s CMOS optical receiver with integrated spatially modulated light detector and equalization. *IEEE Transactions on Circuits and Systems I: Regular Papers* 2010; **57**(11): 2844–2857.
28. Tavernier F, Steyaert M. A high-speed pof receiver with 1 mm integrated photodiode in 180 nm CMOS, In *2010 36th European Conference and Exhibition on Optical Communication (ECOC)*, Torino, Italy, 19-23 September, 2010; 1–3, DOI: 10.1109/ECOC.2010.5621473.
29. Lee D, Han J, Han G, Park SM. An 8.5-gb/s fully integrated CMOS optoelectronic receiver using slope-detection adaptive equalizer. *IEEE Journal of Solid-State Circuits* 2010; **45**(12): 2861–2873.
30. Huang SH, Chen WZ, Chang YW, Huang YT. A 10-Gb/s OEIC with meshed spatially-modulated photo detector in 0.18- μ m CMOS technology. *IEEE Journal of Solid-State Circuits* 2011; **46**(5): 1158–1169. DOI: 10.1109/JSSC.2011.2116430.
31. Dong Y, Martin K. A high-speed fully-integrated POF receiver with large-area photo detectors in 65 nm CMOS. *IEEE Journal of Solid-State Circuits* 2012; **47**(9): 2080–2092. DOI: 10.1109/JSSC.2012.2200529.
32. Atef M, Swoboda R, Zimmermann H. 1.25 gbit/s over 50 m step-index plastic optical fiber using a fully integrated optical receiver with an integrated equalizer. *IEEE Journal of Lightwave Technology* 2012; **30**(1): 118–122. DOI: 10.1109/JLT.2011.2179520.
33. Brandl P, Zimmermann H. 3 gbit/s optical receiver ic with high sensitivity and large integrated pin photodiode. *Electronics Letters* 2013; **49**(8): 552–554. DOI: 10.1049/el.2013.0558.
34. Brandl P, Schidl S, Polzer A, Gaberl W, Zimmermann H. Optical wireless communication with adaptive focus and mems-based beam steering. *IEEE Photonics Technology Letters* 2013; **25**(15): 1428–1431. DOI: 10.1109/LPT.2013.2266574.
35. Castillo-Vazquez M, Puerta-Notario A. Single-channel imaging receiver for optical wireless communications. *IEEE Communications Letters* 2005; **9**(10): 897–899. DOI: 10.1109/LCOMM.2005.10021.
36. Wang K, Nirmalathas A, Lim C, Skafidas E. High-speed optical wireless communication system for indoor applications. *IEEE Photonics Technology Letters* 2011; **23**(8): 519–521.
37. www.vixarinc.com. *680 nm Communications Grade VCSEL*, 2012. Datasheet 680C-0000-x0y1. [12 September 2013].
38. www.mirrorclotech.com. *Gimbal-Less Two-Axis Scanning MEMS Micromirrors*, 2012. Device Datasheet S1911. [14 September 2013].

2.5. OSA Optics Letters 2014

© 2014 Optical Society of America. One print or electronic copy may be made for personal use only. Systematic reproduction and distribution, duplication of any material in this paper for a fee or for commercial purposes, or modifications of the content of this paper are prohibited.

<http://dx.doi.org/10.1364/OL.39.004045>

Automated alignment system for optical wireless communication systems using image recognition

Paul Brandl,* Alexander Weiss, and Horst Zimmermann

Institute of Electrodynamics, Microwave and Circuit Engineering, Vienna University of Technology, Gusshausstrasse 25, 1040 Vienna, Austria

*Corresponding author: paul.brandl@tuwien.ac.at

Received March 20, 2014; revised June 5, 2014; accepted June 6, 2014;
 posted June 6, 2014 (Doc. ID 208663); published June 30, 2014

In this Letter, we describe the realization of a tracked line-of-sight optical wireless communication system for indoor data distribution. We built a laser-based transmitter with adaptive focus and ray steering by a microelectromechanical systems mirror. To execute the alignment procedure, we used a CMOS image sensor at the transmitter side and developed an algorithm for image recognition to localize the receiver's position. The receiver is based on a self-developed optoelectronic integrated chip with low requirements on the receiver optics to make the system economically attractive. With this system, we were able to set up the communication link automatically without any back channel and to perform error-free (bit error rate $<10^{-9}$) data transmission over a distance of 3.5 m with a data rate of 3 Gbit/s. © 2014 Optical Society of America

OCIS codes: (060.2605) Free-space optical communication; (100.3008) Image recognition, algorithms and filters; (130.3990) Micro-optical devices; (250.3140) Integrated optoelectronic circuits.
<http://dx.doi.org/10.1364/OL.39.004045>

Optical wireless communication (OWC) systems provide the opportunity to retrofit indoor wireless communication scenarios in the near future. The almost unlimited data rate of optical communication systems expands on state-of-the-art wireless radio access systems, especially in the case of moderate mobility. Different strategies have been pursued in the last decades to reach certain coverage areas and data rates [1–3] (see Fig. 1).

In a diffuse configuration, a transmitter usually points toward the ceiling, and the reflections cause radiation in a wide range of angles. The receiver, which can be placed anywhere in an office room without needing a line of sight to the transmitter, collects those reflections. The diffuse system shows excellent mobility but at the expense of high transmit power levels. Further, the bit rates are limited due to multipath distortions; in [1] only a data rate of 50 Mbit/s has been reported. Therefore, line-of-sight (LOS) configurations are more attractive, but the challenge is to provide mobility.

To obtain certain coverage and a high data rate, an angle diversity system with a data rate of 1.25 Gbit/s has been proposed in [2]. In this research, the transmitter applied three separate channels, each equipped with a 25 mW laser. The receiver consisted of an optical filter, a collection optical system, and a commercial avalanche photodetector. With this configuration, a field of view (FOV) of approximately $25^\circ \times 8^\circ$, corresponding to a coverage area of $1.3 \text{ m} \times 0.45 \text{ m}$ in a distance of 3 m, was reached. With a more narrow FOV system, it would be possible to considerably reduce the required transmit power while showing the same performance. Moreover, the feasible data rate would be increased and only limited by the available power budget. However, a fixed LOS system has no true mobility.

To overcome this drawback, in [3] an arrangement with an additional tracking and optical steering was implemented. The narrow FOV of the receiver was aligned with a rotating mirror to a wide-angle transmitter. The system was controlled by the information of a

charge-coupled device (CCD) camera. The reported data rate was 1 Gbit/s over a distance of 2 m. A similar approach to realize a tracked OWC system was recently presented in [4] and [5]. In both papers, it was suggested to use a microelectromechanical system (MEMS) with a mirror for beam steering and to couple the light signal back into a fiber after the signal had passed through the free space. This coupling was realized with a rather large effort regarding the optical system in front of the fiber.

Beyond the suggested approaches in [3–5], we verified a system with a MEMS mirror for manual beam steering experimentally [6]. Here in this Letter, we extended our system with an image-recognition system for automated alignment. By doing this, there is no need of a back channel via an infrared remote transmitter or via a Bluetooth channel, which considerably simplifies the system compared with that in [6]. Compared with those in [4] and [5], we simplified the receiver system by using a self-developed monolithically integrated optoelectronic receiver chip [7].

The main working principle can be seen in Fig. 2. For the transmitter working, we used a 680 nm, 2 mW VCSEL (vertical cavity surface emitting laser) from Vixar. The laser has a beam divergence of 16° full width at half-maximum (FWHM). To focus the laser beam, we utilized a lens with a servomechanism, as known from CD/DVD-ROM drives. With this assembly, we were able to focus the

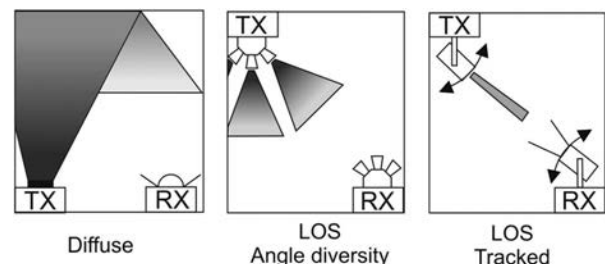


Fig. 1. Different configurations for optical wireless links.

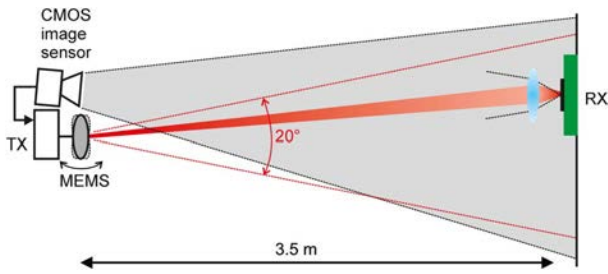


Fig. 2. Principle of tracked OWC system (not to scale).

laser beam to a divergence angle of less than 0.15° FWHM. A gimbal-less two-axis scanning MEMS micro-mirror from Mirrorcle (S1911) was placed after the focusing lens. The mirror has a diameter of 3.6 mm and is aluminum coated. The MEMS mirror has four actuators, two for each axis working in opposite directions. The actuators operate according to the principle of electrostatic force. We measured a maximum FOV of 20° in the x and y directions, each at around 120 V. The MEMS mirror has a mechanical resonance frequency of around 350 Hz; therefore, for static response, a low-pass filter with a cut-off frequency of 140 Hz is recommended, which results in a settling time of approximately 8 ms. The pivoting motion is not linear due to the physical basis in which the force is proportional to the squared voltage. Therefore we used a complementary metal-oxide-semiconductor (CMOS) image sensor (Aptina MT9M001STM) to track the laser beam. The image sensor's size is $6.656 \text{ mm} \times 5.325 \text{ mm}$ and has a resolution of 1280×1024 , horizontal and vertical, respectively. We placed an objective in front of the image sensor with a focal distance $f = 16 \text{ mm}$. This is a good compromise to cover nearly the complete FOV of the MEMS mirror while not receiving a too-small resolution of the picture.

At the receiver side, we applied our self-developed optoelectronic integrated chip. The chip was realized in a standard silicon $0.35 \mu\text{m}$ bipolar CMOS (BiCMOS) process and included a pin-photodiode ($200 \mu\text{m}$ diameter) and a transimpedance amplifier [7]. The chip was glued and bonded on a printed circuit board (PCB). The photodiode was located in the center of the PCB. A convex lens with a diameter of 20 mm and a focal distance of 12 mm was placed in front of the chip to serve as an optical antenna.

The complete system was built up in our office. To control the MEMS mirror, a programmable high-voltage source was applied. The voltage source and the CMOS image sensor were connected to a personal computer (PC), which worked as control unit in this initial research work.

We developed a program in Python for detecting the receiver position (i.e., the PCB having a rectangular shape of $56 \text{ mm} \times 55 \text{ mm}$) and the laser ray position as well as for controlling the high-voltage source steering the MEMS mirror. The main algorithms for image recognition and tracking were taken from the Open Source Computer Vision Library (OpenCV) [8]. This library of programming functions was developed by Intel for real-time computer vision and is now available for free under the open-source Berkeley Software Distribution license.

The communication between the PC and high-voltage source is acquired via an RS-232 interface. Over this connection, the voltage can be controlled, and the actual voltage values and system parameters can be read. The image sensor is connected via universal serial bus (USB) 2.0 (with a maximum signaling rate of 480 Mbit/s) to the PC and provides the images for receiver detection. With the abovementioned 1280×1024 pixel camera and a resolution of 8 bits per pixel, one image has a size of 10 Mbit. We used a frame rate of 30 fps, and, consequently, we obtained a raw data rate of 300 Mbit/s. Even without consideration of data compression, the USB 2.0 connection can handle this amount of data traffic. A direct alignment of the laser ray to the receiver's position would require a known default laser position (for example, when there is no tension on the MEMS mirror) within an adjusted camera view. This direct alignment also would demand the linear pivoting motion of the MEMS mirror. To avoid the adjustment procedure and taking into account the nonlinear pivoting motion of the MEMS mirror, we decided to detect, additionally, the laser point position out of the image.

Figure 3 depicts the flowchart of the developed program. At the beginning, the actual position of the receiver PCB is detected with the help of the speeded-up robust feature (SURF) detection algorithm [9]. The algorithm extracts significant features of the target from a reference picture and searches for these features within the actual picture from the CMOS image sensor. The advantage of using the SURF algorithm is its capability to detect the target, even when it is slightly turned or tilted. Evaluations in [9] showed a repeatability of the SURF detection up to 10% better compared with other detection

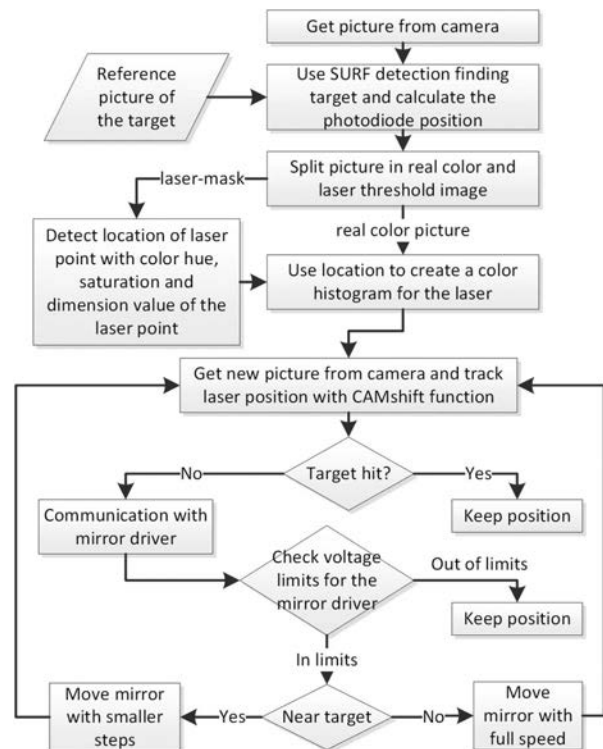


Fig. 3. Flowchart of developed control program.

algorithms at different viewpoint angles. When those features are identified, the actual position of the chip is calculated. Of course, the more features are detected, the more exact is the identification of the position. The SURF algorithm needs a minimum linear resolution of approximately $n = 50$ pixels for detecting the PCB (with a dimension of $x = 56$ mm). We can now calculate a maximum distance between transmitter and receiver:

$$\text{Distance} = \frac{x}{n \cdot x'} \cdot f + 2 \cdot f. \quad (1)$$

X' is the dimension of one pixel, which is $5.2 \mu\text{m}$; f is the above-mentioned focal distance of 16 mm. This results in a maximum distance of approximately 3.5 m. The detection possibility depends on the illumination. We tested the detection performance in an office environment with an illumination of 500 lux (normal office lighting). Then we reduced the illuminance within the office to approximately 100 lux (overcast day outside, no artificial lighting), but no significant influence on the performance was noted.

In the next step, the actual position of the laser point has to be identified. For this, the image will be filtered against typical features of the laser point (color hue, saturation, and dimension value). The position and dimension of the laser point will be used to create a detailed image histogram of this detected point. Starting from the original position and taking into account the histogram information, the laser point can be tracked with the continuously adaptive mean shift (CAMshift) function [8].

Now, knowing the positions of the receiver and laser point, the MEMS mirror can be moved. To speed up the alignment, at the beginning, i.e., when the receiver and the laser point are still farther away from each other, the control voltages can be changed in bigger steps. In our experiments, the maximum step size was limited to 0.5 V. With faster movements of the laser ray, the CAM-shift function was not able to continuously track the laser point. Before steering the MEMS, each new voltage value is controlled against a maximum voltage level in order not to destroy the device. This process continues until the laser ray hits the receiver. Figure 4 shows an image taken by the CMOS image sensor with detected and tagged targets (the receiver and the laser point) by the control program. The green rectangle marks the maximum deviation points reachable with the MEMS mirror. In a distance of 3.5 m, the reachable area has a dimension of $1.23 \text{ m} \times 1.23 \text{ m}$.

We used a commercially available desktop computer with an AMD Phenom II X4 955 central processing unit (CPU) as a control unit. This CPU contains four cores and works with a clock of 3.2 GHz. The main program consists of 824 lines of code and occupies a memory size of 34 kBytes. When the program is executing, it needs about 80 MBytes of RAM and 30% of the processing power from the above-mentioned CPU. The memory requirement can be explained with the fact that at least two live images from the camera are used. One image is a real color picture (see Fig. 4), and the other image is a filtered version for the laser point detection (laser threshold image).

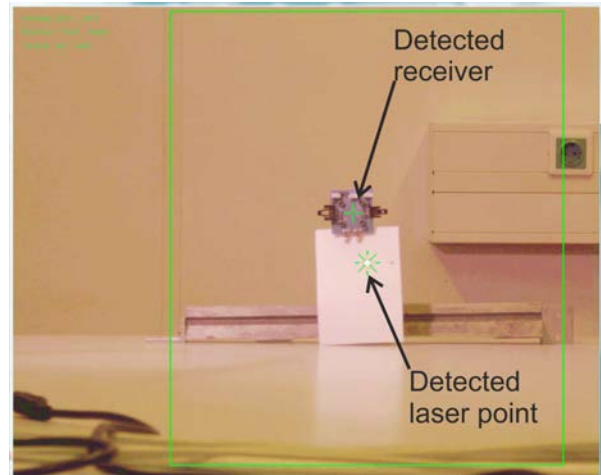


Fig. 4. Image taken with the CMOS image sensor with overlaid calculated positions of receiver and laser spot. The green cross marks the center of the detected receiver; the green star marks the laser point. The green rectangle surrounds the coverage area of the MEMS mirror and camera system.

The diameter of the laser point in a distance of 3.5 m can be calculated with the above-mentioned divergence angle of 0.15° resulting in approximately 9.2 mm. Using transformed Eq. (1), the laser spot diameter corresponds to roughly nine pixels in a distance of 3.5 m. At this distance, the laser spot diameter is considerably smaller than the lens diameter of 20 mm, resulting in the fact that the required accuracy of the alignment can be decreased. At a distance of approx. 7.5 m, the laser spot diameter reaches the diameter of the lens. But, at this distance, the resolution of the camera image is already too low for detecting the receiver.

In the worst case, i.e., when the receiver PCB is placed in one of the corners of the reachable area, a complete alignment time can be determined as follows: for the PCB and laser spot detection, a time of 0.5 – 1 s can be roughly assessed; with a step size of 0.5 V per frame and a frame rate of 30 fps, each actuator of the MEMS needs approximately 8 s to reach its maximum deviation at 120 V. The same time of 8 s is necessary for the second actuator to reach the corner. For fine-tuning of the alignment, a few tenths of a second can be added. This results in a maximum alignment time of around 17 – 18 s.

After using the algorithm to complete the alignment, we measured some eye diagrams. In order to do this, the VCSEL was modulated by a bit pattern generator with a pseudorandom binary sequence (PRBS) of the length $2^{31} - 1$ at a data rate of 3 Gbit/s. The average optical output power of the VCSEL was adjusted to 0.95 mW behind the mirror to meet eye safety regulations. The outputs of the receiver chip were connected to an oscilloscope. Figure 5 shows the clearly opened eye and confirms the successful wireless optical data transmission. A Q-factor of 32 was determined for the eye (Fig. 5), which corresponds to a bit error ratio of 5.4×10^{-225} .

The presented system successfully established a 3 Gbit/s optical communication link over a distance of 3.5 m without any back channel from the receiver to the transmitter. This was accomplished with a self-developed

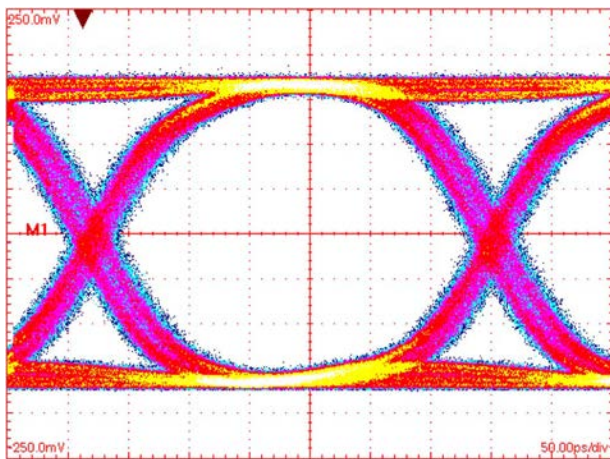


Fig. 5. Measured eye diagram at 3 Gbit/s (PRBS $2^{31} - 1$) over a distance of 3.5 m, 50 mV/div, and 50 ps/div.

algorithm, including image recognition, laser point detection, and control of voltage sources for the MEMS beam steering. The time needed for establishing the link is currently limited by the frame rate of the CMOS camera and the voltage step used for control of the MEMS mirror.

In a future system, the program can be extended in such a way that the receiver will be continuously tracked as well. That would allow communication with slowly moving devices, but this would be computationally

intensive. Nevertheless, the software used is available for embedded system devices such as ARM processors, providing an embedded solution. Especially with an improved CAMshift function, which will allow a larger voltage step size for the MEMS mirror, the time period for alignment can be reduced.

References

1. J. Kahn and J. Barry, *Proc. IEEE* **85**, 265 (1997).
2. H. Le Minh, D. O'Brien, G. Faulkner, O. Bouchet, M. Wolf, L. Grobe, and L. Jianhui, *IEEE Photon. Technol. Lett.* **22**, 1598 (2010).
3. D. R. Wisely, "A 1 Gbit/s optical wireless tracked architecture for ATM delivery," in *IEE Colloquium on Optical Free Space Communication Links*, London, UK, February 19, 1996, pp. 14\1-14\7.
4. K. Wang, A. Nirmalathas, C. Lim, and E. Skafidas, *Opt. Lett.* **37**, 1514 (2012).
5. D. R. Kolev, K. Wakamori, M. Matsumoto, T. Kubo, T. Yamada, and N. Yoshimoto, "Gigabit indoor laser communication system for a mobile user with MEMS mirrors and image sensors," in *International Workshop on Optical Wireless Communications (IWOW)*, Pisa, October 22, 2012, pp. 1-3.
6. P. Brandl, S. Schidl, A. Polzer, W. Gaberl, and H. Zimmermann, *IEEE Photon. Technol. Lett.* **25**, 1428 (2013).
7. P. Brandl and H. Zimmermann, *Electron. Lett.* **49**, 552 (2013).
8. OpenCV, <http://opencv.org>.
9. H. Bay, A. Ess, T. Tuytelaars, and L. Van Gool, *Comput. Vis. Image Underst.* **110**, 346 (2008).

2.6. IEEE JSTQE 2014

© 2014 IEEE. Reprinted, with permission, from Paul Brandl, Stefan Schidl and Horst Zimmermann, "PIN Photodiode Optoelectronic Integrated Receiver Used for 3-Gb/s Free-Space Optical Communication", IEEE JOURNAL OF SELECTED TOPICS IN QUANTUM ELECTRONICS, November/December 2014.

PIN Photodiode Optoelectronic Integrated Receiver Used for 3-Gb/s Free-Space Optical Communication

Paul Brandl, *Student Member, IEEE*, Stefan Schidl, *Student Member, IEEE*,
and Horst Zimmermann, *Senior Member, IEEE*

Abstract—In this paper, an optoelectronic integrated receiver chip including five PIN photodiodes will be presented. A large 200- μm diameter photodiode connected to a high-speed transimpedance amplifier works as a 3-Gb/s receiver for optical wireless communication. Four surrounding photodiodes allow for the adjustment of the incoming laser ray. The complete chip was realized in a silicon 0.35- μm BiCMOS technology to benefit from the available intrinsic zone in this technology. Due to this intrinsic zone and an antireflection coating, the responsivity reaches a value of more than 0.5 A/W for wavelengths from 630 to 760 nm. Furthermore, the capacitance of the center photodiode is less than 0.6 pF for reverse bias voltages larger than 3 V. For proof of concept, a steerable and adjustable light source was built based on a micro-electro-mechanical system mirror, on a focusing unit, and on a direct modulated vertical cavity surface emitting laser with a wavelength of 680 nm. The complete system is capable of establishing a 3-Gb/s data transfer over a distance of 19 m at a BER of $<10^{-9}$, and over a distance of 18 m at a BER of $<10^{-12}$.

Index Terms—Integrated optoelectronics, optical receiver, optical wireless communication (OWC), optoelectronic and photonic sensors.

I. INTRODUCTION

OPTICAL interconnects with their huge bandwidth will play an important role in future indoor communication systems. To compete with well-established RF link systems for indoor applications like wireless local area networks, the costs for the components have to be tremendously low. Those indoor systems use optical wireless beams [1] or cheap polymer optical fibers [2] for distributing high amounts of data. The increasing interest in these systems has been driving research on low-cost, high-speed and mainly fully integrated receivers and transmitters [3]. Very cheap vertical cavity surface emitting laser (VCSEL) diodes, receivers implemented in standard technologies such as silicon CMOS and BiCMOS, and low-cost plastic fibers are available [4].

Optical receivers for indoor wireless systems are similar to receivers for plastic optical fiber links but they differ in a few points. For both applications the optical detector should be large enough to collect the optical signal and to facilitate the alignment. The collection area can be increased with an optical

concentrator (for example a lens). A difference is that optical wireless communication (OWC) systems operate in higher noise environments because of the ambient light. Background radiation from reflected sunlight can be in the order of hundreds of μW . To what extent the receiver sensitivity is affected by background radiation, depends on the feedback resistance (R_{FB}). For a $R_{\text{FB}} = 10 \text{ k}\Omega$ and $R_{\text{FB}} = 100 \Omega$, a background radiation of more than -25 and -3 dBm, respectively, affects the receiver performance [5]. For smaller R_{FB} values, the receiver is less affected by background radiations. Of course, direct sunlight (up to 10 mW) makes a normal operation impossible, but such conditions occur rarely indoor. With a target bit error rate (BER) of less than 10^{-9} ($Q = 6$), a minimum SNR of 15.6 dB is required by the receiver.

The transmit power for class 1 laser devices is limited to 1 mW by eye-safety regulations [6], especially for wavelengths in the visible (380–750 nm) and near-infrared range (750–1400 nm). The 380–850 nm wavelengths range, however, matches the high-responsivity range of high-speed silicon photodiodes (PDs). The opportunity of monolithic integration of silicon PDs with the rest of the receiver circuit (amplifiers, limiters, clock and data recovery circuit . . .) brings many advantages. First of all, it lowers the cost and reduces the size. Second, a fully optoelectronic integrated chip (OEIC) limits the problems associated with packaging and bonding of PD chip and amplifier chip. Third, the interconnect parasitics like pad capacitances and the inductances caused by bond-wires are minimized. A challenge of many known OEICs is a lower sensitivity or data rate compared to most of their discrete counterparts. Some compromises must be made when the photodetector and the following transistors are produced within the same substrate and within the same processing steps. PDs in silicon need a much thicker absorption zone than direct semiconductors like GaAs due to the well-known fact that the absorption coefficient of direct semiconductors is an order of magnitude higher than that of indirect semiconductors like silicon.

In this paper, the focus is placed onto a fully integrated optical receiver for OWC manufactured in standard silicon 0.35 μm BiCMOS technology, where in addition the possibility of easily integrating five PDs on one chip is advantageously exploited for support of centering the light beam on the center detector. In Section II, the structure and the characteristics of the photodiode are explained. In Section III, the entire OEIC—with focus on the implemented circuits including sensitivity measurements—is presented. Section IV describes the OWC system including the transmitter and its micro-electro-mechanical system (MEMS) mirror. In Section V, the results from the measurements and

Manuscript received January 27, 2014; revised May 13, 2014 and June 18, 2014; accepted June 29, 2014. Date of publication July 8, 2014; date of current version August 22, 2014.

The authors are with the Institute of Electrodynamics, Microwave and Circuit Engineering, Vienna University of Technology, Vienna 1040, Austria (e-mail: paul.brandl@tuwien.ac.at; stefan.schidl@tuwien.ac.at; horst.zimmermann@tuwien.ac.at).

Color versions of one or more of the figures in this paper are available online at <http://ieeexplore.ieee.org>.

Digital Object Identifier 10.1109/JSTQE.2014.2336539

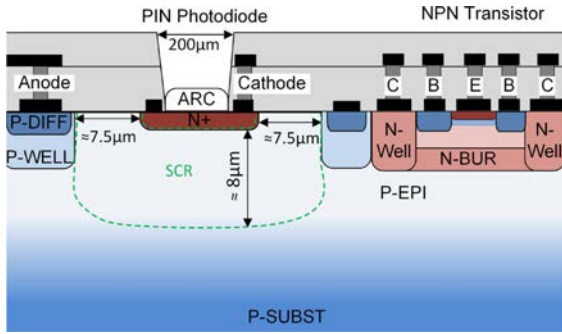


Fig. 1. Cross section of PIN photodiode and bipolar transistor (not to scale), anti-reflection coating (ARC), space-charge region (SCR).

communication link demonstrations are presented. Section VI gives a conclusion of this paper.

II. PIN PHOTODIODE

The speed and the sensitivity are the crucial parameters of a receiver. The sensitivity of an optical receiver is defined as the minimum average optical power necessary to achieve a certain BER. The problem is the rather slow response time of integrated (Bi)CMOS p-n junction PDs depending on several parameters. The penetration deep in silicon increases considerably over the junction depth for many visible and near-infrared wavelengths. Moreover, the electron-hole pairs generated deep below the p-n junction and deep below the depletion region diffuse very slowly to be collected. This diffusion current significantly limits the bandwidth of p-n junction PDs. As a matter of fact, the downscaling of (Bi)CMOS technology and the related increased doping concentration decreases the depletion region width.

Because it is the objective to increase the depletion region as much as possible, the PIN PD is preferred over the simple p-n junction PD. Therefore, PIN PDs are integrated in a BiCMOS technology. In addition, the advantages of bipolar amplifiers compared to CMOS amplifiers are exploited. Bipolar transistors can have at least a by an order of magnitude larger transconductance (g_m) than MOS transistors [7]. This allows for higher PD capacitance, higher gain, and higher bandwidth (B). Further, the equivalent input noise current of a transimpedance amplifier (TIA) for the GHz frequency range in the case of a bipolar front end is lower than that of a JFET or MOSFET [8], [9]. Hence, at higher bit rates the bipolar device produces superior performance against a MOSFET device resulting in higher sensitivity values. The structure of the used, vertical n-p-n-transistor can be seen in Fig. 1, an N+ buried zone builds the collector, a P region the base, and a highly doped N+ area the emitter.

The width of the depletion zone within a PIN PD is approximately equal to the thickness of the intrinsic layer. The carriers generated in the depletion region drift fast in the electric field present in this space-charge region (SCR) resulting in a low transit time. This depletion region and the PD's area are the crucial factors for a further important parameter of the PD, the diode's capacitance. This capacitance and the impedance at the amplifier's input node determine the electrical frequency

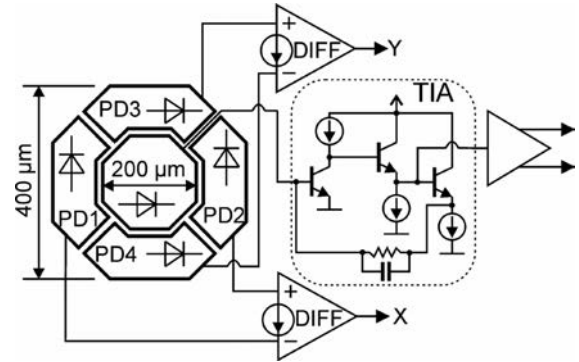


Fig. 2. Optoelectronic integrated receiver block diagram with simplified circuit diagram of the TIA.

response. A thin intrinsic layer resulting in a thin depletion region increases the capacitance. However, minimizing the area for reducing the capacitance is in opposite to one of the most important requirements for OWC detectors, a large detection surface area for easy alignment.

In order to increase the speed of a PD in a certain technology, either the depletion region could be widened by increasing the reverse bias voltage or the diffusion components could be removed completely by a modified PD structure. The reverse bias voltage could only increase to a certain limit depending on the technology in order not to jeopardize the remaining circuitry. A countless number of publications are available dealing with modified PD structures; several recently published papers should be mentioned at this point [10]–[17]. As a common outcome in those papers, either a second PD for collecting the diffusive carriers or a third layer (in most cases a deep N-well) for blocking the diffusion current generated in the deep silicon bulk were used. The bandwidth could be extended to reasonable values for detectors with rather small areas but at the expense of reduced detector responsivity, quotient of photogenerated current and received light power. The responsivity of the detector and the input-referred noise current density of the first amplifier stage (in most cases a TIA) are crucial for the sensitivity of an optical receiver [18] leading to a rather bad sensitivity of the nanometer-CMOS OEICs reported in [11] and [13]. The responsivity depends mainly on the wavelength of the incident radiation, on the PD's properties like the bandgap of the PD's material, the reflection, and the transmission in the isolation and passivation stack on the PD. With an anti-reflection coating (ARC), the reflection of the PD's surface can be minimized. Dependent on the wavelength, the penetration depth varies. In order to get a high responsivity the photogeneration should take place within the SCR of the PD's p-n junction. However, the penetration depth of light with a wavelength of 850 nm is already larger than 10 μm in silicon and that results in a rather poor responsivity for the PIN PD. Therefore, a wavelength of 680 nm was chosen for the experiments reported here.

The OEIC receiver presented in this paper includes five PIN PDs; Fig. 2 shows a block diagram of the complete receiver. For the purpose of high data rate communication, a PD in an

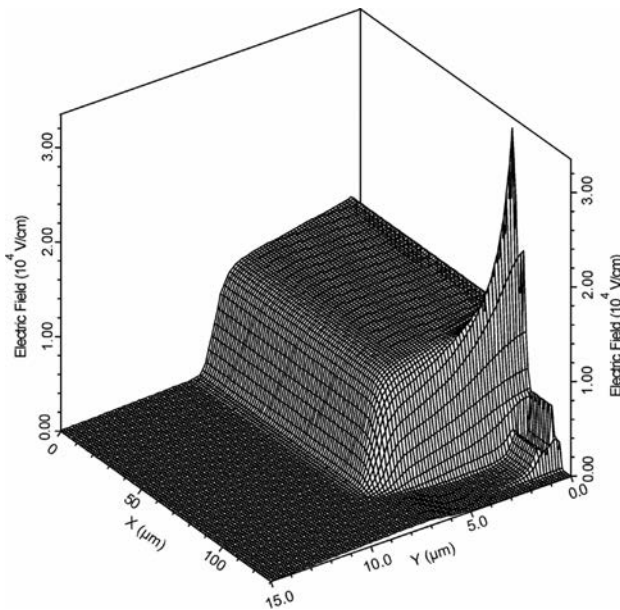


Fig. 3. Simulated electric field strength of the center PIN PD structure at a bias voltage of -8 V.

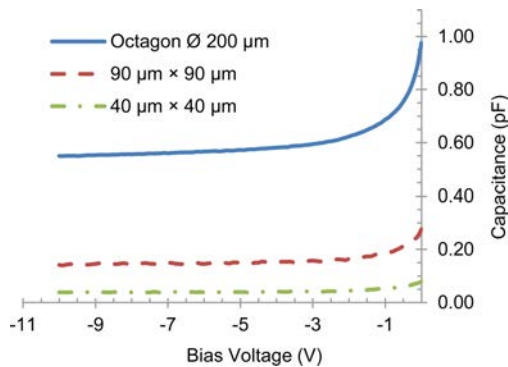


Fig. 4. Voltage dependence of photodiode capacitance.

octagonal shape was placed in the center. This octagonal PD has a diagonal size of $200 \mu\text{m}$ and is surrounded by four PDs that serve for detecting which direction the optical beam is coming from. This information is useful for the application of the receiver in a communication scenario where the laser beam can be adjusted and aligned.

The diameter of the PIN PD was selected because of space constraints and knowledge obtained from previous projects with $0.6 \mu\text{m}$ process technologies [19], [20]. The width of the chip was limited to 1 mm , minus two times the length of bonding pads ($220 \mu\text{m}$) and minus the dimensions for substrate contacts and guard rings. This results in a maximum width of $450 \mu\text{m}$ for the entire PD array.

The cross section of the realized PIN PD can be seen in Fig. 1. The anodes of the PIN PDs are built by the P+ doped substrate. On top of the substrate, a low doped ($< 5 \times 10^{13} \text{ cm}^{-3}$) P- epitaxial layer is grown to a thickness of about $14 \mu\text{m}$. This low

doped zone is working as intrinsic layer to minimize the capacitance and to obtain a reasonable responsivity. However, after all process steps, the thickness of the intrinsic layer is reduced by several micrometers due to the diffusion of boron from the P+ substrate into the epitaxial layer. A highly doped N+ region (source/drain region from normal MOSFETs) builds the cathode of each PIN PD. To increase the drift velocity and to minimize the capacitance, a reverse bias voltage is applied to the substrate via the substrate contact (P-DIFF in P-WELL, see Fig. 1) of the chip. These substrate contacts are made very large in area to minimize the resistance to the highly doped P-substrate. The minimum distance between the P+ anode contact and the N+ cathode is $7.5 \mu\text{m}$ to get a uniform electrical field below the N+ cathode. This assumption is confirmed by semiconductor device simulations (Synopsys Taurus MediciTM), see Fig. 3. To isolate the n-channel MOSFETs from the negative substrate, a third, deep n-well offered by the process is used.

Fig. 4 shows the capacitance as a function of the bias voltage. These measurements were carried out with an Agilent 4284 precision LCR meter. In order to compare and determine the influence of the area, the octagonal PIN PD with an area of $33103 \mu\text{m}^2$ and two square PIN PDs were measured. The size of the square PDs was $40 \mu\text{m} \times 40 \mu\text{m}$ and $90 \mu\text{m} \times 90 \mu\text{m}$, respectively. The relatively small change of the capacitance for voltages below -3 V indicates that the intrinsic region is completely depleted already at -3 V. At a bias voltage of -8 V, the octagonal PIN PD showed a low capacitance of only 554 fF , which consists of area and perimeter capacitance. The perimeter capacitance can be calculated with the sidewall junction capacitance parameter ($0.12 \text{ fF}/\mu\text{m}$) and the center PIN PD's perimeter of approx. $700 \mu\text{m}$ obtained from the layout. This results in a perimeter capacitance of 84 fF . With this number, the area capacitance was calculated to be 470 fF . The outcome of this is that the depletion width can be estimated with the formula of an ideal plate capacitor. With the above mentioned area of $33103 \mu\text{m}^2$, a depletion width of roughly $7.42 \mu\text{m}$ can be calculated for a bias voltage of -8 V. This corresponds well with the depletion width of $8 \mu\text{m}$ obtained from the device simulations, see Fig. 3.

When the PD was included within the complete OEIC, a maximum bias voltage of -7.5 V was applied to the substrate in order not to jeopardize the OEIC. This substrate bias voltage was selected in accordance with the process reliability operation specifications which allow a maximum substrate potential of -8 V. In fact, in the OEIC, the PIN PD's cathode is connected to the base contact of a bipolar transistor, see Fig. 2. That results into an effective PIN PD reverse bias voltage of approx. 8.2 – 8.3 V including the base-emitter voltage.

For responsivity measurements, the light was coupled into the PD with a $62.5 \mu\text{m}$ core-diameter multi-mode optical fiber. The measurements were performed with a monochromator in a wavelength range from 400 to 900 nm done with 5 nm steps. The result can be seen in Fig. 5. For wavelengths between 630 and 760 nm , a high responsivity of larger than 0.5 A/W was reached due to the ARC. This ARC is formed by a thin oxide with a nitride layer on top, having a thickness optimized for red light. At a wavelength of 680 nm , a responsivity of 0.53 A/W

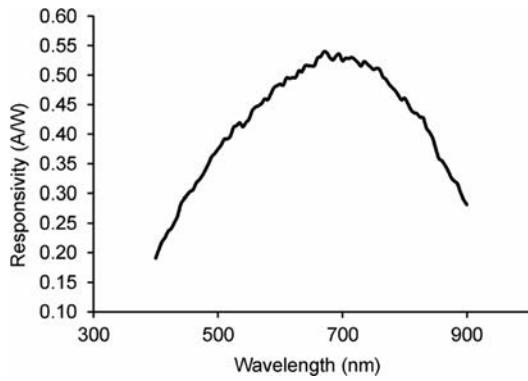


Fig. 5. Measured responsivity of PIN PD.

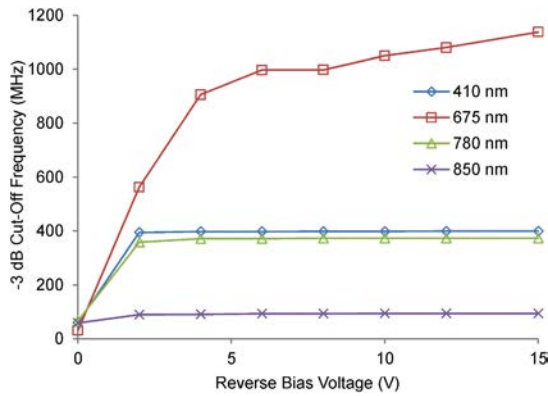


Fig. 6. -3 dB cut-off frequency versus photodiode reverse bias voltage for four wavelengths.

was achieved and at a wavelength of 850 nm, a responsivity of still 0.38 A/W was obtained. That results in very high quantum efficiencies of 96% and 55% for wavelengths of 680 and 850 nm, respectively.

For dynamic characterization, the wafer with the PDs was placed in a wafer prober and the pads were directly connected with RF probes. Several laser diodes with pigtailed fibers were used as sources. The small-signal bandwidth of the PD was measured with a network analyzer HP 8753 by modulation of the laser diode and measuring the ac output signal. Through a bias-tee, the bias voltage of the PD was varied between 0 and -15 V. Fig. 6 shows the -3 dB-cut-off frequencies depending on the reverse bias voltage for four wavelengths. For a bias voltage of -8 V, the following cut-off frequencies were obtained, see Fig. 7: 398 MHz at a wavelength of 410 nm, 998 MHz at a wavelength of 675 nm, 372.7 MHz at a wavelength of 780 nm, and 93.2 MHz at a wavelength of 850 nm. As mentioned above, the cut-off frequency depends mainly on the slow diffusion current generated outside the depletion region. For short wavelengths, the carriers generated in the surface N+ region are crucial and for long wavelengths, the critical zone is the P+ substrate below the edge of the depletion region. According to [21], the approximate $1/e$ -penetration depths for the above mentioned

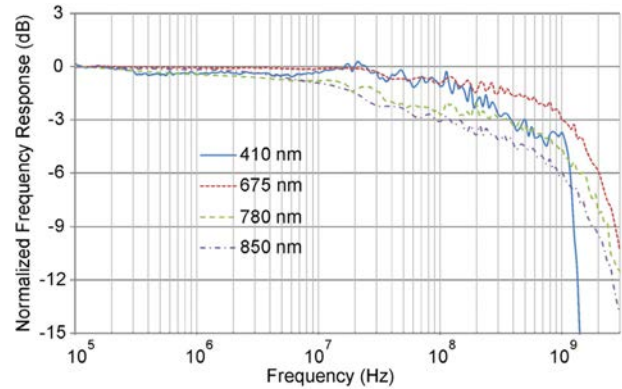


Fig. 7. Measured frequency response for four wavelengths at a bias voltage of -8 V.

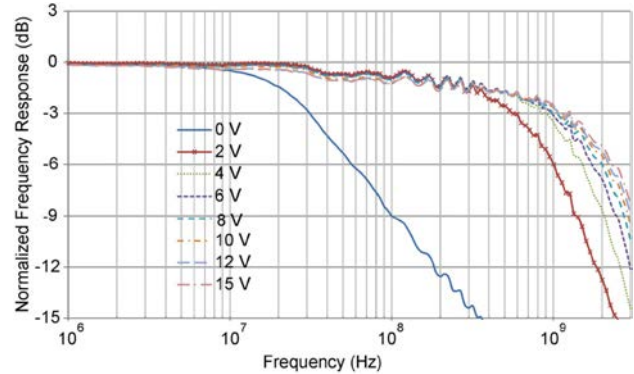


Fig. 8. Measured frequency response for different reverse bias voltages at a wavelength of 675 nm.

wavelengths are 100 nm for 410 nm, $4.1 \mu\text{m}$ for 675 nm, $10 \mu\text{m}$ for 780 nm, and $16 \mu\text{m}$ for 850 nm.

For the 675 nm wavelength, which is almost absorbed in a depth $8 \mu\text{m}$, the higher the reverse bias voltage gets, the more the cut-off frequency increases, even though only slightly for reverse voltages larger than 4 V (see Fig. 8). This can be explained by the increasing electric field and the resulting increase in drift velocity. At a reverse bias voltage of 4 V, the electric field has a strength of about 5000 V/cm for which the drift velocity of electrons starts to saturate. The drift velocity of holes however starts to saturate at 30 000 V/cm [21], which would occur at -24 V reverse bias. Therefore, between -4 and -15 V the bandwidth increases slower than between 0 and -4 V for 675 nm.

For 780 nm with an absorption coefficient of $0.101 \mu\text{m}^{-1}$, carriers up to a depth of $12.2 \mu\text{m}$ have to be collected to reach the corresponding signal level for the -3 dB bandwidth. This can be calculated with the Beer–Lambert law. Between the edge of the region with the high electric field and the $12.2 \mu\text{m}$ there is an average electric field of 400 V/cm. Together with the electron mobility for a mean doping concentration of 10^{16}cm^{-3} , an average drift velocity of approximately $4.7 \times 10^5 \text{cm/s}$ can be estimated for the electrons. That means that the electrons need

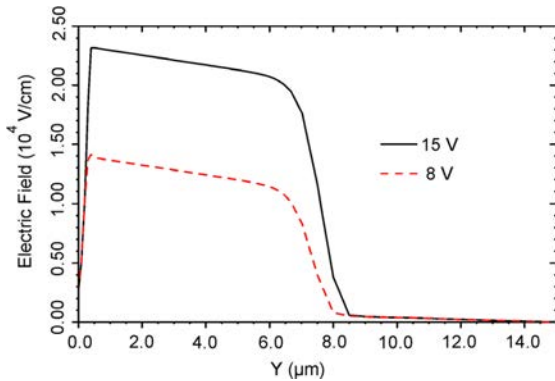


Fig. 9. Simulated electric field strength of the center PIN PD for different reverse bias voltages, cross section of Fig. 3 at $x = 0 \mu\text{m}$.

approx. 0.88 ns from the depth of $12.2 \mu\text{m}$ to reach the edge of the high electric field at a depth of about $8 \mu\text{m}$. Further, the electrons need roughly 0.1 ns to cross the high-field zone with a drift velocity of approx. $8 \times 10^6 \text{ cm/s}$ corresponding to an electric field strength of $1.3 \times 10^4 \text{ V/cm}$. That results in a total transit time t_r of 0.98 ns from a depth of $12.2 \mu\text{m}$ to the N+ cathode. From this transit time, the -3 dB bandwidth can be calculated according to [22] $f_{3\text{dB}} = 2.4/2\pi t_r$, resulting in a -3 dB bandwidth of about 390 MHz. A further increase of the reverse bias voltage only raises the electric field strength within the intrinsic zone, see Fig. 9. However, between 8.5 and $12.2 \mu\text{m}$ the electric field does not change, because it is determined by the doping gradient there. This means that the drift time from 12.2 to $8 \mu\text{m}$ is almost constant at 0.88 ns for the reverse voltage $< -3 \text{ V}$. Therefore, an increase of the reverse voltage has no notable effect on the bandwidth due to the fact that drift velocity of electrons has already been saturated in the intrinsic zone and that the doping gradient due to boron outdiffusion from the P+ substrate causes a much slower carrier drift in a region being almost as thick as the remaining intrinsic layer. Therefore, the bandwidth shows a saturation effect for 780 nm as depicted in Fig. 6.

A large portion of 850 nm light penetrates into the highly doped P-substrate and due to carrier diffusion the bandwidth is rather low.

Light with the short wavelength of 410 nm is absorbed to a large portion in the highly doped N+ cathode region where carrier diffusion dominates. It is pure accident (resulting of N+ thickness and I-layer thickness) that the bandwidth for 410 and 780 nm for reverse biases in excess of 2 V are almost equal.

Taking into account that the light-sensitive area is approximately 20-times the area of the speed-enhanced PDs using normally doped PN diodes [15], the responsivity-bandwidth product of the proposed PIN PD is one order of magnitude larger than that of the PN diodes in standard nanometer CMOS technology.

Each surrounding PD for adjusting the laser beam was built in the same way as the center PIN PD and each has an area of approximately $26100 \mu\text{m}^2$. For the adjustment, two opposite situated PIN PDs are used for a simple detection of the difference

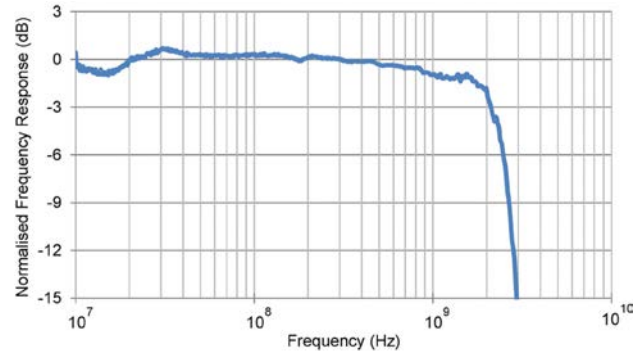


Fig. 10. Measured frequency response of entire OEIC, $\lambda = 675 \text{ nm}$, $V_{\text{sub}} = -7.5 \text{ V}$.

in received light power. This is done by a differential TIA which converts the difference in photocurrent into a corresponding voltage signal. In the next chapter, a detailed description of this differential TIA and the main high data rate receiver is given.

III. CIRCUITS

Transistor parameters did not change although the doping level in the epitaxial layer was reduced by almost two orders of magnitude compared to the standard $0.35 \mu\text{m}$ process. The reasons are the same as already reported in [20] and [23] for a PIN photodiode integration in a $1 \mu\text{m}$ CMOS process and for an N+N-/P-P+ PIN photodiode integrated in $0.6 \mu\text{m}$ BiCMOS technology. In [23] the threshold voltages of N- and P-channel MOSFETs did not change because the MOSFETs are located in P-type and N-type wells, respectively, whose doping levels are in the range of $5 \times 10^{16} \text{ cm}^{-3}$, and because of threshold implants, which result in channel dopings in the order of 10^{17} cm^{-3} . Therefore, a reduction of the P-type doping in the P- intrinsic layer from the original boron concentration of about 10^{15} cm^{-3} to $< 5 \times 10^{13} \text{ cm}^{-3}$ did not have a noticeable effect on the properties of the MOSFETs. In [20], it was also verified that the properties of the bipolar n-p-n transistor did not change due to the high collector and base doping concentrations. Therefore, the original transistor models could be used for circuit design.

A. High Data Rate Receiver

The development of an OEIC in a $0.35 \mu\text{m}$ BiCMOS technology has another advantage. In this technology, bipolar transistors are available and it is a well-known fact that bipolar transistors have a better g_m than MOS transistors. These bipolar transistors allow circuit design for higher gain and higher data rates as compared to circuits composed of only MOS transistors. The first part of the high data rate receiver is a TIA composed of a common-emitter stage followed by two emitter follower stages, a simplified circuit diagram can be seen in Fig. 2. These emitter followers provide for a certain gain peaking at high frequencies. Hence, the bandwidth of the complete high data rate receiver was increased above the -3 dB cut-off frequency of the PIN PD [24]. This resulted in a measured -3 dB bandwidth of the complete receiver circuitry of 2.1 GHz, see Fig. 10. With a second,

identical dummy TIA, a differential circuit structure was designed. The two TIAs are followed by a two-stage amplifier which provides for a gain of roughly 28 dB. An output driver for delivering a differential output voltage of 300 mV into 50 Ω concludes the circuit. The differential structure of the receiver circuit has the big advantage that the receiver becomes insensitive to common-mode noise and low-frequency parts of the input signal. For example, ambient light is canceled out.

For the TIA, the dominate sources of noise are the thermal noise from the feedback resistor R_{FB} and the noise produced by the first bipolar transistor. The bipolar transistor has as dominate noise sources the shot noise associated with the base and collector currents and the thermal noise of the base resistance. Based on [8], the minimum noise performance can be expected with an optimized collector current which minimizes the sum of the collector and base noise current contributions. Further, the input capacitance of the transistor C_{π} should be in the same value range as the PD's capacitance (C_{PD}). To limit the thermal noise current contribution from R_{FB} , the value of R_{FB} should be as large as possible. R_{FB} is the most influencing parameter for the frequency response when C_{PD} is assigned to a fixed value (this value depends mainly on the PD's area). Thus, there is a practical limit how large R_{FB} can be made. The noise performance is so dependent on various parameters that the trade-offs in performance must be obtained from a more detailed analysis. This analysis was done with the help of CAD tools, i.e., VIRTUOSO from Cadence.

The input transistor's emitter area was adjusted to get a C_{π} of 590 fF which corresponds well to the measured C_{PD} of 554 fF. The R_{FB} was varied until the target bandwidth of 2.1 GHz (for a data rate of 3 Gb/s) was reached. That results a value of 830 Ω for R_{FB} . After the optimization process, the simulated noise summary gives an overview of the four biggest contributors: first the thermal noise from R_{FB} with 29%, second the shot noise from the collector current with 16.3%, third the shot noise from the base current with 16.1%, and fourth the thermal noise from the base resistance of the input transistor with 10.7%. The simulated input-referred noise current density is 7.5 pA/ $\sqrt{\text{Hz}}$. With the bandwidth of 2.1 GHz an input-referred rms noise current (i_n^{rms}) can be roughly calculated. Based on [18], the sensitivity of the receiver is: $P_{\text{sens}} = Q \cdot i_n^{\text{rms}} / R$, where the Q-factor is 6 for a target BER of 10^{-9} , R is the measured PIN PD's responsivity of 0.53 A/W at a wavelength of 675 nm. This results in a sensitivity of approximately -24 dBm. To verify this number, a BER measurement depending on the average optical input power was conducted. For a data rate of 3 Gb/s, a sensitivity of -23.4 dBm at a BER of 10^{-9} was obtained [24], see Fig. 11. This result confirms the performance of the complete receiver for high-speed free-space data transmission.

B. Differential TIA

For the surrounding PDs, a circuit which processes the photocurrent difference is needed. The circuit should also be able to suppress the background illumination. Therefore, a current mirror topology for amplifying the photocurrent difference was used. The basic topology of this circuit is shown in Fig. 12. The

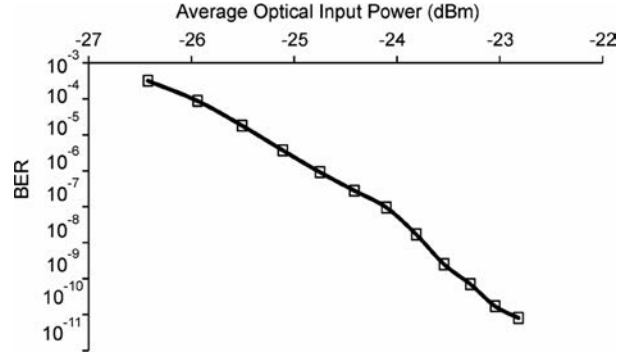


Fig. 11. Sensitivity of high data rate receiver at 3 Gb/s, $2^{31}-1$ PRBS, $\lambda = 675$ nm.

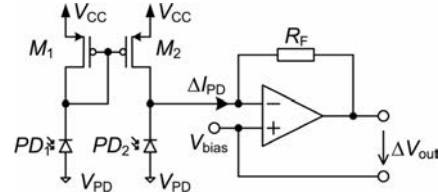


Fig. 12. Processing circuit for the photocurrent difference of the surrounding PDs.

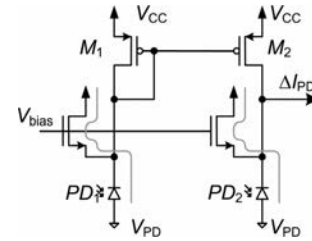


Fig. 13. Voltage clamp circuit for high light power conditions.

two MOSFETs M_1 and M_2 form the current mirror. The difference current ΔI_{PD} is then transformed into an output voltage ΔV_{out} which has a common mode voltage level of V_{bias} . The TIA consists of a two-stage CMOS Miller operational amplifier which was optimized for its low-noise properties. In this implementation, the feedback resistor of the TIA $R_F = 100$ k Ω was chosen. The two differential TIAs are optimized for high sensitivity and have an equivalent input noise current of 1.3 nA with a -3 dB bandwidth of 1.6 MHz. In combination with the power supply voltage of 3.3 V and $V_{\text{bias}} = 1.5$ V the circuit can process a current difference of up to ± 15 μA . The current mirror (formed by M_1 and M_2) was designed to suppress a dc current of larger than 100 μA . For higher photocurrents, the drain potential of M_1 and M_2 would go below 1.5 V, in worst case down to the negative PD bias voltage V_{PD} (-7.5 V). This would exceed the absolute maximum ratings of the used CMOS technology ($V_{\text{DS,max}}$, $V_{\text{GS,max}}$). To overcome this limitation, an additional voltage clamp circuit (see Fig. 13) was employed. The additional NMOS devices turn on before a critical operating

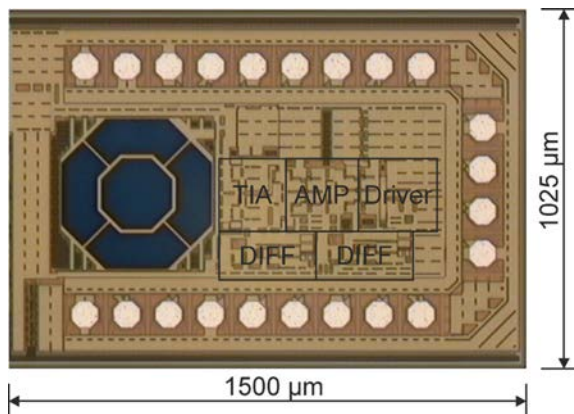


Fig. 14. Photomicrograph of developed OEIC receiver, AMP... two-stage amplifier, DIFF... differential TIA.

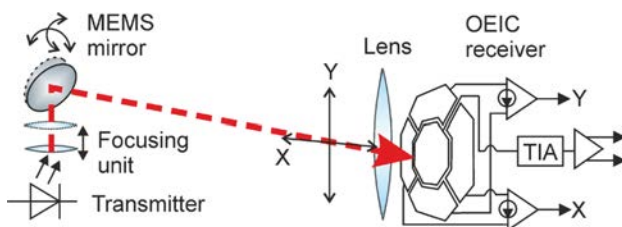


Fig. 15. Simplified OWC system architecture.

condition can occur. If the NMOS devices turn on, they supply the high photocurrent as indicated by the grey line. For normal operating conditions the NMOS devices stay off.

Fig. 14 shows a photomicrograph of the developed OEIC receiver. The whole OEIC receiver including seal rings has an area of $1025 \mu\text{m} \times 1500 \mu\text{m}$ and consumes a current of approximately 75 mA at a supply voltage of 3.3 V.

IV. OWC SYSTEM DESIGN

To verify the performance of the developed OEIC receiver, an optical wireless line-of-sight (LOS) system was designed. Fig. 15 depicts a simplified overview of the complete OWC system. The minimized path loss argues for using LOS links with narrow beams, but a drawback of narrow beams usually is the tiny field of view and the resulting limited coverage area. To combat these limitations, an alignment and focusing possibility was implemented at the transmitter side increasing the coverage area. The alignment of the laser beam was done with a movable mirror controlled by a MEMS. Using a MEMS mirror for beam steering was proposed in [25]. Their system was related on a 1550 nm fiber transmitter demanding a rather complex optical system for emitting into the free space. The use of a 1550 nm wavelength excludes cheap integrated photodetectors fabricated in silicon. The system presented here has the advantage of an included focusing unit resulting into a variable beam spot diameter. This facilitates the alignment process as the coverage area can be scanned with a broad beam until the surrounding PDs

detect a signal. With the feedback from the differential TIAs, the laser ray from the transmitter can be simply aligned and focused onto the receiver.

A. Transmitter Design

The main part of the transmitter is a direct modulated VCSEL with a wavelength of 680 nm. The VCSEL has a maximum optical output power of 2 mW, a -3 dB bandwidth of 3.5 GHz, and is commercially available from Vixar. The VCSEL itself has a beam divergence of roughly 16° full width at half maximum (FWHM).

The focusing element is realized with a pick-up from a commercial optical disc drive. This is done by variation of the distance between lens and laser with an electromagnetic mechanism. The pick-up was selected by dismounting and testing several devices from CD- and DVD-ROM drives. Following the laser ray, a two-axis scanning MEMS mirror from Mirrocle was mounted. The device has four actuators, two for each axis operating in opposing directions. The actuators are working with electrostatic forces. Approximately 5.4° was the measured mechanical tilt of one actuator at a maximum voltage of 120 V which corresponds to a deviation of 0.25° from the datasheet value of 5.15° [26]. This results into a maximum deflection of the laser beam of 10.8° in one direction and that in turn yields into a total field of view of 21.6° in x - and y - direction each. The mirror has a diameter of 3.6 mm and is aluminum coated. All parts of the transmitter, VCSEL, pick-up, and MEMS mirror where assembled into an adjustable mechanical prototype [27].

B. Receiver Design

The OEIC, described in chapter 3, was mounted and bonded onto a PCB. To increase the optical receiver area, a simple convex lens with a diameter of 20 mm and a focal distance of 12 mm was placed in front of the receiver.

V. MEASUREMENTS AND LINK DEMONSTRATION

A. Transmitter

In the first step, the average optical output power was adjusted to approximately 0.94 mW after the MEMS mirror to meet eye-safety regulations. The complete transmitter was mounted on a movable platform and the laser spot was focused onto a smooth wall. The distance between the transmitter and the wall varied from 3 to 20 m. With a monochrome CMOS camera the resulting laser spot was recorded. To calibrate the taken pictures for the consecutive analysis, an optical power meter with a photosensitive area of 1 cm^2 was used.

To determine the beam's expansion, the pictures taken with the camera were analyzed in such a way that the beam width could be calculated. Fig. 16 depicts the beam width in the focused case and unfocused case, in both cases versus the distance. From these diagrams the beam divergence could be calculated. The result is a divergence of approximately 0.15° FWHM and 1.92° FWHM for the focused and unfocused case, respectively. In a distance of about 7.1 m, the laser spot diameter becomes greater than the receiver lens diameter of 20 mm. The flattening

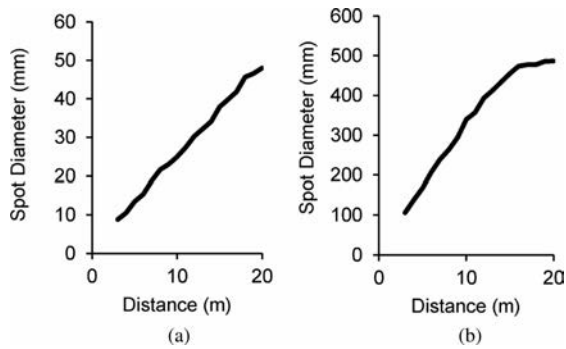


Fig. 16. Laser spot diameter (FWHM) versus distance. (a) Focused case. (b) Unfocused case.

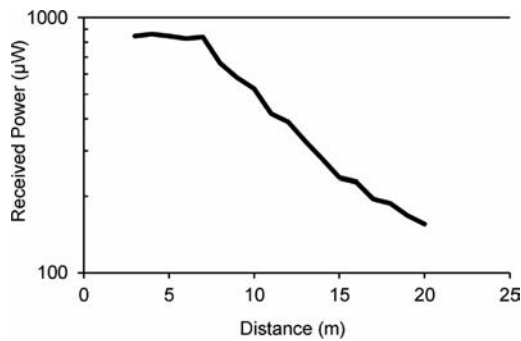


Fig. 17. Received optical power by the lens with a diameter of 20 mm versus distance.

of the curve for the unfocused spot diameter at a distance of around 16 m [see Fig. 16(b)] can be explained as follows: at this distance the laser spot diameter becomes larger than the field of view of the camera which was placed at a fixed distance in front of the wall.

B. Receiver

Fig. 17 confirms the above mentioned distance where the laser spot diameter gets larger than the lens diameter. This figure shows the collected power by the receiver lens. Again, at a distance of around 7.1 m, the received power begins to decrease in accordance with the inverse square law. This received power determines the maximum distance for error-less communication.

With the sensitivity and the area of the center PIN PD, a minimum optical intensity of around $140 \mu\text{W}/\text{mm}^2$ can be calculated for a BER $< 10^{-9}$ (which corresponds to a Q-factor of 6) 3 Gb/s communication. Behind the receiving lens, the laser spot's diameter on the chip surface can be roughly estimated to be at least 1 mm. With an assumed area of 1 mm^2 of the laser spot on the chip surface (which corresponds to a diameter of 1.1 mm), a minimum power of $140 \mu\text{W}$ is needed. The lens itself has losses (reflection and absorption) of about 5%. This returns into a required optical power in front of the lens of approximately $147 \mu\text{W}$. This calculation does not include other factors such as

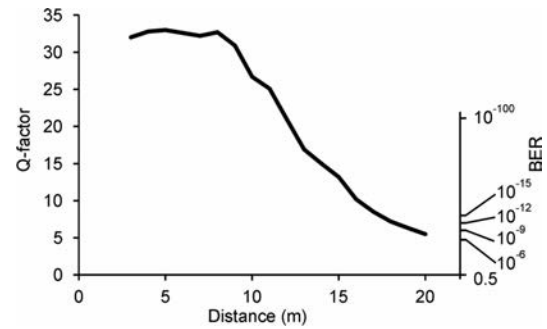


Fig. 18. Measured Q-factor depending on the distance between transmitter and receiver.

losses due to lens aberrations and not perfectly aligned transmitter and receiver. In a distance of 20 m, a received optical power in front of the lens of $155 \mu\text{W}$ was measured. That would mean that in the best case, an error-less communication for a distance of over 20 m could be possible.

C. Data Link Performance

To verify the performance of the OEIC receiver in a real communication scenario, the transmitter and the receiver were placed at different distances in a well-lit laboratory. The luminous intensity measured at the receiver was 500 lux. The VCSEL was modulated by a bit pattern generator with a pseudorandom binary sequence of $2^{31}-1$ at a data rate of 3 Gb/s. The outputs from the differential TIAs were observed with normal voltmeters. With this information, the laser ray was aligned and focused by controlling the MEMS mirror and the pick-up. This was done manually since a fully automatic steering and focusing system would have been out of scope for this initial research. The feedback channel for a fully automated OWC system could be realized in future, however, via Bluetooth, Zigbee, or an infrared remote control transmitter.

The outputs of the high data rate receiver were connected to a digital serial analyzer for eye measurements. This device allows quantifying the eye diagram in the form of a Q-factor and from that factor a corresponding BER can be calculated. The diagram in Fig. 18 depicts the measured Q-factor as a function of the distance between transmitter and receiver. The curve coincides with the previously depicted diagram of the received optical power. At distances larger than approximately 7.1 m, the Q-factor begins to decrease. In fact, at a distance of 19 m, a Q-factor of 6.3 was determined. At a distance of 20 m, the value has fallen to 5.5 which results in a BER of approximately 1.9×10^{-8} . At 18 m distance the BER is below 10^{-12} . Fig. 19 shows the measured eye diagram and Q-factor for a distance of 7, 19, and 20 m, respectively. Those results correspond well to the rough calculations done before. The OWC link offers the possibility of a 3 Gb/s data transfer over a distance of 19 m with an BER less than 10^{-9} . Compared with [28], the data rate and the communication distance were notably increased. At the same time, the costs for the receiver device were minimized due to the usage of a novel integrated receiver design.

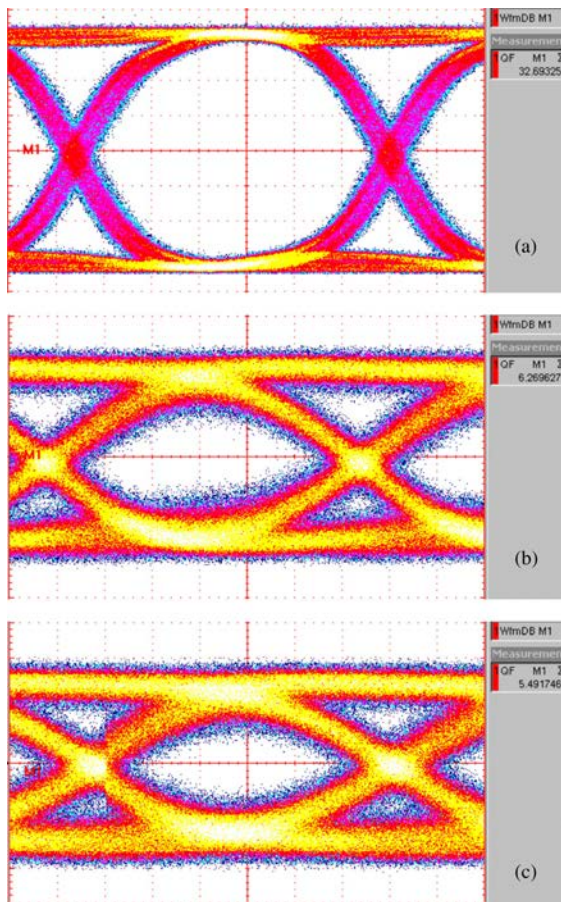


Fig. 19. Measured eye diagram for different distances: (a) 7 m $Q = 32.7$, (b) 19 m $Q = 6.27$, (c) 20 m $Q = 5.49$, 50 mV/div, 50 ps/div.

VI. CONCLUSION

Optoelectronic integrated receiver chips with PIN PDs will build the base for future indoor optical communication systems. These systems can use cheap polymer optical fibers or free-space as transmission media for distributing high amounts of data. In both cases, the optical detector should be as large as possible in order to collect the optical signal. In this paper, the focus was placed on a receiver for optical wireless systems. The presented OEIC has a large PIN photodiode for collecting sufficient optical power to enable high data rate communication up to distances of 19 m. Further, with the additional, surrounding PDs the alignment and adjustment process was notably facilitated. The complete chip was developed in a $0.35 \mu\text{m}$ BiCMOS technology without any process modifications.

ACKNOWLEDGMENT

The authors would like to thank A. Polzer for layouting the photodiodes and W. Gaberl for helpful discussions on TIA design. The authors are also indebted to D. Sommer, K. Bach

and W. Einbrodt from X-FAB Semiconductor Foundries AG in Erfurt, Germany for making the OPTO ASIC process available.

REFERENCES

- [1] J. M. Kahn and J. R. Barry, "Wireless infrared communications," *Proc. IEEE*, vol. 85, no. 2, pp. 265–298, Feb. 1997.
- [2] P. Polishuk, "Plastic optical fibers branch out," *IEEE Commun. Mag.*, vol. 44, no. 9, pp. 140–148, Sep. 2006.
- [3] D. C. O'Brien, G. Faulkner, E. B. Zyambo, K. Jim, D. J. Edwards, P. Stavrinou, G. Parry, J. Bellon, M. J. Sibley, V. A. Lalithambika, V. M. Joyner, R. J. Samsudin, D. M. Holburn, and R. J. Mears, "Integrated transceivers for optical wireless communications," *IEEE J. Sel. Topics Quantum Electron.*, vol. 11, no. 1, pp. 173–183, Jan./Feb. 2005.
- [4] S. Loquai, F. Winkler, S. Wabra, E. Hartl, B. Schmauss, and O. Ziemann, "High-speed, large-area POF receivers for fiber characterization and data transmission ≥ 10 -Gb/s based on MSM-photodetectors," *J. Lightw. Technol.*, vol. 31, no. 7, pp. 1132–1137, Apr. 1, 2013.
- [5] F. Xu, M. Khalighi, and S. Bourennane, "Impact of different noise sources on the performance of PIN- and APD-based FSO receivers," in *Proc. 11th Int. Conf. Telecomm.*, Graz, Austria, Jun. 15–17, 2011, pp. 211–218.
- [6] *Safety of Laser Products—Part 1: Equipment Classification and Requirements*, IEC Standard 60825-1, 2007.
- [7] W. M. C. Sansen, "Comparison of MOST and bipolar transistors," in *Analog Design Essentials*. Dordrecht, The Netherlands: Springer, 2008, ch. 1, pp. 45–47.
- [8] R. G. Smith and S. D. Personick, "Receiver design for optical fiber communication systems," in *Semiconductor Devices for Optical Communication*, vol. 39, H. Kressel, Ed., 2nd ed. New York, NY, USA: Springer-Verlag, 1982, pp. 89–160.
- [9] S. B. Alexander, "Receiver front-end design," in *Optical Communication Receiver Design*. Bellingham, WA, USA: SPIE Press, 1997, pp. 173–222.
- [10] F.-P. Chou, G.-Y. Chen, C.-W. Wang, Y.-C. Liu, W.-K. Huang, and Y.-M. Hsin, "Silicon photodiodes in standard CMOS technology," *IEEE J. Sel. Topics Quantum Electron.*, vol. 17, no. 3, pp. 730–740, May/Jun. 2011.
- [11] J.-S. Youn, M.-J. Lee, K.-Y. Park, H. Rucker, and W.-Y. Choi, "An integrated 12.5-Gb/s optoelectronic receiver with a silicon avalanche photodiode in standard SiGe BiCMOS technology," *Opt. Express*, vol. 20, no. 27, pp. 28153–28162, Dec. 2012.
- [12] J. Li, X. Cheng, H. Yan, and Y. Huang, "Research of monolithic optoelectronic integrated circuit in $0.5 \mu\text{m}$ standard CMOS technology," in *Proc. 5th IEEE Int. Conf. Nano/Micro Eng. Mol. Syst.*, Xiamen, China, Jan. 20–23, 2010, pp. 1141–1144.
- [13] A. C. Carusone, H. Yasotharan, and T. Kao, "CMOS technology scaling considerations for multi-Gbps optical receivers with integrated photodetectors," *IEEE J. Solid-State Circuits*, vol. 46, no. 8, pp. 1832–1842, Aug. 2011.
- [14] N. R. Das and P. Rakshit, "On the frequency response and optimum designs for maximum bandwidth of a lateral silicon photodiode," *J. Lightw. Technol.*, vol. 29, no. 19, pp. 2913–2919, Oct. 1, 2011.
- [15] B. Nakhkoob, S. Ray, and M. M. Hella, "High speed photodiodes in standard nanometer scale CMOS technology: A comparative study," *Opt. Express*, vol. 20, no. 10, pp. 11256–11270, May 2012.
- [16] G. Köklü, R. Etienne-Cummings, Y. Leblebici, G. De Micheli, and S. Carrara, "Characterization of standard CMOS compatible photodiodes and pixels for lab-on-chip devices," in *Proc. IEEE Int. Symp. Circuits Syst.*, Beijing, China, May 19–23, 2013, pp. 1075–1078.
- [17] A. Sharif-Bakhtiar, S. Shahramian, A. Rousson, H. Yasotharan, and T. C. Carusone, "Integrated photodiode characterization in a SiGe BiCMOS process," in *Proc. IEEE Opt. Interconnects Conf.*, Santa Fe, NM, USA, May 5–8, 2013, pp. 68–69.
- [18] E. Säckinger, "Receiver Fundamentals," in *Broadband Circuits for Optical Fiber Communication*. Hoboken, NJ, USA: Wiley, 2005, pp. 54–66.
- [19] P. Brandl, R. Swoboda, W. Gaberl, H. Zimmermann, and E. Leitgeb, "1.25Gbit/s integrated receiver for optical wireless communication systems," in *Proc. IEEE 8th Int. Symp. Commun. Syst. Networks Digital Signal Process.*, Poznan, Poland, Jul. 18–20, 2012, pp. 1–4.
- [20] M. Förtsch, H. Zimmermann, W. Einbrodt, K. Bach, and H. Pless, "Integrated PIN photodiodes in high-performance BiCMOS technology," in *Proc. IEEE Int. Electron Devices Meet.*, San Francisco, CA, USA, Dec. 8–11, 2002, pp. 801–804.
- [21] S. M. Sze and W. K. Ng, "Physics and properties of semiconductors—A review," in *Physics of Semiconductor Devices*, 3rd ed. Hoboken, NJ, USA: Wiley, 2007, pp. 7–75.

- [22] S. M. Sze and W. K. Ng, "Photodetectors and solar cells," in *Physics of Semiconductor Devices*, 3rd ed. Hoboken, NJ, USA: Wiley, 2007, pp. 663–742.
- [23] H. Zimmermann, A. Ghazi, T. Heide, R. Popp, and R. Buchner, "Advanced photo integrated circuits in CMOS technology," in *Proc. 49th Electron. Compon. Technol. Conf.*, San Diego, CA, USA, Jun. 1–4, 1999, pp. 1030–1035.
- [24] P. Brandl and H. Zimmermann, "3 Gbit/s optical receiver IC with high sensitivity and large integrated pin photodiode," *Electron. Lett.*, vol. 49, no. 8, pp. 552–554, Apr. 11, 2013.
- [25] K. Wang, A. Nirmalathas, C. Lim, and E. Skafidas, "High-speed indoor optical wireless communication system with a steering mirror based up-link receiver," in *Proc. 38th Eur. Conf. Exhibition Opt. Commun.*, Amsterdam, The Netherlands, Sep. 2012, pp. 1–3.
- [26] *SI911 Device Datasheet*, Mirrorcle Technologies Inc., Richmond, CA, USA, 2012.
- [27] P. Brandl, S. Schidl, A. Polzer, W. Gaberl, and H. Zimmermann, "Optical wireless communication with adaptive focus and MEMS-based beam steering," *IEEE Photonics Technol. Lett.*, vol. 25, no. 15, pp. 1428–1431, Aug. 1, 2013.
- [28] D. O'Brien, R. Turnbull, H. Le Minh, G. Faulkner, O. Bouchet, P. Porcon, M. El Tabach, E. Gueutier, M. Wolf, L. Grobe, and L. Jianhui, "High-speed optical wireless demonstrators: conclusions and future directions," *J. Lightw. Technol.*, vol. 30, no. 13, pp. 2181–2187, Jul. 1, 2012.



Paul Brandl (S'13) was born in Austria in 1980. He received the Dipl.Ing. degree (corresponding to M.Sc.) in electrical engineering from the Graz University of Technology, Graz, Austria, in 2006. He is currently working toward the Ph.D. degree with the Institute of Electrodynamics, Microwave and Circuit Engineering, Vienna University of Technology, Vienna, Austria.

From 2006 to 2008, he was with AT4wireless, Malaga, Spain, working within the Physical Layer Group for developing testing devices for 3-G and 4-G mobile communication devices. From 2009 to 2010, he was with the Institute of Broadband Communication, Graz University of Technology, designing optical free space communication devices. He joined the Institute of Electrodynamics, Microwave and Circuit Engineering, Vienna University of Technology in 2010. His major fields of research interests include optoelectronic integrated circuits design and its application in optical wireless communication systems.



optical photodetectors for sensor applications.

Stefan Schidl (S'13) was born in Vienna, Austria, in 1984. He received the B.Sc. degree in electrical engineering (with distinction) and the M.Sc. degree in microelectronics (with distinction) from the Vienna University of Technology, Vienna, in 2009 and 2011, respectively, where he is currently working toward the Ph.D. degree in the field of optoelectronic circuit. Since 2011, he has been a Research Assistant with the Institute of Electrodynamics, Microwave and Circuit Engineering, Vienna University of Technology. His research interests include analog circuit design and



Horst Zimmermann (SM'02) received the Dr. Ing. degree from the Fraunhofer Institute for Integrated Circuits (IIS-B), Erlangen, Germany, in 1991. Then, he was an Alexander-von-Humboldt Research-Fellow with Duke University, Durham, NC, USA, where he worked on diffusion in Si, GaAs, and InP. In 1993, he joined the Chair for Semiconductor Electronics with the Kiel University, where he lectured optoelectronics and worked on optoelectronic integration. Since 2000, he has been a Full Professor with the Electronic Circuit Engineering, Vienna University of Technology, Vienna, Austria. His main research interests include design and characterization of analog deep-submicron and nanometer CMOS circuits, as well as optoelectronic integrated CMOS and BiCMOS circuits. He is author of the two Springer books "Integrated Silicon Optoelectronics" and "Silicon Optoelectronic Integrated Circuits" as well as coauthor of "Highly Sensitive Optical Receivers", "Optical Communication over Plastic Optical Fibers: Integrated Optical Receiver Technology", and "Analog Filters in Nanometer CMOS". Furthermore, he is author and coauthor of more than 400 scientific publications.

2.7. IET Electronics Letters 2014

Reproduced by permission of the Institution of Engineering & Technology. Full acknowledgment to P. Brandl, R. Enne, T. Jukic and H. Zimmermann, "Monolithically integrated optical receiver with large-area avalanche photodiode in high-voltage CMOS technology", 9th October 2014.

Monolithically integrated optical receiver with large-area avalanche photodiode in high-voltage CMOS technology

P. Brandl, R. Enne, T. Jukić and H. Zimmermann

A novel monolithically integrated optoelectronic receiver with a 200 μm diameter, high responsivity avalanche photodiode (PD) is presented. The whole receiver was developed in a high-voltage 0.35 μm CMOS technology. This permits high PD bias voltages and the implementation of the receiver circuitry in a single chip. With a PD bias voltage of 65 V, a high responsivity of 30 A/W has been reached at a wavelength of 675 nm. Together with a folded-cascode transimpedance amplifier, the complete receiver achieves a sensitivity of -31.8 dBm at a data rate of 1 Gbit/s with a bit error rate of 10^{-9} and a pseudorandom binary sequence of $2^{31}-1$.

Introduction: Low-cost optoelectronic integrated circuits (OEICs) in the CMOS technology offer a solution for short-haul plastic optical fibre communication systems, optical interconnects and optical wireless communication systems. These applications require rather large-diameter photodiodes (PDs) in order to relax the requirements on the alignment [1]. A large-area PD has also a large capacitance, which reduces sensitivity and bandwidth. Compared to hybrid receivers, monolithically integrated receivers have the advantage of reduced capacitance due to the elimination of parasitics, i.e. capacitance of bond pads. To increase the sensitivity, the internal gain of an avalanche PD (APD) can be used. To exploit the gain of the APD, the APD must be operated at a rather high voltage, which violates the process reliability operation specifications of digital CMOS technologies. To avoid jeopardising the correct function of the circuitry, these specifications must be strictly adhered to.

Several APDs have been integrated with circuitry in the CMOS technology [2–4]. In [2], where a silicon-on-insulator (SOI) technology was used to isolate metal–oxide semiconductor field effect transistors from the high APD reverse bias voltage, a responsivity of >1 A/W at 27.25 V for 650 nm was reported. A lateral APD on SOI for the suppression of slow carrier diffusion was introduced in [3]. P+/n-well and p+/deep-n-well APDs with a thin absorption and multiplication zone were introduced in [4]. The reported OEICs show a trade-off between speed and sensitivity. Moreover, the light-sensitive areas of these APDs were quite small. All these APDs suffered from a low responsivity due to a thin absorption and multiplication region leading to a rather poor sensitivity. We implemented an APD with a thick absorption and a separate multiplication zone leading to a higher responsivity [5]. However, this APD structure requires a higher voltage as compared to the above-mentioned examples [2–4]. Using a high-voltage (HV) CMOS technology specified for 100 V, we were able to successfully implement an APD and a CMOS circuitry in a single chip. This technology allowed us to apply the required HV for the APD while observing all design rules and specifications to keep the circuitry always in safe operating conditions. In this Letter, we present a fully monolithically integrated optical receiver with a 200 μm diameter APD in a 0.35 μm HV CMOS technology. Although the used technology is not dedicated for high-frequency applications, the OEIC offered a 1 Gbit/s data traffic with a sensitivity of -31.8 dBm at a bit error rate (BER) of 10^{-9} .

OEIC structure: The used HV CMOS technology offers different wells to isolate the MOS transistors down to substrate potentials of -100 V. Fig. 1 shows a simplified block diagram of the entire OEIC including an APD and a transimpedance amplifier (TIA). This TIA transforms the photocurrent I_{PH} into a corresponding voltage V_{data} . To reduce the influence of power supply noise and substrate noise, a differential design was used. This differential design is based on a dummy TIA which has the same structure as the main TIA. Together with a proportional–integral (PI) controller, the dummy TIA generates the voltage V_{avg} , which is the average output voltage of V_{data} . These two voltages feed a differential limiting post-amplifier which boosts the amplitude of the signal and clips the high and low bits symmetrically in the case of overload.

The APD [5] uses a high-doped n+ region at the surface of the wafer as a cathode. Below this n+ region, a deep-p well forms the multiplication zone. This deep-p well is embedded in a deep-n well to avoid edge breakdown. Furthermore, the deep-n well reduces the effective p

doping of the deep-p well and of the p-epitaxial layer. This configuration enables a deep penetration of the depletion region into the p -doped epitaxial layer before the breakdown happens. Additionally, the epitaxial layer serves as an absorption zone. Below the epitaxial zone, the p -doped substrate is located and builds the anode of the APD. At a reverse voltage of -68.25 V, the breakdown of the APD is achieved corresponding to a dark current of $1 \mu\text{A}$. The APD has an active diameter of 200 μm , a capacitance of 0.57 pF and a responsivity of 30 A/W corresponding to a gain of 73 at a bias voltage of -65 V for a wavelength of 675 nm. The APD shows a gain-bandwidth product of 42.5 GHz, which results in a -3 dB bandwidth of ~ 582 MHz for a gain of 73.

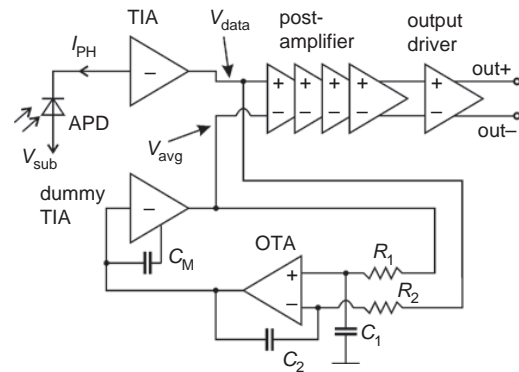


Fig. 1 Simplified block diagram of realised OEIC

As mentioned before, the performance of TIAs is significantly influenced by the input node capacitance. This includes the Miller capacitance (the gate–drain capacitance C_{GD} multiplied by the voltage gain plus one) from the input transistor [6]. To minimise the input node capacitance, we used a folded cascode circuit which reduces the Miller capacitance of the input transistor. The folded cascode is superior to the normal cascode because the drain–source saturation voltage of each transistor can be made larger, which results in a smaller width-to-length ratio of each transistor, keeping the parasitic capacitances small too. The implemented folded-cascode circuit is depicted in Fig. 2a. The input transistor M_1 still has a relatively large width to achieve a high gain and good noise performance. The cascode transistor M_2 provides a low-impedance node for the drain of M_1 , which reduces the Miller effect. Transistors M_3 and M_5 are current sources. M_4 works as a source follower and serves for a low impedance at the output node. The feedback (FB) resistor R_{FB} has a value of 3.7 k Ω resulting in a transimpedance of 3 k Ω . C_{FB} is 33 fF, which guarantees stability of the TIA.

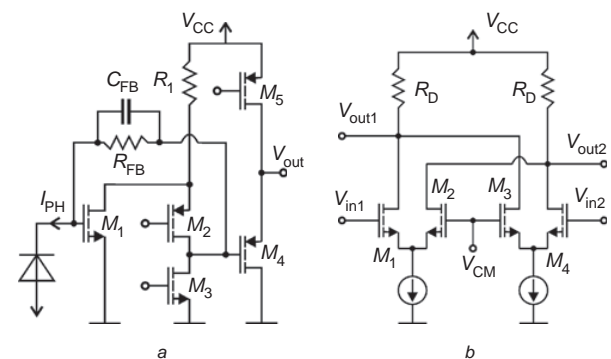


Fig. 2 Simplified circuit diagrams

a Folded cascode used for TIA, feedback

b f_T -doubler used for output driver, common mode control

The dummy TIA uses the same design as the main TIA except for a connection of an additional Miller capacitance C_M . This connection is made at the drain of M_1' (M_1' is equal to M_1 of the main TIA). With $C_M = 670$ fF the bandwidth of the dummy TIA is reduced and therefore its noise contribution is lower. As mentioned above, the output of the dummy TIA represents the averaged output voltage of the main TIA. This is achieved with the help of a PI controller built by R_1 , R_2 , C_1 ,

C2 and an operational transconductance amplifier (OTA). The OTA is designed as a two-stage Miller OTA. It generates a current which corresponds to the average photocurrent I_{PH} . Based on this control system, low-frequency parts of the signal are cancelled out, i.e. ambient light is suppressed as long as the TIA is not overdriven. With the values for $R_1 = R_2 = 1 \text{ M}\Omega$ and $C_1 = C_2 = 5.5 \text{ pF}$, a lower 3 dB cutoff frequency of 589 kHz follows, see Fig. 3.

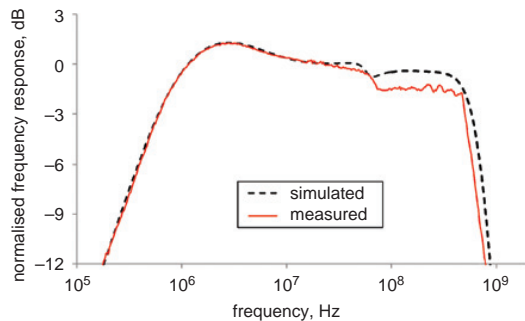


Fig. 3 Normalised frequency response of optical receiver, $V_{sub} = 65 \text{ V}$, $\lambda = 675 \text{ nm}$

The post-amplifier includes four stages and has a gain of 34.9 dB. Each stage consists of a differential amplifier followed by source followers. The source followers serve for impedance transformation, for level shifting and for implementation of peaking due to its inductive behaviour.

The output driver employs an f_T -doubler circuit to be capable of driving high-output currents and not presenting a bandwidth bottleneck. This bottleneck would result from the capacitances of the large transistors of a simple differential amplifier that would be necessary for driving these high currents [6]. Depicted in Fig. 2b, the circuit exhibits an input capacitance of roughly half of the gate-source capacitance C_{GS1} of M_1 (due to the series connection of C_{GS1} and C_{GS2}), while the transconductance is the same as that of M_1 . With an R_D of 75Ω and an off-chip load of 50Ω , the buffer must steer at least 11.6 mA to deliver a single-ended voltage swing of 0.35 V. The complete chip occupies an area of $1615 \times 965 \mu\text{m}^2$ and consumes a current of 39 mA at a supply voltage of 3.3 V.

Measurements and results: For measurement, a vertical cavity surface-emitting laser (VCSEL) with a wavelength of 675 nm was modulated via a bias-T by an HP8753E network analyser or by a bit pattern generator. The laser signal from the VCSEL was brought via a multimode fibre to the APD. In between, there was a manual optical attenuator to control the optical power (measured with an OPHIR NOVA PD300 optical power meter) reaching the APD. To measure the frequency response of the OEIC, one output was connected to the network analyser. The normalised frequency response of the complete chip is depicted in Fig. 3. The measured upper -3 dB cutoff frequency was 500 MHz, not considering the peak at $\sim 3 \text{ MHz}$, which is caused by the FB via the PI controller and the dummy TIA.

As mentioned before, the used HV CMOS process and the MOS transistors are not intended for high-frequency applications. Therefore, the design kit uses the standard MOS transistor model where high-frequency effects are not considered accurately. This is the main reason for the difference between the simulated and measured frequency responses, especially for the 100 MHz lower measured bandwidth. The overall transimpedance of the whole receiver was $168 \text{ k}\Omega$. According to circuit simulations, the TIA possesses an equivalent input noise current of 734 nA (in a bandwidth of 600 MHz) leading together with the low-voltage responsivity of 0.41 A/W (gain = 1) of the APD to a sensitivity of -19.7 dBm (for a Q -factor equal to 6, i.e. $\text{BER} = 10^{-9}$).

For bit error measurements, the outputs of the OEIC were coupled to a bit error analyser. Fig. 4 shows the results of the sensitivity measurements at different data rates, all with a pseudorandom binary sequence (PRBS) of $2^{31}-1$. For a BER of 10^{-9} , the OEIC shows the following

sensitivities: -33.6 dBm at a data rate of 622 Mbit/s, -31.8 dBm at 1 Gbit/s and -28.3 dBm at 1.25 Gbit/s. At a data rate of 1.25 Gbit/s, the receiver bandwidth is too narrow for optimal detection, resulting in distortion [6].

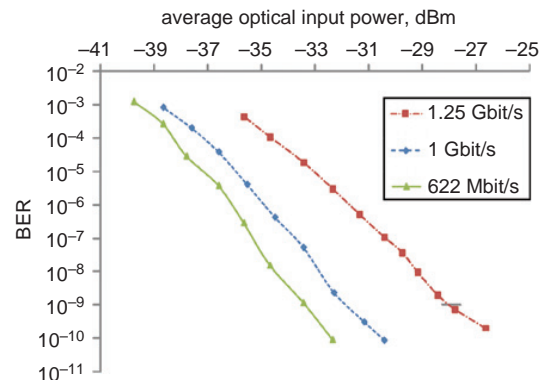


Fig. 4 Sensitivity at different data rates, $2^{31}-1$ PRBS, $\lambda = 675 \text{ nm}$

Conclusion: A monolithically integrated optoelectronic receiver consisting of a large-diameter APD and a TIA has been fabricated in a standard $0.35 \mu\text{m}$ HV CMOS process. The APD exhibits a gain of 73 at a -65 V substrate bias. This leads to a high responsivity of 30 A/W , resulting in a sensitivity of -31.8 dBm at a data rate of 1 Gbit/s. It has to be noted that the APD improves the sensitivity by 12 dB compared to the case when a *pin* PD would be implemented together with the same TIA in the HV CMOS process. The sensitivity of the receiver introduced here compares well with that of the one in 130 nm CMOS on SOI with a sensitivity of -19 dBm at 2 Gbit/s [3]. In [4], the receivers' sensitivities were in the range of -6 to -2.2 dBm due to the thin absorption and multiplication zone of the APDs implemented here.

© The Institution of Engineering and Technology 2014

10 July 2014

doi: 10.1049/el.2014.2504

One or more of the Figures in this Letter are available in colour online.

P. Brandl, R. Enne, T. Jukić and H. Zimmermann (*Institute of Electrodynamics, Microwave and Circuit Engineering, Vienna University of Technology, Gusshausstrasse 25/354, 1040 Vienna, Austria*)

E-mail: paul.brandl@tuwien.ac.at

References

- Brandl, P., and Zimmermann, H.: 'Development of an optoelectronic integrated circuit for indoor optical wireless communication systems', *Trans. Emerging Telecommun. Technol.*, 2014, **25**, (6), pp. 629–637, doi: 10.1002/ett.2777
- Moloney, A.M., Morrison, A.P., Jackson, J.C., Mathewson, A., Alderman, J., Donnelly, J., O'Neill, B., Kelleher, A.M., Healy, G., and Murphy, P.J.: 'Monolithically integrated avalanche photodiode and transimpedance amplifier in a hybrid bulk/SOI CMOS process', *Electron. Lett.*, 2003, **39**, (4), pp. 391–392, doi: 10.1049/el:20030187
- Csutak, S.M., Schaub, J.D., Wang, S., Mogab, J., and Campbell, J.C.: 'Integrated silicon optical receiver with avalanche photodiode', *IEE Proc., Optoelectron.*, 2003, **150**, (3), pp. 235–237, doi: 10.1049/ip-opt:20030391
- Kamrani, E., Lesage, F., and Sawan, M.: 'Low-noise, high-gain transimpedance amplifier integrated with SiAPD for low-intensity near-infrared light detection', *IEEE Sens. J.*, 2014, **14**, (1), pp. 258–269, doi: 10.1109/JSEN.2013.2282624
- Steindl, B., Enne, R., Schidl, S., and Zimmermann, H.: 'Linear mode avalanche photodiode with high responsivity integrated in high-voltage CMOS', *IEEE Electron Device Lett.*, 2014, **35**, (9), pp. 897–899
- Säckinger, E.: 'Broadband circuits for optical fiber communication' (Wiley, Hoboken, NJ, 2005)

2.8. IEEE PTL 2015

© 2015 IEEE. Reprinted, with permission, from Paul Brandl, Reinhard Enne, Tomislav Jukic, and Horst Zimmermann, "OWC Using a Fully Integrated Optical Receiver With Large-Diameter APD", IEEE PHOTONICS TECHNOLOGY LETTERS, March 2015.

OWC Using a Fully Integrated Optical Receiver With Large-Diameter APD

Paul Brandl, Reinhard Enne, Tomislav Jukić, and Horst Zimmermann

Abstract—This letter presents a fully monolithically integrated receiver with a large-diameter avalanche photodiode (APD). Using a standard high-voltage 0.35- μm CMOS technology, the APD is implemented with separated absorption and multiplication regions optimizing the ionization ratio between holes and electrons. This optimized ionization ratio leads to a low excess noise factor of the APD, which considerably improves the receiver's sensitivity to -31.8 dBm at 1 Gbit/s (bit error rate $<10^{-9}$). A 1-Gbit/s wireless optical communication link with a distance of 3.3 m is demonstrated. Due to the highly sensitive receiver, it is possible to omit any kind of input optics, resulting in a wide receiving angle of 68° for a bit error rate of $<10^{-9}$.

Index Terms—Avalanche photodiode, CMOS integrated circuits, integrated optoelectronics, optical receivers, optical wireless communication.

I. INTRODUCTION

THE insatiable appetite for modern personal communication devices to transfer high data rates, increases the demand for optical communication systems with nearly unbounded and license-free bandwidth. All systems, whether tethered over cheap plastic optical fibers (POF) [1] or wireless using the lighting infrastructure known as visible light communication (VLC) [2] or wireless with direct-line-of-sight links [3], [4], need highly sensitive optical receivers (RX) with large-diameter photodiodes for relaxed alignment [1]–[4]. The POF has loss minima at wavelengths of 550 and 650 nm [1]. Therefore those systems work in the visible wavelength range where silicon is an adequate detector material.

Silicon APDs are the preferred optical detectors for applications where the wavelength lies between 400 nm and 1100 nm and low optical power detection is required. The gain, resulting from the avalanche multiplication of the photo-generated carriers, is responsible for an improvement of the signal-to-noise ratio. To get this multiplication process working, an APD must operate at a rather high voltage which makes the integration in a single chip with standard complementary metal-oxide-semiconductor (CMOS) circuitry difficult. The maximum voltages are limited by the (digital) CMOS process reliability specifications. Despite those constraints, several APDs have been integrated with circuitry in CMOS technology [5]–[6]. Those APDs use a simple p-n junction (mostly a p+/n-well junction) to reduce the

Manuscript received September 19, 2014; revised November 25, 2014; accepted December 11, 2014. Date of publication December 22, 2014; date of current version February 4, 2015.

The authors are with the Institute of Electrodynamics, Microwave and Circuit Engineering, Vienna University of Technology, Vienna 1040, Austria (e-mail: paul.brandl@tuwien.ac.at; reinhard.enne@tuwien.ac.at; tjukic@emce.tuwien.ac.at; horst.zimmermann@tuwien.ac.at).

Color versions of one or more of the figures in this letter are available online at <http://ieeexplore.ieee.org>.

Digital Object Identifier 10.1109/LPT.2014.2382333

1041-1135 © 2014 IEEE. Personal use is permitted, but republication/redistribution requires IEEE permission.

See http://www.ieee.org/publications_standards/publications/rights/index.html for more information.

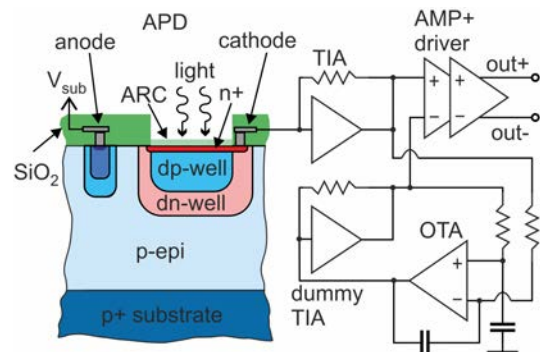


Fig. 1. Cross section of the APD (not to scale) and block diagram of subsequent circuitry including transimpedance amplifier (TIA), operational transconductance amplifier (OTA), differential amplifier (AMP) and output driver, anti-reflection coating (ARC).

required voltage for avalanche multiplication. Due to the simple p-n junction, the avalanche multiplication region serves at the same time as photon absorption region leading to mixed carrier injection. Mixed carrier injection, however, results into a higher excess noise factor [7] with reduced optimum gain value. Hence, the performance of the APD receivers is reduced [8].

By using a high-voltage (HV) CMOS technology specified for 100 V, we were able to implement an APD with separated absorption and multiplication regions and a CMOS circuitry in a single chip. In this letter, we present an optoelectronic integrated circuit (OEIC) with a 200 μm diameter APD. The sensitivity (minimal necessary optical input power for reaching a certain bit error rate (BER)) of the OEIC is considerably improved so that any kind of optics at the RX can be omitted for use as a free-space RX. Consequently, the information bearing laser ray can be received from a wide angle resulting into a huge field of view (FOV) [9].

II. APD OEIC

The OEIC with the monolithically integrated APD was built in a 0.35 μm HV CMOS technology that offers different wells to isolate the MOS transistors down to substrate potentials of -100 V. That fact allowed us to integrate the APD together with circuits on the same silicon chip. Fig. 1 shows a cross section of the APD structure and a simplified block diagram of the subsequent circuitry.

A. Avalanche Photodiode

The APD [10] is based on a reach-through diode [7] with separated multiplication and absorption zones. In this device, the depletion zone reaches the contact layer through

the absorption and multiplication regions. An anti-reflection coating (ARC) is used as top layer, thus improving the responsivity of the APD. The cathode contact is formed by a highly doped n^+ region at the surface of the wafer. A deep p-well below the n^+ region builds the multiplication zone in which secondary electron-hole pairs are generated through impact ionization. This deep p-well has an effective diameter of $196 \mu\text{m}$. The PD's diameter was chosen based on knowledge obtained from previous projects [4], [9]. If all technology parameters scale linear, an improvement of 1.5 dB of SNR can be expected for a 2-times larger PD's area. To avoid edge breakdown, the deep p-well is embedded into a deep n-well. This deep n-well reduces also the effective p doping of the deep p-well and of the p-epitaxial layer. Thus, the depletion region penetrates deeper into the p doped epitaxial layer before breakdown occurs. Most of the incident photons with wavelengths of up to 750 nm are absorbed in this depletion zone (according to the Beer-Lambert law) where primary electron-hole pairs are generated. Below the epitaxial layer, in a depth of approx. $10 \mu\text{m}$ from the surface, the p^+ doped substrate is located and builds the anode of the APD, which is contacted by a large-area substrate contact consisting of deep p-well, p-well and p^+ . The APD shows a breakdown voltage of approx. -68.25 V corresponding to a dark current of $1 \mu\text{A}$.

B. CMOS Circuitry

The cathode of the APD is connected to a transimpedance amplifier (TIA) for converting the photocurrent into a corresponding voltage signal. The TIA is designed in the form of a folded cascode [11]. To reduce the influence of common-mode noise, like power supply noise and substrate noise, a differential design was applied. For this purpose, the dummy TIA generates the average output voltage of the main TIA. The dummy TIA has the same structure as the main TIA and generates the average voltage with the help of a proportional integral controller. This controller is based on an operational transconductance amplifier (OTA). The two voltage signals from the main and dummy TIA are fed into a 4-stage differential amplifier with a gain of 34.9 dB. An f_T -doubler stage builds the output driver for delivering a differential voltage swing of 700 mV into 50Ω . The whole OEIC showed a measured -3 dB cut-off frequency of 500 MHz [11] and a total, differential transimpedance of 161 kV/A .

According to [8], the noise bandwidth for the RX can be calculated as follows

$$BW_n = \frac{1}{H_0^2} \int_0^\infty |H(f)|^2 df \quad (1)$$

where $H(f)$ is the transfer function of the complete OEIC and H_0 is the midband value of $H(f)$. We calculated a $BW_n = 526 \text{ MHz}$ for the complete RX circuitry because the frequency response of the complete OEIC approached the transfer function of a seventh-order low-pass filter. According to this noise bandwidth, the OEIC has an equivalent input root mean square noise current $i_{n,amp}^{rms} = 734 \text{ nA}$. Similar to our previously presented OEIC [4], the center APD is surrounded by four pn photodiodes [12] that serve as detectors

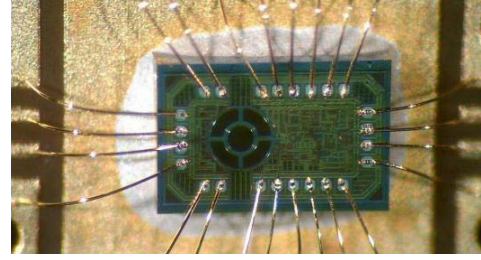


Fig. 2. Photomicrograph of the developed OEIC receiver glued and bonded on a printed circuit board.

identifying from which direction the optical beam is coming. The complete chip consumes a current of 39 mA at a supply voltage of 3.3 V and has a size of $1615 \mu\text{m} \times 965 \mu\text{m}$. For measurements, the chip was directly bonded to a printed circuit board, see Fig. 2.

III. MEASUREMENTS

To verify the performance of the APD and the OEIC, several measurements were conducted. First, we determined the sensitivity of the OEIC and then the APD's carrier ionization ratio k_{eff} . Subsequently, we calculated the APD's excess noise factor and the resulting receiver's BER depending on the distance between transmitter (TX) and RX. To confirm the wide FOV of the lens-less RX, we measured the BER versus the angle of incident rays on the RX.

A. Sensitivity of OEIC

To identify the sensitivity of the OEIC, we counted the bit errors depending on the received optical power. The outputs were coupled to a bit error analyzer. A 675 nm wavelength laser was on-off modulated with a 1 Gbit/s $2^{31} - 1$ pseudorandom binary sequence (PRBS). The laser's extinction ratio $ER = P_1/P_0$ ($P_1 = \text{on-state power for a 1 bit}$ and $P_0 = \text{off-state power for a 0 bit}$) was set to 7. The laser signal was brought via a multimode fiber ($50 \mu\text{m}$ core diameter) to the APD. In between, there was a manual optical attenuator to control the optical power [11]. At this wavelength, the APD showed a responsivity of approx. 32 A/W at -65 V reverse voltage which corresponds to a gain M of 78 with a low-voltage responsivity of 0.41 A/W ($M = 1$). For a BER of 10^{-9} , the sensitivity was -31.8 dBm [11].

B. APD's Carrier Ionization Ratio

Due to the statistical nature of the avalanche process, an APD generates an additional current noise to the photon shot noise. The performance of an APD is degraded by an excess noise factor F and is given by [7]:

$$F = k_{eff} \cdot M + (1 - k_{eff}) \left[2 - \frac{1}{M} \right] \quad (2)$$

where M is the gain and k_{eff} is the effective ratio of the hole to electron ionization coefficients. A low value of k_{eff} is highly desirable in achieving low noise. In particular, in silicon the electron ionization coefficient is larger than

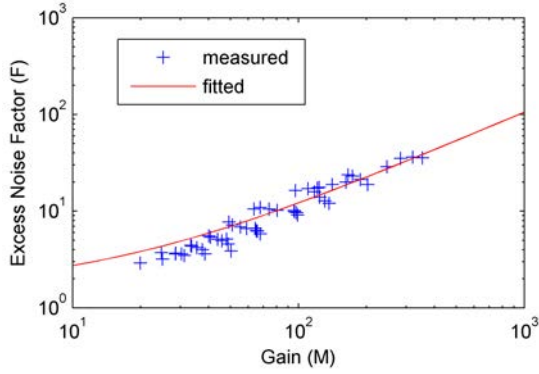


Fig. 3. Excess noise factor as a function of APD's multiplication gain.

that of holes. Therefore, electrons should be swept by the electric field into the multiplication zone (deep p-well) with its higher field. In order to determine k_{eff} , we measured experimentally the dependence of the excess noise factor on the gain. One output of the OEIC was connected to a spectrum analyzer (HP E4402B) to determine the noise power. The illumination of the APD was varied within a region where the multiplied shot noise was the dominant part. This was achieved by increasing the illumination so far that the measured noise power was at least ten times higher than the measured noise power of the OEIC alone, i.e. without light. Therefore, the remaining noise components (e.g. relative intensity noise from the laser source) can be neglected. The excess noise factor is calculated from

$$F = \frac{i_n^2}{2qM^2RP_{in}B} \quad (3)$$

where i_n^2 is the mean-square noise current, q the electronic charge, B the bandwidth, R the unamplified responsivity of 0.41 A/W for the used laser light with a wavelength of 675 nm. P_{in} is the incident light power and M is the multiplication calculated from the measured APD current and primary photocurrent ($= R \cdot P_{in}$). By fitting the McIntyre formula (2) to the measured values we determined experimentally the effective k -factor. Fig. 3 depicts the excess noise factor versus the multiplication gain of the APD. The fitting process results in a $k_{eff} = 0.104$. The k -factor is in a justifiable range compared to commercially available epitaxial APDs ($k_{eff} = 0.06$) with optimally doped and structured layers [13]. A further reason is that the photons penetrate the APD from the suboptimal side. The commercially available diodes are illuminated from the anode side (p^+) and the photons are mainly absorbed in the absorption region where primary electron-hole pairs are generated. Electrons drift to the cathode (n^+) and pass the multiplication region where impact ionization occurs. Holes go in opposing direction and are collected by the anode. Thus, mostly electrons are injected into the multiplication region for a minimum ratio of k_{eff} . The used technology (because of the p^+ substrate) allows only an integrated APD structure with separated absorption and multiplication zones where the cathode (n^+) is on top of the wafer. Consequently, more holes are generated in the multiplication region, thus increasing k_{eff} .

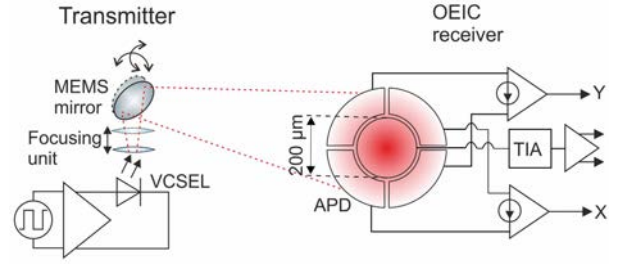


Fig. 4. Simplified schematic of OWC system (not to scale).

C. BER vs. Distance

For testing the performance of the OEIC in an optical wireless communication (OWC) scenario, we used the set-up depicted in Fig. 4. The set-up was installed in our laboratory with normal lighting (500 lux). The TX is built up on a 680 nm wavelength VCSEL, a focusing unit for adjusting the laser beam width and a MEMS based mirror for steering the laser ray. A detailed description of the TX can be found in [4]. The VCSEL was on-off modulated with a $2^{31}-1$ PRBS with a data rate of 1 Gbit/s. The emitted average laser power was adjusted to 0.95 mW in order not to violate eye safety rules. The ER of the laser was set to 12. In the focused case, the laser ray had a divergence angle $\varphi = 0.15^\circ$ at full width at half maximum (FWHM). The average received power P_{avg} (depending on the distance TX – RX) results from this angle and the APD diameter.

The outputs of the OEIC were connected to a bit error analyzer. After exhaustive experiments, the substrate voltage V_{sub} was set to -65.5 V which results roughly in an APD gain M of 110 [10] and an $F = 13.2$. This M corresponds well to a calculated, optimal gain $M_{opt} = 118$ after [8]

$$M_{opt} = \sqrt{\frac{i_{n,amp}^{rms}}{Q \cdot k_{eff} \cdot q \cdot BW_n} - \frac{1 - k_{eff}}{k_{eff}}}. \quad (4)$$

The Q parameter is a measure of the ratio between signal and noise and corresponds to 6 for a target BER of 10^{-9} .

The APD's shot noise is approximated by a Gaussian random variable with different variances i_n^2 for the binary states as the shot noise is larger for a 1 bit than for a 0 bit [8]. The total noise can be calculated

$$i_{n,\{0,1\}}^2 = 2 \cdot q \cdot M^2 \cdot F \cdot (R \cdot P_{in} + I_d) \cdot BW_n + i_{n,amp}^2 \quad (5)$$

where P_{in} is the incident light power depending on P_1 or P_0 . I_d is the dark current which is in the order of a few pA and can be neglected. With the corresponding signal currents $I_{0,1} = M \cdot R \cdot P_{0,1}$ for a transmitted 0 or 1, the BER is given by

$$BER = \frac{1}{4} \left[\operatorname{erfc} \left(\frac{I_1 - I_{avg}}{\sqrt{2i_{n,1}^2}} \right) + \operatorname{erfc} \left(\frac{I_{avg} - I_0}{\sqrt{2i_{n,0}^2}} \right) \right]. \quad (6)$$

I_{avg} is the average signal current obtained from P_{avg} and erfc stands for the complementary error function defined as

$$\operatorname{erfc}(x) = \frac{2}{\sqrt{\pi}} \int_x^\infty \exp(-y^2) dy. \quad (7)$$

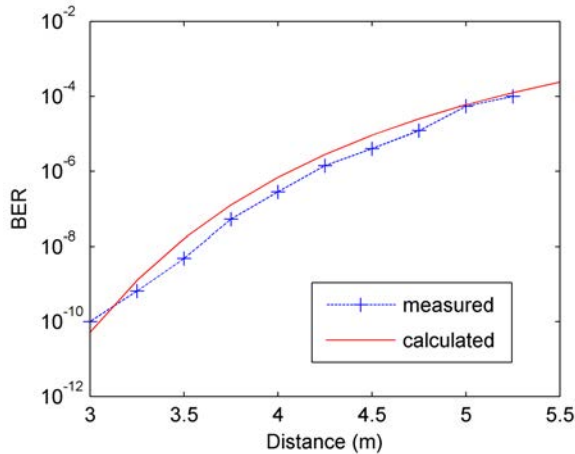


Fig. 5. BER versus distance between transmitter and receiver at 1 Gbit/s.

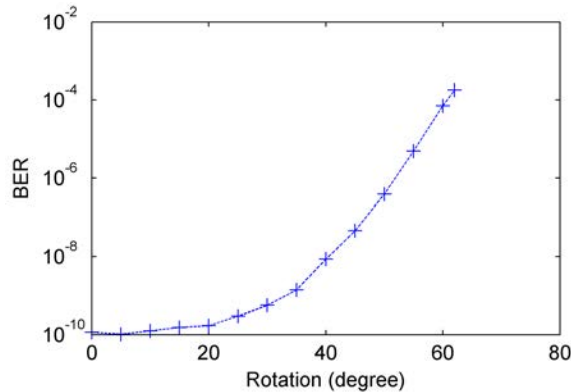


Fig. 6. BER versus rotation of the receiver against the optical axis at 1 Gbit/s, distance = 3 m.

Fig. 5 shows the calculated and measured BER versus the distance between TX and RX. Without any optics at the RX, the OEIC was able to guarantee a 1 Gbit/s free-space data transfer over a distance of up to 3.3 m with a BER lower than 10^{-9} . Compared to [9], we extended the distance by a factor of 6. The measured values show a slightly better performance compared to the calculated results. This can be explained by the actual received power. In the calculations, the laser's irradiance distribution was assumed to be flat with a certain divergence (0.15° FWHM). Indeed, as a well-known fact, the irradiance of a laser is more like a Gaussian beam. That fact leads to a higher irradiance level in the center of the laser spot where the OEIC is placed resulting in a better BER.

D. BER vs. Incidence Angle

For this measurement, the RX was mounted on a rotatable frame in a fixed distance of 3 m from the TX. The laser signal was again modulated with an on-off keying with a data rate of 1 Gbit/s (PRBS = $2^{31} - 1$). The OEIC's outputs were connected to the bit error analyzer. Fig. 6 shows the measured BER as a function of rotation angle φ of the RX. The BER curve depends mainly on the angular power

penalty ($P_{in} \propto P_{avg} \cdot \cos(\varphi)$). Additional losses result from reflections of the ARC and from shadowing effects of the protruding passivation layer and metal layers compared to the ARC layer, see Fig. 1. Up to an angle of 34° , the RX's BER is below 10^{-9} resulting into a FOV of 68° in this configuration. This is a notable improvement compared to [4] where a FOV of only 9° was measured due to the usage of a PIN-photodiode RX and a receiver lens.

IV. CONCLUSION

This letter presents a fully monolithically integrated optical receiver with a $200 \mu\text{m}$ diameter APD in a $0.35 \mu\text{m}$ HV CMOS technology. Although the used technology is not dedicated for high-frequency applications, the OEIC offers a 1 Gbit/s data traffic with a sensitivity of -31.8 dBm (BER = 10^{-9}). This corresponds to an improvement in sensitivity of approx. 7.5 dB compared to [4], whereas the data rate was increased tenfold compared to [5]. To the best of authors' knowledge, this is the most sensitive reported OEIC with a large photodiode area monolithically integrated in a standard CMOS technology. As shown by our experiments and calculations, the OEIC is best suited for future optical communication scenarios. Compared to [3], we achieved the same communication distance with nearly the same data rate without needing complex optical components at the RX.

REFERENCES

- [1] O. Ziemann, S. Loquai, J. Vinogradov, and R. Kruglov, "The 1 gigabit over 1 mm POF story—From vision to standard," in *Proc. 36th ECOC*, Torino, Italia, Sep. 2010, pp. 1–22.
- [2] G. Cossu, R. Corsini, and E. Ciaramella, "High-speed bi-directional optical wireless system in non-directed line-of-sight configuration," *J. Lightw. Technol.*, vol. 32, no. 10, pp. 2035–2040, May 15, 2014.
- [3] D. O'Brien *et al.*, "High-speed optical wireless demonstrators: Conclusions and future directions," *J. Lightw. Technol.*, vol. 30, no. 13, pp. 2181–2187, Jul. 1, 2012.
- [4] P. Brandl, S. Schidl, A. Polzer, W. Gaberl, and H. Zimmermann, "Optical wireless communication with adaptive focus and MEMS-based beam steering," *IEEE Photon. Technol. Lett.*, vol. 25, no. 15, pp. 1428–1431, Aug. 1, 2013.
- [5] E. Fisher, I. Underwood, and R. Henderson, "A reconfigurable single-photon-counting integrating receiver for optical communications," *IEEE J. Solid-State Circuits*, vol. 48, no. 7, pp. 1638–1650, Jul. 2013.
- [6] E. Kamrani, F. Lesage, and M. Sawan, "Low-noise, high-gain transimpedance amplifier integrated with SiAPD for low-intensity near-infrared light detection," *IEEE Sensors J.*, vol. 14, no. 1, pp. 258–269, Jan. 2014.
- [7] P. P. Webb, R. J. McIntyre, and J. Conradi, "Properties of avalanche photodiodes," *RCA Rev.*, vol. 35, pp. 234–278, Jun. 1974.
- [8] R. G. Smith and S. D. Personick, "Receiver design for optical fiber communication systems," in *Semiconductor Devices for Optical Communication*, H. Kressel, Ed., 2nd ed. New York, NY, USA: Springer-Verlag, 1982.
- [9] W. Gaberl, R. Swoboda, and H. Zimmermann, "Integrated optical receiver for lens-less short range free-space gigabit communication," in *Proc. 35th ECOC*, Vienna, Austria, Sep. 2009, pp. 1–2.
- [10] B. Steindl, R. Enne, S. Schidl, and H. Zimmermann, "Linear mode avalanche photodiode with high responsivity integrated in high-voltage CMOS," *IEEE Electron Device Lett.*, vol. 35, no. 9, pp. 897–899, Sep. 2014.
- [11] P. Brandl, R. Enne, T. Jukić, and H. Zimmermann, "Monolithically integrated optical receiver with large-area avalanche photodiode in high-voltage CMOS technology," *Electron. Lett.*, vol. 50, no. 21, pp. 1541–1543, Oct. 2014.
- [12] R. Enne, B. Steindl, K. Schneider-Hornstein, and H. Zimmermann, "PN photodiode in $0.35\text{-}\mu\text{m}$ high-voltage CMOS with 1.2-GHz bandwidth," *J. Opt. Eng.*, vol. 53, no. 11, p. 116114, 2014.
- [13] Excelitas Technologies Corp., Fremont, CA, USA. (2011). *Avalanche Photodiode—A Users Guide*. [Online]. Available: http://www.excelitas.com/downloads/app_apd_a_user_guide.pdf

2.9. IEEE JSSC 2016

© 2016 IEEE. Reprinted, with permission, from Paul Brandl, Tomislav Jukic, Reinhard Enne, Kerstin Schneider-Hornstein, and Horst Zimmermann, "Optical Wireless APD Receiver With High Background-Light Immunity for Increased Communication Distances", IEEE JOURNAL OF SOLID-STATE CIRCUITS, July 2016.

Optical Wireless APD Receiver With High Background-Light Immunity for Increased Communication Distances

Paul Brandl, Tomislav Jukić, Reinhard Enne, Kerstin Schneider-Hornstein,
and Horst Zimmermann, *Senior Member, IEEE*

Abstract—The design and measurement of a monolithically integrated optoelectronic chip consisting of two different receivers are presented. A high-speed receiver for communication including a highly sensitive, large-area avalanche photodiode builds one receiver. A data rate of 1 Gbit/s with a BER $<10^{-9}$ is received with a sensitivity of -31.8 dBm. The second receiver consists of two pn-photodiodes connected to a highly sensitive differential transimpedance amplifier with a nonlinear feedback. This circuit is capable of detecting light power differences down to -90 dBm and is implemented two times. Its purpose is the detection of the light spot's position on the receiver. The complete chip is fabricated in a standard high-voltage $0.35\ \mu\text{m}$ CMOS technology. The performance in a wireless communication scenario with strong background irradiance is explored, and a comparison with published optoelectronic integrated receivers is given.

Index Terms—Avalanche photodiode (APD), CMOS integrated circuits, integrated optoelectronics, OEIC, optical receiver, optical wireless communication, transimpedance amplifier (TIA).

I. INTRODUCTION

TODAY, modern society demands omnipresent low-cost broadband access for their personal communication devices. Optical communication systems with nearly unbounded and license-free bandwidth can satisfy the need after broadband access. Well-known as fiber to the home (FTTH), this high-data-rate traffic reaches our homes, offices, etc., and the traffic has to be distributed in indoor networks. Photonic home area networks can serve for the connection between FTTH and the user devices [1]. Different network systems can be implemented:

- Wireless, by using the LED lighting infrastructure as transmitter, known as visible light communication (VLC) [2];
- Wireless with direct-line-of-sight links [3];
- Tethered, by installing cheap plastic optical fibers (POF) [4] with loss minima at wavelengths of 550 and 650 nm.

Manuscript received December 2, 2015; revised February 3, 2016, March 19, 2016, and April 11, 2016; accepted April 17, 2016. Date of publication May 25, 2016; date of current version June 22, 2016. This paper was approved by Guest Editor Bram Nauta.

P. Brandl, T. Jukić, K. Schneider-Hornstein, and H. Zimmermann are with the Institute of Electrodynamics, Microwave and Circuit Engineering (EMCE), Vienna University of Technology, 1040 Vienna, Austria (e-mail: paul.brandl@tuwien.ac.at).

R. Enne was with EMCE, Vienna University of Technology, Vienna, Austria, and is now with Avago Technology Fiber Austria GmbH, Vienna, Austria.

Color versions of one or more of the figures in this paper are available online at <http://ieeexplore.ieee.org>.

Digital Object Identifier 10.1109/JSSC.2016.2557815

All of those systems work in the wavelength range from 400 nm up to 900 nm where silicon is an adequate detector material.

To relax the alignment procedure, these systems ask for large-diameter photodiodes (PDs), and the receivers have to be highly sensitive due to the limited optical signal power available at the receiver side (because of limited transmit power due to eye safety rules in the case of wireless systems and high attenuation in POFs in the case of tethered systems).

The amplification of an avalanche photodiode (APD) can be used to increase the sensitivity of a receiver. The APD needs a certain amount of electrical field strength inside the device to accelerate the photo-generated carriers sufficiently high for reaching the ionization energy. Hence, the APD needs a rather high bias voltage. That fact makes the integration of an APD in a standard complementary metal-oxide-semiconductor (CMOS) technology difficult because of the maximum allowed voltages stated in the process reliability operation specifications. However, a monolithic solution with an integrated photodiode and receiver circuitry in a chip has significant benefits. This so-called optoelectronic integrated circuit (OEIC) reduces the costs of circuit packaging and is less impaired by parasitics from bond wires and capacitances of bond pads as compared with a hybrid receiver.

Despite those constraints, several solutions of an OEIC for communication purpose with integrated APDs have been published. In [5], the MOSFETs were isolated from the high APD bias voltage by using $1.5\ \mu\text{m}$ CMOS silicon-on-insulator (SOI) technology. To suppress slow carrier diffusion, a lateral APD on $0.13\ \mu\text{m}$ CMOS SOI was presented in [6]. The recently published papers use a simple p-n junction (mostly a p+/n-well junction) to reduce the required voltage for avalanche multiplication. A $0.25\ \mu\text{m}$ SiGe BiCMOS technology was used to implement an APD-OEIC in [7]. In [8] and [9] the APD-OEIC was implemented in a $0.13\ \mu\text{m}$ CMOS technology and a 65 nm technology, respectively. The reached data rates were high (up to 12.5 Gbit/s) in [7]–[9], but the photodiode area was rather small ($10\ \mu\text{m} \times 10\ \mu\text{m}$). The same structure of a p+/n-well was used in [10] where an integrated receiver was implemented in $0.35\ \mu\text{m}$ CMOS technology. In [11], a receiver was presented where the integrated APD was biased beyond the breakdown voltage realized in a $0.13\ \mu\text{m}$ CMOS technology. At this operating point the APD can even detect single photons (single-photon

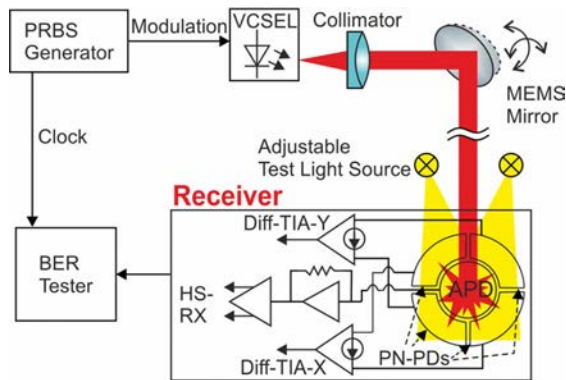


Fig. 1. Block diagram of measurement setup for wireless communication experiment including light sources for investigation of background light immunity.

avalanche diode). This resulted in a sensitivity of -31.7 dBm, but the data rate was rather moderate (0.1 Gbit/s).

As mentioned above, in [7]–[10], a simple p-n junction was used as APD. This means that the APD has only one region that serves at the same time as photon absorption and multiplication region. Consequently, this leads to mixed carrier injection resulting into a higher effective ratio of hole to electron ionization, k_{eff} [12]. A high k_{eff} results in a high excess noise factor with reduced optimum APD gain value. Hence, the APD receiver has a reduced performance [13]. A further disadvantage of these shallow photodiodes is the low dynamic quantum efficiency because of the thin absorption region, resulting in a low external responsivity [14].

A different strategy is the use of high-voltage (HV) CMOS technology [15] which allows much higher voltages between the substrate, different wells, and implants. We pursued this strategy and used a $0.35 \mu\text{m}$ HV CMOS technology specified for 100 V to develop an OEIC consisting of five PDs and three amplifiers. The implemented APD has separated multiplication and absorption zones and shows a high responsivity. This high responsivity allowed for a superior sensitivity of the complete receiver. Due to the used HV CMOS technology, the required higher bias voltages have been applied without harming the process reliability specifications. On the other hand, the used HV technology is not dedicated for high-speed applications. That fact poses a challenge during the circuit design to be comparable with the speed of state-of-the-art receivers. The technology was chosen to realize a tradeoff between APD and circuit performance.

The realized chip consists of three parts: one high-speed receiver (HS-RX) with a $200 \mu\text{m}$ diameter APD and two highly sensitive differential transimpedance amplifiers (Diff-TIAs); see Fig. 1. Four pn-PDs are surrounding the center APD where two opposite situated pn-PDs are connected to one of the Diff-TIAs. The output signal from the Diff-TIAs is an indicator for determining at which position the laser beam is impinging the PD array. Based on this information, an optical wireless communication system can be aligned [16].

Section II of this paper introduces the different implemented photodiodes and shows some measured results from the APD and pn-PD. Section III deals with the design of the different

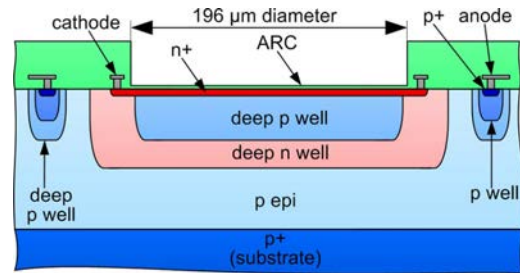


Fig. 2. Cross section of the APD (not to scale).

circuitries, a high-speed receiver (HS-RX) and a Diff-TIA. The measurement results for characterization of the HS-RX and Diff-TIA are presented in Section IV. In addition to the results presented in [17], the advantage of the APD receiver is shown by a comparison to a pn-PD receiver which uses the same receiver circuit. The distance between transmitter and receiver within the communication experiment has been increased compared with previously published results [16], [18], which is shown in Section V. Section VI compares the OEIC with other receivers, and Section VII gives a conclusion.

II. PHOTODIODES IN HV CMOS

The PD converts the impinging light power into an electrical current. The important specifications of photodiodes are the responsivity, the bandwidth, and its capacitance. The capacitance is mainly affected by the PD's area. The bandwidth can be optimized with the drift zone thickness (to suppress slow carrier diffusion) and a high electric field strength. That avoids slow diffusion components and further reduces the capacitance (by increasing the distance in the equivalent plate capacitor formula). The increased doping concentration and reduced circuit supply voltage related to the downscaling of CMOS technology decreases the depletion region width. Hence, a technology with rather large minimal feature size (e.g., $0.35 \mu\text{m}$) has some advantages in producing PDs which are fast and show high responsivity at the same time. The internal gain of an APD can be used to increase the responsivity further, and that fact consequently improves the sensitivity of the receiver.

A. Avalanche Photodiode

The implemented APD [19] operates at substrate potentials down to -70 V while the used HV technology offers different wells to isolate the MOS transistors down to substrate potentials of -100 V. That fact allowed us to integrate the APD together with circuitry on the same chip. Fig. 2 shows a cross section of the APD. The APD is based on a reach-through diode [12] with a separate multiplication zone and a thick absorption region. The p epitaxial (p epi) layer is depleted by a high reverse voltage and forms the thick absorption region. The multiplication zone is built by the deep p well below the highly doped n+ layer. The n+ at the surface of the wafer forms the cathode. The deep p well has a smaller diameter than the n+ layer and it is additionally embedded into a deep n well to avoid edge breakdown. This deep n well reduces also the effective p doping of the deep p well and of the p epi layer

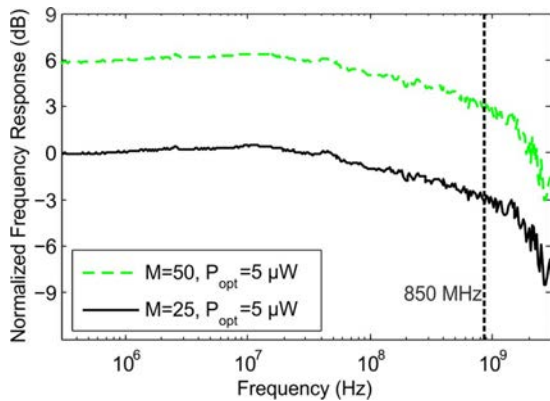


Fig. 3. Normalized frequency response of the APD at two different gain values (M) at 670 nm.

and facilitates the deep penetration of the depletion region into the p epi layer before breakdown. Consequently, the speed of the PD is enhanced by minimizing the diffusion portion of the photocurrent. The p+ substrate builds the anode of the APD. To lower the series resistance through the p epi, the substrate is connected via large-area p+, p well, and deep p well contacts. An antireflection coating (available within a modular process family from an OPTO ASIC process) is used as top layer above the n+ layer to improve the responsivity. The APD has an active diameter (deep p well) of $196 \mu\text{m}$. At a reverse voltage of approximately -65 V , the simulation resulted into an APD's capacitance of 0.57 pF . The unamplified responsivity at a wavelength of 670 nm was measured with 0.41 A/W at a reverse voltage of -0.4 V . Between 600 and 800 nm , the responsivity shows an almost flat shape [19]. At -65 V , a responsivity at approximately 30 A/W was measured, which corresponds to a gain of around 70 .

The breakdown voltage was measured at about -68.25 V corresponding to a dark current of $1 \mu\text{A}$. Fig. 3 shows the normalized frequency response at two different gain values. The curves were normalized with respect to responsivity and showed a -3 dB bandwidth of 850 MHz . For gain values up to 50 , the bandwidth is mainly determined by the transit time of photo-generated carriers through the intrinsic zone. For higher gain values, the avalanche build-up time influences the bandwidth significantly; see Fig. 4.

B. PN Photodiode

The center APD is surrounded by four pn-PDs. The structure is quite similar to the APD except the deep p well and the deep n well are missing below the n+ zone, see Fig. 5. To avoid edge breakdown, a deep n well is implemented at the edges of the n+ zone. Based on this structure, the pn-PD showed a breakdown voltage of more than -180 V [20]. This high breakdown voltage facilitates the design of the geometrical form of surrounding PDs. Compared with the round-shaped APD, the surrounding PDs have some 90 degree corners. Assuming that the surrounding PDs are realized as APDs, these corners can cause a premature breakdown due to increased electrical field strength. This

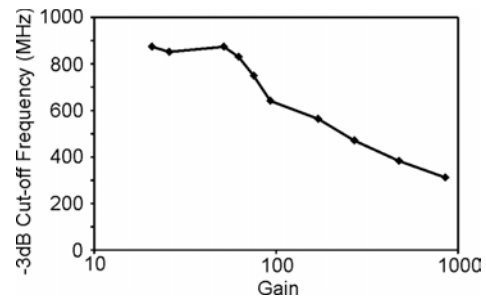


Fig. 4. Gain vs. bandwidth for the APD at $25 \text{ }^\circ\text{C}$, measured with a 675 nm light source.

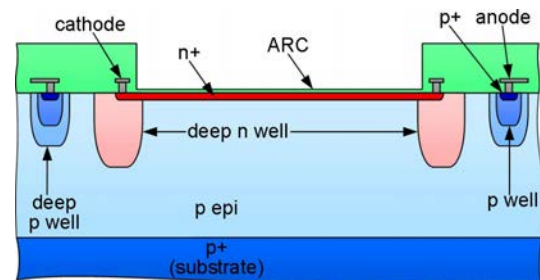


Fig. 5. Cross section of the pn photodiode (not to scale). The diameter of the pn-PD used for characterization was $86 \mu\text{m}$. The surrounding pn-PDs in Fig. 1 had a radial dimension of $96 \mu\text{m}$. The diameter in the pn-PD-HS-RX is $196 \mu\text{m}$.

premature breakdown can limit the voltage range applied to the center APD limiting the available gain values. Not to jeopardize the main goal of a well-working high-speed receiver with an APD, the surrounding PDs were realized with the inferior pn-PDs. The responsivity at a wavelength of 675 nm of the pn-PD was measured to be approx. 430 mA/W at -65 V . This measured responsivity is in the upper range of pn-PDs realized in deep-submicron structure size CMOS technologies. The reported responsivities range from approximately 4 mA/W to 560 mA/W at 850 nm [7]–[9], [21]–[23], [38] and from 250 mA/W to 540 mA/W at around 670 nm [27], [39], [40]. The outer diameter of the active area has a value of $453 \mu\text{m}$. Consequently, one pn-PD has approx. an area of $25600 \mu\text{m}^2$. For a circular-shaped pn-PD with a diameter of $86 \mu\text{m}$ (corresponding to an area of $5809 \mu\text{m}^2$) the capacitance was determined at approx. 0.12 pF at -65 V [20]. Therefore, the capacitance of one surrounding pn-PD element can be estimated with around 0.53 pF . The measured -3 dB cutoff frequency of the $86 \mu\text{m}$ diameter PD at -90 V reverse bias was 1.2 GHz ; see Fig. 6. At -65 V , its -3 dB cut-off frequency was 1.1 GHz . Due to the RC time constant ($R \leq 50 \Omega$ and pn-PD capacitance of 0.12 pF correspond to 24 GHz bandwidth), the limiting factor for this cutoff frequency is the carrier drift time in the space-charge region.

C. Comparison of APD and PN Photodiode

At -65 V substrate bias the p epi layer is completely depleted in APD and pn-photodiodes. The bandwidth of these

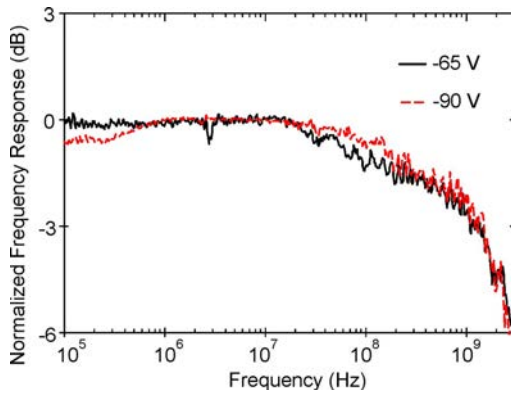


Fig. 6. Normalized frequency response of an 86 μm diameter pn-PD at 675 nm for -65 V and -90 V reverse bias voltage.

diodes depends on the electric field inside the pn-PD and APD. The electric field distribution is different in both photodiodes because of the different doping levels below the n+ region. Due to the deep p well leading to a high electric field strength at the n+/deep p well junction to obtain avalanche multiplication, the electric field strength in the p epi absorption zone of the APD is smaller than in the p epi region of the pn-PD. Therefore, the carrier drift time in the absorption zone of the APD is longer than in the p epi absorption zone of the pn-PD. In addition, the APD shows an amplification build-up time also limiting the maximum bandwidth [24]; see Fig. 4. Because of these two issues, the pn-PD has a larger bandwidth than the APD, when both are operated with the same reverse bias voltage.

III. CIRCUIT DESIGN

As mentioned above, the complete fully monolithically integrated chip consists of two designs: 1) a high-speed receiver with a 200 μm diameter APD for a high-speed data communication and 2) a highly sensitive Diff-TIA with two pn-PDs surrounding the center APD. The Diff-TIA design is implemented two times into the complete chip; see Fig. 1.

A. High-Speed Receiver

A simplified block diagram of the HS-RX including the APD is depicted in Fig. 7. The first stage after the APD is built by a TIA. This main TIA produces a voltage V_{data} . This voltage corresponds to the photocurrent I_{PH} . We used a differential design which is based on the dummy TIA. Due to this differential design, the influence of common-mode noise like power supply noise and substrate noise is minimized. The dummy TIA has the same structure as the main TIA and it generates the voltage V_{avg} which is the average voltage of V_{data} . This is done with the help of a proportional integral controller built by an operational transconductance amplifier (OTA) and some resistors (R_1 , R_2) and capacitors (C_1 , C_2). The two voltages V_{data} and V_{avg} are the input signals for a differential limiting post-amplifier. This amplifier provides the necessary gain to increase the amplitude

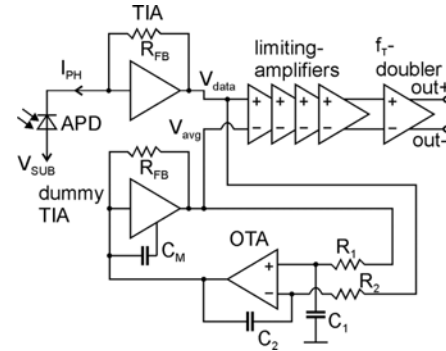


Fig. 7. Simplified block diagram of high-speed receiver.

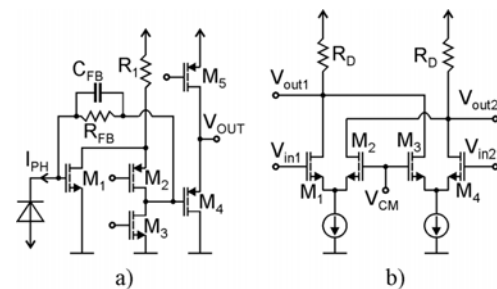


Fig. 8. Simplified circuit diagrams. (a) Folded cascode used as TIA. FB: feedback. (b) f_T -doubler used as output driver. CM: common mode.

of the signal and in the case of overload it clips the high and low bits symmetrically. An f_T -doubler stage builds the final output circuit.

The TIA's noise performance and bandwidth are significantly influenced by the input node capacitance. Concerning bandwidth, the first transistor contributes a high capacitance value to this input node due to the Miller capacitance of the first transistor. A cascode stage can avoid this multiplication. Therefore, we implemented a folded cascode circuit as TIA, such as that published earlier in [25] and [26]. The folded cascode has the advantage to work at low voltages or the drain-source saturation voltage of each transistor can be made larger compared to a normal cascode. This higher saturation voltage can be used to reduce the width-to-length ratio of each transistor, keeping the parasitic capacitances small as well.

Fig. 8(a) shows the simplified circuit diagram of the implemented folded cascode. The main gain is delivered by the input transistor M_1 which aspect ratio was chosen quite large to match with the PD capacitance for minimizing noise [13]. The large current needed by transistor M_1 is supplied via resistor R_1 . Postlayout circuit simulations showed that the solution with R_1 adds lower parasitic capacitance compared to a solution where the current source was realized with a p-channel MOSFET. M_3 and M_5 are current sources. The cascode stage is built by transistor M_2 . The output node of the cascode circuit (drain of M_2) shows high impedance. Therefore, a source follower (M_4) serves for impedance transformation. The feedback resistance R_{FB} has a value of 3.7 k Ω . Together with an attenuation to approximately 0.82 by the

source follower (M_4), the transimpedance V_{OUT}/I_{PH} results into a value of $3\text{ k}\Omega$. The compensation capacitor C_{FB} , in parallel to R_{FB} , has been added to reduce gain-peaking. The value of C_{FB} is 33 fF . During the design process, the parasitic capacitance of the APD was assumed to be 700 fF due to experience with PDs in a similar technology [27]. The simulated -3 dB cutoff frequency of the TIA resulted in approximately 731 MHz , and the TIA showed a simulated input-referred root mean square noise current of 135.6 nA . At a supply voltage of 3.3 V , the TIA consumed a current of 3 mA whereas the input transistor M_1 drew a current of roughly 2.3 mA .

In a fully differential design, the capacitance at the second input should correspond to the capacitance of the PD to get a smooth transfer function. But, having no measurement results of the photodiodes when the design was made and without detailed knowledge of the doping concentrations, the photodiode capacitance can be estimated based on experience with similar process technologies. A solution could be a shielded PD at the second input of a fully differential TIA, but at the costs of chip area and of an additional not-voltage-dependent capacitance due to the shielding metal plane. Especially with APDs, there is the uncertainty with a premature breakdown of the shielded APD before the normal APD reaches the appropriate operating point. This capacitance at the second input and the risk of premature breakdown can be avoided with a pseudo-differential structure with a dummy TIA.

The input-referred noise current of a fully differential circuit is $\sqrt{2}$ times larger than that of the single-ended counterpart. Since in the chosen pseudo-differential structure the capacitance C_M in the dummy TIA reduces the high-frequency part of the noise, the pseudo-differential structure has the potential to increase the input-referred noise by less than $\sqrt{2}$. The challenges with the implemented pseudo-differential structure, however, are the increased power consumption and not eliminated high-frequency power supply noise.

As mentioned above, the structure of the dummy TIA is the same as that of the main TIA except for an additional connection of a capacitance C_M . This capacitance is connected between the drain of transistor M'_1 (M'_1 corresponds to M_1 of the main TIA) and the gate of M'_1 . Hence, the Miller capacitance of the dummy TIA is increased resulting into a lower bandwidth of the dummy TIA. The lower bandwidth reduces the noise contribution of the dummy TIA. However, as mentioned above, the different transfer functions of main and dummy TIA results into a slight asymmetry with respect to the effect of supply noise reduction.

A 2-stage Miller amplifier builds the base for the OTA. Together with $R_1 = R_2 = 1\text{ M}\Omega$ and $C_1 = C_2 = 5.5\text{ pF}$, the OTA produces a current which is the average value of the photocurrent I_{PH} . Due to this control system, the low-frequency parts of the input signal, like background light, will be canceled out as long as the TIA works in the linear region. The OTA in PI-controller configuration leads to an excellent lower cut-off frequency of the pseudo-differential receiver of only 30 kHz , which allows very long sequences of "0" and "1".

The post-amplifier has a complete gain of 34.9 dB and is built of four stages. Each stage consists of a differential

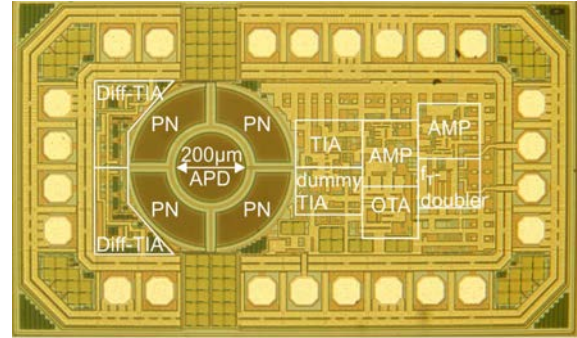


Fig. 9. Photomicrograph of the complete chip with a size of $1615\text{ }\mu\text{m} \times 965\text{ }\mu\text{m}$.

amplifier and a source-follower stage for impedance transformation and level shifting.

To drive an off-chip load of $50\text{ }\Omega$, the transistors of the output stage are quite large resulting into large parasitic capacitances. This leads to a limited bandwidth of the final stage. To minimize the effect of these large parasitic capacitances, the f_T -doubler circuit concept can be applied [28]. Shown in Fig. 8(b), the input capacitance is roughly the half of the gate-source capacitance C_{GS1} of M_1 (because of a series connection of C_{GS1} and C_{GS2}). The f_T -doubler stage delivers a differential voltage swing of 0.7 V into $50\text{ }\Omega$.

The -3 dB cutoff frequency of the complete HS-RX was measured to be 500 MHz [17] and the differential transimpedance of the HS-RX has a value of $161\text{ k}\Omega$. The equivalent input rms noise current of the complete HS-RX was simulated to be 734 nA in a corresponding noise bandwidth of 626 MHz . This high input noise current originates from the not optimized noise performance of the OTA. An RC-filter at the output of the OTA and an additional resistor between this filter and the input of the dummy TIA would reduce the equivalent input noise current to 146 nA according to simulations. In addition, the sensitivity measurements were deteriorated because the limiting amplifiers showed an offset error at the output of a few tens of millivolts. A redesigned HS-RX therefore could achieve a larger OWC distance.

A photomicrograph of the complete chip is shown in Fig. 9. At a supply voltage of 3.3 V , the whole chip consumes a current of 39 mA of which the f_T -doubler needs more than 17 mA and the four-stage limiting amplifier consumes about 15 mA .

B. Differential Highly Sensitive TIAs

As mentioned above, the APD is situated in the center of four circular segment pn-PDs. These pn-PDs are used to place the laser beam optimally on the APD by sensing the difference between opposite directions. To ensure the functionality despite strong background light a current mirror topology with nonlinear feedback was used. The adjustment of the beam is done by a back channel [16].

As depicted in Fig. 10 the nonlinear differential TIA consists of a current mirror, operational amplifier (OPA) in inverting configuration and a nonlinear feedback. The input

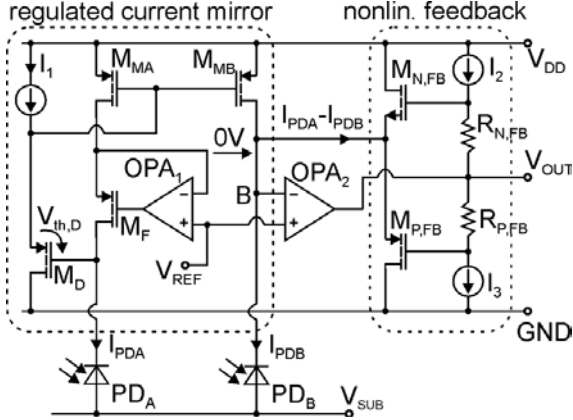


Fig. 10. Simplified circuit diagram of highly sensitive differential TIA.

transistors M_{MA} and M_{MB} are designed in an 8-fold common centroid layout to minimize mismatch of these current mirror transistors. The photocurrent of PD_A is mirrored towards the cathode of PD_B (note that these two photodiodes are arranged opposite in the PD array) and therefore into node B. The difference of the photocurrents flows into the nonlinear feedback which forms a regulation loop with OPA_2 .

The nonlinear feedback circuit is realized as a push-pull stage with the MOSFETs $M_{N,FB}$ and $M_{P,FB}$. The two transistors operate in the subthreshold region showing an exponential behavior. The constant current sources I_2 and I_3 ($I_2 = I_3$) together with the resistors $R_{N,FB}$ and $R_{P,FB}$ are used to set the quiescent current which gives the initial working point for the feedback transistors and thus the initial value of the feedback. The initial working point is present when the output voltage V_{OUT} is equal to the voltage at node B ($V_{(B)}$) and $I_{PDA} - I_{PDB} = 0$. When $V_{OUT} > V_{(B)}$, the gate-source voltage of $M_{N,FB}$ increases what results in a higher current of $M_{N,FB}$. In contrast, the gate-source voltage as well as the current of $M_{P,FB}$ decreases. As a consequence, a current I_{FB} flows into the node B. Under consideration of the exponential subthreshold characteristics [29] the feedback current for voltages $V_{OUT} > V_{(B)}$ is given by

$$\begin{aligned} I_{FB} &= I_{PDA} - I_{PDB} \\ &= I_{0,PMOS} \cdot \exp\left(\frac{V_{GS0,PMOS} - (V_{OUT} - V_{(B)})}{n \cdot V_T}\right) \\ &\quad - I_{0,NMOS} \cdot \exp\left(\frac{V_{GS0,NMOS} + (V_{OUT} - V_{(B)})}{n \cdot V_T}\right). \end{aligned} \quad (1)$$

There V_T is the thermal voltage (kT/q) and n is the nonideality factor. $V_{GS0,NMOS}$ and $V_{GS0,PMOS}$ are the gate-source voltages of the feedback MOSFETs which refer to the quiescent operating point. Their sum is defined by

$$V_{GS0,NMOS} + V_{GS0,PMOS} = I_2 \cdot (R_{N,FB} + R_{P,FB}). \quad (2)$$

For voltages $V_{OUT} < V_{(B)}$, the conditions are reversed. When the voltage difference $|V_{OUT} - V_{(B)}|$ is sufficiently large, the decreasing current part can be neglected and the transfer characteristic can be considered as exponential. Due to the regulation of OPA_2 , a logarithmic function is achieved.

Since the desired output is single-ended, the positive input of the inverting amplifier is supplied with a reference voltage V_{REF} . V_{REF} is on chip generated (not depicted in the figure) to be half of the supply voltage. Consequently, the voltage of node B is fixed to V_{REF} . To overcome systematic deviations due to different drain-source voltages of the current mirror M_{MA} and M_{MB} , the drain voltage of M_{MA} is regulated to the same V_{REF} as the one of M_{MB} .

Therefore, the control loop formed by the operational amplifier OPA_1 and the transistor M_F is inserted. Since OPA_1 consists of only a differential stage driving an active load (also called simple CMOS OTA) and M_F operates as a source follower, no stability issues arise.

The gates of the current mirror transistors M_{MA} and M_{MB} are connected to the photodiode PD_A via the transistor M_D . This ensures the delivery of the photocurrent I_{PDA} for a wide common-mode range. The voltage drop $V_{th,D}$, increases the voltage drop via M_F compared with a configuration without M_D which allows a wider control range of the gate voltage of M_F .

The fact that the drain voltages of M_{MA} and M_{MB} are exactly controlled, a precise differential current $I_{PDA} - I_{PDB}$ can be provided in a wide common-mode range, which is mandatory for the operation with various background light conditions. A dynamic range of more than 10^7 from pA to several tens of μA is achieved.

IV. OEIC CHARACTERISTICS

Here, the main characteristics of the HS-RX and the Diff-TIA are shown. For the HS-RX, sensitivity measurements are presented. The DC-sensitivity and the bandwidth measurement are given for the Diff-TIA.

A. Sensitivity Measurements of HS-RX

One key characteristic of any optical receiver is its sensitivity, the minimum signal level needed to achieve a given bit error rate (BER). For measuring the sensitivity, we used a vertical-cavity surface-emitting laser (VCSEL) with a wavelength of 675 nm. The VCSEL was directly modulated via a bit pattern generator with a pseudorandom binary sequence (PRBS) of $2^{31}-1$. The laser signal was coupled into a multimode fiber (50 μm core diameter) and guided with this fiber to the APD. To control the optical input power at the APD, we used a manual optical attenuator between the VCSEL and the APD and controlled the output power at the end of the fiber with an optical power meter (OPHIR NOVA PD300). The outputs of the OEIC were connected to a bit error analyzer. The results of these sensitivity measurements at different data rates are shown in Fig. 11. To evaluate the advantage of the APD, we built a version of the HS-RX where the APD has been replaced by a pn-PD having a diameter of 196 μm . The sensitivity measurements of this HS-RX with pn-PD are also included in Fig. 11. For the HS-RX with APD the following sensitivities have been measured: -33.6 dBm at a data rate of 622 Mbit/s, -31.8 dBm at 1 Gbit/s and -28.3 dBm at 1.25 Gbit/s. The HS-RX with pn-PD showed the following sensitivities: -19.5 dBm at a data rate of 622 Mbit/s, -18.7 dBm at 1 Gbit/s and

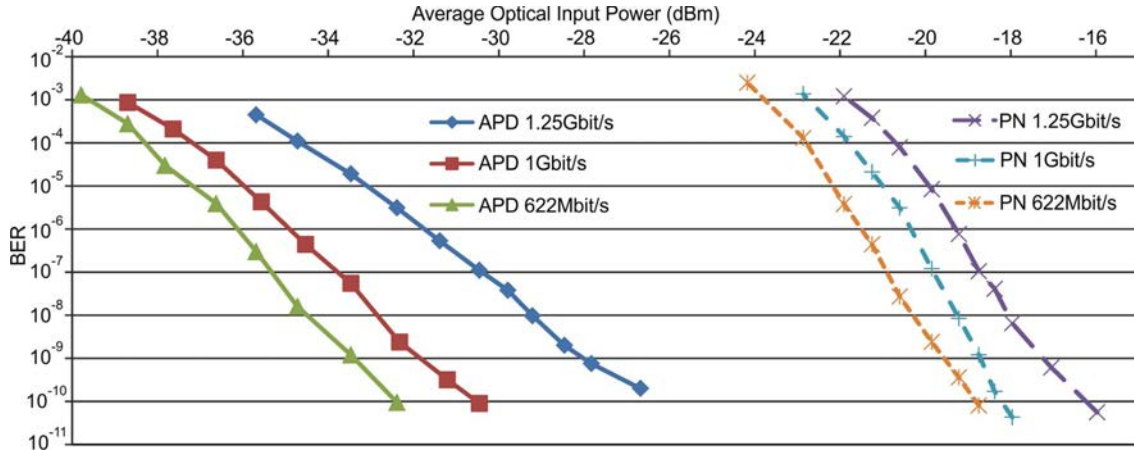


Fig. 11. Sensitivity of two versions of the high-speed receiver, one with an integrated APD ($C_{APD} = 0.57$ pF) and one with an integrated pn-PD ($C_{pn} = 0.62$ pF) at different data rates, $2^{31}-1$ PRBS, $\lambda = 675$ nm.

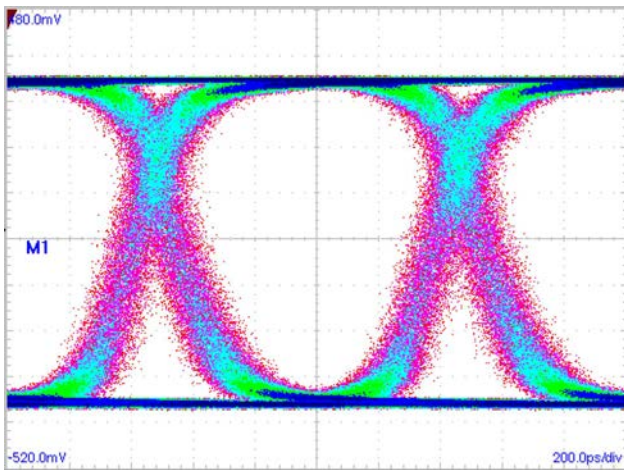


Fig. 12. Measured eye diagram at a data rate of 1 Gbit/s and an average optical input power of -31 dBm, BER of 10^{-9} , $\lambda = 675$ nm, 200 ps/div, 100 mv/div.

-17.2 dBm at 1.25 Gbit/s. Corresponding to these numbers, the improvement by the APD can be calculated: 14 dB at a data rate of 622 Mbit/s, 13 dB at 1 Gbit/s and at least 11.1 dB at 1.25 Gbit/s. These results clearly favor the use of an APD as optical detector. At a data rate of 1.25 Gbit/s, the bandwidth of the receiver is too narrow resulting in intersymbol interference and therefore reducing the performance. Fig. 12 shows the measured eye diagram for a data rate of 1 Gbit/s and a received average optical power of -31 dBm at a BER of below 10^{-9} (BER determined with a bit-error analyzer). As mentioned above, a shifted eye crossing can be observed due to an offset of the limiting amplifiers.

B. DC Response and Bandwidth of Diff-TIA

The challenge when measuring the DC response of the Diff-TIA was to bring a small focused nonmodulated laser spot on a single pn-PD and not on more pn-PDs simultaneously. In order to do this, we used a microscope to focus the laser beam accordingly. At the same time, we used the microscope for adjusting and placing of the laser spot on one of the surrounding pn-PD. The light from a 675 nm

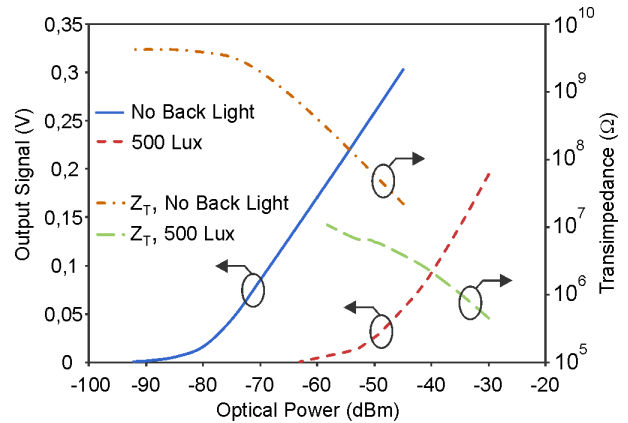


Fig. 13. DC response and resulting transimpedance (Z_T) of the differential TIA depending on differential laser power without background light and with 500 lux illumination.

VCSEL was brought via a multimode fiber to the camera adapter of the microscope. As mentioned above, a manual optical attenuator was placed in between for controlling the optical power. To measure the optical power, the above mentioned power meter was placed below the microscope instead of the receiver. To measure the DC output signal of the corresponding Diff-TIA, we used a digital multimeter (Keithley 2000). The result of this measurement is shown in Fig. 13. We were able to detect a difference in continuous optical power of approx. -90 dBm with the Diff-TIA circuitry when no background light was influencing the detector. In case of background illuminance of 500 lux, the minimum differential detectable signal power was approx. -60 dBm. A normal illuminated office corresponds to 500 lux, this value approximates to an irradiance of $73.2 \mu\text{W}/\text{cm}^2$ in case of light with a wavelength of 555 nm. Of course, the actual irradiance is lower because we used white light. With the complete area of 2 pn-PDs of $51600 \mu\text{m}^2$ which are connected to one Diff-TIA, this irradiance would correspond to a maximum received power of -44.2 dBm. The resulting DC photocurrent from the background irradiance produces an offset current which shifts the Diff-TIA's operating point. At the same time,

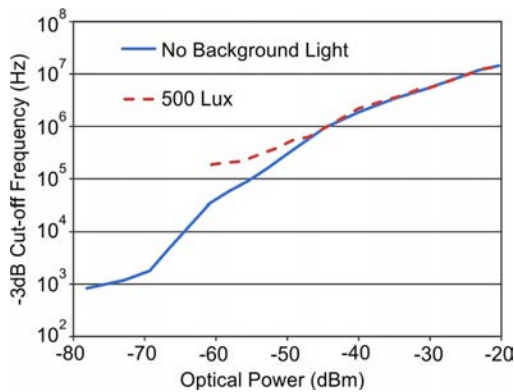


Fig. 14. Bandwidth of the Diff-TIA depending on differential laser power without background light and with 500 lux illumination.

this offset current reduces the nonlinear feedback resistance resulting into a lower responsiveness; see Fig. 13.

With the pn-PD's responsivity of 0.43 A/W at a wavelength of 675 nm and the measured received laser power and output voltage, the overall transimpedance of the Diff-TIA can be calculated. The results are included in Fig. 13. The transimpedance varies in a range from approx. 5 G Ω down to 400 k Ω .

For frequency measurements we used a network analyzer (Agilent 4395A) to modulate the 675 nm VCSEL via a bias-T. Once again, the laser signal was focused on one pn-PD and the second PD of the Diff-TIA received only light from the background illumination. Fig. 14 shows the measured -3 dB cutoff frequency of the Diff-TIA depending on the laser power impinging on one pn-PD. This measurement was performed under two background light conditions. In the case of 500 lux background illumination, the cutoff frequency was measured to be in a range from 180 kHz up to 14 MHz depending on the laser power impinging on the one pn-PD. Without background light, the bandwidth of the Diff-TIA ranges from about 900 Hz to 14 MHz (and for -60 dBm signal power the bandwidth is about 40 kHz); see Fig. 14.

The responsiveness of -60 dBm and the available bandwidth of approximately 180 kHz of the Diff-TIA facilitate the detection of the impinging laser ray under background light condition (with 500 lux). This makes the Diff-TIA well suited for scenarios in a normally illuminated office.

V. WIRELESS COMMUNICATION EXPERIMENTS

We used the experiment setup shown in Fig. 1 to test the OEIC in an optical wireless communication scenario. The setup was installed in our laboratory with normal lighting (500 lux). A 680 nm wavelength VCSEL was used as transmitter with an output power of 810 μ W. In contrast to [16], an adjustable collimating lens was used to focus the laser beam. The superior focusing serves for a smaller laser spot in a wider distance. At a distance of approximately 7 m, the laser spot has a diameter of around 6 mm corresponding to a divergence angle of roughly 0.05 degrees [full-width at half-maximum (FWHM)] whereas in [16] the beam's divergence angle had a value of 0.15 degrees (FWHM). For steering the laser ray, a MEMS-based mirror was used [16]. A bit pattern generator modulated the VCSEL with a $2^{31}-1$ PRBS

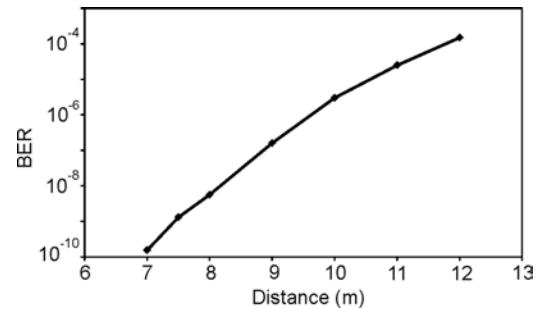


Fig. 15. BER versus distance between transmitter and receiver at 1 Gbit/s.

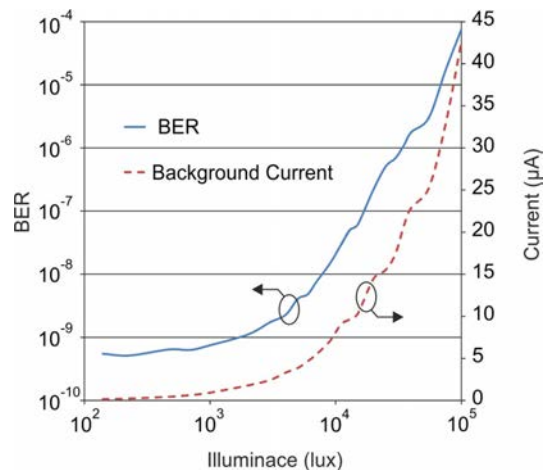


Fig. 16. Measured BER (1 Gbit/s) of the HS-RX under different background illuminance for a transmission distance of 3 m [18]. The resulting PD current caused by the background illumination is shown in the second curve.

with a data rate of 1 Gbit/s. The modulation was simple on-off keying and the extinction ratio was set to 7. The OEIC was glued and bonded on a printed circuit board, and the outputs of the HS-RX were connected to a bit-error analyzer. The substrate voltage of the OEIC was set to approximately -65.5 V. Fig. 15 depicts the measured BER versus distance between transmitter and receiver. The HS-RX was able to deliver 1 Gbit/s over a distance of more than 7.3 m with a BER below 10^{-9} . These measurements were performed without any optics at the receiver side. Compared with our previously published result [16], we extended the distance by a factor of 2.2 by improving the laser beam's divergence angle at the transmitter side.

For determining the behavior under different background light conditions, we placed the transmitter at a distance of approximately 7 m resulting in a BER below 10^{-9} . An adjustable cold light source (Euromex LE.5210) was used to simulate different background light conditions at the receiver side. To save measuring time, we only measured the BER at three different points (500, 2000, and 10000 lux). The obtained values were compared with some previous measurements and the OEIC showed the same behavior as published earlier [18]; see Fig. 16. This is a matter of fact because the obtained BER depends only on the signal and background irradiance in front of the receiver for this experiment. Fig. 16 shows the BER for a distance of 3 m between transmitter and receiver but with a more divergent laser ray.

TABLE I
PERFORMANCE COMPARISON WITH PUBLISHED OEICs

Ref.	Data Rate	PD Area	Sensitivity	BER	Technology	λ	Chip Size	Power
	Gbit/s	μm^2	dBm			nm	mm^2	mW
[31]	0.622	2346	-31.6	10^{-9}	n-type SOI †	850	NA	37
[6]	2	2500	-19	10^{-9}	0.13 μm SOI CMOS	850	0.6×0.8	31
[32]	2.5	74558	-20.1	10^{-9}	0.6 μm BiCMOS	660	0.87×0.89	170
[33]	3	2500	-19	10^{-11}	0.18 μm CMOS	850	0.38×0.54‡	50
[34]	0.3	207106	-24.3	10^{-9}	0.6 μm BiCMOS	850	1.49×1.93	27
[35]	2.5	2500	-4.5	10^{-12}	0.18 μm CMOS	850	0.62×0.86	138
[36]	0.125	74558	-35	10^{-9}	0.6 μm BiCMOS	675	0.4×0.5	66
[37]	1.25	132548	-23	10^{-9}	0.5 μm BiCMOS	660	1.55×0.92‡	85
[38]	4.5	2982	-3.8	10^{-12}	0.13 μm CMOS	850	1.5×1.18	74
[39]	0.6	785398	-10	10^{-12}	0.18 μm CMOS	660	2.4×1.5	40
[21]	5	5625	-3	10^{-12}	0.18 μm CMOS	850	0.86×0.84	183
[22]	8.5	4900	-3.2	10^{-12}	0.13 μm CMOS	850	1.46×0.07	47
[23]	10	2506	-6	10^{-11}	0.18 μm CMOS	850	0.95×0.8	145
[40]	3.125	62500	-3.8	10^{-12}	65 nm CMOS	670	0.27	50
[41]	1.25	132548	-19.6	10^{-9}	0.6 μm BiCMOS	660	1.44×0.91	100
[42]	3	33113	-23.4	10^{-9}	0.35 BiCMOS	675	1.44×0.89	237
[43]	4	62500	-3.2	10^{-12}	65 nm CMOS	670	0.24	46
[11]	0.1	51471	-31.7	10^{-9}	0.13 μm CMOS	450	0.24×0.21	190
[10]	2.4	8284	-22	10^{-11}	0.35 μm CMOS	800	1×0.7	16
This work	1	31416	-31.8	10^{-9}	0.35 μm HV CMOS	675	1.615×0.965	129

† structure size not stated. ‡ estimated from microphotograph.

This curve is also valid for the used laser here with a less divergent ray. Therefore, the distance between transmitter and receiver can be increased, resulting in the same irradiance levels. The HS-RX can guarantee a BER below 10^{-9} up to an illuminance of 2000 lux. The corresponding photocurrent from the background light is also shown in Fig. 16. This DC current resulting from the background illumination is the main reason for additionally produced shot noise increasing the BER [13]; see Fig. 16.

VI. COMPARISON OF FULLY INTEGRATED OPTICAL RECEIVERS

A fair comparison of different fully integrated optical receivers is not easy, especially in the case of wireless receivers. Many parameters influence the performance of an optical receiver with its photodiode. From a system point of view, the optical receiver sensitivity is one of the most important parameters. The optical receiver sensitivity is defined as the minimum optical input power, averaged over time, needed to achieve a specified BER [30]. The total input-referred receiver noise, the detector noise, and the detector responsivity affect the optical sensitivity.

The responsivity is influenced by the used wavelength and the quantum efficiency which is a measure of how effective photons generate electron-hole pairs inside the photodiode.

The detector noise, for detectors based on photodiodes, is represented in the form of shot noise produced in the pn-junction. For pn and pin (p-doped intrinsic n-doped) photodiodes, the shot noise has little impact on the optical sensitivity. For APDs, the noise is more significant because the shot noise also gets amplified by the multiplication. The APD provides even more noise than simply the

amplified shot noise due to the random nature of the gain process.

The input-referred noise current spectrum of a TIA has two major components: the noise from the feedback resistor and the noise from the amplifier front-end, the first transistor stage. The value of the feedback resistor is mainly influenced by the input node capacitance. Feedback resistor and input node capacitance affect the bandwidth of the TIA and consequently the equivalent noise bandwidth. The input capacitance is influenced by the PD's capacitance which depends on the area of the PD. The sensitivity in most publications was measured with a fiber (50 μm or 6–9 μm core diameter) where the influence of the area has little impact. Especially in OWC applications, the PD's receiving area has a crucial influence in contrast to fiber systems. In OWC systems the light spot's diameter (up to almost 1 cm) is much larger than the diameter of the PD resulting into a certain irradiance (W/m^2) at the receiver. A large PD area can collect more of the impinging irradiance resulting into a higher signal current. Therefore, the PD area of an OWC receiver should be an important parameter when comparing different receivers. Fiber receivers were often compared by using a figure of merit (FOM) considering also the feature size of the used technology. However, for the application data rate and sensitivity are much more important than the feature size of the receiver. In fact, FOMs where the feature size is in the denominator are somewhat misleading especially when the development, mask, and chip costs of low-volume ASICs in nanometer-size technologies are considered. Up to now, no fair FOM has yet been defined in the literature, especially in case of receivers for OWC.

When specifying sensitivity, this must be done with respect to a reference BER. All of these parameters result into a

specific sensitivity S of a particular receiver at a certain data rate, wavelength, BER, and area of the PD.

In Table I, the HS-RX is compared with PD/APD receivers with rather large-area photodiodes (at least an area of approximately $2500 \mu\text{m}^2$ which corresponds to a quadratic shape photodiode with a side length of $50 \mu\text{m}$) published within the past 15 years. We consider receivers with integrated PDs in CMOS, BiCMOS, and CMOS SOI technology, respectively. The minimum structure sizes of these technologies are from $0.6 \mu\text{m}$ down to 65 nm . The influence of different PRBS sequences on the sensitivity has been omitted due to often not available data. The nearest results are from $0.5 \mu\text{m}$ and $0.6 \mu\text{m}$ BiCMOS implementations using pin photodiodes. They profit from the available bipolar transistors with their higher transconductance (g_m) compared with MOS transistors. This allows for higher PD capacitance, higher gain, and bandwidth. The receivers produced in technologies with smaller structure sizes suffer from the low responsivity values of the shallow implemented pn-PDs. As mentioned in Section II, the downscaling of CMOS technology and the related increased doping concentration is to the disadvantage of the responsivity.

VII. CONCLUSION

Future optical communication systems for indoor data distribution will benefit from cheap and robust fully integrated receiver solutions. To that end, we presented a highly sensitive receiver with a large-diameter APD. The large diameter makes the receiver attractive for optical wireless communication or for systems with cheap POF as transport media. The complete OEIC was implemented in a standard $0.35 \mu\text{m}$ HV CMOS technology. The advantage of this technology for realizing a highly effective APD with a higher responsivity compared with technologies with smaller minimum structure size was presented. Together with the implemented high-speed circuitry, a 1 Gbit/s data rate with a sensitivity of -31.8 dBm at a BER $< 10^{-9}$ has been reached. Although the technology used is not dedicated to high-frequency applications, we report for the first time on such a high-data-rate transmission over a distance of more than 7 m without any optical components at the receiver using this monolithically integrated receiver in silicon with a sensitivity of -31.8 dBm . Possibilities for a redesign to reduce the equivalent input noise current of the HS-RX are included which will enable a further increase in transmission distance. The additional photodiodes and differential TIAs facilitate the alignment procedure in a notable way. The reliability of the OEIC under strong background irradiance has been confirmed which is especially important for wireless applications.

REFERENCES

- [1] A. M. J. Koonen and E. Tangdionga, "Photonic home area networks," *J. Lightw. Technol.*, vol. 32, no. 4, pp. 591–604, Feb. 2014.
- [2] P802.15.7—IEEE Standard for Short-Range Wireless Optical Communication, C/LM-LAN/MAN Standards Committee Std., Rev. P802.15.7, Oct. 2015.
- [3] D. C. O'Brien, "High speed infrared optical wireless for home access networks," in *Proc. SPIE Broadband Access Commun. Technol.*, San Francisco, CA, USA, Feb. 2014.
- [4] O. Ziemann, S. Loquai, J. Vinogradov, and R. Kruglov, "The 1 gigabit over 1 mm POF story — From vision to standard," in *Proc. IEEE 36th ECOC*, Torino, Italy, Sep. 2010, pp. 1–22.
- [5] A. M. Moloney *et al.*, "Monolithically integrated avalanche photodiode and transimpedance amplifier in a hybrid bulk/SOI CMOS process," *Electron. Lett.*, vol. 39, no. 4, pp. 391–392, Feb. 2003.
- [6] S. M. Csutak, J. D. Schaub, S. Wang, J. Mogab, and J. C. Campbell, "Integrated silicon optical receiver with avalanche photodiode," *Proc. Inst. Electr. Eng.—Optoelectron.*, vol. 150, no. 3, pp. 235–237, Jun. 2003.
- [7] J.-S. Youn, M.-J. Lee, K.-Y. Park, H. Rucker, and W. Choi, "An integrated 12.5-Gb/s optoelectronic receiver with a silicon avalanche photodetector in standard SiGe BiCMOS technology," *Opt. Exp.*, vol. 20, no. 27, pp. 28153–28162, Dec. 2012.
- [8] J.-S. Youn, M.-J. Lee, K.-Y. Park, and W.-Y. Choi, "10-Gb/s 850-nm CMOS OEIC receiver with a silicon avalanche photodetector," *IEEE J. Quantum Electron.*, vol. 48, no. 2, pp. 229–236, Feb. 2012.
- [9] H.-Y. Jung, J.-M. Lee, and W.-Y. Choi, "A high-speed CMOS integrated optical receiver with an under-damped TIA," *IEEE Photon. Technol. Lett.*, vol. 27, no. 13, pp. 1367–1370, Jul. 2015.
- [10] E. Kamrani, F. Lesage, and M. Sawan, "Low-noise, high-gain transimpedance amplifier integrated with SiAPD for low-intensity near-infrared light detection," *IEEE Sensors J.*, vol. 14, no. 1, pp. 258–269, Jan. 2014.
- [11] E. Fisher, I. Underwood, and R. Henderson, "A reconfigurable single-photon-counting integrating receiver for optical communications," *IEEE J. Solid-State Circuits*, vol. 48, no. 7, pp. 1638–1650, Jul. 2013.
- [12] P. P. Webb, R. J. McIntyre, and J. Conradi, "Properties of avalanche photodiodes," *RCA Rev.*, vol. 35, pp. 234–278, Jun. 1974.
- [13] R. G. Smith and S. D. Personick, "Receiver design for optical fiber communication systems," in *Semiconductor Devices for Optical Communication*, H. Kressel, Ed., 2nd ed. New York, NY, USA: Springer, 1982, pp. 89–160.
- [14] S. M. Sze and W. K. Ng, "Photodetectors and solar cells," in *Physics of Semiconductor Devices*, 3rd ed. Hoboken, NJ, USA: Wiley, 2007, pp. 663–742.
- [15] Y. S. Kim, I. S. Jun, and K. H. Kim, "Design and characterization of CMOS avalanche photodiode with charge sensitive preamplifier," *IEEE Trans. Nucl. Sci.*, vol. 55, no. 3, pp. 1376–1380, Jun. 2008.
- [16] P. Brandl, R. Enne, T. Jukic, and H. Zimmermann, "OWC using a fully integrated optical receiver with large-diameter APD," *IEEE Photon. Technol. Lett.*, vol. 27, no. 5, pp. 482–485, Mar. 2015.
- [17] P. Brandl, R. Enne, T. Jukic, and H. Zimmermann, "Monolithically integrated optical receiver with large-area avalanche photodiode in high-voltage CMOS technology," *Electron. Lett.*, vol. 50, no. 21, pp. 1541–1543, Oct. 2014.
- [18] P. Brandl, R. Enne, and H. Zimmermann, "Optical wireless receiver circuit with integrated APD and high background-light immunity," in *Proc. 41st ESSCIRC*, Graz, Austria, Sep. 2015, pp. 48–51.
- [19] B. Steindl, R. Enne, S. Schidl, and H. Zimmermann, "Linear mode avalanche photodiode with high responsivity integrated in high-voltage CMOS," *IEEE Electron Device Lett.*, vol. 35, no. 9, pp. 897–899, Sep. 2014.
- [20] R. Enne, B. Steindl, K. Schneider-Hornstein, and H. Zimmermann, "Pn photodiode in $0.35 \mu\text{m}$ high-voltage CMOS with 1.2-GHz bandwidth," *SPIE Opt. Eng.*, vol. 53, no. 11, pp. 114–116, Nov. 2014.
- [21] T. S.-C. Kao, F. A. Musa, and A. Chan Carusone, "A 5-Gbit/s CMOS optical receiver with integrated spatially modulated light detector and equalization," *IEEE Trans. Circuits Syst. I, Reg. Papers*, vol. 57, no. 11, pp. 2844–2857, Nov. 2010.
- [22] D. Lee, J. Han, G. Han, and S. M. Park, "An 8.5-Gb/s fully integrated CMOS optoelectronic receiver using slope-detection adaptive equalizer," *IEEE J. Solid-State Circuits*, vol. 45, no. 12, pp. 2861–2873, Dec. 2010.
- [23] S.-H. Huang, W.-Z. Chen, Y.-W. Chang, and Y.-T. Huang, "A 10-Gb/s OEIC with meshed spatially-modulated photo detector in $0.18\text{-}\mu\text{m}$ CMOS technology," *IEEE J. Solid-State Circuits*, vol. 46, no. 5, pp. 1158–1169, May 2011.
- [24] B. Saleh and M. Teich, "Semiconductor photon detectors," in *Fundamentals of Photonics*. Hoboken, NJ, USA: Wiley, 2007, pp. 748–803.
- [25] N. Haralabidis, D. Loukas, K. Misiakos, and S. Katsafouros, "A transimpedance CMOS multichannel amplifier with a 50Ω -wide output range buffer for high counting rate applications," *IEEE J. Solid-State Circuits*, vol. 32, no. 1, pp. 135–138, Jan. 1997.

- [26] K. Schrodinger, J. Stimma, and M. Mauthe, "A fully integrated CMOS receiver front-end for optic Gigabit Ethernet," *IEEE J. Solid-State Circuits*, vol. 37, no. 7, pp. 874–880, Jul. 2002.
- [27] P. Brandl, S. Schidl, and H. Zimmermann, "PIN photodiode optoelectronic integrated receiver used for 3-Gb/s free-space optical communication," *IEEE J. Sel. Topics Quantum Electron.*, vol. 20, no. 6, pp. 391–400, Nov.–Dec. 2014.
- [28] S. Galal and B. Razavi, "10-Gb/s limiting amplifier and laser/modulator driver in 0.18- μ m CMOS technology," *IEEE J. Solid-State Circuits*, vol. 38, no. 12, pp. 2138–2146, Dec. 2003.
- [29] Y. Tsvividis, "The four-terminal MOS structure," in *Operation and Modelling of the MOS Transistor*, 2nd ed. New York, NY, USA: Oxford Univ., 1999, ch. 4, pp. 125–206.
- [30] E. Säckinger, "Receiver fundamentals," in *Broadband Circuits for Optical Fiber Communication*. Hoboken, NJ, USA: Wiley, 2005, pp. 45–104.
- [31] R. Li, J. D. Schaub, S. M. Csutak, and J. C. Campbell, "A high-speed monolithic silicon photoreceiver fabricated on SOI," *IEEE Photon. Technol. Lett.*, vol. 12, no. 8, pp. 1046–1048, Aug. 2000.
- [32] R. Swoboda and H. Zimmermann, "2.5 Gbit/s silicon receiver OEIC with large diameter photodiode," *Electron. Lett.*, vol. 40, no. 8, pp. 505–507, Apr. 2004.
- [33] S. Radovanovic, A.-J. Annema, and B. Nauta, "A 3-Gb/s optical detector in standard CMOS for 850-nm optical communication," *IEEE J. Solid-State Circuits*, vol. 40, no. 8, pp. 1706–1717, Aug. 2005.
- [34] M. Fortsch, H. Zimmermann, and H. Pless, "220-MHz monolithically integrated optical sensor with large-area integrated PIN photodiode," *IEEE Sensors J.*, vol. 6, no. 2, pp. 385–390, Apr. 2006.
- [35] W.-Z. Chen and S.-H. Huang, "A 2.5 Gbps CMOS fully integrated optical receiver with lateral PIN detector," in *Proc. IEEE CICC*, San Jose, CA, USA, Sep. 2007, pp. 293–296.
- [36] W. Gaberl and H. Zimmermann, "Integrated optical receiver for lens-less free-space communication," in *Proc. 34th IEEE ECOC*, Brussels, Belgium, 2008, pp. 1–2.
- [37] W. Gaberl, R. Swoboda, and H. Zimmermann, "Integrated optical receiver for lens-less short range free-space gigabit communication," in *Proc. 35th IEEE ECOC*, Vienna, Austria, 2009, pp. 1–2.
- [38] F. Tavernier and M. Steyaert, "High-speed optical receivers with integrated photodiode in 130 nm CMOS," *IEEE J. Solid-State Circuits*, vol. 44, no. 10, pp. 2856–2867, Oct. 2009.
- [39] F. Tavernier and M. Steyaert, "A high-speed POF receiver with 1 mm integrated photodiode in 180 nm CMOS," in *Proc. 36th IEEE ECOC*, Torino, Italy, 2010, pp. 1–3.
- [40] Y. Dong and K. W. Martin, "A high-speed fully-integrated POF receiver with large-area photo detectors in 65 nm CMOS," *IEEE J. Solid-State Circuits*, vol. 47, no. 9, pp. 2080–2092, Sep. 2012.
- [41] M. Atef, R. Swoboda, and H. Zimmermann, "1.25 Gbit/s over 50 m step-index plastic optical fiber using a fully integrated optical receiver with an integrated equalizer," *J. Lightw. Technol.*, vol. 30, no. 1, pp. 118–122, Jan. 2012.
- [42] P. Brandl and H. Zimmermann, "3 Gbit/s optical receiver IC with high sensitivity and large integrated pin photodiode," *Electron. Lett.*, vol. 49, no. 8, pp. 552–554, Apr. 2013.
- [43] Y. Dong and K. W. Martin, "A 4-Gbps POF receiver using linear equalizer with multi-shunt-shunt feedbacks in 65-nm CMOS," *IEEE Trans. Circuits Syst. II, Exp. Briefs*, vol. 60, no. 10, pp. 617–621, Oct. 2013.



Paul Brandl received the Dipl. Ing. degree in electrical engineering from Graz University of Technology, Graz, Austria, in 2006. He is currently working towards the Ph.D. degree at the Vienna University of Technology, Vienna, Austria.

From 2006 to 2008, he was with AT4wireless, Malaga, Spain, working within the physical layer group for developing testing devices for 3G and 4G mobile communication devices. From 2009 to 2010, he was with the Institute of Broadband Communication at Graz University of Technology, Austria, designing optical free space communication devices. He joined the Institute of Electrodynamics, Microwave and Circuit Engineering at Vienna University of Technology in 2010. His major field of interest is optoelectronic integrated circuits design and its application in optical wireless communication systems.



Tomislav Jukić received the Mag. Ing. degree in electrical engineering from Josip Juraj Strossmayer University, Osijek, Croatia, in 2014. He is currently working toward the Ph.D. degree at the Institute of Electrodynamics, Microwave and Circuit Engineering, Vienna University of Technology, Vienna, Austria.

His fields of interests are optoelectronics, analog CMOS and BiCMOS circuits, optical communication systems, and optoelectronic integrated circuit design.



Reinhard Enne received the Dipl. Ing. degree and Dr.techn. degree in electrical engineering from Vienna University of Technology, Vienna, Austria, in 2009 and 2012, respectively.

From 2009 to 2015, he was with the Institute of Electrodynamics Microwave and Circuit Engineering, Vienna University of Technology, Vienna, Austria, where he worked in the research field of CMOS compatible avalanche photodetectors, in the field of integrated power converters and electronic-photonics integration. Since 2015, he has been with Avago Technology Fiber Austria GmbH, Vienna, Austria.



Kerstin Schneider-Hornstein received the Dipl. Ing. and Dr.techn. degrees from the Vienna University of Technology, Vienna, Austria, in 2000 and 2004, respectively.

Since 2001, she has been with the Institute of Electrodynamics, Microwave and Circuit Engineering, Vienna University of Technology, Vienna, Austria. Her major fields of interest are optoelectronics and integrated circuit design. She is author of the book *Highly Sensitive Optical Receivers* (Springer, 2006).



Horst Zimmermann (M'98–SM'02) received the Dr.-Ing. degree from the Fraunhofer Institute for Integrated Circuits (IIS-B), Erlangen, Germany in 1991.

Then, he was an Alexander-von-Humboldt Research Fellow with Duke University, Durham, NC, USA, where he worked on diffusion in Si, GaAs, and InP. In 1993, he joined the Chair for Semiconductor Electronics at Kiel University, where he lectured optoelectronics and worked on optoelectronic integration. Since 2000, he has been a Full Professor of electronic circuit engineering with the Vienna University of Technology, Vienna, Austria. His main interests are in design and characterization of analog deep-sub-micron, nanometer CMOS and optoelectronic integrated (Bi)CMOS circuits as well as electronic-photonics integration. He is author of the books *Integrated Silicon Optoelectronics* (Springer, 2010) and *Silicon Optoelectronic Integrated Circuits* (Springer, 2004) as well as coauthor of *Highly Sensitive Optical Receivers* (Springer, 2006), *Optical Communication Over Plastic Optical Fibers: Integrated Optical Receiver Technology* (Springer, 2013), *Analog Filters in Nanometer CMOS* (Springer, 2014), *Comparators in Nanometer CMOS Technology* (Springer, 2015), and *Optoelectronic Circuits in Nanometer CMOS Technology* (Springer, 2016). Furthermore, he is the author and coauthor of more than 450 scientific publications.

3. Comparison and Conclusion

The main focus of this thesis was the design of monolithically integrated optical receiver chips with large-diameter photodiodes for use in indoor wireless optical communication systems. The large PDs relaxed the alignment procedure when establishing a wireless communication link. One receiver was realized in a $0.35\ \mu\text{m}$ BiCMOS process and included five pin-PDs. The other receiver was realized in a $0.35\ \mu\text{m}$ HV-CMOS process and included an APD and four pn-PDs. Both processes were provided by X-FAB Semiconductor Foundries AG. The BiCMOS process is based on a high-speed opto CMOS process extended by three additional layout layers to include the bipolar transistor. The HV-CMOS process is defined with respect to high performance and high voltage applications. Different wells with different doping concentrations were used to realize an APD structure with separated absorption and multiplication zones.

In both processes, a high-speed receiver circuit with a large-diameter PD was developed. These receivers served for communication and were built of the following blocks: (1) the PD for converting the optical signal into a current signal, (2) a transimpedance amplifier to transform the current into a voltage signal, (3) an additional TIA and an operational amplifier to generate a differential data signal out of the single-ended signal, (4) several differential amplifier blocks to boost the signal, and (5) an output driver. In the same chip, two times a highly sensitive differential TIA which was connected to two opposite situated PDs was implemented. Those PDs were placed around the central large PD. This setup allowed the detection of the laser spot's position impinging on the PDs. With this information, the laser ray was aligned via a feedback channel.

A detailed comparison of various parameters of OEICs for communication is shown in table 3.1. Fig. 3.1 depicts the compared OEICs according to their sensitivity and data rate. The red crosses mark the two receivers presented in this thesis, the blue circles are the remaining receivers from table 3.1. The pin-PD BiCMOS and the APD-HV-CMOS receiver are compared with OEICs with a PD area of at least

2500 μm^2 . The receivers were produced in different technologies with structure sizes from 0.6 μm down to 65 nm within the last 15 years. As stated in the IEEE JSSC 2016 paper, a fair comparison of fully integrated optical receivers is not easy, even in the case of wireless receivers. The main parameters are the sensitivity and the area of the photodiode. In contrast to fiber receivers, the PD's area is very important when designing OWC receivers. The sensitivity depends on the data rate, the BER, and the wavelength via the responsivity. The influence of the pseudorandom bit sequence (PRBS) on the sensitivity was omitted due to often not available data. With these variables a normalized sensitivity S_{norm} can be calculated:

$$S_{norm} = 10 \log_{10} \left[\left(10^{\frac{S}{10}} \right) \left(\frac{bitrate_{target}}{bitrate} \right) \left(\frac{BER_{target}}{BER} \right) \left(\frac{\lambda}{\lambda_{target}} \right) \left(\frac{area_{target}}{area} \right) \right]$$

where S is the sensitivity. The target bit rate was 1 Gbit/s and the target BER was 10^{-9} . The wavelength was normalized to the used 675 nm. The effective APD's area of 30172 μm^2 was used as target area. With this normalized sensitivity, a rough comparison of different OEICs could be done. Fig. 3.1 shows clearly the enhancement in speed and sensitivity which has been gained with both designed receivers, although the PDs' areas were even larger than the PDs' areas from most publications found in the comparison table 3.1.

In this thesis, also the advantages of a narrow laser beam with the possibility of steering the laser ray were explored. Therefore, a complete new transmitter was designed. A directly modulated VCSEL with a wavelength of 680 nm was applied as source. To steer and to get a certain coverage area, a mirror based on a MEMS was used to deviate the laser beam. The focus of the laser beam was influenced with a movable lens via an electromechanical system. A detailed measurement of the laser ray's expansion was conducted with the help of a camera. The developed transmitter allowed for a characterization of the receiver chips in a real wireless communication scenario. Several communication experiments were done to determine the influence of distance and angle between transmitter and receiver as well as the influence of background illumination on the receiver. The whole system allowed transmission of data rates of up to 3 Gbit/s to nearly 20 m in the case of the pin-PD OEIC version with a receiver lens. The APD-OEIC was able to establish a link over a distance of 7 m without the need of any receiving optics. Of course, optical wireless will not compete against RF communication technologies, but OWC can complement RF communication systems. Fully integrated optical receivers in cheap standard technologies can open the door for making OWC systems a cheap mass product.

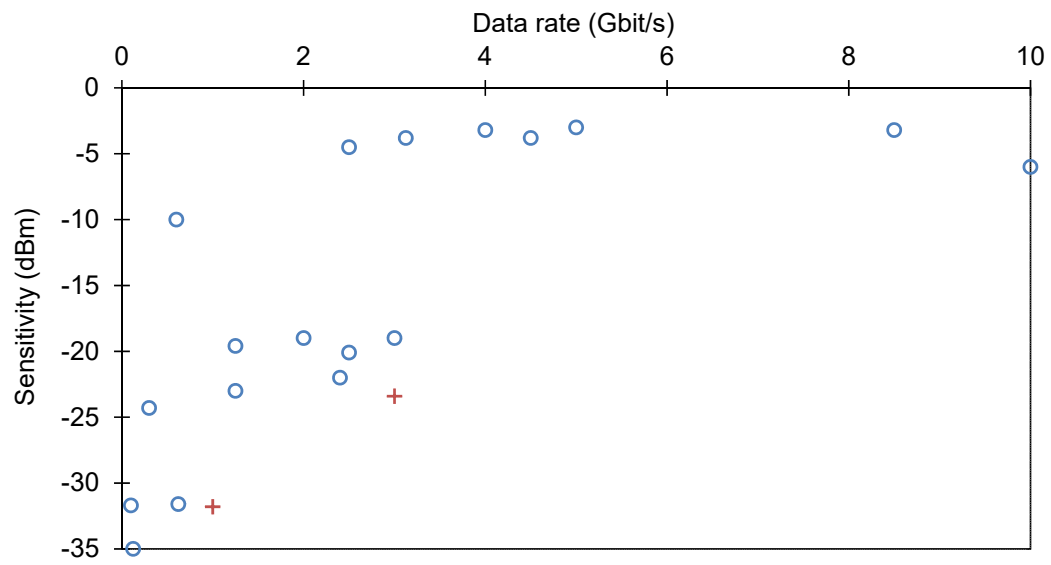


Figure 3.1.: Comparison of OEICs with large area PDs. The red crosses are the pin-PD OEIC and the APD-OEIC, respectively. The blue circles are the OEICs from table 3.1.

3. Comparison and Conclusion

Table 3.1.: Performance comparison of OEICs with large area PDs

Ref.	Data Rate	PD Area	S	BER	Technology	λ	Chip Size	Power Cons.	S_{norm}
	Gbit/s	μm^2	dBm			nm	mm^2	mW	dBm
[67]	0.622	2346	-31.6	10^{-9}	n-type SOI	850	NA	37	-17.44
[68]	2	2500	-19	10^{-9}	0.13 μm SOI CMOS	850	0.6×0.8	31	-10.19
[57]	2.5	74558	-20.1	10^{-9}	0.6 μm BiCMOS	660	0.87×0.89	170	-28.11
[69]	3	2500	-19	10^{-11}	0.18 μm CMOS	850	0.38×0.54	50	-12.82
[70]	0.3	207106	-24.3	10^{-9}	0.6 μm BiCMOS	850	1.49×1.93	27	-26.44
[71]	2.5	2500	-4.5	10^{-12}	0.18 μm CMOS	850	0.62×0.86	138	2.09
[46]	0.125	74558	-35	10^{-9}	0.6 μm BiCMOS	675	0.4×0.5	66	-29.9
[47]	1.25	132548	-23	10^{-9}	0.5 μm BiCMOS	660	1.55×0.92	85	-30.49
[72]	4.5	2982	-3.8	10^{-12}	0.13 μm CMOS	850	1.5×1.18	74	-0.53
[73]	0.6	785398	-10	10^{-12}	0.18 μm CMOS	660	2.4×1.5	40	-23.28
[74]	5	5625	-3	10^{-12}	0.18 μm CMOS	850	0.86×0.84	183	-2.94
[75]	8.5	4900	-3.2	10^{-12}	0.13 μm CMOS	850	1.46×0.07	47	-4.85
[76]	10	2506	-6	10^{-11}	0.18 μm CMOS	850	0.95×0.8	145	-5.06
[64]	3.125	62500	-3.8	10^{-12}	65 nm CMOS	670	0.27	50	-13.19
[63]	1.25	132548	-19.6	10^{-9}	0.6 μm BiCMOS	660	1.44×0.91	100	-27.09
[77]	4	62500	-3.2	10^{-12}	65 nm CMOS	670	0.24	46	-13.67
[66]	0.1	51471	-31.7	10^{-9}	0.13 μm CMOS	450	0.24×0.21	190	-25.78
[58]	2.4	8284	-22	10^{-11}	0.35 μm CMOS	800	1×0.7	16	-20.32
pin-OEIC	3	33113	-23.4	10^{-9}	0.35 μm BiCMOS	675	1.44×0.89	237	-28.58
APD-OEIC	1	30172	-31.8	10^{-9}	0.35 μm HV-CMOS	675	1.615×0.965	129	-31.8

Bibliography

- [1] A. M. J. Koonen and E. Tangdionga, "Photonic home area networks," *Journal of Lightwave Technology*, vol. 32, no. 4, pp. 591–604, Feb. 2014. DOI: [10.1109/JLT.2013.2283145](https://doi.org/10.1109/JLT.2013.2283145) (cit. on p. 1).
- [2] R. Ramirez-Iniguez, S. M. Idrus, and Z. Sun, *Optical Wireless Communications, IR for wireless connectivity*. Auerbach Publications, Taylor & Francis Group, Boca Raton, FL, 2008, ISBN: 978-0-8493-7209-4. DOI: [10.1201/9781420013443](https://doi.org/10.1201/9781420013443) (cit. on pp. 1, 9).
- [3] IEC Standard 60825-1, *Safety of laser products - part 1: Equipment classification and requirements*, 2007 (cit. on p. 1).
- [4] A. G. Bell, "Upon the production and reproduction of sound by light," *Journal of the Society of Telegraph Engineers*, vol. 9, no. 34, pp. 404–426, 1880. DOI: [10.1049/jste-1.1880.0046](https://doi.org/10.1049/jste-1.1880.0046) (cit. on p. 3).
- [5] F. Gfeller and U. Bapst, "Wireless in-house data communication via diffuse infrared radiation," *Proceedings of the IEEE*, vol. 67, no. 11, pp. 1474–1486, Nov. 1979. DOI: [10.1109/PROC.1979.11508](https://doi.org/10.1109/PROC.1979.11508) (cit. on pp. 3, 5).
- [6] J. R. Barry, *Wireless infrared communications*. Norwell, Massachusetts USA: Kluwer Academic Publishers Group, 1994, ISBN: 0-7923-9476-3 (cit. on pp. 4, 7).
- [7] T.-S. Chu and M. Gans, "High speed infrared local wireless communication," *IEEE Communications Magazine*, vol. 25, no. 8, pp. 4–10, Aug. 1987. DOI: [10.1109/MCOM.1987.1093675](https://doi.org/10.1109/MCOM.1987.1093675) (cit. on p. 5).
- [8] J. Kahn and J. Barry, "Wireless infrared communications," *Proceedings of the IEEE*, vol. 85, no. 2, pp. 265–298, Feb. 1997. DOI: [10.1109/5.554222](https://doi.org/10.1109/5.554222) (cit. on pp. 5–7).
- [9] IrDA. (2016). Infrared Data Association, [Online]. Available: <http://www.irda.org/> (visited on 10/03/2016) (cit. on p. 5).

- [10] M. J. McCullagh and D. R. Wisely, "155 Mbit/s optical wireless link using a bootstrapped silicon apd receiver," *Electronics Letters*, vol. 30, no. 5, pp. 430–432, Mar. 1994. DOI: [10.1049/e1:19940308](https://doi.org/10.1049/e1:19940308) (cit. on p. 5).
- [11] J. Grubor, S. Randel, K. D. Langer, and J. W. Walewski, "Broadband information broadcasting using LED-based interior lighting," *Journal of Lightwave Technology*, vol. 26, no. 24, pp. 3883–3892, Dec. 2008. DOI: [10.1109/JLT.2008.928525](https://doi.org/10.1109/JLT.2008.928525) (cit. on p. 5).
- [12] VLCC. (2016). Visible Light Communications Consortium, [Online]. Available: <http://www.vlcc.net/> (visited on 10/29/2016) (cit. on p. 5).
- [13] IEEE Standards Association. (2011). P802.15.7—IEEE Standard for Short-Range Wireless Optical Communication, [Online]. Available: http://www.ieee802.org/15/pub/IEEE%20802_15%20WPAN%2015_7%20Revision1%20Task%20Group.htm (visited on 10/07/2016) (cit. on p. 5).
- [14] J. M. Kahn, R. You, P. Djahani, A. G. Weisbin, B. K. Teik, and A. Tang, "Imaging diversity receivers for high-speed infrared wireless communication," *IEEE Communications Magazine*, vol. 36, no. 12, pp. 88–94, Dec. 1998. DOI: [10.1109/35.735884](https://doi.org/10.1109/35.735884) (cit. on p. 6).
- [15] J. B. Carruther and J. M. Kahn, "Angle diversity for nondirected wireless infrared communication," *IEEE Transactions on Communications*, vol. 48, no. 6, pp. 960–969, Jun. 2000. DOI: [10.1109/26.848557](https://doi.org/10.1109/26.848557) (cit. on p. 6).
- [16] G. Yun and M. Kavehrad, "Indoor infrared wireless communications using spot diffusing and fly-eye receivers," *Canadian Journal of Electrical and Computer Engineering*, vol. 18, no. 4, pp. 151–157, Oct. 1993. DOI: [10.1109/CJECE.1993.6593942](https://doi.org/10.1109/CJECE.1993.6593942) (cit. on p. 6).
- [17] D. O'Brien, R. Turnbull, H. L. Minh, G. Faulkner, O. Bouchet, P. Porcon, M. E. Tabach, E. Gueutier, M. Wolf, L. Grobe, and J. Li, "High-speed optical wireless demonstrators: Conclusions and future directions," *Journal of Lightwave Technology*, vol. 30, no. 13, pp. 2181–2187, Jul. 2012. DOI: [10.1109/JLT.2012.2193874](https://doi.org/10.1109/JLT.2012.2193874) (cit. on pp. 6, 27).
- [18] D. R. Wisely, "A 1 Gbit/s optical wireless tracked architecture for ATM delivery," in *Proc. IEE Colloquium Optical Free Space Communication Links*, Feb. 1996, pp. 14/1–14/7. DOI: [10.1049/ic:19960199](https://doi.org/10.1049/ic:19960199) (cit. on p. 6).
- [19] V. Jungnickel, A. Forck, T. Haustein, U. Krüger, V. Pohl, and C. Helmolt, "Electronic tracking for wireless infrared communications," *IEEE Transactions on Wireless Communications*, vol. 2, no. 5, pp. 989–999, Sep. 2003. DOI: [10.1109/TWC.2003.817419](https://doi.org/10.1109/TWC.2003.817419) (cit. on p. 6).

-
- [20] M. Castillo-Vázquez and A. Puerta-Notario, "Self-orienting receiver for indoor wireless infrared links at high bit rates," in *Proc. The 57th IEEE Semianual Vehicular Technology Conf., VTC 2003-Spring*, vol. 3, Apr. 2003, pp. 1600–1604. DOI: [10.1109/VETECS.2003.1207092](https://doi.org/10.1109/VETECS.2003.1207092) (cit. on p. 6).
- [21] M. Castillo-Vazquez and A. Puerta-Notario, "Single-channel imaging receiver for optical wireless communications," *IEEE Communications Letters*, vol. 9, no. 10, pp. 897–899, Oct. 2005. DOI: [10.1109/LCOMM.2005.10021](https://doi.org/10.1109/LCOMM.2005.10021) (cit. on pp. 6, 14).
- [22] A. Street, P. Stavrinou, D. O'brien, and D. Edwards, "Indoor optical wireless systems-a review," *Springer Optical and Quantum Electronics*, vol. 29, pp. 349–378, 3 1997, ISSN: 0306-8919. DOI: [10.1023/A:1018530828084](https://doi.org/10.1023/A:1018530828084) (cit. on p. 7).
- [23] D. O'Brien, M. Katz, P. Wang, K. Kalliojarvi, S. Arnon, M. Matsumoto, R. Green, and S. Jivkova, "Short-range optical wireless communications," in *Wireless World Research Forum*, 2005, pp. 1–22 (cit. on p. 7).
- [24] R. Green, H. Joshi, M. Higgins, and M. Leeson, "Recent developments in indoor optical wireless systems [Optical wireless communications]," *IET, Communications*, vol. 2, no. 1, pp. 3–10, 2008, ISSN: 1751-8628. DOI: [10.1049/iet-com:20060475](https://doi.org/10.1049/iet-com:20060475) (cit. on p. 7).
- [25] Z. Ghassemlooy, S. Arnon, M. Uysal, Z. Xu, and J. Cheng, "Emerging optical wireless communications-advances and challenges," *IEEE Journal on Selected Areas in Communications*, vol. 33, no. 9, pp. 1738–1749, Sep. 2015. DOI: [10.1109/JSAC.2015.2458511](https://doi.org/10.1109/JSAC.2015.2458511) (cit. on p. 7).
- [26] S. Hranilovic, *Wireless Optical Communication Systems*. Springer New York, 2005, ISBN: 978-0-387-22784-9. DOI: [10.1007/b99592](https://doi.org/10.1007/b99592) (cit. on p. 7).
- [27] Z. Ghassemlooy, W. Popoola, and S. Rajbhandari, *Optical Wireless Communications, System and Channel Modelling with MATLAB®*. CRC Press, Taylor & Francis Group, Boca Raton, FL, 2012, ISBN: 978-1-4398-5188-3. DOI: [10.1201/b12687](https://doi.org/10.1201/b12687) (cit. on p. 7).
- [28] G. P. Agrawal, *Fiber-Optic Communication Systems*, 3rd ed. John Wiley & Sons, Inc., New York, 2002, ISBN: 0-471-21571-6 (cit. on p. 7).
- [29] S. B. Alexander, *Optical Communication Receiver Design*. SPIE Optical Engineering Press, Bellingham, Washington, 1997, ISBN: 9780819420237. DOI: [10.1117/3.219402](https://doi.org/10.1117/3.219402) (cit. on pp. 7, 8, 11).
- [30] K. J. Ebeling, *Integrierte Optoelektronik*, German, 2nd ed. Springer-Verlag Berlin Heidelberg, 1992, ISBN: 978-3-540-54655-9. DOI: [10.1007/978-3-662-07945-4](https://doi.org/10.1007/978-3-662-07945-4) (cit. on p. 8).

- [31] H. Zimmermann, *Integrated Silicon Optoelectronics*, 2nd ed., ser. Springer Series in Optical Sciences. Springer Berlin Heidelberg, 2010, vol. 148, ISBN: 978-3-642-01520-5. DOI: [10.1007/978-3-642-01521-2](https://doi.org/10.1007/978-3-642-01521-2) (cit. on pp. 9, 16).
- [32] G. Winstel, C. Weyrich, W. Heywang, and R. Müller, *Optoelektronik II*, German, ser. Halbleiter-Elektronik. Springer-Verlag Berlin Heidelberg, 1986, vol. 11, ISBN: 3-540-16019-1. DOI: [10.1007/978-3-642-82640-5](https://doi.org/10.1007/978-3-642-82640-5) (cit. on p. 9).
- [33] R. J. McIntyre, "Multiplication noise in uniform avalanche diodes," *IEEE Transactions on Electron Devices*, vol. ED-13, no. 1, pp. 164–168, Jan. 1966. DOI: [10.1109/T-ED.1966.15651](https://doi.org/10.1109/T-ED.1966.15651) (cit. on p. 10).
- [34] P. P. Webb, R. J. McIntyre, and J. Conradi, "Properties of Avalanche Photodiodes," *RCA Review*, vol. 35, pp. 234–278, Jun. 1974 (cit. on p. 10).
- [35] Excelitas Technologies. (2016). Avalanche photodiode - a user guide, [Online]. Available: http://www.excelitas.com/downloads/app_apd_a_user_guide.pdf (visited on 08/23/2016) (cit. on p. 10).
- [36] F. Xu, M. A. Khalighi, and S. Bourennane, "Impact of different noise sources on the performance of PIN- and APD-based FSO receivers," in *Proc. 11th Int. Conf. on Telecommunications (ConTEL)*, Graz, Austria, Jun. 2011, pp. 211–218 (cit. on p. 10).
- [37] R. G. Smith and S. D. Personick, "Receiver design for optical fiber communication systems," in *Semiconductor Devices for Optical Communication*, ser. Topics in Applied Physics, H. Kressel, Ed., 2nd ed., vol. 39, Springer Berlin Heidelberg, 1982, pp. 89–160, ISBN: 978-3-540-11348-5. DOI: [10.1007/3-540-11348-7_26](https://doi.org/10.1007/3-540-11348-7_26) (cit. on pp. 11–13).
- [38] T. van Muoi, "Receiver design for high-speed optical-fiber systems," *Journal of Lightwave Technology*, vol. 2, no. 3, pp. 243–267, Jun. 1984. DOI: [10.1109/JLT.1984.1073617](https://doi.org/10.1109/JLT.1984.1073617) (cit. on pp. 11, 12).
- [39] B. Razavi, *Design of Integrated Circuits for Optical Communications*, 2nd ed. John Wiley & Sons, Inc., Hoboken, New Jersey, 2012, ISBN: 978-1-118-33694-6 (cit. on pp. 11, 16).
- [40] E. Säckinger, *Broadband Circuits for Optical Fiber Communication*. John Wiley & Sons, Inc., Hoboken, New Jersey, 2005, ISBN: 9780471726401. DOI: [10.1002/0471726400](https://doi.org/10.1002/0471726400) (cit. on pp. 11, 16).
- [41] K. Wang, A. Nirmalathas, C. Lim, and E. Skafidas, "High-speed indoor optical wireless communication system with single channel imaging receiver," *Optics Express*, vol. 20, no. 8, pp. 8442–8456, Apr. 2012. DOI: [10.1364/OE.20.008442](https://doi.org/10.1364/OE.20.008442) (cit. on pp. 14, 27).

- [42] K. Wang, A. Nirmalathas, C. Lim, and E. Skafidas, "High-speed optical wireless communication system for indoor applications," *IEEE Photonics Technology Letters*, vol. 23, no. 8, pp. 519–521, Apr. 2011. DOI: [10.1109/LPT.2011.2113331](https://doi.org/10.1109/LPT.2011.2113331) (cit. on pp. 14, 27).
- [43] D. C. O'Brien, G. E. Faulkner, E. B. Zyambo, K. Jim, D. J. Edwards, P. Stavrinou, G. Parry, J. Bellon, M. J. Sibley, V. A. Lalithambika, V. M. Joyner, R. J. Samsudin, D. M. Holburn, and R. J. Mears, "Integrated transceivers for optical wireless communications," *IEEE Journal of Selected Topics in Quantum Electronics*, vol. 11, no. 1, pp. 173–183, Jan. 2005. DOI: [10.1109/JSTQE.2004.841471](https://doi.org/10.1109/JSTQE.2004.841471) (cit. on p. 14).
- [44] J. Zeng, V. Joyner, J. Liao, S. Deng, and Z. Huang, "A 5Gb/s 7-channel current-mode imaging receiver front-end for free-space optical MIMO," in *Proc. 52nd IEEE Int. Midwest Symp. Circuits and Systems*, Aug. 2009, pp. 148–151. DOI: [10.1109/MWSCAS.2009.5236130](https://doi.org/10.1109/MWSCAS.2009.5236130) (cit. on p. 14).
- [45] H. L. Minh, D. O'Brien, G. Faulkner, O. Bouchet, M. Wolf, L. Grobe, and J. Li, "A 1.25-Gb/s indoor cellular optical wireless communications demonstrator," *IEEE Photonics Technology Letters*, vol. 22, no. 21, pp. 1598–1600, Nov. 2010. DOI: [10.1109/LPT.2010.2073696](https://doi.org/10.1109/LPT.2010.2073696) (cit. on pp. 14, 27).
- [46] W. Gaberl and H. Zimmermann, "Integrated optical receiver for lens-less free-space communication," in *Proc. 34th European Conf. Optical Communication*, Sep. 2008, pp. 1–2. DOI: [10.1109/ECOC.2008.4729541](https://doi.org/10.1109/ECOC.2008.4729541) (cit. on pp. 14, 90).
- [47] W. Gaberl, R. Swoboda, and H. Zimmermann, "Integrated optical receiver for lens-less short range free-space gigabit communication," in *Proc. 35th European Conf. Optical Communication*, Sep. 2009, pp. 1–2 (cit. on pp. 14, 16, 90).
- [48] M.-J. Lee and W.-Y. Choi, "A silicon avalanche photodetector fabricated with standard CMOS technology with over 1 THz gain-bandwidth product," *Optics Express*, vol. 18, no. 23, pp. 24 189–24 194, Nov. 2010. DOI: [10.1364/OE.18.024189](https://doi.org/10.1364/OE.18.024189) (cit. on p. 15).
- [49] J. S. Youn, M. J. Lee, K. Y. Park, and W. Y. Choi, "10-Gb/s 850-nm CMOS OEIC receiver with a silicon avalanche photodetector," *IEEE Journal of Quantum Electronics*, vol. 48, no. 2, pp. 229–236, Feb. 2012. DOI: [10.1109/JQE.2011.2170405](https://doi.org/10.1109/JQE.2011.2170405) (cit. on pp. 15, 20).
- [50] C. K. Tseng, K. H. Chen, W. T. Chen, M. C. M. Lee, and N. Na, "A high-speed and low-breakdown-voltage silicon avalanche photodetector," *IEEE Photonics Technology Letters*, vol. 26, no. 6, pp. 591–594, Mar. 2014. DOI: [10.1109/LPT.2014.2300853](https://doi.org/10.1109/LPT.2014.2300853) (cit. on p. 15).

- [51] M. Yamamoto, M. Kubo, and K. Nakao, "Si-oeic with a built-in pin-photodiode," *IEEE Transactions on Electron Devices*, vol. 42, no. 1, pp. 58–63, 1995. DOI: [10.1109/16.370035](https://doi.org/10.1109/16.370035) (cit. on p. 16).
- [52] G. Köklü, R. Etienne-Cummings, Y. Leblebici, G. D. Micheli, and S. Carrara, "Characterization of standard CMOS compatible photodiodes and pixels for lab-on-chip devices," in *Proc. IEEE Int. Symp. Circuits and Systems (ISCAS2013)*, May 2013, pp. 1075–1078. DOI: [10.1109/ISCAS.2013.6572036](https://doi.org/10.1109/ISCAS.2013.6572036) (cit. on p. 16).
- [53] A. Sharif-Bakhtiar, S. Shahramian, A. Rousson, H. Yasotharan, and T. C. Carusone, "Integrated photodiode characterization in a SiGe BiCMOS process," in *Proc. Optical Interconnects Conf*, May 2013, pp. 68–69. DOI: [10.1109/OIC.2013.6552927](https://doi.org/10.1109/OIC.2013.6552927) (cit. on p. 16).
- [54] B. Nakhkoob, S. Ray, and M. M. Hella, "High speed photodiodes in standard nanometer scale cmos technology: A comparative study," *Optics Express*, vol. 20, no. 10, pp. 11 256–11 270, May 2012. DOI: [10.1364/OE.20.011256](https://doi.org/10.1364/OE.20.011256) (cit. on p. 16).
- [55] H. Zimmermann, *Silicon Optoelectronic Integrated Circuits*, ser. Springer Series in Advanced Microelectronics. Springer Berlin Heidelberg, 2004, vol. 13, ISBN: 978-3-642-07351-9. DOI: [10.1007/978-3-662-09904-9](https://doi.org/10.1007/978-3-662-09904-9) (cit. on p. 16).
- [56] F. Tavernier and M. Steyaert, *High-Speed Optical Receivers with Integrated Photodiode in Nanoscale CMOS*, 1st ed., ser. Analog Circuits and Signal Processing. Springer-Verlag New York, 2011, vol. 5, ISBN: 978-1-4419-9924-5. DOI: [10.1007/978-1-4419-9925-2](https://doi.org/10.1007/978-1-4419-9925-2) (cit. on p. 16).
- [57] R. Swoboda and H. Zimmermann, "A 2.5-gpbs silicon receiver OEIC with large-diameter photodiode," *Electronics Letters*, vol. 40, no. 8, pp. 505–507, Apr. 2004. DOI: [10.1049/e1:20040346](https://doi.org/10.1049/e1:20040346) (cit. on pp. 17, 27, 90).
- [58] E. Kamrani, F. Lesage, and M. Sawan, "Low-noise, high-gain transimpedance amplifier integrated with SiAPD for low-intensity near-infrared light detection," *IEEE Sensors Journal*, vol. 14, no. 1, pp. 258–269, Jan. 2014. DOI: [10.1109/JSEN.2013.2282624](https://doi.org/10.1109/JSEN.2013.2282624) (cit. on pp. 20, 90).
- [59] B. Steindl, R. Enne, S. Schidl, and H. Zimmermann, "Linear mode avalanche photodiode with high responsivity integrated in high-voltage CMOS," *IEEE Electron Device Letters*, vol. 35, no. 9, pp. 897–899, Sep. 2014. DOI: [10.1109/LED.2014.2336678](https://doi.org/10.1109/LED.2014.2336678) (cit. on p. 20).
- [60] Vixarinc, *680 nm Communications Grade VCSEL, Datasheet 680c-0000-xoy1*, www.vixarinc.com, May 2012 (cit. on p. 21).

-
- [61] Maxim Integrated Products, *MAX3740A, 3.2Gbps SFP VCSEL Driver with Diagnostic Monitors*, www.maximintegrated.com, 2012 (cit. on p. 21).
- [62] Mirrorcle Technologies, *Gimbal-Less Two-Axis Scanning MEMS Micromirrors, Device datasheet s1911*, www.mirrorcletech.com, Sep. 2012 (cit. on p. 22).
- [63] M. Atef, R. Swoboda, and H. Zimmermann, "1.25 gbit/s over 50 m step-index plastic optical fiber using a fully integrated optical receiver with an integrated equalizer," *Journal of Lightwave Technology*, vol. 30, no. 1, pp. 118–122, 2012. DOI: [10.1109/JLT.2011.2179520](https://doi.org/10.1109/JLT.2011.2179520) (cit. on pp. 27, 90).
- [64] Y. Dong and K. Martin, "A high-speed fully-integrated POF receiver with large-area photo detectors in 65 nm CMOS," *IEEE Journal of Solid-State Circuits*, vol. 47, no. 9, pp. 2080–2092, 2012. DOI: [10.1109/JSSC.2012.2200529](https://doi.org/10.1109/JSSC.2012.2200529) (cit. on pp. 27, 90).
- [65] F. Aznar, C. Sanchez-Azqueta, S. Celma, and B. Calvo, "Gigabit receiver over 1 mm SI-POF for home area networks," *Journal of Lightwave Technology*, vol. 30, no. 16, pp. 2668–2674, Aug. 2012. DOI: [10.1109/JLT.2012.2205220](https://doi.org/10.1109/JLT.2012.2205220) (cit. on p. 27).
- [66] E. Fisher, I. Underwood, and R. Henderson, "A reconfigurable single-photon-counting integrating receiver for optical communications," *IEEE Journal of Solid-State Circuits*, vol. 48, no. 7, pp. 1638–1650, Jul. 2013. DOI: [10.1109/JSSC.2013.2253222](https://doi.org/10.1109/JSSC.2013.2253222) (cit. on pp. 27, 90).
- [67] R. Li, J. D. Schaub, S. M. Csutak, and J. C. Campbell, "A high-speed monolithic silicon photoreceiver fabricated on SOI," *IEEE Photonics Technology Letters*, vol. 12, no. 8, pp. 1046–1048, Aug. 2000. DOI: [10.1109/68.868003](https://doi.org/10.1109/68.868003) (cit. on p. 90).
- [68] S. M. Csutak, J. D. Schaub, S. Wang, J. Mogab, and J. C. Campbell, "Integrated silicon optical receiver with avalanche photodiode," *IEE Proceedings-Optoelectronics*, vol. 150, no. 3, pp. 235–237, Jun. 2003. DOI: [10.1049/ip-opt:20030391](https://doi.org/10.1049/ip-opt:20030391) (cit. on p. 90).
- [69] S. Radovanovic, A. J. Annema, and B. Nauta, "A 3-Gb/s optical detector in standard CMOS for 850-nm optical communication," *IEEE Journal of Solid-State Circuits*, vol. 40, no. 8, pp. 1706–1717, Aug. 2005. DOI: [10.1109/JSSC.2005.852030](https://doi.org/10.1109/JSSC.2005.852030) (cit. on p. 90).
- [70] M. Förtsch, H. Zimmermann, and H. Pless, "220-MHz monolithically integrated optical sensor with large-area integrated PIN photodiode," *IEEE Sensors Journal*, vol. 6, no. 2, pp. 385–390, Apr. 2006. DOI: [10.1109/JSEN.2006.870168](https://doi.org/10.1109/JSEN.2006.870168) (cit. on p. 90).

- [71] W. Z. Chen and S. H. Huang, "A 2.5 Gbps CMOS fully integrated optical receiver with lateral PIN detector," in *Proc. IEEE Custom Integrated Circuits Conf.*, Sep. 2007, pp. 293–296. DOI: [10.1109/CICC.2007.4405736](https://doi.org/10.1109/CICC.2007.4405736) (cit. on p. 90).
- [72] F. Tavernier and M. Steyaert, "High-speed optical receivers with integrated photodiode in 130 nm CMOS," *IEEE Journal of Solid-State Circuits*, vol. 44, no. 10, pp. 2856–2867, Oct. 2009. DOI: [10.1109/JSSC.2009.2028755](https://doi.org/10.1109/JSSC.2009.2028755) (cit. on p. 90).
- [73] —, "A high-speed POF receiver with 1 mm integrated photodiode in 180 nm CMOS," in *Proc. 36th European Conf. and Exhibition Optical Communication*, Sep. 2010, pp. 1–3. DOI: [10.1109/ECOC.2010.5621473](https://doi.org/10.1109/ECOC.2010.5621473) (cit. on p. 90).
- [74] T. S. C. Kao, F. A. Musa, and A. C. Carusone, "A 5-Gbit/s CMOS optical receiver with integrated spatially modulated light detector and equalization," *IEEE Transactions on Circuits and Systems I: Regular Papers*, vol. 57, no. 11, pp. 2844–2857, Nov. 2010. DOI: [10.1109/TCSI.2010.2050231](https://doi.org/10.1109/TCSI.2010.2050231) (cit. on p. 90).
- [75] D. Lee, J. Han, G. Han, and S. M. Park, "An 8.5-Gb/s fully integrated CMOS optoelectronic receiver using slope-detection adaptive equalizer," *IEEE Journal of Solid-State Circuits*, vol. 45, no. 12, pp. 2861–2873, Dec. 2010. DOI: [10.1109/JSSC.2010.2077050](https://doi.org/10.1109/JSSC.2010.2077050) (cit. on p. 90).
- [76] S. H. Huang, W. Z. Chen, Y. W. Chang, and Y. T. Huang, "A 10-Gb/s OEIC with meshed spatially-modulated photo detector in 0.18- CMOS technology," *IEEE Journal of Solid-State Circuits*, vol. 46, no. 5, pp. 1158–1169, May 2011. DOI: [10.1109/JSSC.2011.2116430](https://doi.org/10.1109/JSSC.2011.2116430) (cit. on p. 90).
- [77] Y. Dong and K. W. Martin, "A 4-Gbps POF receiver using linear equalizer with multi-shunt-shunt feedbacks in 65-nm CMOS," *IEEE Transactions on Circuits and Systems II: Express Briefs*, vol. 60, no. 10, pp. 617–621, Oct. 2013. DOI: [10.1109/TCSII.2013.2273839](https://doi.org/10.1109/TCSII.2013.2273839) (cit. on p. 90).

Appendix

Appendix A.

Matlab-Code

A.1. Irradiance distribution of laser source

The received light power is an important factor for calculating the SNR or BER for an optical receiver. In case of OWC receiver, this power can be calculated by the area of the PD and the irradiance (received power per unit area) produced by the laser ray impinging the PD. The main goal of the following MATLAB® code was to determine the power distribution of the laser spot. The measurement procedure included the following steps:

1. The transmitter with the VCSEL was placed on a movable platform and the spot was placed on a smooth wall. The focus of the spot was adjusted either to a perfectly focused point or to a broad spot.
2. In a distance of approx. 2.5 m was placed a CMOS camera UI-1220SE-M-GL from IDS ¹ with a monochromatic sensor and a resolution of 752×480 pixels. In front of the camera was mounted a objective with a focus length of 16 mm from Pentax².
3. To minimize the influence of background light, the measurements were done during the night. The remaining background light was measured with an optical power meter OPHIR NOVA PD300 with a photosensitive area of 1 mm^2 . This measurement showed a power of approx. 25 nW which was in the range of noise.
4. To calibrate the laser spot pictures according to dimensions, a picture from a graticule with one line each cm was taken, see fig. A.1. The length of 1 pixel

¹<https://en.ids-imaging.com/home.html>

²<http://www.ricoh-imaging.eu/>

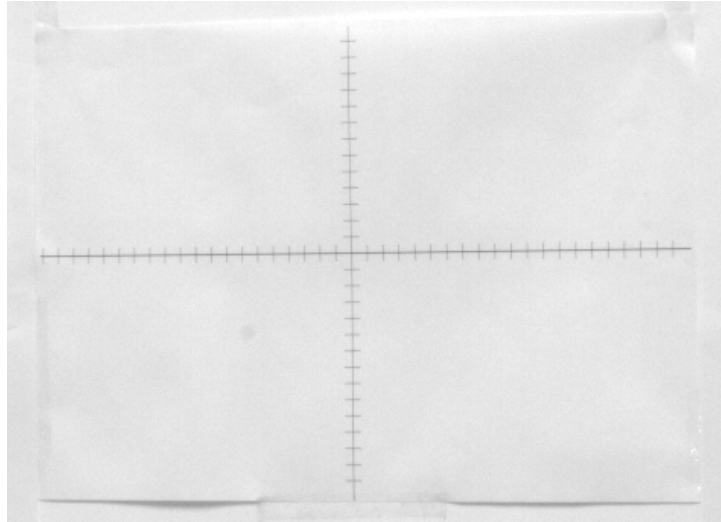
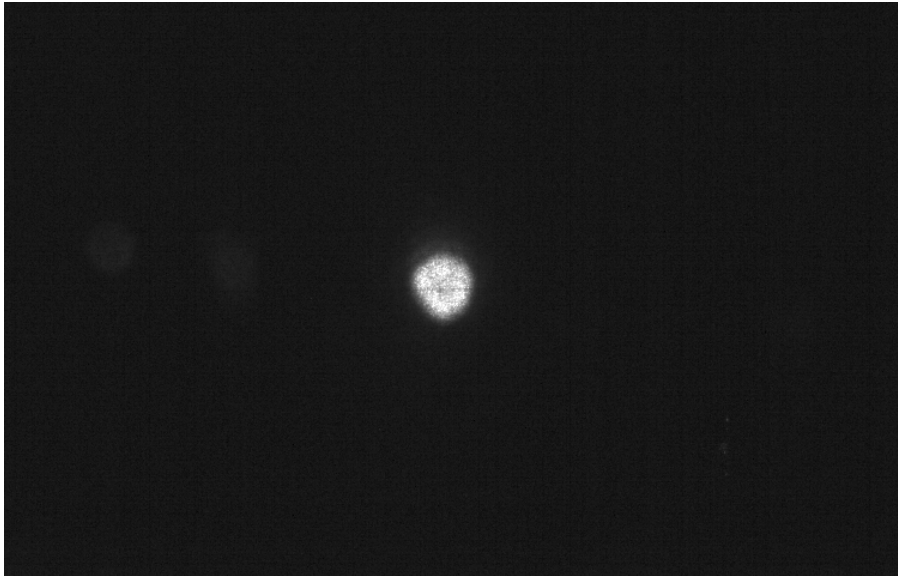


Figure A.1.: Taken picture from a graticule to calibrate the laser spot pictures

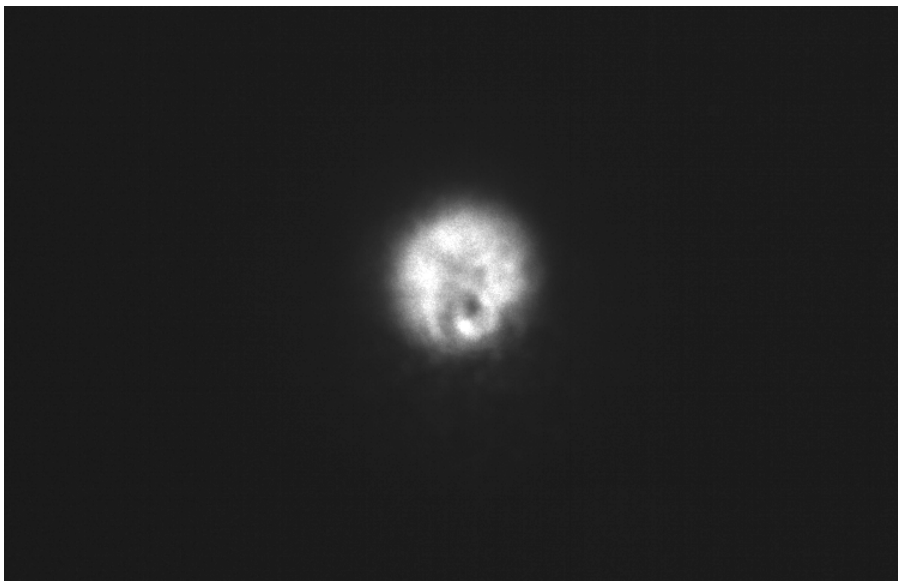
corresponds to approx. 0.96 mm.

5. The transmitter was placed in distances starting from 3 m up to 20 m in steps of 1 m. At each step a picture of the laser spot focused on the center of the graticule was taken. To calibrate the pictures regarding the optical power, the laser power in the center of the graticule was measured with the optical power meter. Fig. [A.2a](#) shows the focused laser spot from a distance of 20 m and fig. [A.2b](#) shows the unfocused laser spot from a distance of 3 m.
6. These pictures, the measured laser power values and the distance built the input parameters for the MATLAB® code.

The results were the laser spot diameter in the focused and unfocused case and the received power with a certain area for example with a lens. All the results from the calculations were saved into an excel sheet. For further details on the algorithm see the comments within the code on the following pages.



(a)



(b)

Figure A.2.: Taken pictures from laser spot: (a) focused laser, 20 m distance, (b) unfocused laser, 3 m distance.

Appendix A. Matlab-Code

```
%% Calculation of laser spot power distribution
% Paul Brandl
% 2013-12-13

%% loading measured values from excel table
[~, ~, raw] = xlsread('Leistungen.xlsx','Tabelle1','A4:A21');
distance = reshape([raw{:}],size(raw)); %distance between laser and wall

[~, ~, raw] = xlsread('Leistungen.xlsx','Tabelle1','C4:C21');
P_Focus = reshape([raw{:}],size(raw)); % measured power in  $\mu\text{W}$  of
                                         % focused laser spot

clearvars raw;

%% load picture from graticule to determine pixel size
graticule = imread('fadenkreuz.bmp');

imtool(graticule); % select "Pixel Region" in Tools menu
% the result is the following variable:
PixelM = 0.96; % 1 pixel corresponds to 0.96 mm

%horizontal dimension of the picture in mm
x_coord = (-375:1:376).*PixelM;
y_coord = (-239:1:240).*PixelM; %vertical dimension of the picture in mm

dim_pic = size(graticule);

%%%%%%%%%%%%%%%%%%%%%%%%%%%%%%%%%%%%%%%%%%%%%%%%%%%%%%%%%%%%%%%%%%%%%%%%%%
%% variables definition:
f = @(x) (sum(sum(x))); % function for nlfiter
% horizontal focused spot diameter
Spot_dia_h_f = zeros(1,length(distance));
Spot_dia_v_f = zeros(1,length(distance)); %vertical focused spot diameter
% unfocused case
Spot_dia_h_noF = zeros(1,length(distance));
Spot_dia_v_noF = zeros(1,length(distance));

P_lens = zeros(1,length(distance)); % received power with a lens
radius = 10; % of radius 10 mm
```

```

%%
for i=1:length(distance)

    lens_mask = zeros(dim_pic);    % mask for the area of the lens
    noise_mask = ones(dim_pic);    % mask for filtering out noise
    %% unfocused case
    pic_name_noF = sprintf('%dmof.bmp',i+2); % generate picture name
    hPicName_noF = imread(pic_name_noF);    % load actual picture
    hPicName_noF = double(hPicName_noF);
    % maximum value of picture (255)
    MaxPicVal_noF = max(max(hPicName_noF));
    % find spot whit Full Width at Half Maximum (FWHM)
    [row_noF,column_noF] = find(hPicName_noF > MaxPicVal_noF/2);
    % calculate unfocused spot diameter
    Spot_dia_h_noF(i) = (1 + max(column_noF)-min(column_noF))*PixelM;
    Spot_dia_v_noF(i) = (1 + max(row_noF)-min(row_noF))*PixelM;

    %% focused case
    pic_name_f = sprintf('%dm.bmp',i+2); % generate picture name
    hPicName_f = imread(pic_name_f);    % load actual picture
    hPicName_f = double(hPicName_f);    % convert to double values

    MaxPicValue = max(max(hPicName_f)); % maximum value of picture (255)
    % find spot whit Full Width at Half Maximum (FWHM)
    [row_f,column_f] = find(hPicName_f > MaxPicValue/2);
    % calculate horizontal spot diameter
    Spot_dia_h_f(i) = (1 + max(column_f)-min(column_f))*PixelM;
    % calculate vertical spot diameter
    Spot_dia_v_f(i) = (1 + max(row_f)-min(row_f))*PixelM;
    % round the diameters for calculating the masks
    Spot_round_h = ceil(Spot_dia_h_f(i));
    Spot_round_v = ceil(Spot_dia_v_f(i));

    % center of column
    Pos_column = min(column_f) + round((max(column_f)-min(column_f))/2);
    % center of row
    Pos_row = min(row_f) + round((max(row_f)-min(row_f))/2);

```

```

% mask for deleting noise
noise_mask(Pos_row-Spot_round_h:Pos_row+Spot_round_h,...
           Pos_column-Spot_round_v:Pos_column+Spot_round_v)=0;
% applying noise mask to get a picture with only noise values
noise_mask=hPicName_f.*noise_mask;
% average noise value per pixel
Noise_Pixel = ceil((sum(sum(noise_mask)))/...
                  (dim_pic(1)*dim_pic(2)-2*Spot_round_h*2*Spot_round_v));
% for receive lens power calculations
pic_noNoise = hPicName_f-Noise_Pixel;
% sum up to get watt per cm2
pic_WperCM2 = nlfilter(hPicName_f,[10,10],f);
% generate some nice pictures
%figure;
%mesh(x_coord, y_coord, pic_WperCM2);

% measured power / sum of the pixel values
WperPixel = P_Focus(i)/pic_WperCM2(Pos_row,Pos_column);

%% circle mask for the lens calculated according to
% BRESENHAM'S CIRCLE ALGORITHM
Spot_round_h = 0;
Spot_round_v = radius;
dist = 3 - 2*radius;

while (Spot_round_h<Spot_round_v)
    lens_mask(Pos_row:Pos_row+Spot_round_h,...
              Pos_column:Pos_column+Spot_round_v) = 1;
    lens_mask(Pos_row-Spot_round_h:Pos_row,...
              Pos_column:Pos_column+Spot_round_v) = 1;
    lens_mask(Pos_row:Pos_row+Spot_round_h,...
              Pos_column-Spot_round_v:Pos_column) = 1;
    lens_mask(Pos_row-Spot_round_h:Pos_row,...
              Pos_column-Spot_round_v:Pos_column) = 1;
    lens_mask(Pos_row:Pos_row+Spot_round_v,...
              Pos_column:Pos_column+Spot_round_h) = 1;
    lens_mask(Pos_row-Spot_round_v:Pos_row,...
              Pos_column:Pos_column+Spot_round_h) = 1;

```

```

    lens_mask(Pos_row:Pos_row+Spot_round_v,...
              Pos_column-Spot_round_h:Pos_column) = 1;
    lens_mask(Pos_row-Spot_round_v:Pos_row,...
              Pos_column-Spot_round_h:Pos_column) = 1;

    Spot_round_h =Spot_round_h+1;
    if dist < 0
        dist = dist +4*Spot_round_h +6;
    else
        Spot_round_v =Spot_round_v-1;
        dist = dist+4*(Spot_round_h-Spot_round_v) + 10;
    end;

end;

% applying lens mask
pic_lense = pic_noNoise.*lens_mask;

P_lens(i) = sum(sum(pic_lense));
% power collected by the lens
P_lens(i) = P_lens(i)*WproPixel;

end;
%%%%%%%%%%%%%%%%%%%%%%%%%%%%%%%%%%%%%%%%%%%%%%%%%%%%%%%%%%%%%%%%%%%%%%%%
%% write results in new excel file
filename = 'LaserCharact.xlsx';
xlswrite(filename,{'distance'},1,'B1');
xlswrite(filename,{'[m]'},1,'B2');
xlswrite(filename,distance,1,'B3');
xlswrite(filename,{'Spot_H'},1,'C1');
xlswrite(filename,{'[mm]'},1,'C2');
xlswrite(filename,Spot_dia_h_f,1,'C3');
xlswrite(filename,{'Spot_V'},1,'D1');
xlswrite(filename,{'[mm]'},1,'D2');
xlswrite(filename,Spot_dia_v_f,1,'D3');
xlswrite(filename,{'P_Linse'},1,'E1');
xlswrite(filename,{'[pW]'},1,'E2');
xlswrite(filename,P_lens',1,'E3');

```

```
xlswrite(filename,{'Spot_H_noF'},1,'G1');  
xlswrite(filename,{'[mm]'},1,'G2');  
xlswrite(filename,Spot_dia_h_noF',1,'G3');  
xlswrite(filename,{'Spot_V_noF'},1,'H1');  
xlswrite(filename,{'[mm]'},1,'H2');  
xlswrite(filename,Spot_dia_v_noF',1,'H3');
```

A.2. APD Ionization Coefficient

As stated in section 1.1.2, the effective ionization ratio k_{eff} is an important parameter for describing the performance of an APD. The ionization ratio determines the maximum applicable multiplication. The lower the ratio is, the lower the additional excess noise of the APD is. The ionization ratio was determined by: (1) measuring and calculation the excess noise factor $F(M)$ and the multiplication M ; and (2) fitting the equation for the excess noise (1.9)

$$F(M) = k_{eff}M + (1 - k_{eff}) \left(2 - \frac{1}{M} \right)$$

into the results. The measurement setup is depicted in fig. A.3. The source was built by a 635 nm laser in continuous wave mode. A transimpedance amplifier (TIA) AD8015 from Analog Devices³ was used in the setup. This TIA was connected to a probe tip to contact the APDs directly on the wafer. The following steps were executed to obtain k_{eff} :

1. The unity responsivity R at gain = 1 was determined by measuring the optical power impinging at the APD and the photocurrent I_{PD} . The APD bias voltage was sufficiently below avoiding multiplication inside the APD.
2. At the same time, the power generated from the background noise of the measurement circuit was identified. This background noise is mainly generated by the TIA and measured with the spectrum analyzer (SA):

$$p_{n,TIA} = \int_{1MHz}^{100MHz} p(f)df$$

where $p(f)$ is the power spectral density and the lower and upper frequency limits were chosen accordingly to a liner operation of the TIA.

3. The bias voltage was increased to a level that the effect of multiplication was observed. By measuring the amplified I_{PD} and the optical power P_{opt} , the multiplication M was calculated: $M = I_{PD} / (R \cdot P_{opt})$.
4. The total noise was determined with the SA by using the band power function:

$$p_{n,tot} = \int_{1MHz}^{100MHz} p(f)df.$$

From this total noise the background noise was subtracted to get the noise produced by the APD: $p_{n,APD} = p_{n,tot} - p_{n,TIA}$.

³<http://www.analog.com>

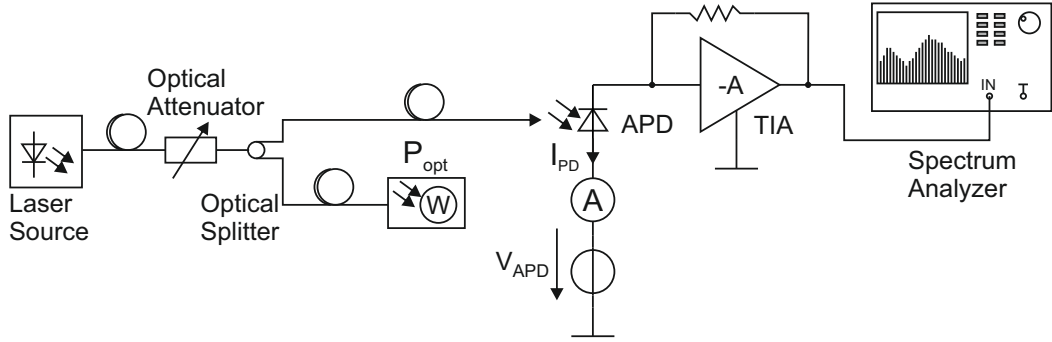


Figure A.3.: APD noise measurement setup for determining the ionization ratio k_{eff} .

5. After calculation the corresponding squared output voltage

$$v_{n,APD}^2 = p_{n,APD} \cdot R$$

where $R (= 50\Omega)$ is the input resistance of the SA, the equivalent input noise current was calculated:

$$i_{n,APD}^2 = \frac{v_{n,APD}^2}{R_{FB}^2}.$$

R_{FB} is the feedback resistance of the TIA.

6. The excess noise factor was calculated accordingly to equation (1.10)

$$i_{n,APD}^2 = 2qRP_{opt}M^2F(M)BW.$$

7. The steps 3 to 6 were repeated for several optical power and APD bias voltage values.
8. The obtained excess noise and multiplication values built the input for the fitting algorithm.

The following MATLAB® code includes also the control of the measurement devices via IEEE-488 (GPIB) and standard commands for programmable instruments (SCPI).

```

%% APD Excess-Noise Messung
% Paul Brandl,
% 2014-07-23
% SA = spectrum analyzer
% The spectrum analyzer has to be adjusted accordingly to the
% 'State' file 'APDNOISE.STA' saved on the SA:
% average detector, 1 MHz start frequency, 400 MHz stop frequency
% 5 dB attenuation, 10 kHz resolution BW, 100 kHz video BW
% 2001 points
% SA: File->Load->Type: State->'APDNOISE.STA'->Load Now

%% set parameters manually for testing
V_APD_start = -50; % Volt
V_APD_end = -65; % Volt
V_APD_step = -1; % Volt

numMeasVal = floor((V_APD_end-V_APD_start)/V_APD_step + 1);

V_APD_meas = zeros(numMeasVal,1);
I_APD_meas = zeros(numMeasVal,1);

P_TIA_OUT = zeros(numMeasVal,1);
%% Set up of Amperemeter
% Find a GPIB object.
Ameter = instrfind('Type', 'gpib', 'BoardIndex', 0,...
                  'PrimaryAddress', 16, 'Tag', '');

% Create the GPIB object if it does not exist
% otherwise use the object that was found.
if isempty(Ameter)
    Ameter = gpib('NI', 0, 16);
else
    fclose(Ameter);
    Ameter = Ameter(1);
end

% Connect to instrument object, Ameter.
fopen(Ameter);

```

```
% Communicating with instrument object, Ameter.
fprintf(Ameter, ':CONF:CURR:DC');
fprintf(Ameter, ':INIT:CONT ON');

%% Set up of Elektrometer
% Find a GPIB object.
Emeter = instrfind('Type', 'gpib', 'BoardIndex', 0,...
                  'PrimaryAddress', 23, 'Tag', '');

% Create the GPIB object if it does not exist
% otherwise use the object that was found.
if isempty(Emeter)
    Emeter = gpib('NI', 0, 23);
else
    fclose(Emeter);
    Emeter = Emeter(1);
end

% Connect to instrument object, Emeter.
fopen(Emeter);

%% Set up of Spectrum Analyzer
% Find a GPIB object.
SpecAn = instrfind('Type', 'gpib', 'BoardIndex', 0,...
                  'PrimaryAddress', 18, 'Tag', '');

% Create the GPIB object if it does not exist
% otherwise use the object that was found.
if isempty(SpecAn)
    SpecAn = gpib('NI', 0, 18);
else
    fclose(SpecAn);
    SpecAn = SpecAn(1);
end

set(SpecAn, 'Timeout', 100.0);
% Connect to instrument object, SpecAn.
fopen(SpecAn);
```

```

fprintf(SpecAn, ':SENS:AVER:STAT 4'); % set average of SA
fprintf(SpecAn, ':SENS:SWE:TIME 7'); % set sweep time of SA
fprintf(SpecAn, ':INIT:CONT 0');

%% Measurement
fprintf(Emeter, ':SOUR:VOLT %.2f', V_APD_start);
fprintf(Emeter, ':OUTPUT:STATE ON;');

for i = 1:numMeasVal
    V_APD_meas(i) = V_APD_start+(V_APD_step*(i-1));
    fprintf(Emeter, ':SOUR:VOLT %.2f', V_APD_meas(i));
    pause(0.5);

    fprintf(SpecAn, ':INIT:IMM');
    xy = query(SpecAn, '*OPC?'); % wait on finishing of measurement
    P_TIA_OUT(i) = str2double(query(SpecAn, ':CALC:MARK1:Y?'));

    I_APD_meas(i) = str2double(query(Ameter, ':FETCh?'));
end

fprintf(Emeter, ':OUTPUT:STATE off');
%% Default state of SA

fprintf(SpecAn, ':SENS:AVER:STAT 0');
fprintf(SpecAn, ':SENS:SWE:TIME 5');
fprintf(SpecAn, ':INIT:CONT 1');

% Disconnect from instrument object
fclose(Emeter);
fclose(Ameter);
fclose(SpecAn);

% Clean up all objects.
delete(Emeter);
delete(Ameter);
delete(SpecAn);

%% Calculation of Excess Noise Factor and Ionization Coefficient
% constants

```

Appendix A. Matlab-Code

```
E_charge = 1.602176e-19;    % As
Responsivity = 0.41;        % A/W
Transimp = 10000;          % V/A
minFreq = 50e6;            % Hz lower frequency for integration
maxFreq = 150e6;          % Hz upper frequenz for Integration
                            % in this range the AC curve is constant
% variable for saving APD gain and excess noise factor
M_apd = zeros(numMeasVal,1);
F_ex = zeros(numMeasVal,1);

%% measured power from SA in case of no light -> noise of TIA
PowerDark_dBm = -53.3; %
PowerDark = (10^(PowerDark_dBm/10))/1000; % noise power of TIA in Watt

% actual light power measured with optical power meter
LightPower = 10e-9; % Watt
I_ph = LightPower*Responsivity; % unamplified photo current in A

%%
for Nr = 1:1:numMeasValues

    M_apd(Nr) = -I_APD_meas(Nr)/I_ph;

    Power_Band = ((10^((P_TIA_OUT(Nr)+6)/10))/1000)-PowerDark ; % W

    % calculate equivalent input noise current
    % (P=U^2/R, R = 50 Ohm)
    In_in2 = (Power_Band*50)/(Transimp^2);

    % calculate excess noise factor
    F_ex(Nr) = In_in2/(M_apd(Nr)^2*2*E_charge*(maxFreq-minFreq)*I_ph);

end

figure(1);
plot(M_apd,F_ex,'-+');
hold on;
hold off;
%%%%%%%%%%%%%%%%%%%%%%%%%%%%%%%%%%%%%%%%%%%%%%%%%%%%%%%%%%%%%%%%%%%%%%%%
M_cal = logspace(1,3);
```

```

% fit to curve from McIntyre
[fit_erg, godnes] = createFit(M_apd,F_ex);    % fit
keff = coeffvalues(fit_erg)    % determine keff

% calculate curve based on fitted keff
F_cal = keff*M_cal+(1-keff)*(2-1./M_cal);
%%%%%%%%%%%%%%%%%%%%%%%%%%%%%%%%%%%%%%%%%%%%%%%%%%%%%%%%%%%%%%%%%%%%%%%%
%% Create figure
figure1 = figure;

set(figure1,'OuterPosition', [600,500,450,400] )

% Create axes
axes1 = axes('Parent',figure1,'YScale','log','YMinorTick','on',...
    'XScale','log',...
    'XMinorTick','on',...
    'Position',[0.13 0.17 0.83 0.78],...
    'FontSize',9,...
    'FontName','Arial');
box(axes1,'on');
hold(axes1,'all');

% Create loglog
loglog(x,y,'Parent',axes1,'Marker','+','LineStyle','none',...
    'DisplayName','measured');

% Create loglog
loglog(M_cal,F_cal,'Parent',axes1,'LineWidth',0.5,'Color',[1 0 0],...
    'DisplayName','fitted');

% Create xlabel
xlabel('Gain (M)','FontSize',9,'FontName','Arial');

% Create ylabel
ylabel('Excess Noise Factor (F)','FontSize',9,'FontName','Arial');

% Create legend
legend1 = legend(axes1,'show');

```

```
set(legend1,...
    'Position',[0.3 0.75 0.17 0.11]);

% 2-column text IEEE-format
width = 8.8 ;high = 6;

set(figure1,'Paperunits','centimeters');
set(figure1,'PaperSize',[width high]);
set(figure1,'Paperposition',[0,0,width,high]);

print(figure1,'ExNoiseF.tif','-dtiff', '-r600')
% print(figure1,'ExNoiseF.pdf','-dpdf', '-r600')
hold off;
```

Fit function

```
function [fitresult, gof] = createFit(x, y)
%CREATEFIT(X,Y)
% Create a fit.
%
% Data for 'test1' fit:
%     X Input : x
%     Y Output: y
% Output:
%     fitresult : a fit object representing the fit.
%     gof : structure with goodness-of fit info.
%
% See also FIT, CFIT, SFIT.
% Auto-generated by MATLAB on 06-Aug-2014 22:30:24
%% Fit: 'test1'.
[xData, yData] = prepareCurveData( x, y );

% Set up fittype and options.
ft = fittype('a*x+(1-a)*(2-1/x)', 'independent', 'x', 'dependent', 'y');
opts = fitoptions('Method','NonlinearLeastSquares');
opts.Display = 'Off';
opts.StartPoint = 0.05;
```



```
% Fit model to data.  
[fitresult, gof] = fit( xData, yData, ft, opts );
```


Appendix B.

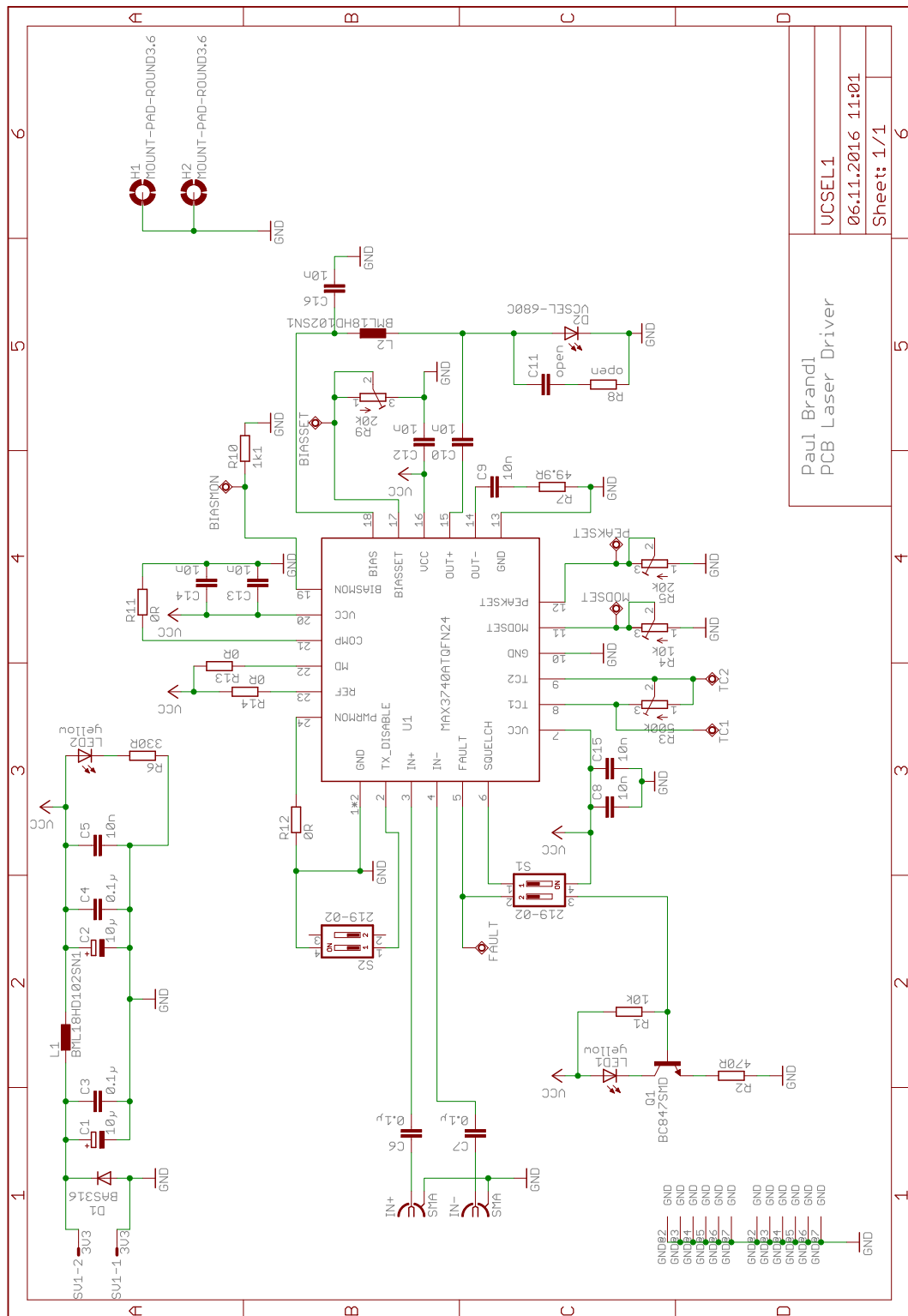
PCB Layouts

B.1. PCB for VCSEL and Laser driver

On the following page is depicted the schematic for the laser source. This PCB includes a 680 nm communication grade VCSEL from Vixar and a 3.2 Gbps laser driver MAX3740A from Maxim Integrated Products. Additionally, there are several potentiometers, switches and miscellaneous passive components included in the schematic. The main information for designing the PCB is taken from the documentation of an evaluation kit for the MAX3740A. For the start-up the following steps must be done:

1. TX-DISABLE must be connected with GND, switch S2-1 set to ON;
2. R-BIASSET (R9): The maximum allowed current for the VCSEL is 7 mA which corresponds to minimum resistor value of 5 k Ω . At 10 k Ω flows a current of approx. 4.5 mA.
3. At the BIASMON voltage output the bias current can be checked according to $I_{bias} = 9 \times V_{biasmon} / 1100$.
4. R-PEAKSET (R5) is set to 20 k Ω to switch off peaking.
5. R-MODSET (R4) is set to approx. 8 k Ω to get a modulation current of around 2 mA.
6. R-TC (R3) is set to zero to switch off the temperature compensation.
7. At the differential inputs must be applied a differential signal with min. 250 mVpp up to max. 2.2 Vpp.
8. Applying of the supply voltage of 3.3 V.
9. Adjusting R-MODSET till the optical amplitude has the adequate value.

Appendix B. PCB Layouts



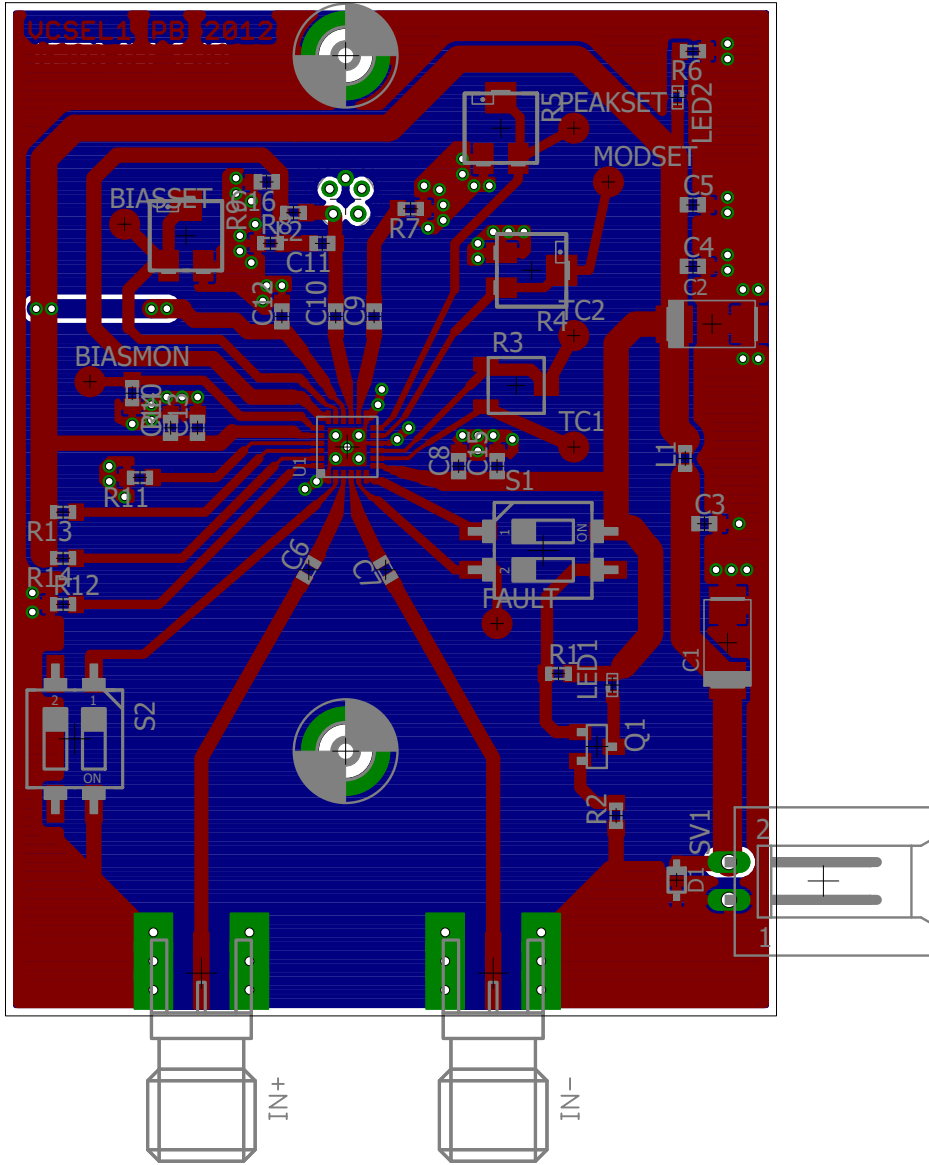
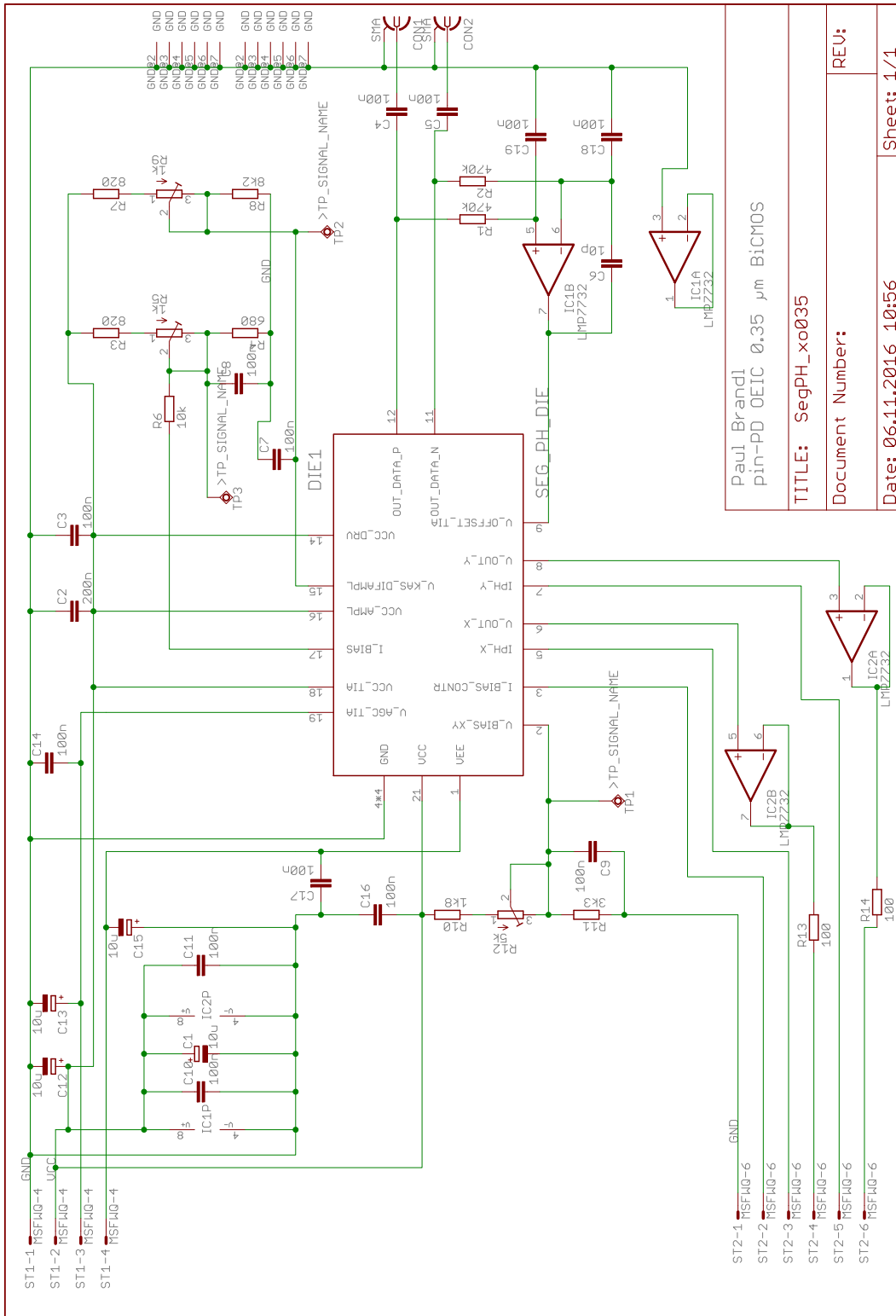


Figure B.1.: PCB for the VCSEL and the laser driver, scale 2:1.

B.2. PCB for BiCMOS OEIC

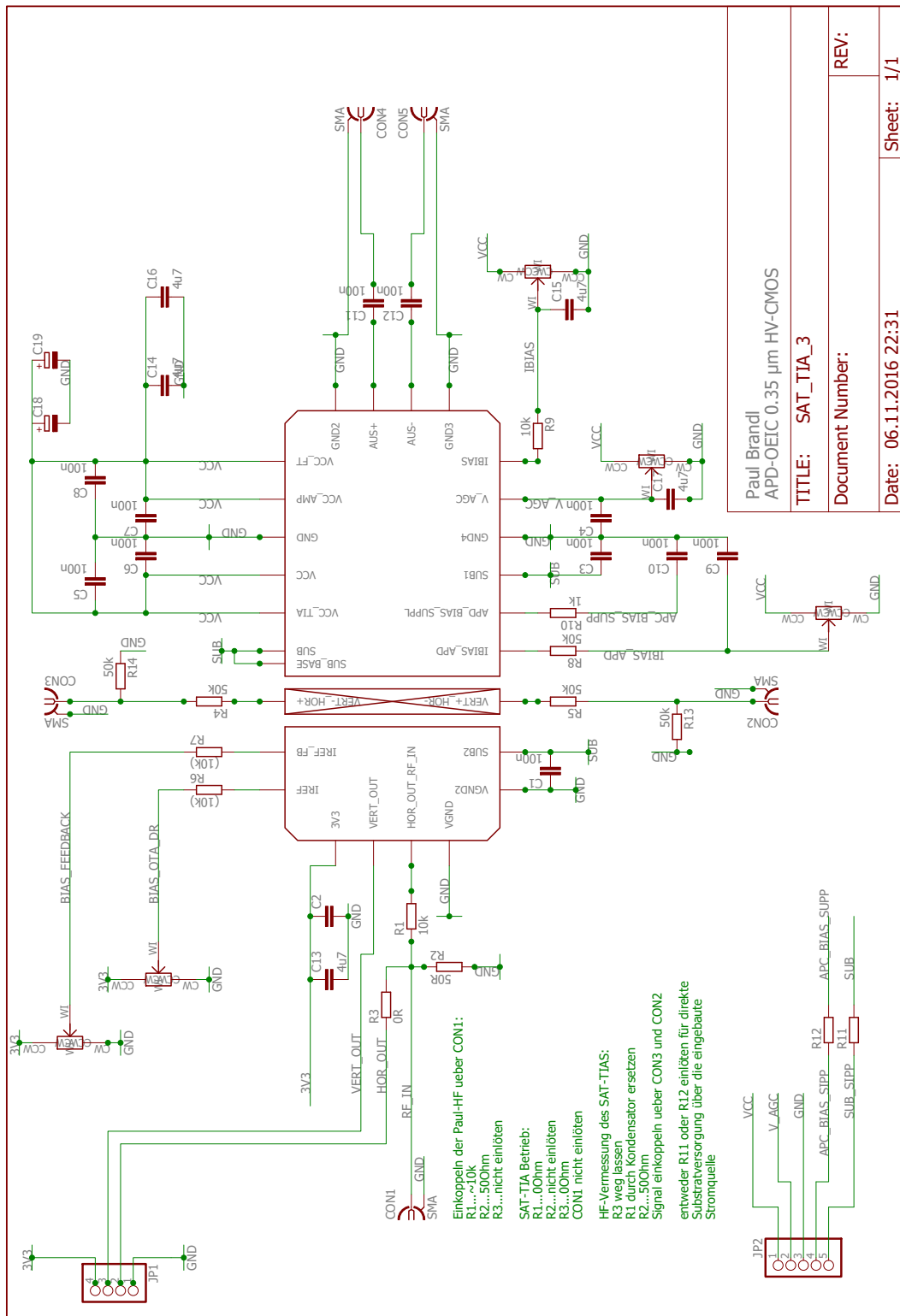
The PCB for the pin-PD OEIC was done on a FR4 material with a thickness of 0.5 mm. To enable direct bonding on the PCB, the PCB had to be covered with a gold layer. The structure size of the PCB was set to 5 mils (0.127 mm). The bias current of the complete OEIC can be adjusted with the potentiometer R5. The differential amplifiers include a cascode stage where the bias voltage of the cascode transistors was set with the potentiometer R9. The potentiometer R12 was used to set the reference voltage for the sensor circuitry which was connected to the surrounding PDs. There is a single voltage output indicating which PD was receiving more optical power. Depending on whether the output voltage is higher or smaller than the reference voltage, the one or the other PDs receives more optical power. Both output signal voltages X and Y were buffered with a low noise rail-to-rail operational amplifier LMP7732 from Texas Instruments. An additional LMP7732 amplifier was used to build the integration circuit to generate the average voltage of the data signal. This voltage was transformed into a current and represented the input signal for the dummy TIA.



B.3. PCB for HV-CMOS APD-OEIC

The PCB for the APD-OEIC was also done on FR4 with a thickness of 0.5 mm. The chip was glued and bonded in the center of the PCB. The potentiometer IBIAS was used to adjust the main bias current of the high-speed receiver. With the potentiometer connected to the V_AGC pin the gate voltage of a MOS-FET for influencing the feedback resistance was controlled. The design included a bias circuitry for the APD. The potentiometer IBIAS_APD was used to set the max. charge current through the APD. The PCB included also supplemental components to characterize the highly-sensitive differential TIA. This means additional connecting possibilities, potentiometers and supplies. With the potentiometer BIAS_OTA_DR the bias current of the differential TIA was influenced. The feedback circuit of the differential TIA was realized with current sources. The current through these sources was adjusted with the potentiometer BIAS_FEEDBACK.

Appendix B. PCB Layouts



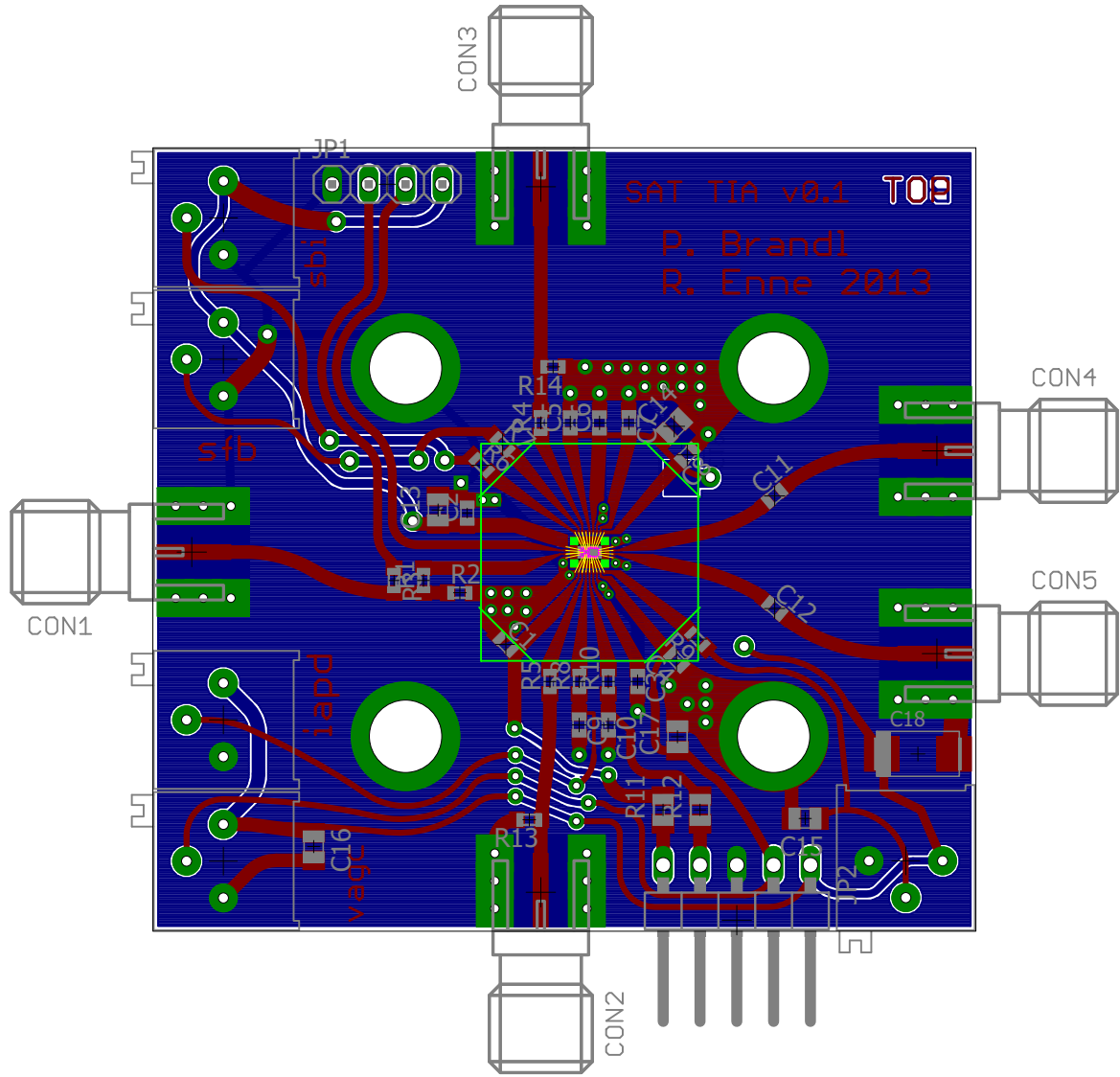


Figure B.3.: PCB for the realized APD-OEIC in $0.35\ \mu\text{m}$ HV-CMOS technology, scale 2:1.

Appendix C.

List of Own Publications

Journal articles

- [1] P. Brandl, T. Jukić, R. Enne, K. Schneider-Hornstein, and H. Zimmermann, "Optical wireless APD receiver with high background-light immunity for increased communication distances," *IEEE Journal of Solid-State Circuits*, vol. 51, no. 7, Jul. 2016. DOI: [10.1109/JSSC.2016.2557815](https://doi.org/10.1109/JSSC.2016.2557815).
- [2] P. Brandl, R. Enne, T. Jukić, and H. Zimmermann, "OWC using a fully integrated optical receiver with large-diameter APD," *IEEE Photonics Technology Letters*, vol. 27, no. 5, pp. 482–485, Mar. 2015. DOI: [10.1109/LPT.2014.2382333](https://doi.org/10.1109/LPT.2014.2382333).
- [3] P. Brandl, S. Schidl, A. Polzer, W. Gaberl, and H. Zimmermann, "Corrections to "optical wireless communication with adaptive focus and MEMS-based beam steering " [Aug 1 2013 1428-1431]," *IEEE Photonics Technology Letters*, vol. 26, no. 23, p. 2411, Dec. 2014. DOI: [10.1109/LPT.2014.2359582](https://doi.org/10.1109/LPT.2014.2359582).
- [4] P. Brandl, R. Enne, T. Jukic, and H. Zimmermann, "Monolithically integrated optical receiver with large-area avalanche photodiode in high-voltage CMOS technology," *Electronics Letters*, vol. 50, no. 21, pp. 1541–1543, Oct. 2014. DOI: [10.1049/el.2014.2504](https://doi.org/10.1049/el.2014.2504).
- [5] P. Brandl, S. Schidl, and H. Zimmermann, "PIN photodiode optoelectronic integrated receiver used for 3-Gb/s free-space optical communication," *IEEE Journal of Selected Topics in Quantum Electronics*, vol. 20, no. 6, pp. 391–400, Nov. 2014. DOI: [10.1109/JSTQE.2014.2336539](https://doi.org/10.1109/JSTQE.2014.2336539).

- [6] P. Brandl, A. Weiss, and H. Zimmermann, "Automated alignment system for optical wireless communication systems using image recognition," *OSA Optics Letters*, vol. 39, no. 13, pp. 4045–4048, Jul. 2014. DOI: [10.1364/OL.39.004045](https://doi.org/10.1364/OL.39.004045).
- [7] P. Brandl and H. Zimmermann, "Development of an optoelectronic integrated circuit for indoor optical wireless communication systems," *Wiley Transactions on Emerging Telecommunications Technologies*, vol. 25, no. 6, pp. 629–637, 2014. DOI: [10.1002/ett.2777](https://doi.org/10.1002/ett.2777).
- [8] P. Brandl, S. Schidl, A. Polzer, W. Gaberl, and H. Zimmermann, "Optical wireless communication with adaptive focus and MEMS-based beam steering," *IEEE Photonics Technology Letters*, vol. 25, no. 15, pp. 1428–1431, Aug. 2013. DOI: [10.1109/LPT.2013.2266574](https://doi.org/10.1109/LPT.2013.2266574).
- [9] P. Brandl and H. Zimmermann, "3 Gbit/s optical receiver IC with high sensitivity and large integrated pin photodiode," *Electronics Letters*, vol. 49, no. 8, pp. 552–554, Apr. 2013. DOI: [10.1049/el.2013.0558](https://doi.org/10.1049/el.2013.0558).
- [10] P. Brandl, R. Swoboda, W. Gaberl, and H. Zimmermann, "Integrated optical receiver for indoor wireless gigabit communication," *Elsevier Optics Communications*, vol. 285, no. 6, pp. 1075–1077, 2012. DOI: <http://dx.doi.org/10.1016/j.optcom.2011.11.111>.
- [11] N. Vokić, P. Brandl, K. Schneider-Hornstein, B. Goll, and H. Zimmermann, "10 Gb/s switchable binary 4-PAM receiver and ring modulator driver for 3-D optoelectronic integration," *IEEE Journal of Selected Topics in Quantum Electronics*, vol. 22, no. 6, pp. 1–9, Nov. 2016. DOI: [10.1109/JSTQE.2016.2564644](https://doi.org/10.1109/JSTQE.2016.2564644).
- [12] D. Milovančev, T. Jukić, P. Brandl, B. Steindl, and H. Zimmermann, "OWC using a monolithically integrated 200 μm APD OEIC in 0.35 μm BiCMOS technology," *OSA Optics Express*, vol. 24, no. 2, pp. 918–923, Jan. 2016. DOI: [10.1364/OE.24.000918](https://doi.org/10.1364/OE.24.000918).

Conference proceedings

- [1] P. Brandl, R. Enne, and H. Zimmermann, "Optical wireless receiver circuit with integrated APD and high background-light immunity," in *IEEE Proc. ESSCIRC 2015 - 41st European Solid-State Circuits Conf. (ESSCIRC)*, Graz, Austria, Sep. 2015, pp. 48–51. DOI: [10.1109/ESSCIRC.2015.7313825](https://doi.org/10.1109/ESSCIRC.2015.7313825).

-
- [2] P. Brandl, W. Gaberl, R. Enne, K. Schneider-Hornstein, and H. Zimmermann, "Highly sensitive 2 Gb/s optoreceiver with CMOS compatible avalanche photodiode," in *Proc. 22nd Austrian Workshop Microelectronics (Austrochip)*, Graz, Austria, Oct. 2014, pp. 1–4. DOI: [10.1109/Austrochip.2014.6946309](https://doi.org/10.1109/Austrochip.2014.6946309).
- [3] P. Brandl and H. Zimmermann, "Optoelectronic integrated circuit for indoor optical wireless communication with adjustable beam," in *Proc. IEEE 8th Conf. Network and Optical Communications (NOC) 18th European Conf. and Optical Cabling and Infrastructure (OC&I)*, Graz, Austria, Jul. 2013, pp. 149–152. DOI: [10.1109/NOC-OCI.2013.6582881](https://doi.org/10.1109/NOC-OCI.2013.6582881).
- [4] P. Brandl, R. Swoboda, W. Gaberl, H. Zimmermann, and E. Leitgeb, "1.25 Gbit/s integrated receiver for optical wireless communication systems," in *Proc. IEEE 8th Int. Conf. on Communication Systems, Networks and Digital Signal Processing (CSNDSP) Symp.*, Poznan, Poland, Jul. 2012, pp. 1–4. DOI: [10.1109/CSNDSP.2012.6292683](https://doi.org/10.1109/CSNDSP.2012.6292683).
- [5] P. Brandl, R. Swoboda, W. Gaberl, and H. Zimmermann, "Optical Wireless Communication at 1.25 Gbit/s with Integrated Receiver in 0.5 μm BiCMOS Technology," in *Proc. 19th Austrian Workshop Microelectronics (Austrochip)*, Vienna, Austria, Oct. 2011, pp. 63–66.
- [6] P. Brandl, T. Plank, and E. Leitgeb, "Optical wireless links in future space communications with high data rate demands," in *Proc. IEEE Int. Workshop Satellite and Space Communications IWSSC 2009*, Siena, Italy, Sep. 2009, pp. 305–309. DOI: [10.1109/IWSSC.2009.5286359](https://doi.org/10.1109/IWSSC.2009.5286359).
- [7] D. Milovančev, P. Brandl, N. Vokić, B. Goll, K. Schneider-Hornstein, and H. Zimmermann, "Optical receivers in 0.35 μm BiCMOS for heterogeneous 3D integration," in *Proc. IEEE 19th Int. Symp. Design and Diagnostics of Electronic Circuits Systems (DDECS)*, Kosice, Slovakia, Apr. 2016, pp. 1–5. DOI: [10.1109/DDECS.2016.7482450](https://doi.org/10.1109/DDECS.2016.7482450).
- [8] A. Polzer, W. Gaberl, R. Swoboda, P. Brandl, J. M. Fedeli, C. Kopp, L. Vivien, and H. Zimmermann, "High sensitivity 80 Gbps parallel optical receiver for hybrid integrated ge photodiodes," in *Proc. 8th IEEE Int. Conf. Group IV Photonics*, London, UK, Sep. 2011, pp. 86–88. DOI: [10.1109/GROUP4.2011.6053724](https://doi.org/10.1109/GROUP4.2011.6053724).
- [9] E. Leitgeb, T. Plank, M. S. Awan, P. Brandl, W. Popoola, Z. Ghassemlooy, F. Ozek, and M. Wittig, "Analysis and evaluation of optimum wavelengths for free-space optical transceivers," in *Proc. IEEE 12th Int. Conf. Transparent Optical Networks*, Munich, Germany, Jun. 2010, pp. 1–7. DOI: [10.1109/ICTON.2010.5549009](https://doi.org/10.1109/ICTON.2010.5549009).

- [10] M. S. Awan, P. Brandl, E. Leitgeb, F. Nadeem, T. Plank, and C. Capsoni, "Results of an optical wireless ground link experiment in continental fog and dry snow conditions," in *Proc. IEEE 10th Int. Conf. Telecommunications ConTEL 2009*, Zagreb, Croatia, Jun. 2009, pp. 45–49.
- [11] E. Leitgeb, M. S. Awan, P. Brandl, T. Plank, C. Capsoni, R. Nebuloni, T. Javornik, G. Kandus, S. S. Muhammad, F. Ghassemlooy, M. Loschnigg, and F. Nadeem, "Current optical technologies for wireless access," in *Proc. IEEE 10th Int. Conf. Telecommunications ConTEL 2009*, Zagreb, Croatia, Jun. 2009, pp. 7–17.
- [12] E. Leitgeb, P. Brandl, T. Plank, M. Loschnigg, F. Ozek, M. S. Awan, and M. Wittig, "Reliable optical wireless links used as feeder links between earth and satellite," in *Proc. IEEE 11th Int. Conf. Transparent Optical Networks*, Azores, Portugal, Jun. 2009, pp. 1–7. DOI: [10.1109/ICTON.2009.5184993](https://doi.org/10.1109/ICTON.2009.5184993).
- [13] M. S. Awan, P. Brandl, E. Leitgeb, F. Nadeem, L. Csugai-Horvath, and R. Nebuloni, "Transmission of high data rate optical signals in fog and snow conditions," in *Proc. IEEE 1st Int. Conf. Wireless Communication, Vehicular Technology, Information Theory and Aerospace Electronic Systems Technology Wireless VITAE 2009*, Aalborg, Denmark, May 2009, pp. 702–706. DOI: [10.1109/WIRELESSVITAE.2009.5172534](https://doi.org/10.1109/WIRELESSVITAE.2009.5172534).
- [14] E. Leitgeb, M. S. Awan, T. Plank, N. Perlot, C. Capsoni, R. Nebuloni, T. Javornik, G. Kandus, F. Nadeem, P. Brandl, S. S. Muhammad, M. Loschnigg, M. S. Khan, E. Duca, and S. Betti, "Investigations on free-space optical links within SatNEx II," in *Proc. IEEE 3rd European Conf. Antennas and Propagation*, Berlin, Germany, Mar. 2009, pp. 1707–1711.
- [15] S. S. Muhammad, P. Brandl, E. Leitgeb, O. Koudelka, and I. Jelovcan, "VHDL based FPGA implementation of 256-ary PPM for free space optical links," in *Proc. IEEE 9th Int. Conf. Transparent Optical Networks*, vol. 3, Rome, Italy, Jul. 2007, pp. 174–177. DOI: [10.1109/ICTON.2007.4296273](https://doi.org/10.1109/ICTON.2007.4296273).

Research reports

- [1] P. Brandl, T. Plank, E. Leitgeb, N. Witternigg, M. Schönhuber, B. Hillbrand, and N. Djaja, "WP50 (Extension) (TN5) System Design of reliable high capacity feeder links through the atmosphere," ESA, ESA/ESTEC Contract 21992/08/NL/US, 2010.

-
- [2] P. Brandl, T. Plank, E. Leitgeb, N. Witternigg, M. Schönhuber, and B. Hillbrand, "WP40 (TN4) System Design of reliable high capacity feeder links through the atmosphere," ESA, ESA/ESTEC Contract 21992/08/NL/US, 2010.
- [3] P. Brandl, N. Witternigg, E. Leitgeb, B. Hillbrand, F. Nadeem, T. Plank, and P. Zeller, "WP30 Trade-off of optical technologies and techniques for reliable free space optical communications through the atmosphere," ESA, ESA/ESTEC Contract 21992/08/NL/US, 2009.
- [4] P. Brandl, M. S. Khan, M. Saleem Awan, F. Nadeem, E. Leitgeb, T. Plank, N. Witternigg, and M. Schönhuber, "WP20 Assessment of optical technologies and techniques for reliable free space optical communications through the atmosphere," ESA, ESA/ESTEC Contract 21992/08/NL/US, 2009.
- [5] M. Schönhuber, N. Witternigg, E. Leitgeb, P. Brandl, T. Plank, B. Hillbrand, F. Nadeem, P. Zeller, and M. Dominguez, "Feasibility Assessment of Optical Technologies & Techniques for Reliable High Capacity Feeder Links – Final Report," ESA, ESA/ESTEC Contract 21992/08/NL/US, 2011.
- [6] N. Witternigg, M. Schönhuber, P. Brandl, E. Leitgeb, T. Plank, and M. Dominguez, "WP10 Establishment of user requirements and telecom scenarios for future high capacity feeder links," ESA, ESA/ESTEC Contract 21992/08/NL/US, 2009.

Appendix D.

Curriculum Vitae

Paul Brandl

Personal Details

Date of birth: 17 January 1980
Place of birth: Feldbach, Austria
Nationality: Austrian
Permanent address: Hanningerweg 20
4501 Neuhofen an der Krems
Austria
E-Mail: pbrandl@gmx.at



Education

04/2010 – present Ph.D. studies at Technische Universität Wien
Institute of Electrodynamics, Microwave and
Circuit Engineering
06/2006 Graduation to Dipl-Ing. at Technische Universität Graz
Master Thesis: Hardware-Implementierung von PPM
für Lichtfunksysteme
09/2004 – 06/2005 Polytech Lille, France
Exchange programme
10/2000 – 06/2006 Studies of Electrical Engineering at Technische

Universität Graz
Telecommunication engineering and electronics
09/1994 – 06/1999 Upper Secondary School for Technology, HTL Weiz
Automation and Control

Work Experience

08/2016 – present Development Engineer at DICE GmbH & Co KG
(major owned by Infineon Technologies AG), Linz, Austria
04/2010 – 07/2016 Project Assistant at the Institute of Electrodynamics,
Microwave and Circuit Engineering,
Technische Universität Wien
12/2008 – 06/2010 Research Assistant at the Institute of
Broadband Communication, Technische Universität Graz
10/2006 – 10/2008 Development Engineer at AT4wireless, Malaga, Spain
07/2000-08/2002 Technician at Rosendahl Maschinen GmbH
Pischelsdorf, Austria

Professional Skills

Analog and mixed-signal integrated circuit design
Optoelectronic integrated circuit design
Development of optical communication systems
Proficient in CADENCE environment
Measurement and instrumentation on wafer and system level
FPGA programming, Altera Quartus, Xilinx ISE and EDK
Programming of signal processors, TI Code Composer
LabVIEW, Matlab/Simulink
Proficient in VHDL, C, C++

Language Skills

German: native
English: fluent
Spanish: fluent
French: intermediate
Portuguese: basic

October 2016